Spatial and temporal metrology of coherent ultrashort pulses inthe extreme-ultraviolet domain

Hugo Dacasa Pereira

To cite this version:

Hugo Dacasa Pereira. Spatial and temporal metrology of coherent ultrashort pulses inthe extreme-ultraviolet domain. Optics [physics.optics]. Université Paris Saclay (COmUE), 2017. English. NNT : 2017SACLX041 . tel-01668564

HAL Id: tel-01668564
https://pastel.hal.science/tel-01668564

Submitted on 20 Dec 2017

NNT : 2017SACLX041

Thèse de doctorat
de l'Université Paris-Saclay
préparée au Laboratoire d'Optique Appliquée

École doctorale n°572
École Doctorale Ondes et Matière
Spécialité de doctorat: Physique

par

Hugo DACASA PEREIRA

Spatial and temporal metrology of coherent ultrashort pulses in the extreme-ultraviolet domain

Thèse présentée et soutenue à Palaiseau, le 29 septembre 2017.

Composition du Jury :

M. Marino Marsi	Professeur	UPsud	(Président du jury)
M. Pedro Velarde	Professeur	UPM	(Rapporteur)
M. Jan Lüning	Professeur	UPMC	(Rapporteur)
M. Guillaume Dovillaire	Ingénieur de recherche	Imagine Optic	(Examinateur)
Mme. Anne L'Huillier	Professeure	LLC	(Examinatrice)
M. Philippe Zeitoun	Directeur de recherche	LOA	(Directeur de thèse)

universite
PARIS-SACLAY

ÉCOLE DOCTORALE
Ondes et Matière
(EDOM)

Titre : Métrologie spatiale et temporelle des impulsions cohérentes et ultra-brèves dans le domaine ultraviolet extrême

Mots clefs : Harmonique d'ordre élevé, Laser à électrons libres, Front d'onde, Laser X, Métrologie temporelle, Amplification à dérive de fréquence

Résumé : Aujourd'hui, il existe trois sources principales délivrant des impulsions ultra-brèves de rayonnement ultraviolet extrême (UVX). Les harmoniques d'ordre élevé (HHG, en anglais) générés dans les gaz rares peuvent fournir des impulsions attosecondes. Cependant, leur énergie, le plus souvent de l'ordre du nanojoule, limite les applications. L'amplification des impulsions harmoniques dans les plasmas créés par laser (SXRL, en anglais) peut fournir des énergies de plusieurs dizaines de microjoules. Des énergies plus élevées peuvent être obtenues avec les lasers à électrons libres (LEL) UVX injectés, mais ce sont des très grandes infrastructures ayant un accès plus limité.

Ces dernières années, des progrès significatifs ont été réalisés avec chacune des ces sources, avec pour objectif la génération d'impulsions plus brèves. Il est devenu nécessaire de développer des nouvelles techniques de métrologie temporelle des impulsions XUV ultra-brèves. De plus, beaucoup d'expériences, comme celles impliquant des phénomènes non-linéaires, nécessitent de hautes intensités UVX. La focalisation efficace des impulsions de faibles énergies peut significativement augmenter le domaine d'application. De bons fronts d'onde sont nécessaires pour focaliser les impulsions UVX à haute intensité, et les optiques doivent aussi être de bonne qualité et alignées avec précision.

Dans cette thèse, les propriétés spatiales des harmoniques d'ordre élevé ont été étudiées en profondeur grâce à un senseur de front d'onde UVX. Cet appareil, couplé à une source HHG a démontré être utile pour la caractérisation de table et à la longueur d'onde ainsi que pour l'optimisation de systèmes optiques UVX. Le problème de la mise en place de la caractérisation temporelle d'impulsions UVX est aussi discuté en détail, et deux nouveaux schémas pour la complète reconstruction d'impulsions de LEL injectés et de lasers X à plasma sont présentés. Finalement, la première implantation d'un système d'amplification à dérive de fréquence (CPA, en anglais) sur un LEL UVX est présentée et son implantation pour les lasers X à plasmas est aussi discutée.

Title : Spatial and temporal metrology of coherent ultrashort pulses in the extreme-ultraviolet domain

Keywords : High-harmonic generation, Free-electron laser, Wavefront, X-ray laser, Temporal metrology, Chirped pulse amplification

Abstract : Nowadays, there are three main of ultrashort pulses in the extreme-ultraviolet (XUV) spectral domain. High-order harmonic generation (HHG) in rare gases is able to provide attosecond pulses. However, their energy, often of the order of nanojoules, limits their number of applications. Amplification of such pulses in laser-driven plasmas can provide energies of tens of microjoules. Higher pulse energies can be obtained from seeded XUV free-electron lasers (FELs), large-scale facilities with more limited accessibility.

In recent years, significant progress has been made with each of these sources towards the generation of shorter pulses. It is thus necessary to develop new techniques for full temporal metrology of ultrashort XUV pulses. Additionally, many experiments, such as those involving nonlinear phenomena, require high XUV intensities. Efficient focusing of low-energy pulses can significantly increase their range of application. Good wavefronts are required in order to focus light pulses to high intensities, and the optics must be of high quality and precisely aligned.

In this thesis, the spatial properties of high-harmonic pulses are extensively explored thanks to the use of an XUV Hartmann wavefront sensor. This device is also proven here to be useful for tabletop, at-wavelength characterization and optimization of XUV optical systems with HHG sources. The problem of performing full temporal characterization of XUV pulses is also discussed in detail, and two new schemes for complete pulse reconstruction for seeded XUV FELs and seeded SXRLs are presented. Finally, the first implementation of chirped pulse amplification (CPA) in a seeded XUV FEL is reported, and its implementation in seeded SXRLs is discussed as well.

Université Paris-Saclay
Espace Technologique / Immeuble Discovery
Route de l'Orme aux Merisiers RD 128 / 91190 Saint-Aubin, France

Acknowledgements

I would like to start by thanking Philippe Zeitoun for his continued guidance, support, and patience during these four years at the Laboratoire d'Optique Appliquée. Everything that is reported in this thesis was ultimately achieved thanks to him. I could not have had a better supervisor, and I wish we can keep working together in the future.

Secondly, I would also like to thank all former and current members of our team with whom I have worked directly. Benoît Mahieu and Lu Li helped me greatly during my first steps in the world of scientific research, and I cannot thank them enough for their support. The current team members, Elena Longo, Jayanath C. P. Koliyadu, Daniel Adjei, and the recently arrived Domenico Alj have made the long writing process much more bearable during my final year as a PhD student.

There are many other researchers from LOA who have helped me with experiments, given valuable advice for my work, or just had a chat every now and then. In particular, other members from the FLEX group, Stéphane Sebban, Julien Gautier, Fabien Tissandier, and Antoine Rousse, as well as people from other teams such as Magali Lozano, Jean-Philippe Rousseau, Davide Boschetto, Yi Liu, Aline Vernier, Geoffrey Gallé, Carla Alves, Mariusz Lejman, and many others. Many thanks, in particular, to Isabel González for all the coffee breaks during this last year.

I wish to acknowledge my many collaborators from France and abroad. I am very grateful to Eduardo Oliva from UPM, Spain, from whom I learned a lot during my first months here. Special thanks also to Mabel Ruiz-López and Davide Bleiner from Empa, Switzerland. I also want to thank the people with whom I have worked in different labs around Europe, such as David Garzella from CEA, France, David Gauthier and Giovanni de Ninno from FERMI, Italy, and Stephen White and Brendan Kettle from QUB, UK. Thanks as well to Ombeline de la Rochefoucauld and Guillaume Dovillaire from Imagine Optic. Finally, I am also very grateful for the time I spent doing experiments at the LLC, Sweden, with Piotr Rudawski, Sylvain Maclot, Anne L'Huillier and the rest of their great group.

Je tiens à remercier aussi aux autres gens du LOA que d'une façon ou d'autre ont été nécessaires pour le bon déroulement de mon travail de thèse. Je n'aurais pas pu faire face à l'abominable bureaucratie française sans l'aide de tout l'équipe du sécretariat, Octavie Verdun, Lucie Huguet, Carole Gratpanche, Sandrine Tricaud, Patricia Toullier et Catherine Buljore. En plus, la plupart de nos expériences de laboratoire auraient été carrément impossibles sans le travail des membres de l'atélier mécanique, Jean-Lou Charles, Bernard Allali et Florian Oper. Je voudrais rémercier aussi au reste de l'équipe de soutien, Grégory Iaquaniello, Mouhcine Adraoui, Thomas Lavergne et Maxence Le Sourd.

Quiero dar las gracias a toda la gente de España que he tenido la suerte de conocer en París durante estos últimos años, especialmente a Ana Albertos, Maricarmen Baena, Pilar Aranguren, Marta Sánchez y María Delgado. Y de paso me gustaría también agradecer su apoyo a otros amigos de varias partes del país, sobre todo a Isabel Valverde, Clara Lázaro, Julia García, Geanna Marín, Nazareth López, Tomás Lama y Alba Muñoz.

Xa para rematar, gustaríame agradece-lo seu continuo apoio a meus pais, Antonio Dacasa e María Dolores Pereira, e a meu irmán Borja Dacasa. Moitas grazas tamén a tódolos meus amigos de Ourense, salientando a Kevin Huete, Paula Rodríguez, Raquel Pérez, Sara Vázquez, Ariana López, Patricia Gutiérrez, Raquel Vázquez, Guillermo de Andrés, Antón Fernández, Andrea Barros, Lucía Fernández, Aldara Méndez e a Tamara Fernández.

Moitísimas grazas por todo, Elia do Souto. Sen ti, nada disto tería sido posíbel.

The work reported in this thesis was partially funded by H2020 Laserlab Europe n° 654148, H2020 FET-Open grant n° 665207 VOXEL, the COST Action MP1203, PALM FEL-Shaping and École Polytechnique.

List of abbreviations

ASE	Amplified spontaneous emission
BBO	Beta barium borate
CCD	Charge-coupled device
CEP	Carrier-envelope phase
CHG	Coherent harmonic generation
CPA	Chirped pulse amplification
EUV/XUV	Extreme ultraviolet
FEL	Free-electron laser
FROG CRAB	Frequency-resolved optical gating for complete reconstruction of attosecond bursts
FTSI	Fourier-transform spectral interferometry
FWHM	Full width at half maximum
GD	Group delay
GDD	Group delay dispersion
HGHG	High-gain harmonic generation
HHG	High-order harmonic generation
IR	Infrared
PDI	Point diffraction interferometry
PM	Primary mirror
PV	Peak-to-valley
QSS	Quasi-steady-state
RMS	Root mean square
SASE	Self-amplified spontaneous emission
SEA TADPOLE	Spatially encoded arrangement for temporal analysis by dispersing a pair of light E-fields
SHG	Second harmonic generation
SM	Secondary mirror
SPIDER	Spectral phase interferometry for direct electric-field reconstruction
SXRL	Soft-X-ray laser
TCE	Transient collisional excitation
THG	Third harmonic generation
TOD	Third order dispersion
TBP	Time-bandwidth product
VMI	Velocity map imaging
WDM	Warm dense matter
WFS	Wavefront sensor

Contents

Introduction

High-order harmonic generation (HHG) in gases, which provides coherent and ultrashort pulses in the extreme ultraviolet (XUV or EUV) and soft-X-ray domains, was demonstrated in the 1980s [1, 2, 3]. However, it was not until the 2000s that its range of applications underwent a strong boost, along with plasma-based seeded soft-X-ray lasers (SXRLs) [4] and XUV free-electron lasers (FELs) [5]. Some of their applications include plasma physics [6], materials science [7], chemistry [8] or biology [9]. These laser-like sources, like visible lasers, generate collimated and generally polarized beams [5, 10, 11] with good spatial and temporal coherent properties [11, 12, 13, 14, 15]. In the last decade, their spectral range $(10\,\mathrm{eV} - 1\,\mathrm{keV})$ has been extended to the hard-X-ray range $(1 - 10\,\mathrm{keV})$, thanks to further development of FELs [16].

Despite their successful implementation for a wide range of applications, further development of these sources remains limited by the difficulty to achieve full spatial and temporal metrology of the beams they provide. In particular, developing accurate techniques for full temporal characterization of XUV pulses is fundamental in order to achieve shorter durations. Significant progress has been made in recent years towards the measurement of the duration of high-harmonic pulses, which have been observed under $100\,\mathrm{as}$ [17]. However, most of the techniques for HHG pulses cannot be applied to seeded SXRLs due to their particular properties or to FELs due to their intrinsic shot-to-shot instability. Indeed, FELs are based on the amplification of stochastic emission unless seeded by an external pulse [5]. This thesis reports the adaptation of two potentially single-shot techniques for full temporal metrology of seeded XUV FELs and plasma-based SXRLs seeded by high-harmonic pulses.

Along with achieving shorter pulse durations, one of the main goals of the XUV and X-ray sources community has been to achieve higher intensities, which requires efficient focusing. FEL facilities are generally equipped with very high quality X-ray optics, which ensure tight focusing if the incoming beam has a good wavefront and the optics are precisely aligned. These two issues require the use of dedicated wavefront sensors (WFS), commercially available nowadays for the XUV and X-ray domains.

The situation is different for HHG sources. The few experiments performed so far on the topic of spatial metrology of high-harmonic pulses show a large disparity in the achieved wavefronts, from diffraction-limited [18] to relatively poor ones [19, 20]. These sources are becoming more and more common thanks to their capabilities for tabletop experiments in the XUV domain. However, the study of nonlinear phenomena requires high intensities, and thus tight focusing of the harmonic beams. Since high harmonics are used to seed both plasma-based SXRLs and FELs, it is of major importance to improve our understanding of their spatial properties and, in particular, the link between the driving laser and the harmonic wavefronts. This topic is explored experimentally in this thesis. Additionally, the use of an XUV WFS for real-time optimization of the alignment of a focusing optical system for high harmonics is also demonstrated.

Besides tighter focusing, achieving higher intensities requires increasing the pulse energy as well. One way to achieve this is the implementation of chirped pulse amplification (CPA) schemes for seeded XUV sources [21]. This topic is discussed in this thesis as well, and the first implementation of this scheme in a seeded XUV FEL is reported. The manuscript is structured as follows:

The theory and basic properties of HHG are presented in chapter 1. Then, the principles of wavefront metrology by means of an XUV Hartmann WFS are laid out. Two experiments are reported in this chapter in which this sensor is used to study the spatial properties of single high-harmonic pulses as a function of the generation conditions, as well as the influence of the driving pulse wavefront.

Chapter 2 explores the possibility of using high harmonic beams for tabletop and at-wavelength characterization of multilayer XUV optics by means of wavefront metrology. The use of the XUV Hartmann sensor for fast and precise optimization of XUV focusing systems for high-harmonic radiation is also reported.

In chapter 3, a pump-probe experiment is reported in which high-harmonic pulses were used to probe the properties of radiatively heated warm dense aluminum samples, in order to compare the results to the predictions of two existing numerical models.

The problem of temporal metrology of ultrashort pulses in the XUV domain is discussed in detail in chapter 4. The possibility of transferring existing methods for visible and infrared lasers to shorter wavelengths is explored. Then, two new schemes for full, single-shot, temporal characterization of pulses from XUV seeded FELs and plasma-based SXRL seeded by high-harmonics are reported.

Chapter 5 reports the first implementation of chirped pulse amplification in a seeded XUV FEL. The possibility of applying this technique to seeded SXRLs is also discussed, as well as the implementation of more efficient pulse compressors based on conical diffraction geometry.

Lastly, a brief summary of this work is presented, as well as some future prospects for ultrafast XUV sources.

CHAPTER 1

High-harmonic generation in gases: spatial properties

Contents

High-order harmonic generation (HHG) in gases is a highly nonlinear optical process by which a linearly polarized laser pulse is focused on a gas jet or cell to intensities of the order of $10^{14-15}\,\mathrm{W/cm^2}$, producing spatially [12, 13] and temporally coherent [14] ultrashort pulses [22] at odd, integer multiples of its frequency [1, 2, 3], generally in the ultraviolet (UV), extreme ultraviolet (XUV or EUV) or soft-X-ray regimes [23, 24].

Due to its properties, such as a its spectrum or its temporal and spatial coherence, HHG is a useful tabletop source of short-wavelength radiation for a wide range of applications, including nonlinear XUV optics [25], attosecond physics [26, 27, 28], XUV spectroscopy [29] or plasma physics [6].

This chapter focuses on HHG in gases and their spatial properties. HHG was first discovered experimentally during the 1980s [1, 2, 3], and explained theoretically during the subsequent years [30, 31]. Simply put, high-harmonics are generated when the driving laser ionizes electrons from the atoms of the medium, which are then accelerated in its electric field, and then recombined back with their parent ion, converting their kinetic energy into photons. This is known as the three-step model of HHG, which is explained in detail in section 1.1, along with other theoretical aspects related to it. In section 1.2, the Salle Corail high-harmonic beamline of LOA is presented, as well as several experimental aspects of HHG. Lastly, section 1.3 reports two experiments in which the spatial properties of high-harmonic pulses are studied in detail, as well as their relation to the driving laser.

1.1 Theory and basic characteristics of high-harmonic generation in gases

To understand high-harmonic generation, two separate processes must be studied: the emission of an atom under the electric field of the laser, and the effect of the propagation medium as a whole, mainly the phase matching, but also the absorption of the generated radiation by the gas itself. High-harmonic radiation generated in gases consists of coherent [32], ultrashort [22], and linearly polarized pulses [10]. Its spectrum consists in a frequency comb, containing only odd multiples of the angular frequency of the driving laser, called the fundamental frequency ω_0, which is usually in the infrared (IR) range [33].

Three different spectral regions can be defined [34], based on the dependence of harmonic intensity with respect to the harmonic order q: a so-called *perturbative region* for low orders, where the intensity decreases with q, a *plateau*, where the harmonic intensity is constant with respect to q, and a *cutoff*, where the intensity quickly decreases to zero with q. A typical harmonic spectrum can be seen in figure 1.1. The broad spectra usually obtained by HHG in gases allow for the generation of trains of attosecond pulses [35].

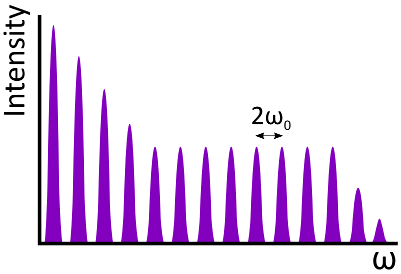

Figure 1.1: Schematic drawing of a typical spectrum obtained through high-harmonic generation in gas, consisting of odd multiples of the fundamental frequency ω_0.

The cutoff marks the maximum harmonic order that can be generated. It was found experimentally [36, 37] to be:

$$E_{max} = 3.17U_p + I_p, \tag{1.1}$$

where $U_p = \frac{e^2E^2}{4m\omega^2}$ is the ponderomotive potential of the electron with mass m and charge e, in the electric field E of the driving laser of angular frequency ω, and I_p is the ionization potential of the atom. This means that, in order to generate very short wavelengths, it is necessary to use a gas with a high ionization potential, generally a noble gas like argon, neon or xenon, and a driving laser with long wavelength and high intensity. However, increasing laser intensity indefinitely is actually detrimental to the generation due to ionized electrons not recombining with their parent ions and thus not emitting photons.

Another important characteristic of any laser-driven source is its conversion efficiency [38]. In the case of HHG in gases, it is usually very low and dependent on the particular gas used. Values such as 10^{-7} were measured in early experiments with neon [39], for example. To improve it, one must first optimize the phase-matching conditions, which are explained in section 1.1.2. Several methods are available to further optimize the generation, for example, it is possible to use a long gas cell instead of a jet, to increase interaction volume [40]. This, along with loose focusing geometry to obtain longer Rayleigh lengths, will increase the interaction volume, thus increasing the energy output as long as the phase matching is kept. However, it is also important to consider that the medium can also absorb the harmonics [3, 41, 42] and choose the medium length to match the confocal parameter of the driving laser. Using this and other methods, improved conversion efficiencies have been reported over the years by different teams, such as 10^{-6} [43] and $1.5 \cdot 10^{-5}$ [40] for the case of argon or $4 \cdot 10^{-5}$ [41] for xenon.

1.1.1 Single-atom response

The most successful theoretical models for HHG in gas jets were proposed during the early 90's. They are based on studying the behavior of a single atom subjected to the electric field of the laser. There are two main approaches which will be summarized in the next sections: a semiclassical model [30] and a quantum model [31].

1.1.1.1 The semiclassical approach: three-step model

The semiclassical model presented in this section was developed in 1993 to explain several non-linear phenomena: high-harmonic generation, double ionization and above-threshold ionization. It is based on applying Newtonian physics to study the movement of ionized electrons in the electric field of the linearly polarized driving laser [30]. This section, however, focuses solely on HHG. The process is divided in three separate steps, illustrated in figure 1.2:

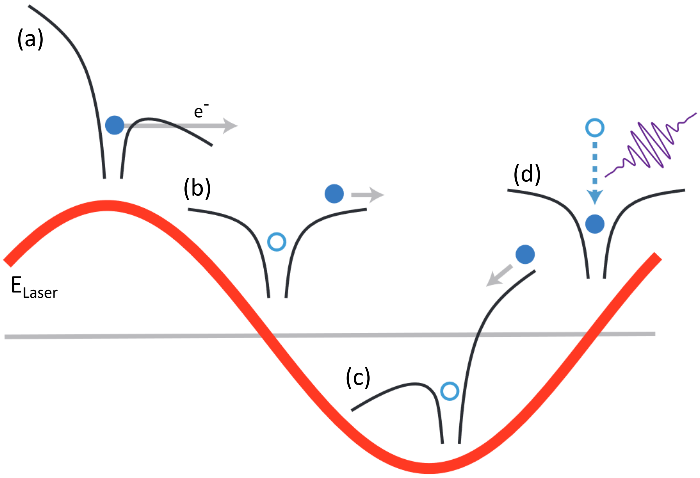

Figure 1.2: Schematic drawing summarizing the three-step model, showing the effect of the electric field of the driving laser on the Coulomb potential that binds the electron to the gas atom. The first step is the tunnel ionization of the electron (a), which is then accelerated away from the atom (b). The electron is then accelerated in the opposite direction when the external field is reversed (c), and finally it is recombined with its parent ion, emitting XUV radiation (d). Taken from [44].

The first step is the ionization of the atom. There are different ionization processes, excluding resonances, that can occur depending on the intensity of the laser pulse focused on the gas:

- *Multiphoton ionization* [45] occurs at lower intensities than the other types, and is based on an electron absorbing several photons to gain enough energy to overcome its ionization potential, transitioning to a free state.

- *Tunnel ionization* occurs when the laser intensity is higher than $\sim 10^{13}\ \mathrm{W/cm^2}$. In this regime, the laser's electric field is comparable to the Coulomb potential that binds an electron from the outer shell of the atom, and affects the total potential to which the electron is subjected. During the maxima of the laser field, the total potential becomes a narrow barrier, so twice during an optical cycle, the electron can transition to a free state via tunneling [46].

- When the laser intensity is very high, *barrier-suppression ionization* occurs instead. In this case, the electric field acting on the atom is so strong that it completely suppresses the atomic potential, with the electron easily transitioning to a free state [47].

The HHG process begins with the tunnel ionization of an electron. The second step consists on the acceleration of the electron by the laser electric field. The model uses classical mechanics to describe the electron motion in the field, which has the form $\vec{E}(t) = E_0 \cos(\omega t)\,\vec{e_x} + \alpha E_0 \sin(\omega t)\,\vec{e_y}$, where $\alpha = 0$ for linear polarization, as is the case for HHG, and takes a value between -1 and $+1$ for circular or elliptical polarization. The magnetic field of the laser and the electric field from the ion are neglected, and the initial conditions of position and velocity of the electron right after ionization are considered to equal 0. The motion of the electron is described by:

$$v_x = v_0 \sin(\omega t) + v_{0x} \qquad v_y = -\alpha v_0 \cos(\omega t) + v_{0y} \tag{1.2}$$

$$x = x_0\,(-\cos(\omega t)) + v_{0x} t + x_{0x} \qquad y = \alpha x_0\,(-\sin(\omega t)) + \alpha v_{0y} t + y_{0y}, \tag{1.3}$$

where $v_0 = \frac{eE_0}{m\omega}$, $x_0 = \frac{eE_0}{m\omega^2}$ and v_{0x}, v_{0y}, x_{0x} and y_{0y} are given by the initial conditions. It can be seen that, when using a linearly polarized driving laser, as in the case of HHG (i. e. $\alpha = 0$), the electron movement is restricted to the direction of the laser polarization. Then, as the last step of the process, the electric field changes sign for the second half of the laser optical cycle, and the electron is recombined with its parent ion. In doing so, the kinetic energy it gained inside the field, plus its ionization potential are emitted as a single, energetic photon. The whole process occurs every half cycle of the driving laser.

From the previous equations, it can be shown that for circularly or elliptically polarized light, the electron does not always go back to its parent ion, so that harmonics are not emitted efficiently. The equations also allow for the calculation of the probability that an electron has of recombining as a function of its kinetic energy, which in turn leads to the expression of the cutoff $E_{max} = 3.17U_p + I_p$, in agreement with the experimentally found equation given earlier. $3.17U_p$ is the maximum kinetic energy that an electron can have for it to recombine with its parent ion. Given that the cutoff energy is directly proportional to the laser intensity, generating shorter wavelengths, as well as increasing the overall harmonic output, should be achieved by having the highest possible laser intensity. However, this is counter-productive due to causing barrier-suppression ionization. In this regime, the ionized electrons do not return to the ion, meaning that there is both a lower and upper limits for laser intensity for efficient HHG.

The harmonic emission can be calculated by obtaining the wave function Ψ of the electron in the continuum, and calculating with it the expectation value of the dipole operator, $\langle\Psi|ex|\Psi\rangle$. With this, the model can predict the spectrum emitted by a single atom. This is explained in further detail in the next section.

1.1.1.2 The quantum approach: Lewenstein's model

In the year 1994, a fully quantum model of the single-atom emission of HHG in gases was presented [31], accounting for quantum effects not included in the semiclassical model. The behavior of the electron in the driving electric field is described in terms of quantum mechanics in the frame of the strong field approximation (SFA), by studying the evolution of the wave packet and calculating the dipole matrix. Assuming an atom subjected to a linearly polarized and monochromatic electric field, and using natural units for simplicity ($e = m = \hbar = 1$), the Schrödinger equation describing the system is:

$$i\frac{\partial\left|\Psi(\vec{x},t)\right\rangle}{\partial t} = \left(-\frac{1}{2}\nabla^2 + V(\vec{x}) - E\cos(t)x\right)\left|\Psi(\vec{x},t)\right\rangle \tag{1.4}$$

The next assumptions are made as well:

- The photon energy of the driving laser is much lower than the ionization potential of the atom, $I_p \gg \omega$. A single photon will not ionize the atom.
- The ponderomotive potential is greater than said ionization potential, $U_p > I_p$. This condition means that the electron in the continuum will be mostly affected by the electric field, with negligible effects of the atomic potential $V(x)$.
- Ionization is assumed to be weak. This happens when the laser intensity is below saturation intensity, that in which all atoms are ionized, $U_p \ll U_{sat}$.

These conditions ensure that tunneling ionization is the predominant process, with laser intensities in the range $10^{14} - 10^{15}$ W/cm^2.

The initial state of the atom, that in which the electron is bound, is noted by $|0\rangle$. Then, at the instant t', the electron tunnels out of the ion when the electric field reaches its peak in the optical cycle, transitioning to the continuum, where its state is noted by $|\vec{v}\rangle$. As mentioned before, the model seeks to calculate the matrix elements of the atomic dipole. The matrix element for the bound-free transition (again, taking $e = 1$) is then $d_x(\vec{v}) = \langle\vec{v}|x|0\rangle$. The wave function of the electron must be obtained first by solving equation 1.4. First, the wave function is assumed to have the form:

$$\left|\Psi(\vec{x},t)\right\rangle = e^{iI_pt}\left(a(t)\left|0\right\rangle + \int d^3\vec{v}\; b(\vec{v},t)\left|\vec{v}\right\rangle\right), \tag{1.5}$$

where the second term is treated as a perturbation of the initial state $a(t)\,|0\rangle$ ($a(t) \simeq 1$). It can be obtained by solving another Schrödinger equation, leading to:

$$b(\vec{v},t) = i\int_0^t dt' E\cos t'\, d_x(\vec{v}+\vec{A}(t)-\vec{A}(t'))\exp\left(-i\int_{t'}^t dt''\left(I_p + \frac{(\vec{v}+\vec{A}(t)-\vec{A}(t''))^2}{2}\right)\right), \tag{1.6}$$

where $\vec{A}(t) = -E\sin(t)\vec{e_x}$ is the vector potential of the laser field, and the integral is calculated from the instant of ionization t' to the instant of recombination, t. This wave function is then introduced in the definition of dipole, $x(t) = \langle\Psi(t)|x|\Psi(t)\rangle$, and the canonical momentum $\vec{p} = \vec{v} + \vec{A}$ is introduced, yielding:

$$x(t) = i\int_0^t dt' \int d^3\vec{p}\, E\cos(t')\, d_x(\vec{p}-\vec{A}(t'))\, d_x^*(\vec{p}-\vec{A}(t))\exp(-iS(\vec{p},t,t')) \tag{1.7}$$

$$S(\vec{p},t,t') = \int_{t'}^{t} dt'' \left(I_p + \frac{(\vec{p}-\vec{A}(t''))^2}{2}\right). \tag{1.8}$$

Equation 1.7 is the sum of the probability amplitudes of the electron transition to the continuum at time t' with momentum $\vec{p}$, and the propagation of the wave function, where it acquires a phase related to the semiclassical action $S(\vec{p},t,t')$ at the time t of recombination, with a probability amplitude of $d_x^*(\vec{p}-\vec{A}(t))$.

Having found the dipole matrix, the harmonic spectrum can be calculated, given by the Fourier transform of $x(t)$. It can be seen that all the even Fourier components vanish from the calculation due to the central symmetry of the atomic potential $V(x)$, which leads to the emission of only odd harmonics, as observed experimentally.

Along with the emitted spectrum, the cutoff law is also obtained, with the form:

$$E_{max} = 3.17U_p + I_p F(I_p/U_p), \tag{1.9}$$

where the factor $F(I_p/U_P)$ takes a value of 1.3 when $I_p \ll U_p$, and approaches 1 when I_p increases. This shows a remarkable agreement with both the semiclassical three-step model and with experimental data.

The model also allows for the study of conversion efficiency as a function the laser wavelength and pulse duration. It was found that, if a particular harmonic order can be generated by two lasers with different wavelengths, and is in the plateau for both cases, the laser with the shorter wavelength will generate it more efficiently. This is related to the fact that the optical cycle is shorter for shorter wavelengths, decreasing the spreading of the electron wave packet during the acceleration stage. Additionally, shorter pulses generate harmonics more efficiently. This is due to the fact that generation actually happens during the first optical cycles of the laser pulse, with the rest of its energy not being converted into harmonic radiation due to the depletion of the ground state in the medium, hence the widespread use of femtosecond lasers for HHG.

1.1.2 Propagation in the gas: phase matching and absorption

The resulting harmonic radiation generated in a gas jet is the superposition of the emission of the individual atoms contained in it. In order to generate harmonics efficiently, the generated fields must interfere constructively. This is a key condition known as *phase matching*, which occurs when the phase mismatch between the driving laser and the generated radiation is minimum in the medium.

Due to the non-perturbative response of the atoms to the fundamental laser field, there is an additional phase shift between the fundamental and harmonic fields. This shift is produced when the ionized electron transfers an additional phase, acquired during its movement in the electric field, to the emitted radiation. It depends on the laser intensity and can affect several properties of the resulting beam, such as angular distribution [48] or coherence [32].

The condition for perfect phase matching can be expressed in terms of wave vectors, as a consequence of the conservation of momentum, as $\delta\vec{k} = 0$ [49], leading to:

$$\delta\vec{k} = \vec{k_q} - q\vec{k_0} - \vec{K} = 0 \quad \rightarrow \quad \vec{k_q} = q\vec{k_0} + \vec{K}, \tag{1.10}$$

where $\vec{k_q}$ is the wave vector of the q^{th} harmonic, $\vec{k_0}$ is the wave vector of the fundamental beam, assumed to be Gaussian, and $\vec{K}$ is the effective atomic phase wave vector. The harmonic wave vector can be shown to be the gradient of the phase of the q^{th} component of atomic polarization in the gas:

$$\vec{k_q}(r,z) = \vec{\nabla}\arg(P_q). \tag{1.11}$$

The wave vector of the fundamental beam, expressed in cylindrical coordinates, is calculated with the Gouy phase:

$$\vec{k_0}(r,z) = \frac{\omega}{c}\vec{e_z} + \vec{\nabla}\arg\left[\frac{1}{2(z_R + iz)}\exp\left(-\frac{\omega r^2}{2c(z_R + iz)}\right)\right], \tag{1.12}$$

where $z_R = \pi w_0^2/\lambda$ is its Rayleigh length, with w_0 being the beam waist after focusing. Finally, the atomic wave vector is the gradient of the atomic phase created by an electron and its parent ion, thus having the form:

$$\vec{K}(r,z) = \vec{\nabla}\Phi_{at}(r,z) = \vec{\nabla}\left(q\omega t - \frac{1}{\hbar}S(\vec{p_{st}}, t', t)\right), \tag{1.13}$$

where the semiclassical action $S(\vec{p_{st}}, t', t)$ is integrated over the relevant electron trajectories, determined by the principle of stationary action, whose canonical momentum is labeled as $\vec{p_{st}}$. The semiclassical action, and the atomic phase as a consequence, is strongly dependent on the intensity of the driving laser, thus varying greatly with position. It is also different for short and long electron trajectories, through its dependence on t' and t.

Figure 1.3 shows schematic distributions of $\vec{k_0}$ and $\vec{K}$ around the focus of the driving laser. While $\vec{k_0}$ essentially follows the propagation axis, converging before the focus and diverging afterwards, $\vec{K}$ equals 0 at the focus, and points away from it at every other point. Once these distributions are known, the phase-matching conditions can be studied with respect to the position of the focus relative to the medium. Figure 1.4 shows diagrams of how these three wave vectors combine, in four different cases.

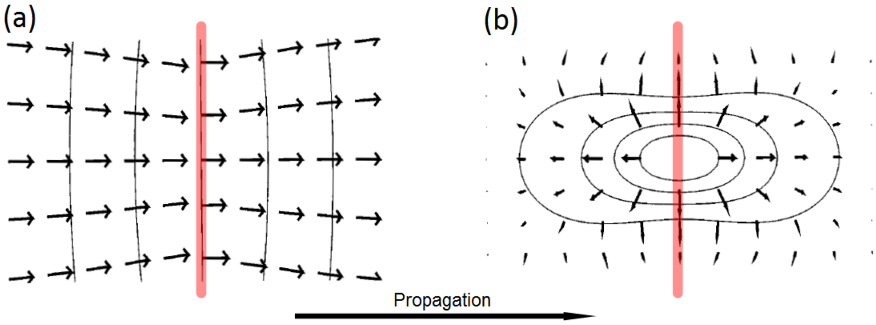

Figure 1.3: Spatial distributions of (a) $\vec{k}_0$ and (b) $\vec{K}$ around the focus. The red lines mark the position of the focal plane. Taken from [49].

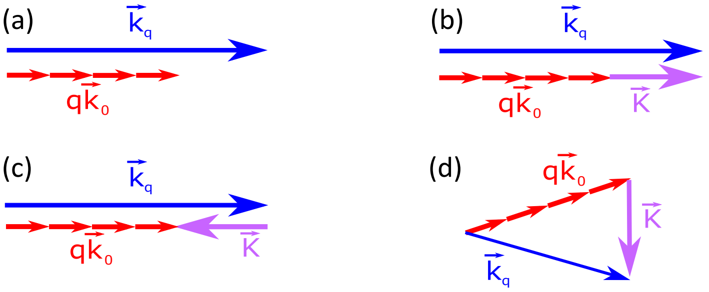

Figure 1.4: Phase matching diagrams for different points in space. (a) On axis, laser focused on the gas, (b) on axis, laser focused before the gas, (c) on axis, laser focused after the gas, and (d) off axis, laser focused before the medium.

In figure 1.4 (a), when the beam is focused exactly on the gas jet, $\vec{\mathrm{K}}$ equals 0 on axis, so that there is a phase mismatch between the driving and harmonic beams. In the case shown in figure 1.4 (b), for points on axis placed after the focal spot, the effective atomic wave vector eliminates this phase mismatch, realizing collinear phase matching. This proves that, in order to efficiently generate high harmonics, the driving beam must be focused before the gas. The cases (c) and (d) of the figure are given in different parts of the driving beam when it is focused after the gas. Figure 1.4 (c) shows that for points on axis, $\vec{\mathrm{K}}$ hinders phase matching, so that on-axis harmonics are emitted with very poor efficiency. In other points off axis, in figure 1.4 (d), all three vectors have different directions, so that noncollinear phase matching occurs. For this reason, placing the gas before the focus can result in an annular harmonic beam [32].

It is important to note as well that the phase mismatch depends on the harmonic order q, so the phase-matching conditions vary for different orders. Since it is also affected by the electric field of the driving laser, different orders can be generated at different points around the focus, and at different times along the duration of the driving pulse. Phase matching conditions are also different for each gas, due to the atomic phase and its dependence on ionization potential (see equations 1.8 and 1.13).

Perfect phase matching, however, cannot be achieved over an indefinitely long distance in the medium, but only inside a limited length along the propagation axis z where the value of $|\delta\vec{k}|$ is kept small. The coherence length is defined as $L_{coh} = |\frac{\pi}{k_q - qk_0}|$, which represents the distance between two atoms emitting radiation with a phase shift of π. Harmonic radiation emitted by atoms placed at a longer distance will interfere destructively, so the length of the medium L_{med} should be kept smaller than L_{coh} to avoid this.

Another macroscopic phenomenon limiting the efficiency of the HHG is the absorption of the emitted radiation by the gas medium. The absorption length $L_{abs} = \frac{1}{\rho\sigma}$, where ρ is the atomic density and σ is the ionization cross section, is defined as the distance after which the harmonic yield is reduced by a factor of e [50]. These three characteristic lengths allow for the estimation of the number of emitted photons in the q^{th} order, per unit of time and area, as:

$$N_q \propto \frac{4L_{abs}^2}{1 + \left(\frac{2\pi L_{abs}}{L_{coh}}\right)^2} \left[1 + e^{-\frac{L_{med}}{L_{abs}}} - 2\cos\left(\pi\frac{L_{med}}{L_{coh}}\right) e^{-\frac{L_{med}}{2L_{abs}}}\right]. \tag{1.14}$$

This equation allows for the study of the variation of N_q as a function of L_{med}, shown in figure 1.5 for several values of L_{coh}.

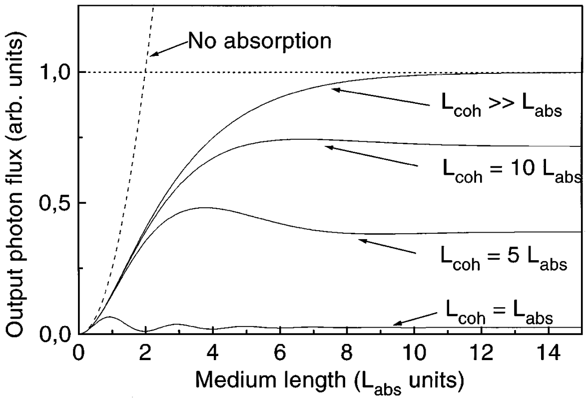

Figure 1.5: Variation of the emitted harmonic flux as a function of the medium length, in units of absorption length, for different values of the coherence length. Taken from [50].

It can be seen from the figure that, even for large values of L_{coh}, the emission saturates regardless of how much L_{med} is increased. This is due to absorption in the medium, which establishes an upper limit to the number of photons that can be obtained. If this is the case, the generation is said to be absorption-limited. Experimentally, this can be observed by using a variable-length gas cell [51]. The figure also shows that, in order to obtain at least half of the maximum possible output, there are two conditions that must be met:

$$L_{med} > 3L_{abs}, \; L_{coh} > 5L_{abs}. \tag{1.15}$$

Long and short electron trajectories or quantum paths

The return time of an electron to its parent ion can be defined as $\tau = t - t'$, the difference between its time t of recombination and its time t' of ionization, or the time that it spends in the continuum. For a given photon energy, there may be more than one electron trajectory leading to its emission. Generally, for harmonics in the plateau there are two dominant trajectories, with different return times. They are called the short and long trajectories or, more accurately, quantum paths [31]. They often referred to as τ_1 and τ_2, respectively, with τ_1 being shorter tan half a laser period, and τ_2 being close to a full period [52]. In the case of cutoff harmonics, only one quantum path contributes significantly to harmonic emission [53].

In terms of the single-atom response, the different quantum paths contribute with different phase behaviors to the dipole moment, in both amplitude and phase [54]. With respect to the generating medium, the return time affects the phase Φ_{at} acquired by the electron during its acceleration in the continuum, and thus the phase mismatch (see equation 1.10) between the fundamental and harmonic fields. As a consequence, long and short quantum paths have different conditions for optimum phase matching, and one can be better phase matched than the other. Due to the different phase acquired by electrons going through different quantum paths, interaction between two paths can occur, by means of quantum interference [55, 56]. This interaction has been experimentally observed in harmonic beams via interferometry of the far field [51, 57].

It has been shown that high-harmonics coming from short and long quantum paths have different spatial and temporal properties. Two distinct spatial regions have been observed in the far field of harmonics in the plateau region [14]. Short quantum paths are responsible for the inner, less divergent part of the beam, which has higher temporal coherence than the outer part, created by long quantum paths. Thus, the harmonics from τ_1 are less divergent than those from τ_2. These two regions are not present for harmonic orders in the cutoff, where only one quantum path is significant.

1.2 High-harmonic generation in the laboratory: the Salle Corail beamline at LOA

Operating since early 2016, the high-harmonic beamline in the Salle Corail laboratory of LOA uses a Ti:Sapphire IR laser to generate high harmonics in a gas cell. The laser emits pulses of 800-nm light with an approximate duration of $30\,\mathrm{fs}$ and $3.5\,\mathrm{mJ}$ of energy, with a repetition rate of $4\,\mathrm{kHz}$. The Salle Corail replaces and is based on an older laboratory built in 2005, the Salle Orange, where our group performed experiments until it was shut down in mid 2015.

A schematic drawing and a picture of the Salle Corail beamline can be seen in figure 1.6. It must be noted that high harmonics must be generated under vacuum, in order to evacuate the generating gas, and due to XUV radiation being absorbed by air. The backing pressure inside the three vacuum chambers during operation is of the order of than $10^{-5}\,\mathrm{mbar}$. Another particular characteristic of XUV radiation is the fact that refractive lenses are not as efficient in this range as they are for IR light, for two reasons. Firstly, the refraction index of most materials is close to 1 at these wavelengths [58], and secondly, most materials are also highly absorbing for XUV radiation. Fresnel zone plates, based on diffraction, may be used for focusing instead, but they produce chromatic aberration [58] and are thus not useful for high harmonics due to their wide spectrum. Focusing in the XUV range is usually done with mirrors. However, most materials exhibit low reflectivities for XUV radiation unless used in grazing incidence [58]. For this reason, when dealing with XUV and X-ray optics, the angle of incidence is often defined with respect to the mirror surface rather than the normal. To avoid confusion, it will be referred to it as *grazing angle* in this thesis. Multilayer mirrors are commonly used in the XUV and X-ray ranges to provide high reflectivities at higher grazing angles such at 45° when necessary. They are also used to select a particular wavelength, selected through the number and thickness of the layers, for which reflectivities higher than 60% can be achieved [59, 60].

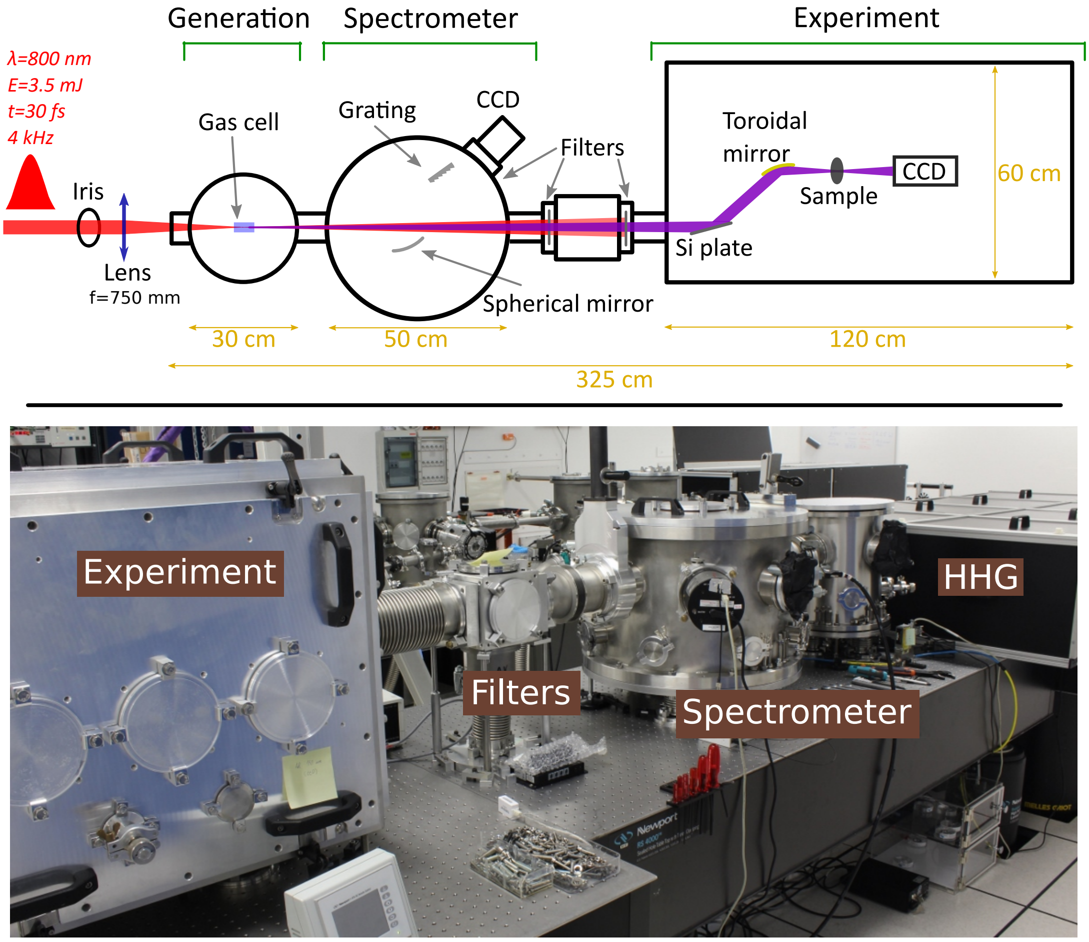

Figure 1.6: Schematic drawing (top) and picture (bottom) of the high-harmonic beamline at the Salle Corail laboratory in LOA.

Inside the first chamber, labeled HHG in the picture, high harmonics are generated by focusing the IR laser with a lens of focal distance $750\,\mathrm{mm}$ on a $12\text{-}\mathrm{mm}$ gas cell, filled with argon or neon. The second chamber contains a simple spectrometer, consisting of a silica-glass spherical mirror ($\mathrm{f} = 1\,\mathrm{m}$), which can be moved in and out of the beam path, and a reflective diffraction grating with a groove density of $450\,\mathrm{gr/mm}$, both used in grazing incidence ($< 10^{\circ}$). The spectrometer uses a Pixis XO 400B charge-coupled device (CCD) camera manufactured by Princeton Instruments, with $1340\mathrm{x}400$ square pixels of side $20\,\mu\mathrm{m}$. The third and final chamber is used for different experiments. Flat silicon mirrors are used for alignment, with grazing angles lower than 10°, providing 87% reflectivity at $\lambda = 32\,\mathrm{nm}$ [61]. The beam is focused with a gold-coated toroidal mirror when necessary. Its size is $100\mathrm{x}30\,\mathrm{mm}^2$, with radii of curvature $1500\,\mathrm{mm}$ and $50\,\mathrm{mm}$.

Experimentally, there are several parameters that have an influence on HHG:

- **The fundamental wavelength**. The cutoff law (equation 1.1) shows that, for a given intensity at focus, the longer the fundamental wavelength, the shorter the wavelengths that can be obtained through HHG. This is the reason why IR sources are generally used, with some laboratories using even longer wavelengths to extend the cutoff [62].

- **The IR pulse energy**. Due to the relatively low pulse energy of $3.5\,\mathrm{mJ}$, tight focusing should be used to ensure that the focus achieves intensities of the order of $10^{15}\,\mathrm{W/cm}^2$. A lens with a focal distance of $750\,\mathrm{mm}$ is currently in place. The low energy carried by a single harmonic pulse, around picojoule level, is compensated with the high repetition rate of the beamline, in terms of average power.

- **The IR pulse duration**. Shorter pulses have been shown to produce more efficient harmonics than longer ones, hence why ultrashort pulses of $30\,\mathrm{fs}$ are used (see section 1.1.1.2).

- **The gas medium**. As seen in figure 1.10, different gases yield different spectra, with different cutoff energies due to their different ionization potentials. It will be shown below that neon can be used to obtain wavelengths around $15\,\mathrm{nm}$, while argon yields more intense radiation around $30\,\mathrm{nm}$. Additionally, xenon allows for the generation of longer wavelengths around $60\,\mathrm{nm}$. As mentioned at the beginning of section 1.1, each gas also yields different conversion efficiencies [63].

- **The length of the gas cell**. A longer gas cell provides a higher interaction volume between laser and gas. However, using a cell of excessive length can hinder harmonic yield due to absorption (see figure 1.5). Its length can be chosen with respect to the Rayleigh length z_R of the focused IR beam, which is in turn a function of the focal length f of the lens used, through the relation $z_R = \lambda f^2/\pi w_{0i}^2$, where w_{0i} is the beam diameter before the lens. In general, it is best to use a cell with a length approximately equal to the confocal parameter $b = 2z_R$. Longer gas cells are thus used with longer focal lengths and vice versa. In Salle Corail, a cylindrical cell with $12\text{-}\mathrm{mm}$ cell is typically used, with other lengths such as 5 or $15\,\mathrm{mm}$ being available as well.

- **The gas pressure**. If the gas is introduced in the cell at a very low pressure, the number of emitters will be low, resulting in a low harmonic yield. Increasing the pressure leads to a fast improvement of the conversion efficiency due to the increase of the coherence length $\mathrm{L_{coh}}$. For high pressures, depending on the IR intensity at focus, the efficiency can either saturate, or decrease due to ionization in the gas [64]. The highest conversion efficiency was obtained in this setup with pressures around $60\,\mathrm{mbar}$ for argon and $40\,\mathrm{mbar}$ for neon. Figure 1.7 shows three harmonic footprints recorded with argon at three different pressures, with all other parameters kept constant. They were recorded with a Pixis 400B CCD camera, placed $2.2\,\mathrm{m}$ after the gas cell.

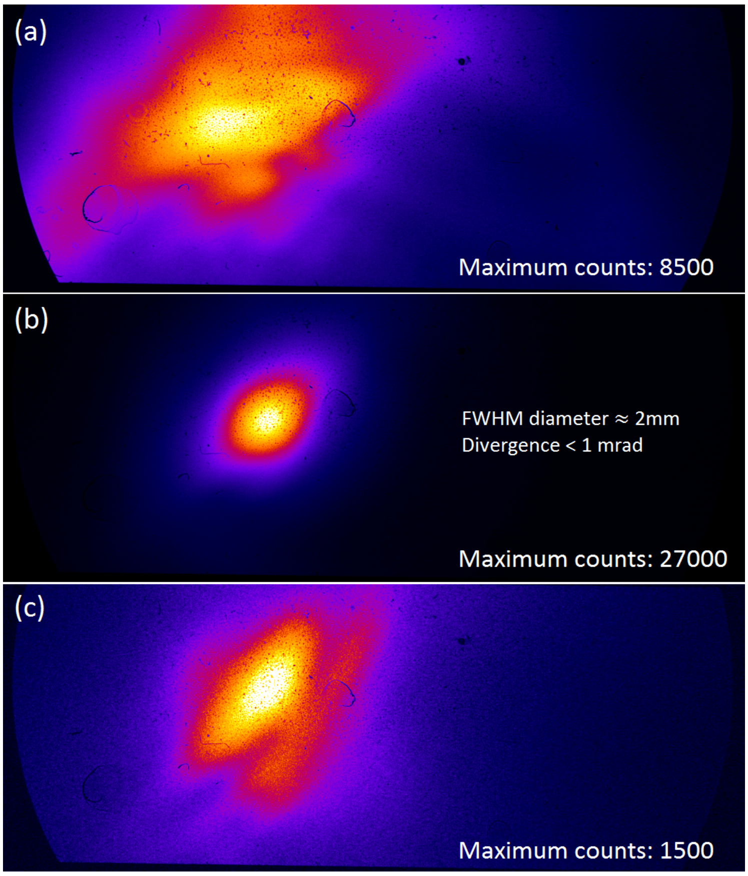

Figure 1.7: High harmonic beams obtained in Salle Corail a 12-mm cell filled with argon at various pressures, (a) 30 mbar, (b) 65 mbar and (c) 90 mbar. IR beam diameter was 11 mm, and 40 shots were accumulated in all cases. False color, white and orange represent high counts, while purple and black represent low counts.

- **The IR beam diameter**. The transverse profile of the IR beam is Gaussian, with a diameter of $20\,\mathrm{mm}$. However, clipping the beam with an iris can significantly affect the conversion efficiency. An apertured beam carries less energy, and it no longer has a Gaussian profile, but a truncated Gaussian one. In this case, the focusing geometry changes [63], as well as size of the focal spot, and thus the intensity. The intensity distribution at focus and along the propagation axis is dictated by the truncation coefficient, defined as the ratio between the area of the aperture and the area of the beam at the plane of the aperture [65]. The Gouy phase is also different for truncated Gaussian beams, which in turn affects the phase matching conditions [66] and thus the conversion efficiency. In the Salle Corail beamline, using a focal distance of $750\,\mathrm{mm}$, aperture diameters close to $12\,\mathrm{mm}$ were seen to provide the highest harmonic energy, both with argon and neon, as well as a more circular intensity profile. Figure 1.8 shows the footprints of harmonics generated in argon with the full beam in one case, and the beam apertured down to $12\,\mathrm{mm}$ in the other, while keeping all other parameters constant. Very visible differences are present for pointing, divergence, shape, and intensity.

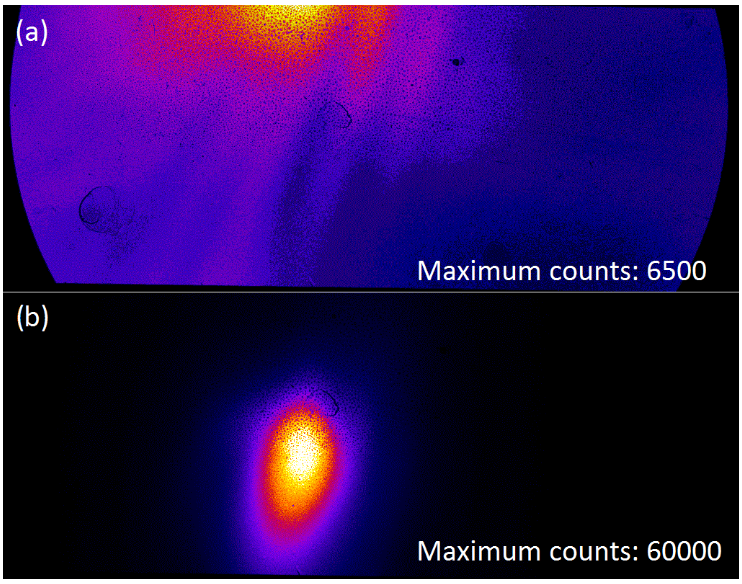

Figure 1.8: High harmonic beams obtained in Salle Corail a 12-mm cell filled with argon at 60 mbar, with (a) the full IR beam (200 accumulated shots) and (b) the IR beam clipped to a 12-mm diameter (400 accumulated shots). False color, white and orange represent high counts, while purple and black represent low counts.

While not affecting the generation itself, filtering the leftover IR beam also affects the resulting beam available for experiments. Once the generation has taken place, the remaining IR beam propagates collinearly with the harmonics, while being several orders of magnitude more intense due to the low conversion efficiencies of HHG. It is usually filtered out by the use of metallic filters which can transmit the desired wavelengths. For the XUV range, materials such as aluminum or indium are commonly used. These filters also reduce the energy of the harmonic beam, and affect its spectrum according to their transmissive properties (see figure 1.9). In Salle Corail, aluminum filters with thicknesses of $150\,\mathrm{nm}$ and $300\,\mathrm{nm}$ are used. Note that the surfaces of these filters generally have a thin oxidation layer, further reducing their transmittance [51]. These layers usually have thicknesses close to $5\,\mathrm{nm}$. Figure 1.10 shows two spectra obtained in the Salle Corail beamline, using aluminum filters with a harmonic beam generated in argon and neon. The different spectra are also due to the fact that each gas absorbs different wavelengths.

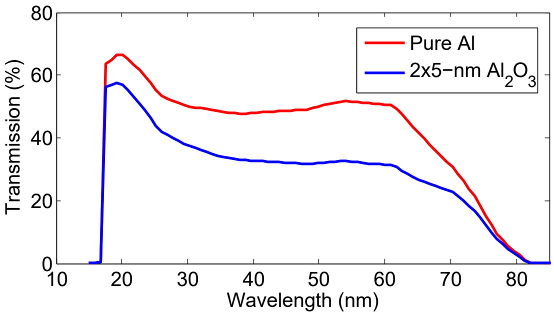

Figure 1.9: Calculated transmission of a 300-nm thick aluminum filter as a function of wavelength, without oxidation (red line) and assuming two layers of 5-nm-thick Al_2O_3 *(blue line). Data from the Center for X-Ray Optics (CXRO) [61].*

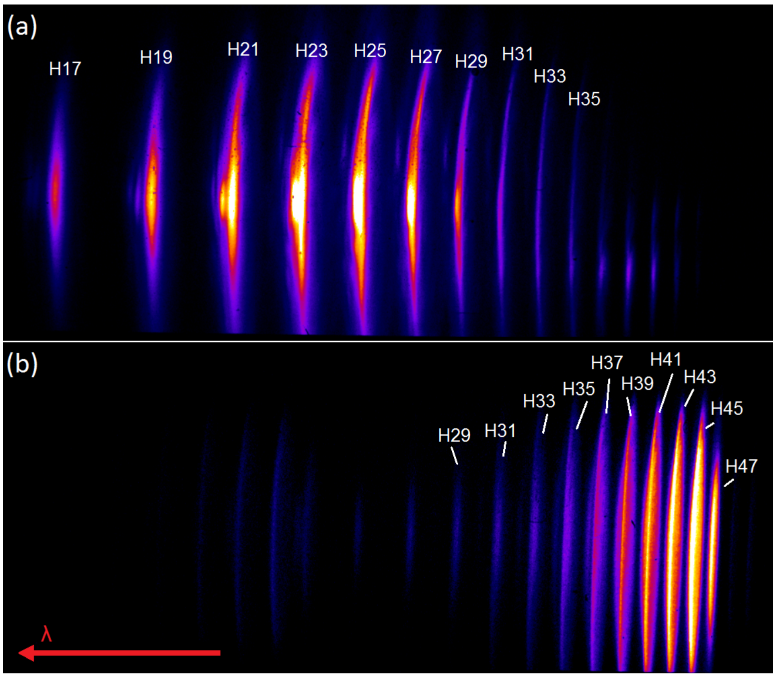

Figure 1.10: Harmonic spectra obtained in the Salle Corail beamline for (a) argon (10 mbar, 40 accumulated shots) and (b) neon (30 mbar, 120 accumulated shots). The iris diameter was kept at 13 mm. Traces of the second diffraction order from the grating can be seen on the left side of both images.

1.3 Spatial properties of high harmonics

Several current and potential applications of high harmonics, such as imaging, require good spatial quality. Others, especially those involving nonlinear processes, require high intensities. This intensity $\mathrm{I} = \frac{\mathrm{E}}{\mathrm{t\,S}}$, defined as the energy E of the pulse divided by its duration t and area S, can be increased by optimizing those three parameters. Pulse energy can be increased by improving the phase matching and choosing the medium length adequately, while its duration is mainly given by the duration of the driving pulse. To further improve intensity at focus, the size of the focal spot must be reduced by improving the spatial properties of the beam, given by its intensity distribution and its wavefront. The wavefront is defined as the locus of points having the same phase. From the standpoint of geometrical optics, it is defined as the surface perpendicular to the light beams.

The wavefront has a large impact on how a laser beam is propagated and focused. In the case of visible or IR laser pulses, the wavefront can be optimized through the use of adaptive optics, introducing a deformable mirror (DM) in the beam path [67]. The surface of this kind of mirrors can be deformed to compensate for any distortions on the initial wavefront. This technology can be transferred to the XUV domain for its use with high harmonic radiation. A DM for XUV radiation must be multilayered [68] or used in grazing incidence [69], in order to have a high reflectivity.

However, being a secondary source of radiation, it is clear that the spatial properties of high harmonics must be influenced by those of the generating IR beam [32], which might enable the optimization of harmonic wavefronts by modifications in the IR beam only, which is simpler to achieve.

1.3.1 Measurement and description of harmonic wavefronts

A high-harmonic pulse is essentially an electromagnetic wave, which means that, in order to fully characterize it in the spatial, spectral or temporal domain, both its amplitude and phase must be known. In the spatial domain, the amplitude is its intensity distribution, measurable with an integrating detector such as a CCD camera, as it was shown in the previous section. However, these detectors are not sensitive to spatial phase, so they cannot provide complete characterization of the spatial properties of the beam. Some techniques which have been used to measure spatial phase in the XUV region include point diffraction interferometry [70] or shearing interferometry [71]. However, the use of a wavefront sensor (WFS) has the advantage of measuring both intensity distribution and wavefront at the same time.

1.3.1.1 The Hartmann wavefront sensor

The Hartmann wavefront sensor was first described in 1900 [72]. Over the years, this type of sensor has been used in many applications, such as ophthalmology or for the adaptive optics of astronomical telescopes. Hartmann sensors were first used for XUV light pulses in the year 2003 [73], to accurately characterize synchrotron radiation at $\lambda = 13.4\,\mathrm{nm}$.

A Hartmann WFS consists on a mask, or *Hartmann plate*, containing an array of square holes, placed before a CCD camera. Each of these holes, also referred to as *subpupils*, samples a portion of the wavefront. The direction of propagation of the beamlets diffracted by those holes is given by the local slope of the wavefront at the Hartmann plate. The resulting diffraction patterns are recorded in the CCD, and their positions are then compared to reference positions, obtained via a previous calibration of the WFS.

The sensor used in the experiments described in this thesis was built and calibrated in collaboration with Imagine Optic. It uses a Princeton Instruments Pixis XO 1024B back-illuminated CCD camera, with a resolution of $1024\text{x}1024$ square pixels of side $13\,\mu\text{m}$, placed $211\,\text{mm}$ after the 100-μm-thick nickel Hartmann plate. The plate contains an array of $34\text{x}34$ square holes of side $110\,\mu\text{m}$, separated by $387\,\mu\text{m}$. The holes are rotated by 25° to prevent the diffracted beamlets from overlapping each other on the CCD, and the sensor has a numerical aperture of $\text{NA} = 0.01$. Figure 1.11 shows the working principle of the sensor, and the sensor itself can be seen in figure 1.12. Note that the center of the plate has no hole, which is used in experiments for alignment purposes. If the sensor is correctly aligned, and the beam is perpendicular to it, the center of the CCD will not be illuminated.

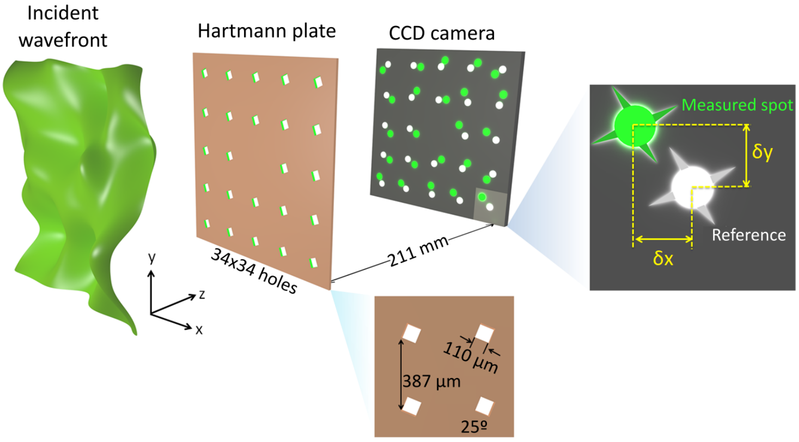

Figure 1.11: Schematic drawing of the principle of operation of the Hartmann wavefront sensor. Taken from [74].

Shack-Hartmann sensors are another kind of WFS based on similar principles, in which the Hartmann plate is replaced by an array of microlenses, which focus the beam instead of diffracting it, thus providing better signal-to-noise ratios. In the XUV region, they are based on Bragg-Fresnel diffractive lenses. However, Hartmann sensors are usually preferred, since the small separation between the subpupils in the Hartmann plate provides better sampling of the wavefront [75]. Additionally, the focusing provided by the diffractive lenses used in XUV Shack-Hartmann sensors is highly chromatic, limiting its accuracy for the case of non-monochromatic radiation such as high harmonics.

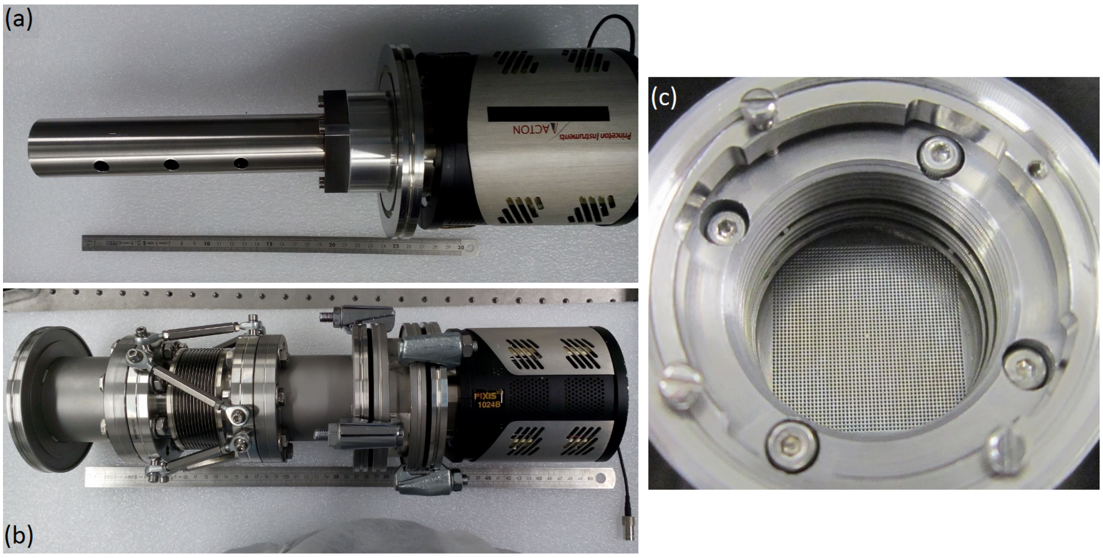

Figure 1.12: Pictures of the Hartmann WFS used in this thesis. (a) The CCD and the tube containing the Hartmann plate, (b) the full WFS with the necessary attachments for alignment and operation with vacuum chambers, and (c) close-up of the Hartmann plate.

1.3.1.2 Sensor calibration

There are two steps to follow when preparing the XUV Hartmann sensor. First, the Hartmann plate must be put in place and aligned correctly, and then, the reference beam must be recorded.

The plate is aligned by using visible light, taking advantage of the Talbot effect [76]. The Talbot effect is a diffraction effect in which a plane wave illuminates a diffractive optical element, in this case the Hartmann plate, and creates $1:1$ images of it at regular positions along the z axis. A diode laser emitting at $635\,\mathrm{nm}$ was used for this step. The plate is then moved along the z axis in order to find a position in which such an image is created on the CCD chip. The formed image is then used to align the plate, by aligning the image itself with the axes of the CCD. This ensures that the plate is parallel to the chip and perpendicular to the incident beam. This step of the sensor preparation also allows for an accurate measurement of the distance between holes and the plate-chip distance, $387.105\,\mu\mathrm{m}$ and $211.007\,\mathrm{mm}$, respectively. The image of the Hartmann plate recorded by the XUV CCD can be seen in figure 1.13.

Once this is done, in order to calibrate the sensor, it must be illuminated with a known wavefront to be used as a reference for the measurements. Such reference wavefront is generally obtained by spatial filtering of an XUV beam with a pinhole. This will result in a circular diffracted beam with a FWHM (full width at half maximum) diameter given by:

$$\mathrm{d} = \frac{1.22\,\lambda\,\mathrm{D}}{\mathrm{d}_{\mathrm{PH}}}, \tag{1.16}$$

where D is the pinhole-sensor distance and $\mathrm{d_{PH}}$ is the diameter of the pinhole. The central part of the Airy disk in the resulting diffracted beam can be assumed to be diffraction-limited [58]. To perform an accurate calibration, the Hartmann plate must be illuminated by less than half of the disk [77].

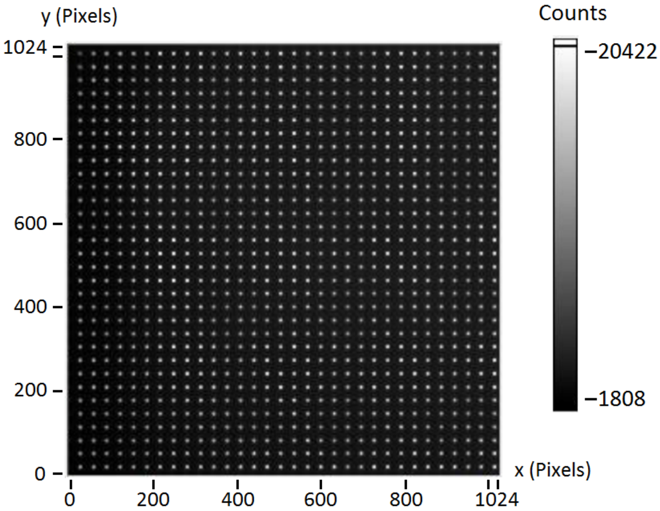

Figure 1.13: Hartmann plate imaged with magnification 1 on the CCD chip illuminated with 635-nm visible light, due to the Talbot effect. Note that the central part of the chip is illuminated despite the lack of a hole. This only appears when illuminating with long wavelengths due to diffraction mixing light incoming from several subpupils. This does not occur when using high harmonics.

We calibrated the sensor described above at the Salle Orange beamline at LOA, by filtering a high-harmonic beam with a round pinhole of diameter $5\,\mu\mathrm{m}$. Figure 1.14 shows a schematic drawing and a picture of the setup. The sensor must be placed far from the pinhole to allow the beam to diverge enough to cover the Hartmann plate. The sensor can be aligned when in vacuum through the use of the hexapod seen in figure 1.12 (b). When the sensor is aligned, the center of the CCD chip is not illuminated by the beam, due to the center of the plate not containing a hole.

Figure 1.15 shows one the resulting images obtained for the calibration, which was performed using an average of several wavefronts. Each of the spots corresponds to a hole or subpupil of the Hartmann mask. Note the center of the CCD not being illuminated, as mentioned above, as well as the tilted diffraction patterns to avoid overlapping. Due to the low transmission of the pinhole and the large divergence of the reference beam, an acquisition time of $300\,\mathrm{s}$ $(3\cdot10^5$ laser shots) was necessary to acquire an image with a high signal-to-noise ratio. This acquisition time can be reduced by using a larger pinhole, but the diffracted beam would be less divergent, increasing the distance at which the sensor has to be placed. Note that the sensor remains calibrated for its use with any other source, which is not the case for interferometric techniques for wavefront measurements. The sensitivity of the WFS can also be calculated from the calibration, and it was found to be $0.6\,\mathrm{nm}$ root mean square (RMS), equivalent to $\lambda/50$ for $\lambda = 30\,\mathrm{nm}$.

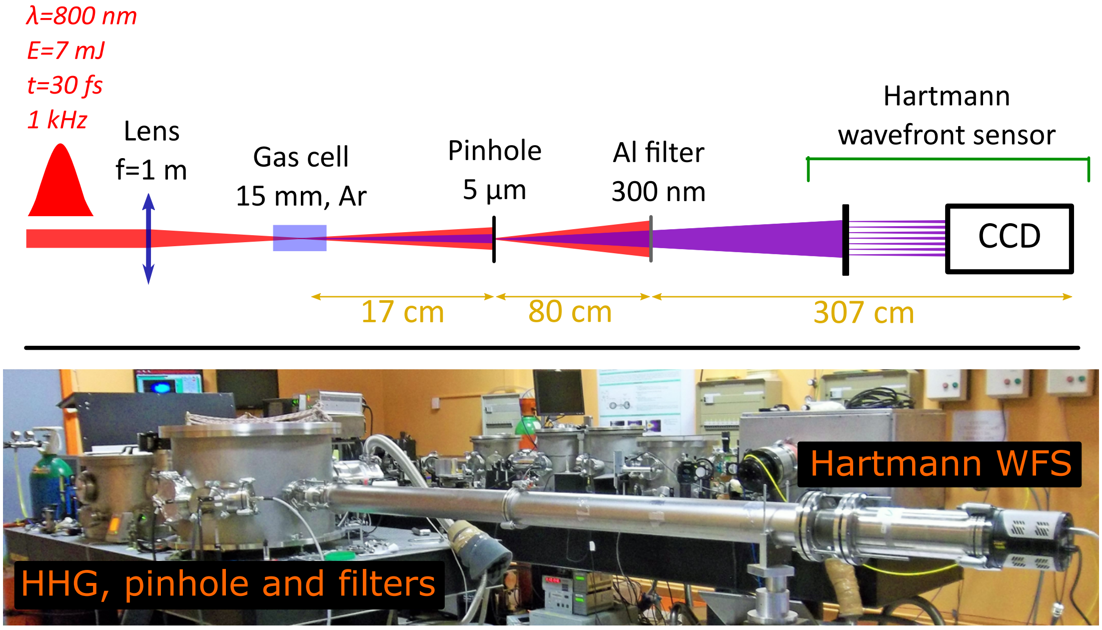

Figure 1.14: Schematic drawing (top) and picture (bottom) of the setup used for the Hartmann WFS calibration at LOA.

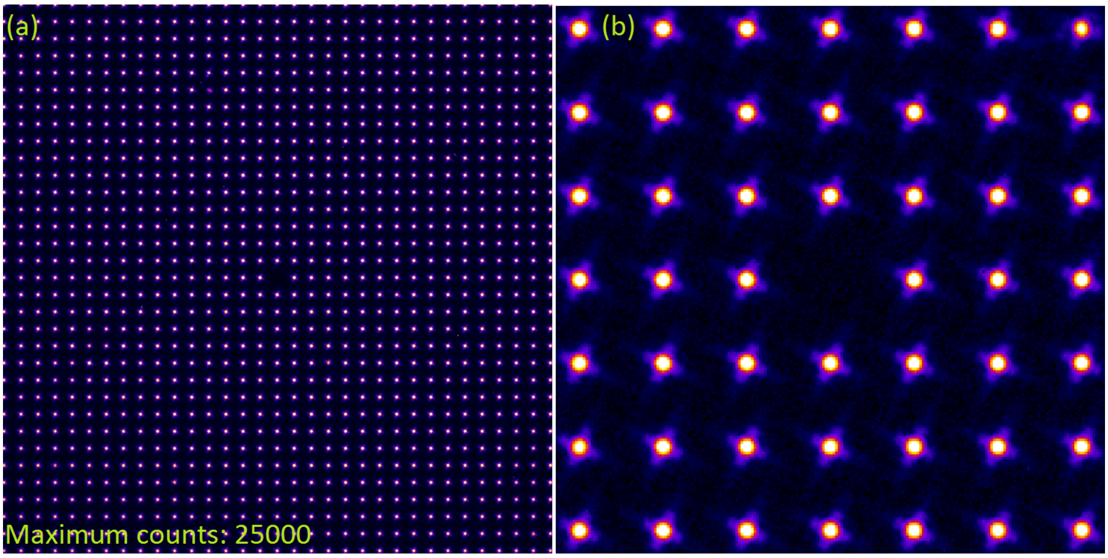

Figure 1.15: (a) Full image recorded with the sensor when illuminated by the reference beam produced by the 5-μm pinhole and (b) zoom on the central part of the CCD chip, showing the non-illuminated region used for alignment. Note the tilt in the diffraction patterns, caused by the tilted holes of the Hartmann plate. False color, white and orange represent high counts, while purple and black represent low counts.

1.3.1.3 Wavefront reconstruction

For the case of the XUV Hartmann sensor used in this thesis, all wavefronts have been reconstructed using the HASO software developed by Imagine Optic, which automatically performs all the calculations described in this section, once the sensor has been calibrated. The software can also perform several types of reconstructions, and calculate several parameters associated to the wavefront.

The first step for the reconstruction of the wavefront $\Phi(x,y)$ of an unknown beam is the calculation of the positions of the diffracted beamlets, in terms of their centroids, with respect to the reference positions obtained via calibration. The centroid of any intensity distribution $I(x,y)$ dependent on x and y is given in the x direction, and analogously for the y direction, by [78]:

$$\overline{x} = \frac{\int_{-\infty}^{+\infty}\int_{-\infty}^{+\infty} I(x,y)\ x\ dx\ dy}{\int_{-\infty}^{+\infty}\int_{-\infty}^{+\infty} I(x,y)\ dx\ dy}. \tag{1.17}$$

This equation, however, must be modified for the Hartmann sensor to account for the discrete pixels contained in the CCD chip. In this case, the x and y axes are replaced by two discrete parameters, i and j, and the integrals are replaced by summations in a finite array of points. The centroid position in x is then:

$$\overline{x} = \frac{\sum_{i=i_{min}}^{i_{max}}\sum_{j=j_{min}}^{j_{max}} I(i,j)\ i}{\sum_{i=i_{min}}^{i_{max}}\sum_{j=j_{min}}^{j_{max}} I(i,j)}\ s, \tag{1.18}$$

where $I(i,j)$ is the intensity measured by the pixel in the position (i,j) and s is the spacing of the pixels along the x or y axes. It must be noted that there is an intensity threshold, so pixels measuring intensities lower than it will not be considered for the calculation. This is done in order to avoid calculation errors caused by electronic noise coming from the CCD or light diffracted out of the first order. The relative positions of the measured centroids allow for the calculation of the local slopes of the wavefront in as:

$$\beta_x = \frac{d\Phi(x,y)}{dx} = \frac{\delta x}{l} \qquad \beta_y = \frac{d\Phi(x,y)}{dy} = \frac{\delta y}{l}, \tag{1.19}$$

where δx and δy are the distances between measured and reference positions in the x and y axes (see figure 1.11), and l is the distance between the Hartmann plate and the CCD chip.

Once the local slopes have been obtained, the full wavefront $\Phi(x,y)$ can be reconstructed. It is important to note, however, that this is only true for coherent beams. In the case of an incoherent beam, only the wave vector distribution can be measured. Being the spatial phase of the beam, the wavefront is generally given in radians, but it can be converted to units of the beam wavelength, knowing that one wavelength λ is equivalent to a phase of 2π rad. There are two main types of wavefront reconstruction algorithms: zonal and modal.

- **Zonal reconstruction**. This type of reconstruction algorithm is aimed at minimizing the error in the calculation. This is done by scanning the entire array of data points. Then, the wavefront height at each point is calculated by taking its neighboring points into account, resulting in:

  $$\Phi_{n,m} = \sum_{j=-1}^{1} \sum_{i=-1}^{1} I_{n+i,m+j} \left[\Phi_{n+i,m+j} + \left(\frac{\frac{\partial \Phi}{\partial x_{n,m}} + \frac{\partial \Phi}{\partial x_{n+i,m+j}}}{2} \right) \delta \right], \tag{1.20}$$

  where $\Phi_{n,m}$ is the wavefront at the point (n,m), δ is the separation between the (n,m) integration area and the $(n+i,m+j)$ integration area, and $I_{n+i,m+j}$ is the intensity measured in the $(n+i,m+j)$ integration area. The algorithm takes many iterations through the data to increase the accuracy of the result. The method used for this type of reconstruction is known as successive over-relaxation [79], and it has the advantage of being useful for beams of any shape.

- **Modal reconstruction**. This type of reconstruction algorithm fits the data to a set of orthogonal polynomials. Legendre polynomials are used for square-shaped pupils, and Zernike polynomials for circular pupils. This method can accurately determine low-frequency aberrations, such as astigmatism or spherical aberration, and quantifies them via the coefficients of the polynomials [80]. Lists of low-order Zernike and Legendre polynomials can be found in appendix A.

  Zernike polynomials are commonly used in the XUV regime since the beams have approximately circular shapes. There are even and odd polynomials, defined respectively as:

  $$Z_n^m(\rho,\theta) = \begin{cases} +A_n^m R_n^m(\rho)\cos(m\theta) & \text{if} \quad m \geq 0 \\ -A_n^m R_n^m(\rho)\sin(m\theta) & \text{if} \quad m < 0 \end{cases} \tag{1.21}$$

  where n and m are integers and follow the condition $n \geq m$. ρ is the radial distance, $0 \leq \rho \leq 1$, θ is the azimuthal angle and A_n^m are normalization coefficients. R_n^m, the radial part of the polynomials, is defined as:

  $$R_n^m(\rho) = \sum_{k=0}^{(n-m)/2} \frac{(-1)^k (n-k)!}{k!\left(\frac{n+m}{2}-k\right)!\left(\frac{n-m}{2}-k\right)!} \rho^{n-2k}, \tag{1.22}$$

  if $n-m$ is even, and $R_n^m(\rho) = 0$ otherwise. The normalization coefficients A_n^m can be defined in two different ways, depending on the normalization used, referred to as the root mean square (RMS) and peak-to-valley (PV) normalizations.

  - In the *RMS normalization*, the coefficients take the form:

    $$A_n^m = \sqrt{\left(\frac{2(n+1)}{1+\delta_m}\right)}, \tag{1.23}$$

    with $\delta_m = 1$ when $m = 0$, and $\delta_m = 0$ when $m \neq 0$ [81].

- The *standard* or *PV normalization* uses $A_n^m = 1$ for all cases.

When using Zernike modal wavefront reconstruction, the wavefront is expressed in polar coordinates as a linear combination of the polynomials:

$$\Phi(\rho,\theta) = \sum_{N}^{N_{max}} a_N \, Z_N(\rho,\theta), \tag{1.24}$$

where a_N is the Zernike coefficient corresponding to the N^{th} polynomial, Z_N, when the first N_{max} polynomials are used for the fit.

Figure A.1, in the appendix, shows plots of the first 15 Zernike polynomials used by the HASO wavefront reconstruction software. Table A.1 includes the expressions for the first 32 polynomials, along with the corresponding normalization coefficients for the RMS normalization.

1.3.1.4 Description of a wavefront and backpropagation

A reconstructed wavefront can be described by several parameters, depending on the type of reconstruction used [82]. The main parameters are its RMS error and its peak-to-valley (PV). Those two parameters are always present regardless of the type of reconstruction used, and can be given in units of distance or wavelength. For the case of a modal reconstruction, the Zernike or Legendre coefficients are also calculated.

- **Root mean square error (RMS)**. It is the standard deviation of the wavefront, defined by:

$$\mathrm{RMS} = \sqrt{\frac{\sum_{\mathrm{subpupils}} (\mathrm{WF_{sp}} - \mu)^2}{\mathrm{N_{sp}}}}, \tag{1.25}$$

  where μ is the mean of the wavefront surface (the *piston*), $\mathrm{WF_{sp}}$ is the calculated value of the wavefront in a particular subpupil, and $\mathrm{N_{sp}}$ is the total number of subpupils used in the wavefront reconstruction. According to the Maréchal criterion, a wavefront is said to be diffraction-limited when its RMS is lower than $\lambda/14$ [83].

- **Peak-to-valley (PV)**. It is the difference between the maximum and the minimum values of the wavefront.

As an example, figure 1.16 shows a wavefront taken in the same setup used for the calibration of the Hartmann WFS (see figure 1.14), with the pinhole replaced by an iris. This was done to measure only the central part of the beam, which has been observed to be less aberrated than the outermost part [19, 84]. The beam was generated within a 15-mm-long gas cell filled with argon at $30\,\mathrm{mbar}$, with the driving IR beam apertured down to $15.8\,\mathrm{mm}$. Figures 1.16 (a) and (b) present the raw image and the reconstructed wavefront, respectively, with each wavefront data point corresponding to one of the illuminated subpupils of the Hartmann plate. Zonal reconstruction was used.

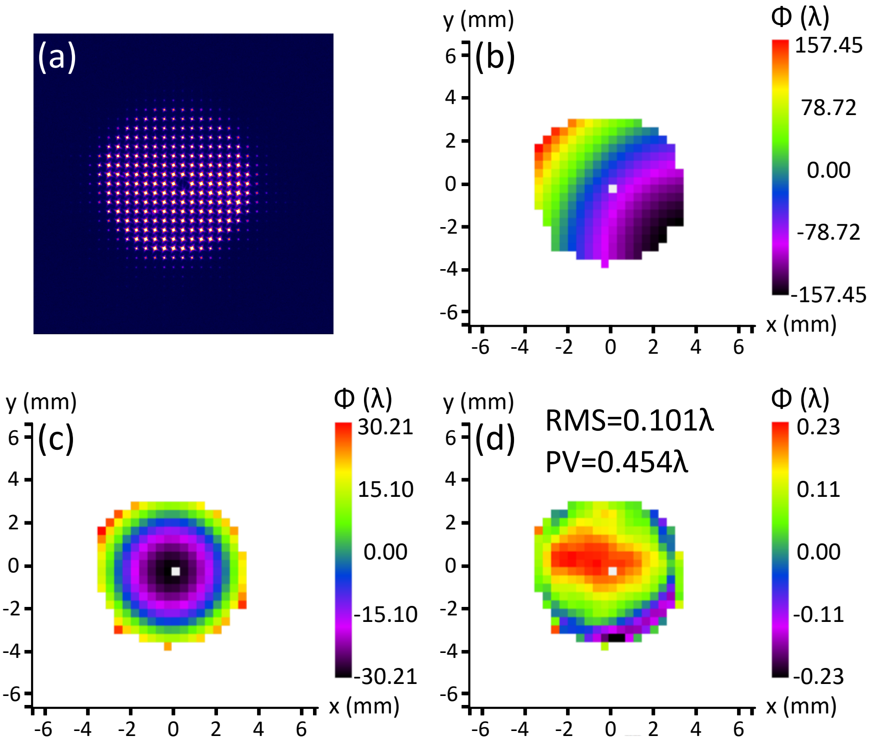

Figure 1.16: Clipped high-harmonic beam measured with the Hartmann sensor in Salle Orange, after accumulation of 1000 shots. (a) Raw image in false color (cropped), (b) full reconstructed wavefront, (c) spherical wavefront when the effects of tilt are filtered, and (d) wavefront after filtering tilt and defocus, all in units of λ.

The full reconstructed wavefront presents *tilt*. This aberration is not actually part of the wavefront, but rather caused by the harmonic beam not being perfectly perpendicular to the sensor or, more accurately, not perfectly collinear with the reference beam used during calibration. For this reason, the wavefront carries information about the beam pointing. Once the tilt is numerically filtered out, the true wavefront is obtained, presented in figure 1.16 (c). High-harmonic wavefronts have been measured to be spherical [84], and the spherical part of the wavefront, usually called *defocus*, carries information about the distance between the source and the sensor. The defocus, however, is usually much more significant than other aberrations, and is thus filtered out as well to allow for their study. What remains is shown in figure 1.16 (d), and represents the deviation of the wavefront from being perfectly spherical, characterized by the two parameters introduced above.

Assuming that the high-harmonic beam has a central wavelength of $\lambda = 32\,\mathrm{nm}$, the wavefront shows $\mathrm{RMS} = 0.101\lambda \simeq \lambda/10$ and $\mathrm{PV} = 0.454\lambda \simeq \lambda/2$. A total of 1000 shots were accumulated for this image, due to the low power of the high harmonics generated in the Salle Orange beamline. This means that the wavefront of a single harmonic pulse cannot be measured, and only an average can be taken instead. This will be discussed in more detail in the next section. Note that, throughout this thesis, the word *wavefront* is used to refer to the wavefront after tilt and defocus have been removed.

The intensity distribution (not shown in the figure) is simply calculated by summing the counts of the CCD pixels corresponding to each subpupil. With the intensity distribution and wavefront of a coherent beam, its propagation at any given point can be calculated. In particular, several parameters describing the beam can be calculated at any point of its path by means of the moments method [85]. The central second spatial (x, y) and angular (u, v) moments are calculated with the intensity distribution and the local slopes as:

$$\left\langle x^2 \right\rangle = \frac{\sum_{i,j}(x_{i,j} - \langle x \rangle)^2 I_{i,j}}{\sum_{i,j} I_{i,j}} \tag{1.26}$$

$$\langle xu \rangle = \frac{\sum_{i,j}(\beta_{x,i,j} - \langle \beta_x \rangle)(x_{i,j} - \langle x \rangle) I_{i,j}}{\sum_{i,j} I_{i,j}} \tag{1.27}$$

$$\left\langle u^2 \right\rangle = \frac{\sum_{i,j}(\beta_{x,i,j} - \langle \beta_x \rangle)^2 I_{i,j}}{\sum_{i,j} I_{i,j}} + \left(\frac{\lambda}{2\pi}\right)^2 \frac{\sum_{i,j}((\partial_x I)^2/I)}{\sum_{i,j} I_{i,j}}, \tag{1.28}$$

where $\langle x \rangle$ and $\langle \beta_x \rangle$ are the first moments over x and β_x, respectively, and the indices (i, j) are used to indicate a particular subpupil. With these variables, the values of the width d, divergence θ, beam quality factor M^2, waist diameter d_0, Rayleigh length z_R and waist position z_0 can all be calculated at any given point as follows [86]:

$$\begin{gathered} d = 4\sqrt{\langle x^2 \rangle}, \qquad \theta = 4\sqrt{\langle u^2 \rangle}, \qquad M^2 = \frac{4\pi}{\lambda}\sqrt{\langle x^2 \rangle \langle u^2 \rangle - \langle xu \rangle^2}, \\ d_0 = \frac{4M^2\lambda}{\pi\theta}, \qquad z_R = \frac{d_0}{\theta}, \qquad z_0 = \frac{z_R \langle xu \rangle}{|\langle xu \rangle|}\sqrt{\left(\frac{d}{d_0}\right)^2 - 1}. \end{gathered} \tag{1.29}$$

If the wavefront and intensity distribution of a beam are known at a given point, they can be calculated at any point along the z axis by the use of Fresnel-Kirchhoff propagation:

$$I(x, y, z) = \left| \frac{ik}{2\pi z} \int_{\infty}\!\!\int \sqrt{I(x', y')} e^{ik\Phi(x'y')} e^{\frac{ik[(x-x')^2 + (y-y')^2]}{2z}} dx'dy' \right|^2, \tag{1.30}$$

with x', y' and x, y being the Cartesian coordinates of two parallel planes, separated by a distance z, and $\Phi(x', y')$ being the value of the measured wavefront at a given point, in units of distance. Backpropagation is useful for cases where direct measurement of the intensity distribution is not easy or possible, such as the shape of a focal spot, where a CCD camera could be damaged or not provide enough resolution. In this case, backpropagating the beam measured in the far field is a more suitable option. In the case of HHG, backpropagation can be used to show the shape and size of the harmonic source in the generating medium.

1.3.2 Experimental study of the spatial properties of single high-harmonic pulses

The generation of high-harmonic beams with high spatial quality can be useful for applications like imaging [87], holography [88] or as a seed of a plasma amplifier [11]. Good spatial quality also allows for tighter focusing [89], leading to higher intensities useful for experiments involving nonlinear phenomena, such as two-photon ionization of gases [90]. The study of harmonic wavefronts can lead to better knowledge on the physical process of HHG, as well as lead to new ways of optimizing them.

This section describes the results obtained in an experiment that we carried out in collaboration with the atomic physics group of the Lund Attosecond Science Center (LASC), at the Lund Laser Centre (LLC) in Sweden. It was conducted in the HHG beamline of the Lund High-Power Laser Facility, and its main goal was studying in detail how the harmonic wavefronts depend on the generation parameters, as well as finding how they relate to the spatial properties of the generating IR beam. The high harmonics generated in this beamline have pulse energies of several nanojoules, making it possible to take single-shot wavefront measurements.

1.3.2.1 Background and objectives

Several studies have been carried out in recent years on the subject of the spatial properties of high harmonics. One of the first experiments on the wavefronts of high harmonics made use of the technique of point diffraction interferometry [84], in the year 2003. However, it was limited by an error in the wavefront measurement of $\lambda/15$ RMS, too close to the Maréchal criterion to ensure a good accuracy. Furthermore, only the defocus was characterized, without measuring higher-order aberrations.

Another experiment, carried out in 2008, made use of a Hartmann sensor to measure harmonic wavefronts from argon, with many sets of generation conditions [19], with a degree of accuracy of $\lambda/120\ \mathrm{RMS}$. The main goal of this experiment was to find out how to optimize the high-harmonic spatial quality, in order to improve the seeding of plasma-based soft-X-ray lasers [11]. The generation conditions were chosen so that the beam would be stable and with a good quality, with a photon flux lower than the maximum achievable in the setup. Due to this, 1000 to 5000 shots were accumulated for each measurement. The optimum wavefront had an RMS of $(0.15 \pm 0.02)\lambda$, with little variation with respect to the generation parameters. From the obtained Zernike coefficients, the main aberration was found to be astigmatism, in both the harmonic and the IR beams. This result hints at the relation between both the IR and harmonic wavefronts.

This link between wavefronts was investigated in another experiment carried out in the same year [20]. In this case, a deformable mirror was placed in the path of the IR laser and used to modify its wavefront by introducing different aberrations, with emphasis on astigmatism at 0°, seeing that it was the dominant aberration in both beams before correction through the DM. Then, IR wavefronts and the harmonic wavefronts they generate were recorded. 100 harmonic shots were accumulated for each measurement. It was found that the least astigmatic harmonic wavefront was not found when the IR beam was least astigmatic. Instead, it was found when the Zernike coefficient corresponding to

0-degree astigmatism had a value of -0.2. This shows that, while the IR and harmonic wavefronts are clearly related, this relation is more complex than a simple transfer of one beam to the other. Additionally, the best IR wavefront yielded the highest conversion efficiency.

A common trait in the experiments summarized here is the fact that hundreds or thousands of harmonic shots had to be accumulated to take the reported measurements. This means that only average wavefronts are measured, and the wavefront of a single harmonic pulse remains unknown, as well as its shot-to-shot stability.

The experiment described in the following was carried out with the objective of studying the spatial properties of high-harmonic pulses in detail, and the influence of the IR wavefront and the generation parameters. In the HHG beamline of the Lund High-Power Laser Facility, at LLC, through careful phase matching and the use of loose focusing geometry, the generated harmonic pulses have enough energy for single-shot wavefront measurements, giving new insight into the physics of the HHG process, as well as its shot-to-shot variations. While there have been experiments in which the intensity distribution of harmonic pulses was measured in single-shot regime [51], this is, to the best of our knowledge, the first systematic study of the full spatial characteristics of individual high-harmonic pulses.

1.3.2.2 Experimental setup

The experimental setup used for this experiment can be seen in figure 1.17 (a). The laser used for HHG is a Ti:Sapphire laser emitting 40-fs pulses of 800-nm wavelength, at a repetition rate of $10\,\mathrm{Hz}$ and with s-polarization. The pulse energy can be varied, with values close to $25\,\mathrm{mJ}$ used for efficient HHG. The high harmonics are generated in loose focusing geometry to optimize the conversion efficiency, by using a focal length of $9\,\mathrm{m}$, and a 6-cm-long cylindrical gas cell filled with argon. The focal plane is located $25\,\mathrm{cm}$ after the cell. The backing pressure in the setup is close to $10^{-7}\,\mathrm{mbar}$.

After generation, the harmonic and IR beams are sent to a fused silica plate, set at a grazing angle of 10°. The plate reflects the harmonics, but transmits most of the energy on the driving IR pulse thanks to an anti-reflective coating. The beam is sent through a 200-mm-thick aluminum filter that eliminates the remaining IR energy towards a gold-coated flat mirror. This mirror can be rotated in order to send the harmonic beam towards a spectrometer, a CCD camera for footprint recording, or the Hartmann WFS, for which case the grazing angle is 15°. The calculated reflectivities of both mirrors and the transmission of the filter are presented in figures B.1 in appendix B.

The spectrometer is made up of an entrance slit, a toroidal mirror, a reflective diffraction grating and a microchannel plate on which an image of the slit is formed. The CCD is an Andor iKon-L 936 camera, with $2048\text{x}2048$ pixels of side $13.5\,\mathrm{\mu m}$, and it allows for the harmonic pulse energy to be calculated, thanks to a previous calibration. Each harmonic pulse has an energy of several nanojoules after the two mirrors and the filter. Since the harmonic beam has a very low divergence due to the loose focusing geometry, the Hartmann WFS had to be placed as far as possible from the gas cell, about $9.4\,\mathrm{m}$, in order to illuminate enough subpupils for an accurate wavefront reconstruction.

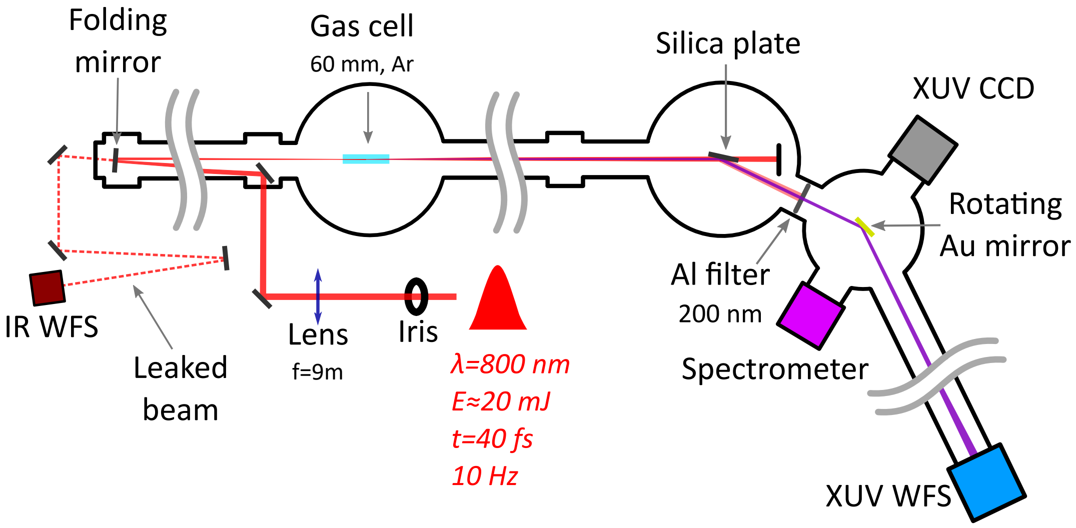

Figure 1.17: Schematic drawing of the experimental setup for the measurement of single-shot high-harmonic wavefronts. The last mirror can be rotated to send the beam towards the CCD or the spectrometer as well.

A Shack-Hartmann wavefront sensor, provided by Imagine Optic, was used to measure the wavefront of the driving IR beam through a leak on a flat mirror. This, coupled with the high energy per harmonic pulse, allows for the simultaneous measurement of the full spatial properties of a single harmonic pulse and the IR pulse that generated it.

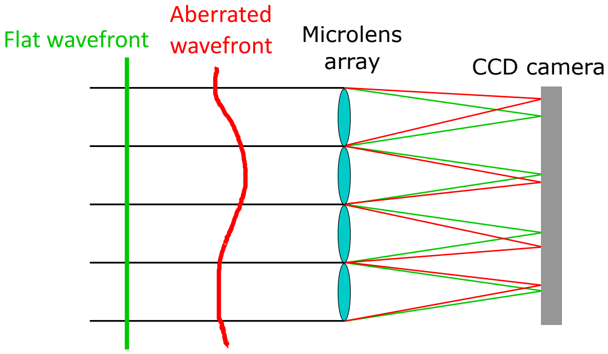

Figure 1.18: Schematic drawing of the principle of a Shack-Hartmann sensor. The relative positions of the focal spots with respect to reference positions are used to reconstruct the wavefront.

The working principle of the IR Shack-Hartmann wavefront sensor, which can be seen in figure 1.18, is similar to that of a Hartmann sensor, described in section 1.3.1.1, with the exception that the beam is sampled by an array of microlenses instead of apertures [91]. The position of the focused beamlet on the CCD chip depends on the local slope of the wavefront. By focusing the beamlets instead of diffracting them, Shack-Hartmann sensors provide a higher signal-to-noise ratio than Hartmann sensors, as well as a more precise determination of the spot position [92]. The Shack-Hartmann sensor used in this experiment is a HASO3-32 sensor, consisting in an array of $40\text{x}32$ microlenses of diameter $151.1\,\mu\text{m}$, and a Basler A311f CCD camera, with $656\text{x}494$ pixels of side $9.9\,\mu\text{m}$.

1.3.2.3 Single-shot high-harmonic wavefronts

Several series of measurements were performed in order to study how the generation parameters affect the wavefront of a harmonic pulse. In order to account for shot-to-shot variations in the high harmonics, five single-shot harmonic and IR wavefronts were acquired simultaneously for every set of generation parameters. The footprint and spectrum of the high harmonics were measured for all cases as well, along with the pulse energy.

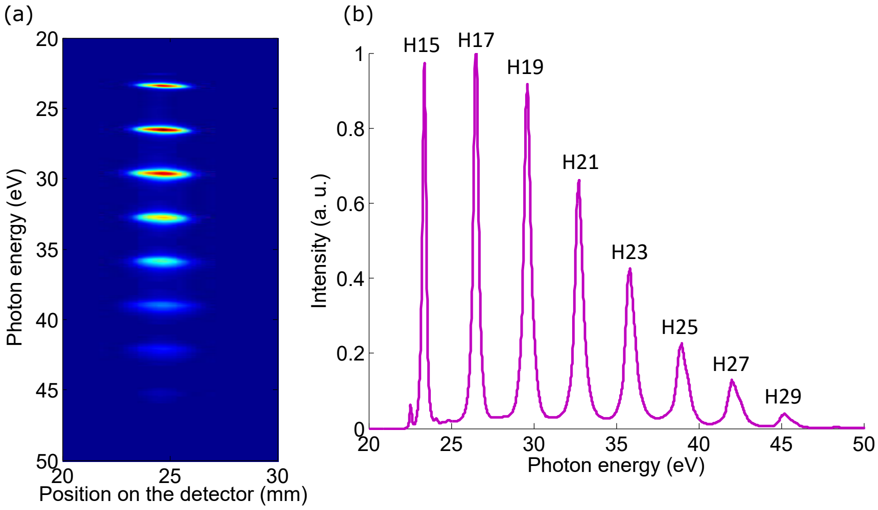

Figure 1.19: (a) Picture taken with the spectrometer (zoom) and (b) high-harmonic spectrum obtained from it.

Note that the full harmonic beam is used for these measurements, including all generated orders. Figure 1.19 shows a typical spectrum generated in the setup, in this case with an IR pulse energy of $E_{IR} = 18.4\,\text{mJ}$, an iris diameter of $22\,\text{mm}$, and a gas pressure of $p = 189\,\text{mbar}$, measured in the pipe conducting the gas towards the cell, where the pressure is estimated to be closer to $10\,\text{mbar}$. In order to optimize the signal-to-noise ratio, a total of 500 harmonic pulses were accumulated for every spectrum acquisition.

A single-shot footprint measured after the spectrum can be seen in figure 1.20. The high-harmonic beam has an elliptical shape, with an approximate FWHM size of $1.25\,\text{mm}$ along its major axis, and $0.93\,\text{mm}$ along the minor axis. Both pointing and ellipticity of the beam varied throughout the experiment when the generation conditions were changed.

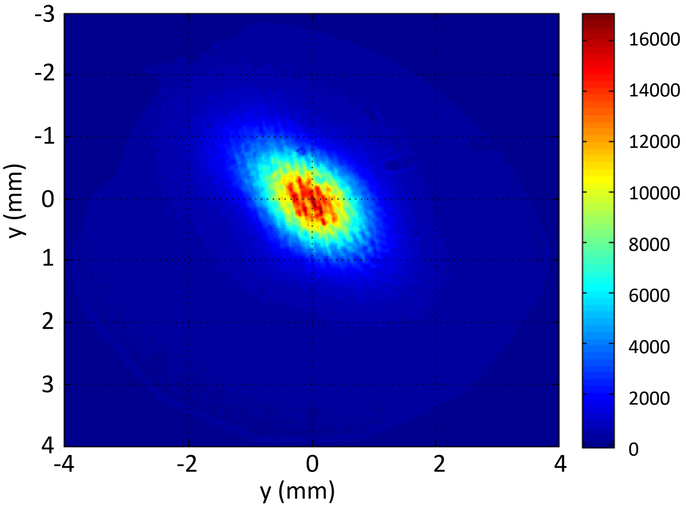

Figure 1.20: Typical single-shot footprint (zoom) of the harmonic beam measured by the CCD camera.

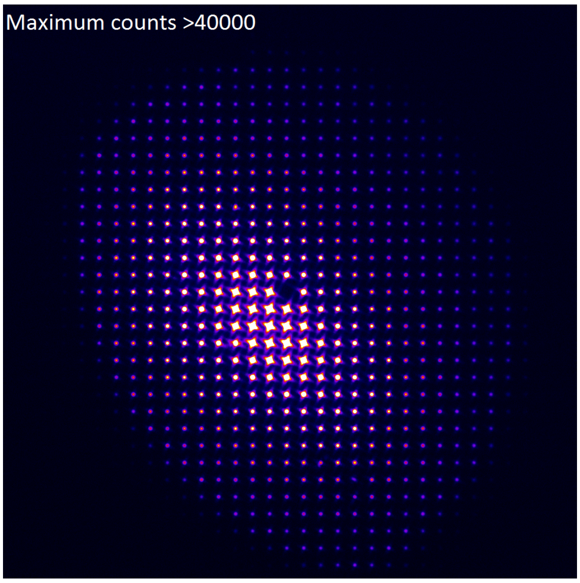

Figure 1.21: Raw image measured by the Hartmann XUV wavefront sensor with a single high-harmonic pulse. False color, white and orange represent high counts, while purple and black represent low counts.

After measuring spectrum and footprint, the beam is sent to the Hartmann WFS. Figure 1.21, shows the raw image obtained with a single shot for the same generation parameters. This image allows for a coarse estimation of the beam size on the Hartmann plate along the axes of the ellipse. The approximate FWHM sizes are $3.4\,\mathrm{mm}$ and $2.1\,\mathrm{mm}$.

It can be seen from the image that there are a significant amount of subpupils registering a very low number of counts compared to the central ones, usually around 1000. While the HASO software will calculate the local wavefront slope in those subpupils, their lower signal-to-noise ratio leads to a more imprecise determination of the centroid of the diffracted beam, thus leading to an overestimation of the wavefront error. An intensity threshold is applied in the software in order to reduce the error in the wavefront reconstruction. The applied intensity thresholds are generally of 5%. Those values are such that at least the 90% of the pulse energy is considered, while ruling out the least illuminated subpupils. Additionally, it must be noted that, in other measurements taken in the experiment where the pulse energy was lower, the counts in those subpupils are even lower and are thus not taken into account by the software. For this reason, applying an intensity threshold also allows for a better comparison of their wavefronts, regardless of harmonic pulse energy.

The resulting wavefront can be seen in figure 1.22, along with the intensity distribution. Zonal reconstruction was used due to the elliptical shape of the beam. The beam is measured in units of $\lambda = 42\,\mathrm{nm}$, corresponding to harmonic 19. The WFS sensitivity of $0.6\,\mathrm{nm}$ RMS is equivalent to $\lambda/70 = 0.014\lambda$ at this wavelength.

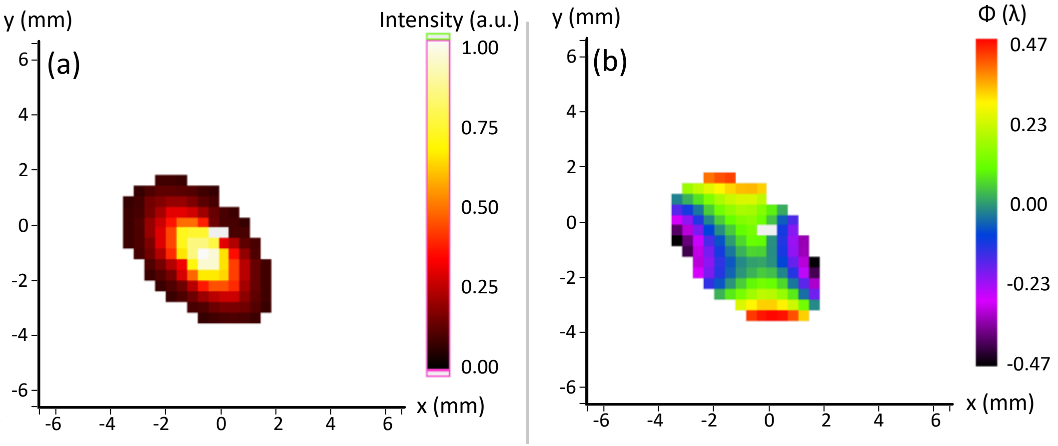

Figure 1.22: Intensity distribution (a) and wavefront (b) of the harmonic beam, obtained from the previous image. A 5% intensity threshold was applied for increased accuracy.

After five consecutive measurements, we find an average wavefront RMS value of $(0.226 \pm 0.036)\lambda$ and a PV value of $(1.028 \pm 0.146)\lambda$. The relative standard deviation of both quantities is nearly 15%. The most prominent aberration is clearly astigmatism at 0°, consistent with previous results in kHz lasers [20]. Zonal reconstruction, however, does not allow for the calculation of the Zernike coefficients, but the software does allow to rule out the effects of astigmatism at 0° and astigmatism at 45°. Figure 1.23 shows the wavefronts after eliminating astigmatism at 0° and both of them. For simplicity, the latter will be referred to as the *residual wavefront* in this thesis. In these cases, the RMS has a value of $(0.070 \pm 0.012)\lambda$ and $(0.042 \pm 0.010)\lambda$, respectively. These quantities allow for the calculation of how much these two aberrations contribute to the RMS value of the full wavefront. The contribution of astigmatism at 0° is $(0.156 \pm 0.025)\lambda$, while astigmatism at 45° is much less significant, with a value of $(0.028 \pm 0.007)\lambda$. Note that the astigmatism contained in a wavefront can be oriented towards any direction, and decomposed in these two aberrations. The direction of astigmatism is characterized by the angle between it and the x axis defined by the Hartmann WFS. In the example of figure 1.22 (b), the average angle of astigmatism is $6.6 \pm 0.5^\circ$.

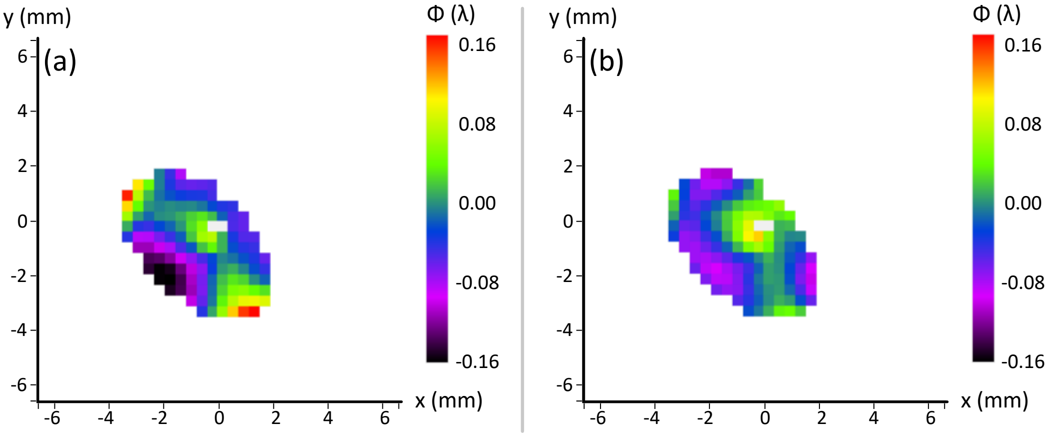

Figure 1.23: Resulting harmonic wavefront after removing the contribution of astigmatism at 0° (a) and after removing astigmatism at both 0° and 45° (b).

Optics calibration

It is important to note that the harmonic beam is reflected by two mirrors, and it is also filtered before being measured by the WFS. All these optics can introduce additional aberrations in the wavefront, which can be known through calibration with a reference beam. The procedure to calibrate the optics is similar to the one used to calibrate the sensor itself (see section 1.3.1.2). The harmonic beam is spatially filtered by a 100-μm pinhole placed in the beam path. This creates a beam with a known spherical wavefront, with a size similar to that of the full beam. This reference beam is then reflected by the optics and measured in the WFS. The resulting calibration wavefront can be seen in figure 1.24. Due to the low amount of energy transmitted through the pinhole, 200 pulses were accumulated for each acquisition.

The measured calibration wavefront has an RMS value of $(0.022 \pm 0.005)\lambda$ and a PV value of $(0.101 \pm 0.018)\lambda$, averaged over 5 single-shot acquisitions. It must be noted that the calibration beam is smaller than the direct beam measured throughout the experiment. Furthermore, the pointing of the latter moved due to the many different HHG conditions that were used. For this reason, different parts of the mirror not probed with the calibration were used during the measurements. This means that the calibration wavefront cannot be systematically subtracted from the measurements for correction. Nevertheless, the RMS and PV values are smaller than those measured in the direct beam shown above by a factor of 10, so the aberrations induced by the optics are negligible by comparison to those present in the harmonic wavefront. In particular, it is also important to note that the calibration beam is barely astigmatic, so the astigmatism at 0° present in the direct beam (see figure 1.22) is intrinsic to it, and not caused by the optics. Since this beam is circular, modal wavefront reconstruction can be used to illustrate this. The resulting Zernike coefficients for the lowest-order aberrations can be seen in table 1.1, showing that astigmatism at 0° is actually not the most significant aberration.

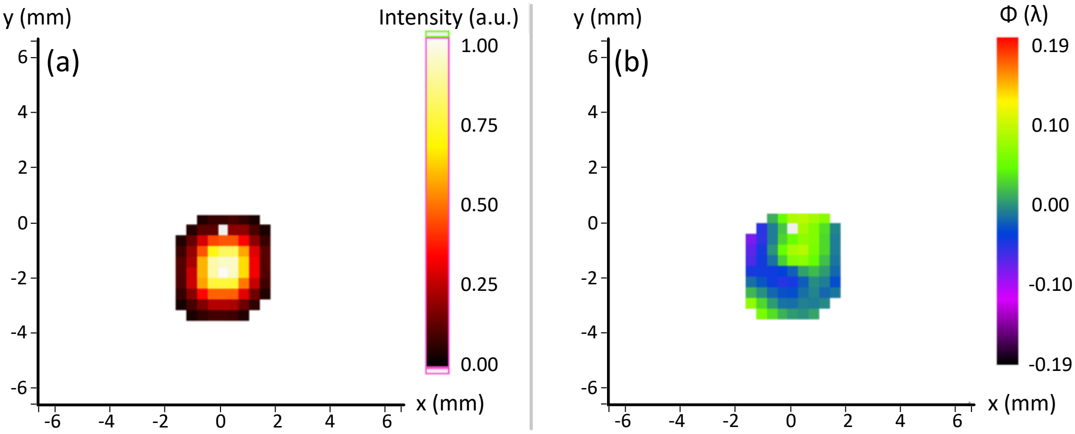

Figure 1.24: Intensity (a) and wavefront (b) of the calibration beam, obtained by spatially filtering the harmonic beam with a 100-μm pinhole, measured after propagation through the setup.

N	*Aberration*	*Average Zernike coefficient (λ)*
4	Astigmatism at 0°	-0.0186
5	Astigmatism at 45°	0.0217
6	Coma at 0°	-0.0088
7	Coma at 90°	-0.0153
8	Spherical aberration	0.0048

Table 1.1: Lowest-order Zernike coefficients (standard normalization) obtained via modal wavefront reconstruction of the reference beam, with a pupil of radius 1.8 mm. These values show that the astigmatism observed in the full harmonic beam is not caused by the optics.

Once this step is finished, single-shot high-harmonic wavefronts are measured as a function of several parameters involved in the HHG process. These parameters are the IR pulse energy, the gas pressure, the IR beam diameter, its chirp, the direction of its polarization, and the position of the focal plane with respect to the gas cell.

IR pulse energy

The energy contained in the driving IR pulse is a key parameter for HHG, since it affects the intensity at focus and thus the conversion efficiency. Higher IR energies will generate more energetic high-harmonic pulses, as long as the intensity stays below the threshold for barrier-suppression ionization. In this experiment, the energy of the IR pulses can be changed by using a half-wave plate in front of a linear polarizer, following Malus' law. Three different values of IR pulse energy were used for this series of measurements: $14.7\,\mathrm{mJ}$, $18.4\,\mathrm{mJ}$, and $21.9\,\mathrm{mJ}$. All other parameters were kept constant, with an aperture diameter of $22\,\mathrm{mm}$ and a gas pressure of $189\,\mathrm{mbar}$. Pulse energy is measured with a powermeter and averaged over hundreds of pulses, with standard deviations of the order of $1\,\mathrm{mJ}$.

The generated harmonic spectrum for each IR energy value can be seen in figure 1.25. The three spectra are nearly identical, their main difference being that the harmonic peaks become slightly wider for higher IR energies.

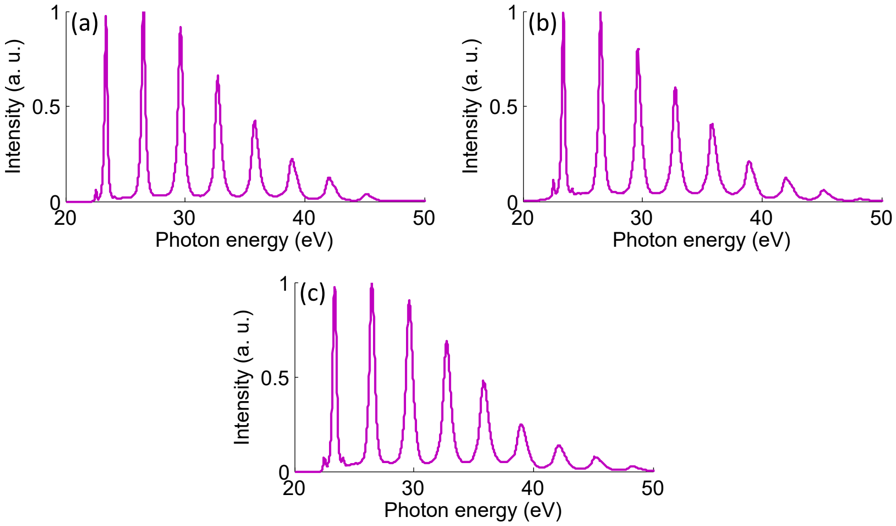

Figure 1.25: Normalized high-harmonic spectra generated with different IR pulse energies: (a) 14.7 mJ, (b) 18.4 mJ, and (c) 21.9 mJ.

Five single-shot harmonic wavefronts were acquired for each case. The average harmonic pulse energy arriving at the CCD in each case can be seen in figure 1.26, showing a quasi-linear trend for the studied interval. The values presented in this and subsequent figures are obtained by averaging the five measured values, with the error bars representing the standard deviation, giving insight into the shot-to-shot variations of the high-harmonic beam. The typical intensity distributions can be seen in figure 1.27, with one example for each IR energy value. Note that the three images have been normalized to use the same colormap, in order to properly showcase the different pulse energies. It can be seen that the harmonic beam becomes larger, more elliptical and more intense for higher values of IR pulse energy. The corresponding harmonic wavefronts are presented in figure 1.28. The same color scale is used in the three images.

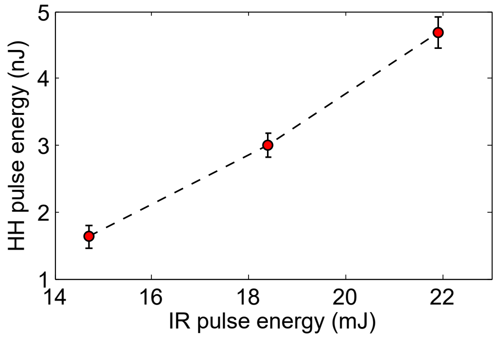

Figure 1.26: Energy of a high-harmonic pulse as a function of IR pulse energy. All values have been averaged over five separate acquisitions, with the standard deviation presented in the error bars.

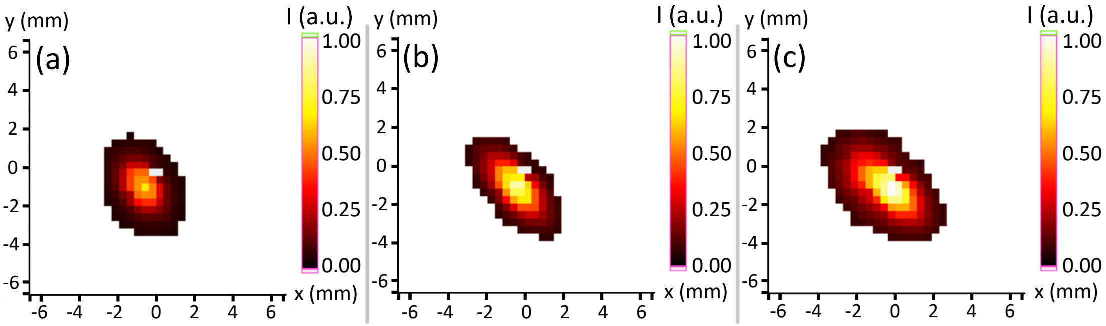

Figure 1.27: Single-shot high-harmonic intensity distributions for different IR pulse energies: (a) 14.7 mJ, (b) 18.4 mJ, and (c) 21.9 mJ. The same intensity scale is used in all images.

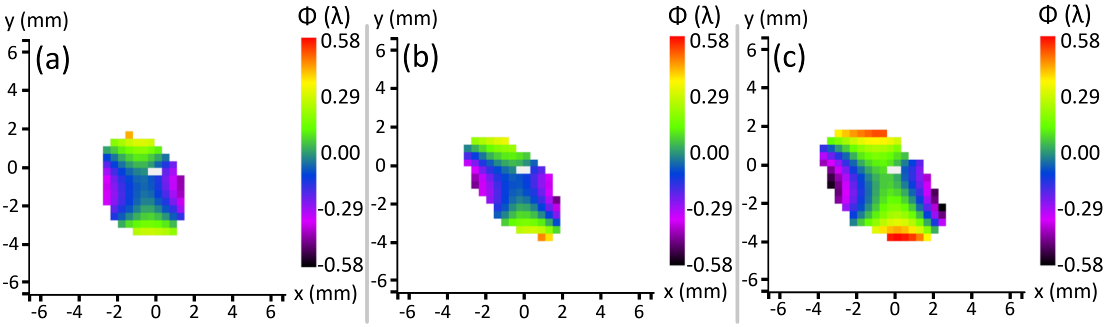

Figure 1.28: Single-shot high-harmonic wavefronts for different IR pulse energies: (a) 14.7 mJ, (b) 18.4 mJ, and (c) 21.9 mJ. The same color scale is used in all cases for the sake of comparison.

As it was seen above, astigmatism at 0° is the dominant aberration, being more significant for higher IR energies. The average wavefront RMS and PV values, seen in figures 1.29 (a) and (b), respectively, both increase and become less stable with the IR energy. The HASO software allows for astigmatism at 0° and 45° to be ruled out. The RMS and PV values of the so-called residual wavefront are shown in figures 1.29 (c) and (d). This, in turn, allows for the exact contribution of these aberrations to the overall wavefront to be quantified. The contribution of astigmatism at 0° to RMS is included in figures 1.29 (e), and also increases with IR energy. Finally, figure 1.29 (f) shows the angle of the astigmatism as a function of IR pulse energy, which does not change significantly, as it stays always positive and lower than 7°. Astigmatism at 45° is not shown since it is tens of times less significant in all cases, as evidenced by the angle of astigmatism being always close to 0°.

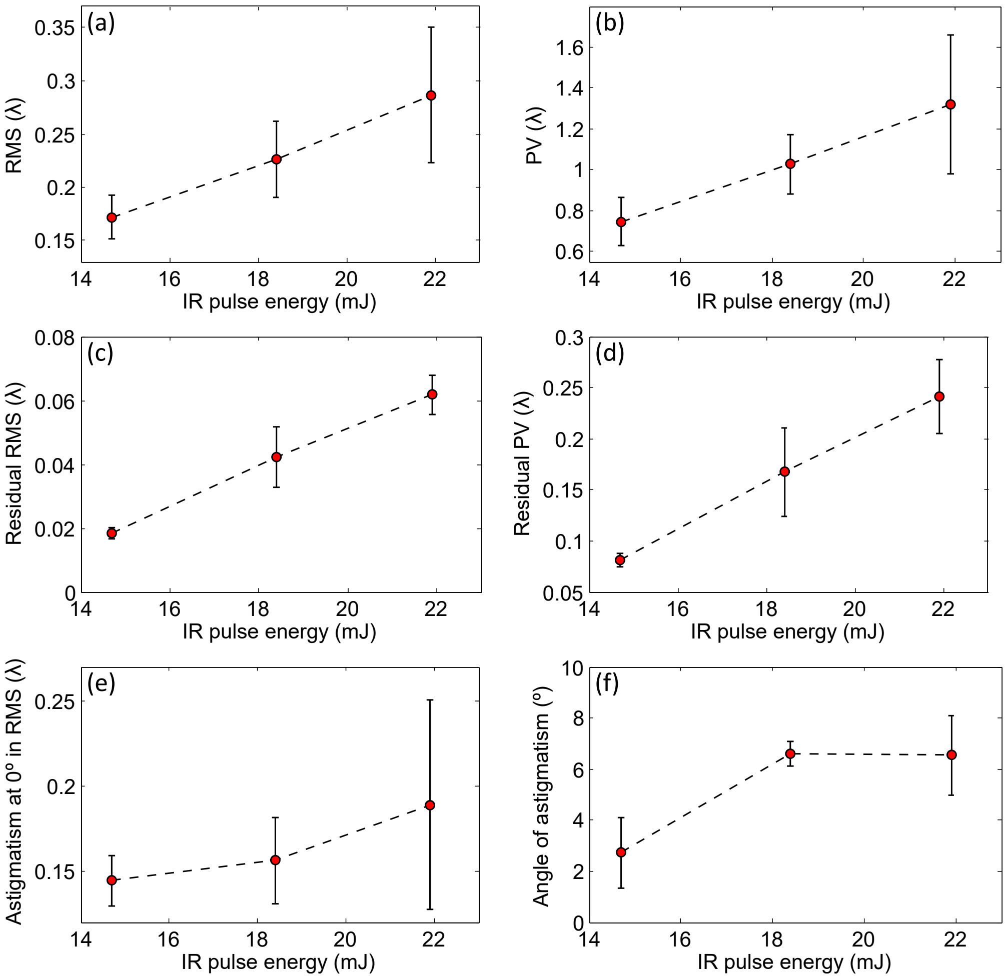

Figure 1.29: Evolution of several parameters describing the high-harmonic wavefront with respect to the IR pulse energy: (a) RMS, (b) PV, (c) residual RMS, (d) residual PV, (e) contribution of astigmatism at 0° to the wavefront RMS, and (f) angle of astigmatism.

Figure 1.30 shows the *residual* harmonic wavefronts after astigmatism at 0° and 45° have been ruled out. The wavefront presented in figure 1.30 (c) suggests the presence of coma at 0° (see figure A.1 in appendix A).

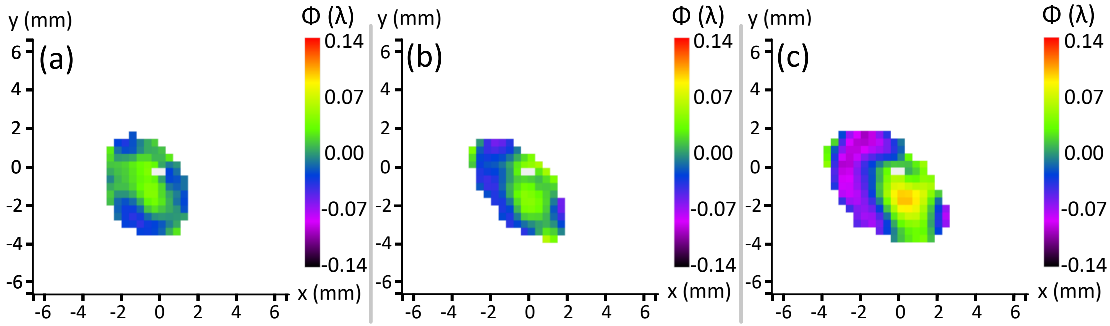

Figure 1.30: Residual high-harmonic wavefronts, without astigmatism, for different IR pulse energies: (a) 14.7 mJ, (b) 18.4 mJ, and (c) 21.9 mJ.

Having measured the intensity distribution and wavefront, the harmonic pulse can be backpropagated in order to find the intensity distribution at the harmonic source in the gas cell. The calculated harmonic source for each value of the IR energy can be seen in figure 1.31. As is the case of the far-field intensity distribution, it is visibly elliptical, and more so when increasing the driving pulse energy. The FWHM size has been measured along both axes of the ellipse for all cases, and can be seen in figures 1.32 (a) and (b). The increase in ellipticity with IR energy is evidenced by the fact that the size along the minor axis is almost independent of IR energy, while the major axis increases with it. In both cases, the source size becomes more unstable with higher energy.

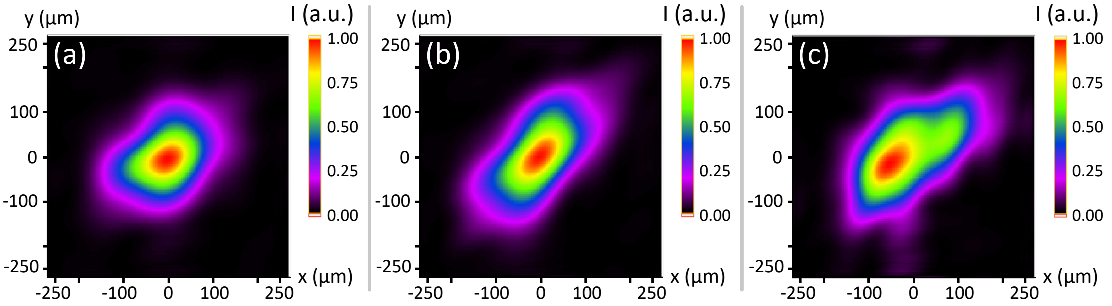

Figure 1.31: Calculated high-harmonic source for different IR pulse energies: (a) 14.7 mJ, (b) 18.4 mJ, and (c) 21.9 mJ.

The Strehl ratio of each distribution is also calculated, and it is shown to decrease for higher IR energies, as seen in figure 1.32 (c). The Strehl ratio is defined as the ratio of the peak intensity of the measured distribution and the peak intensity for the case of an unaberrated, diffraction-limited wavefront [93], thus varying between 0 and 1.

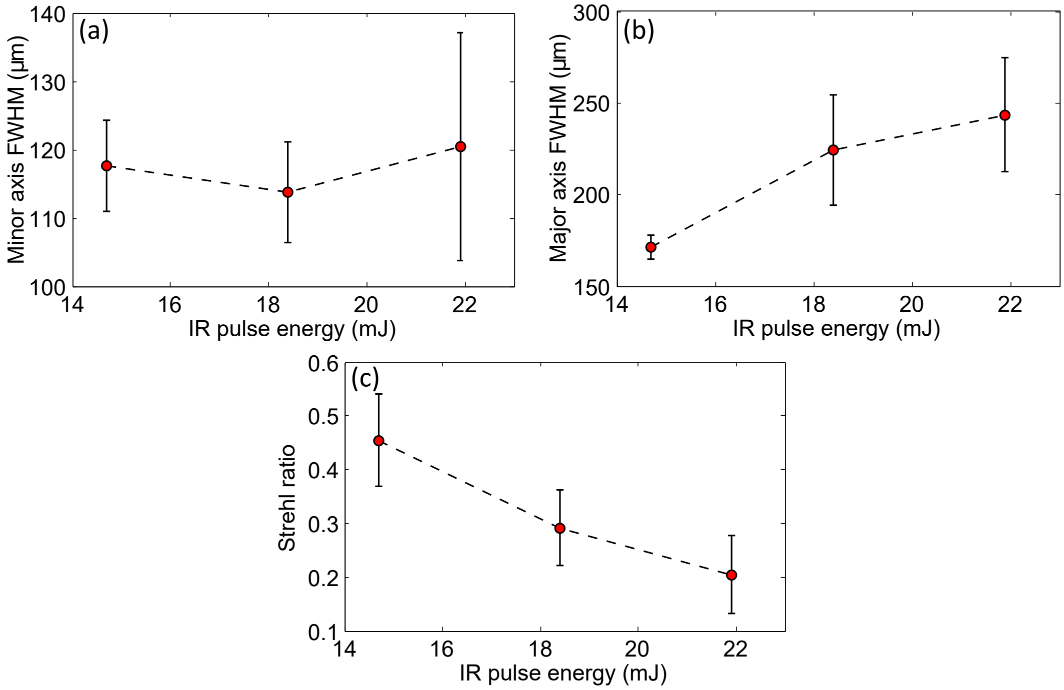

Figure 1.32: FWHM size of the calculated high-harmonic source along the minor (a) and major (b) axes, and (c) Strehl ratio as a function of IR pulse energy.

It can be seen that, when staying below the intensity threshold of barrier-suppression ionization in the gas atoms, increasing the energy of the driving pulse increases the energy of the harmonic output. This higher harmonic pulse energy appears to lead, in turn, to more aberrated wavefronts, probably due to the fact that the more energetic IR pulses produce more elongated harmonic sources, as seen after backpropagation of the measured pulses.

Gas pressure

Another key parameter for HHG is the pressure at which the argon gas is pumped to the cell. This parameter greatly affects the conversion efficiency, since it is related to the number of emitters present in the medium, as well as its absorption properties. Thus, we studied its effects on the harmonic wavefront. A total of ten pressure values were used, from $48\,\mathrm{mbar}$ to $228\,\mathrm{mbar}$ in steps of $20\,\mathrm{mbar}$. IR pulse energy was kept at $21.9\,\mathrm{mJ}$, and the iris diameter was $22\,\mathrm{mm}$. Further reducing or increasing the pressure beyond the aforementioned values resulted in extremely low signals. The harmonic spectra generated for six of those pressures can be seen in figure 1.33. In general, lower pressures yield fewer and lower harmonic orders. For example, the 29^{th} harmonic is only generated above $148\,\mathrm{mbar}$.

The values of harmonic pulse energy are shown in figure 1.34. As expected, harmonic signal is low for low pressures, increasing significantly with pressure until a maximum is reached. The intensity distributions corresponding to six of the probed pressure values can be seen in figure 1.35. As seen in the previous series of measurements, the beam is more elliptical when it is most intense, for pressures around $150\,\mathrm{mbar}$, while keeping a more circular distribution for the less intense cases. Further increasing the gas pressure hinders harmonic emission due to the gas absorbing the generated radiation.

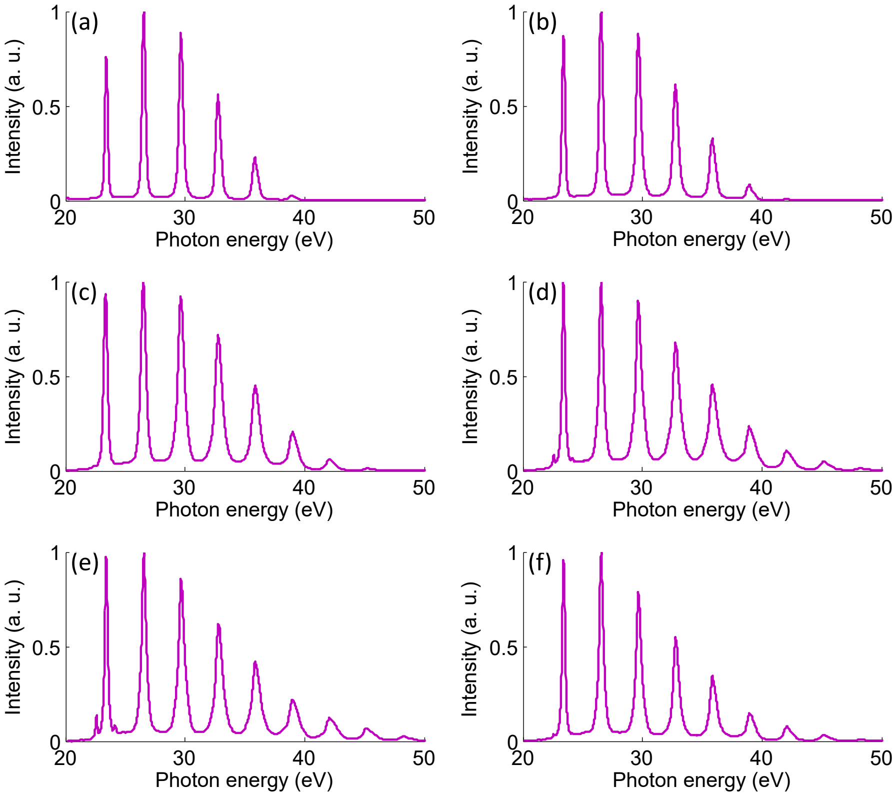

Figure 1.33: Normalized high-harmonic spectra generated with different pressures: (a) 48 mbar, (b) 68 mbar, (c) 108 mbar, (d) 148 mbar, (e) 188 mbar, and (f) 228 mbar.

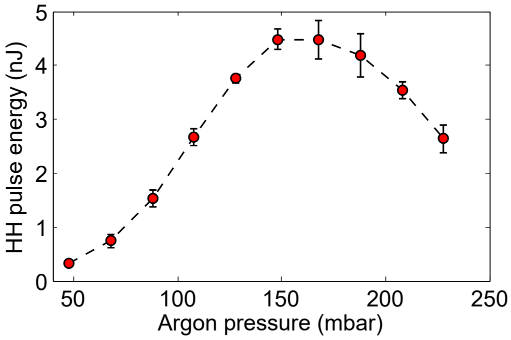

Figure 1.34: Energy of a high-harmonic pulse as a function of pressure.

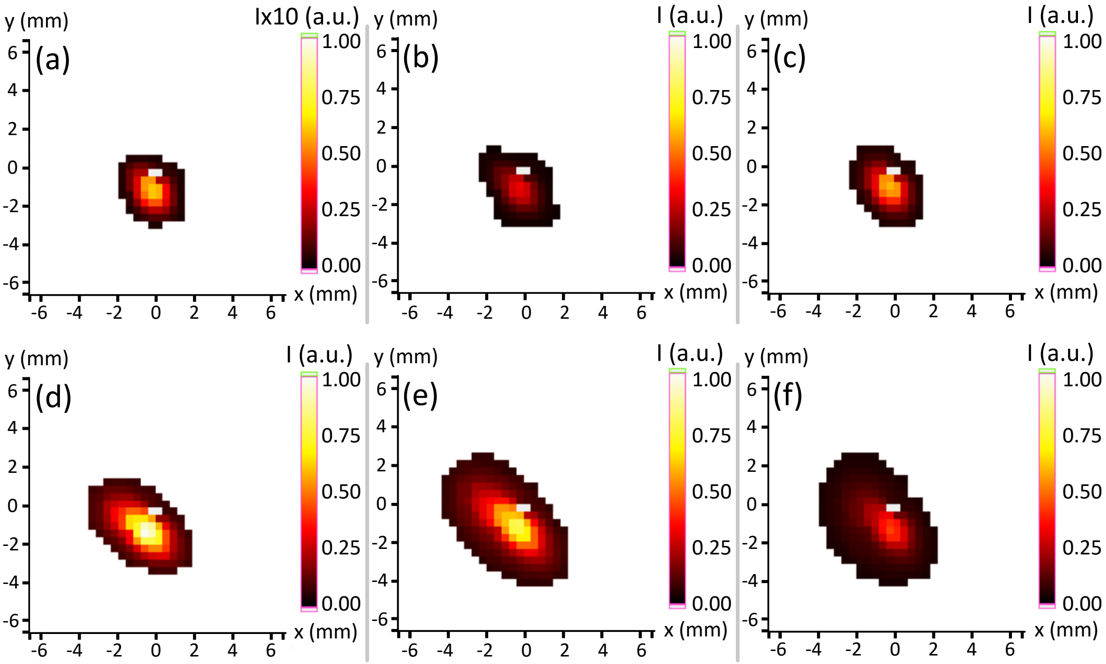

Figure 1.35: Single-shot high-harmonic intensity distributions for different pressures: (a) 48 mbar, (b) 68 mbar, (c) 108 mbar, (d) 148 mbar, (e) 188 mbar, and (f) 228 mbar. The scale was changed in (a) to make the beam more visible.

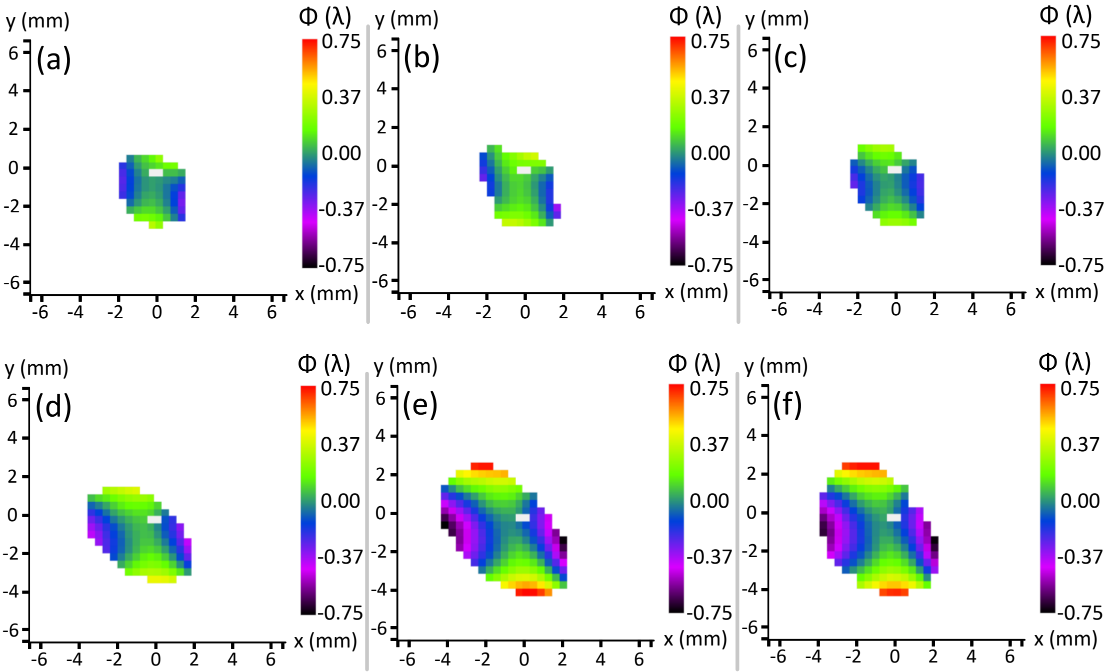

Figure 1.36: Single-shot high-harmonic wavefronts for different pressures: (a) 48 mbar, (b) 68 mbar, (c) 108 mbar, (d) 148 mbar, (e) 188 mbar, and (f) 228 mbar.

The corresponding harmonic wavefronts are shown in figure 1.36. They become increasingly aberrated with pressure, and astigmatism at $0°$ is still the dominant aberration. The RMS and PV values can be seen in figures 1.37 (a) to (d) to increase and become more unstable for higher pressures, as does the amount of astigmatism at $0°$, in figure 1.37 (e). Interestingly, the angle of astigmatism plotted in figure 1.37 (f) changes significantly for low pressure values, taking values close to $8°$ above $128\,\mathrm{mbar}$.

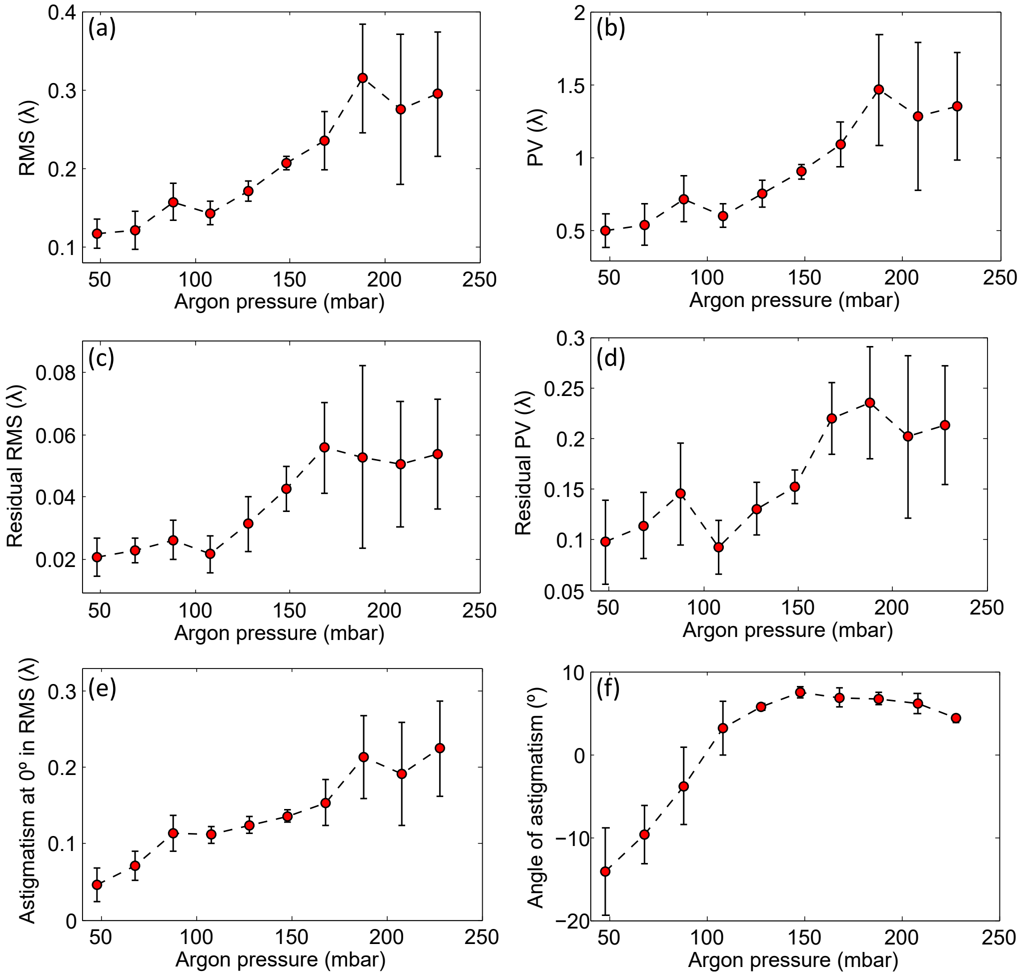

Figure 1.37: Evolution of several parameters describing the high-harmonic wavefront with respect to the gas pressure: (a) RMS, (b) PV, (c) residual RMS, (d) residual PV, (e) contribution of astigmatism at 0° to the wavefront RMS, and (f) angle of astigmatism.

The residual wavefronts after ruling out astigmatism at $0°$ and $45°$ can be seen in figure 1.38. As with the previous series of measurements, some coma at $0°$ is present, which becomes more significant at higher pressures.

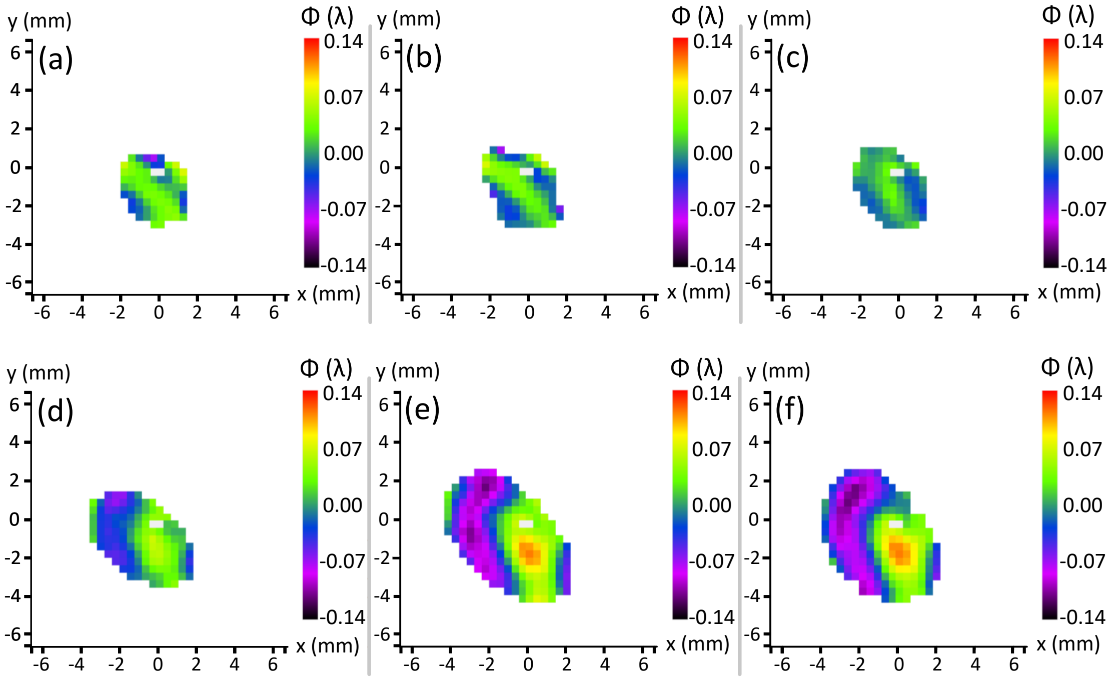

Figure 1.38: Residual high-harmonic wavefronts without astigmatism for different pressures: (a) 48 mbar, (b) 68 mbar, (c) 108 mbar, (d) 148 mbar, (e) 188 mbar, and (f) 228 mbar.

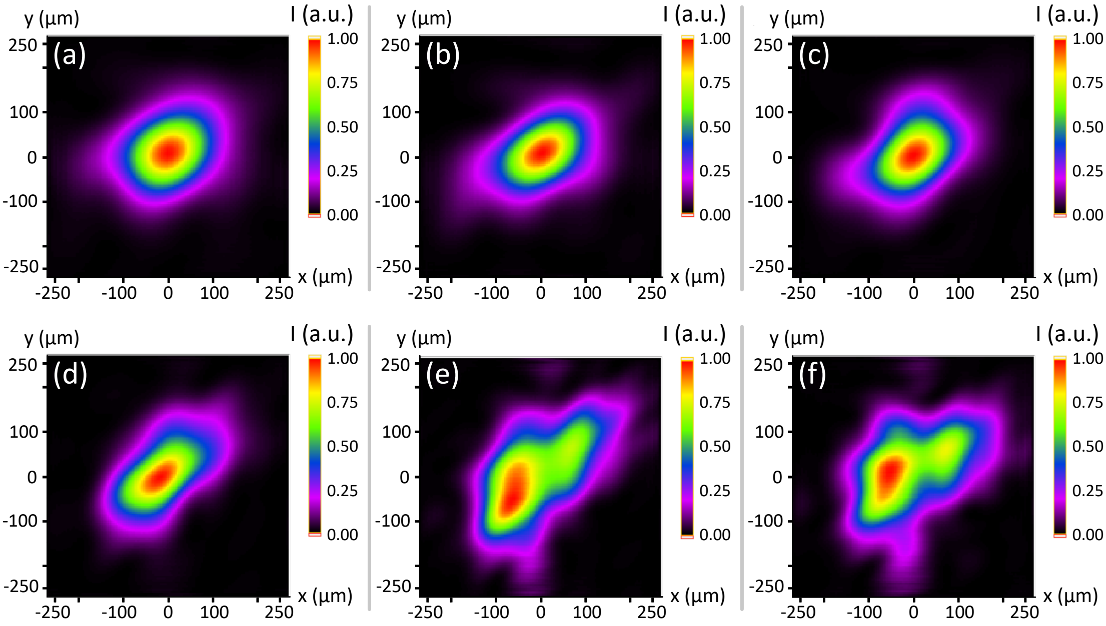

Figure 1.39: Calculated high-harmonic source for different pressures: (a) 48 mbar, (b) 68 mbar, (c) 108 mbar, (d) 148 mbar, (e) 188 mbar, and (f) 228 mbar.

Backpropagation of the pulses shown in the previous figures leads to the calculated harmonic sources presented in figure 1.39. The source is almost circular for lower pressures, and becomes more elongated and distorted when pressure is increased. For the case of $228\,\mathrm{mbar}$, two local maxima can be seen, suggesting that filamentation might be taking place inside the gas cell [94]. The average source size as a function of pressure is plotted in figures 1.40 (a) and (b). These reveal that higher pressures not only create a bigger source, but its size is less stable as well. The overall spatial quality of the source decreases when pressure is increased, as evidenced in figure 1.40 (c).

Increasing the pressure too much leads not only to lower harmonic energy, but also to a more aberrated wavefront. Intermediate pressures, between $150\,\mathrm{mbar}$ and $200\,\mathrm{mbar}$, yield beams with high energy and good spatial quality and stability. If necessary, better wavefronts can be obtained with low pressures, at the cost of energy.

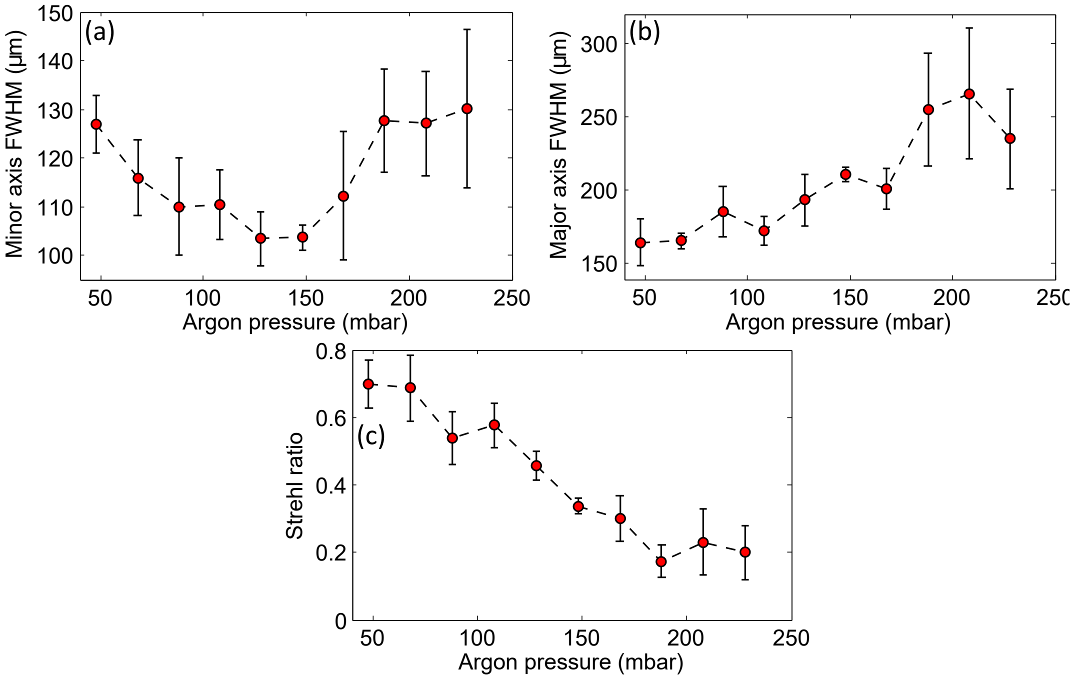

Figure 1.40: FWHM size of the calculated high-harmonic source along the minor (a) and major (b) axes, and (c) Strehl ratio as a function of pressure.

Iris aperture

The influence that the aperture applied to the IR beam has on HHG is complex, due to how the focusing geometry is affected by it. A truncated Gaussian beam will produce a focal spot and Rayleigh length dependent on this aperture, leading to significant changes in both conversion efficiency and the spatial profiles of the generated harmonic beams [63, 66]. For this experiment, 10 different iris diameters were used, varying between $17\,\mathrm{mm}$ and $35\,\mathrm{mm}$ in steps of $2\,\mathrm{mm}$. Smaller diameters or a fully open iris lead to almost nonexistent harmonic signal. The gas pressure was kept at $189\,\mathrm{mbar}$ for this series of measurements. The IR pulse energy was not changed. However, the actual energy arriving at the gas cell was dependent on the iris diameter as seen in table 1.2. The harmonic spectra measured for six of those diameter values can be seen in figure 1.41. Smaller and larger diameters lead to more irregular spectra, as well as less intensity in higher harmonic orders. For example, the 31^{st} order is only present for a diameter of $21\,\mathrm{mm}$, while using $17\,\mathrm{mm}$ only generates up to the 23^{rd} order.

Iris diameter (mm)	*IR energy (mJ)*	*Iris diameter (mm)*	*IR energy (mJ)*
17	15.8	27	31.9
19	21.2	29	34.7
21	24.2	31	37.5
23	26.9	33	40.4
25	28.6	35	41.4

Table 1.2: Measured IR pulse energy for different aperture diameters.

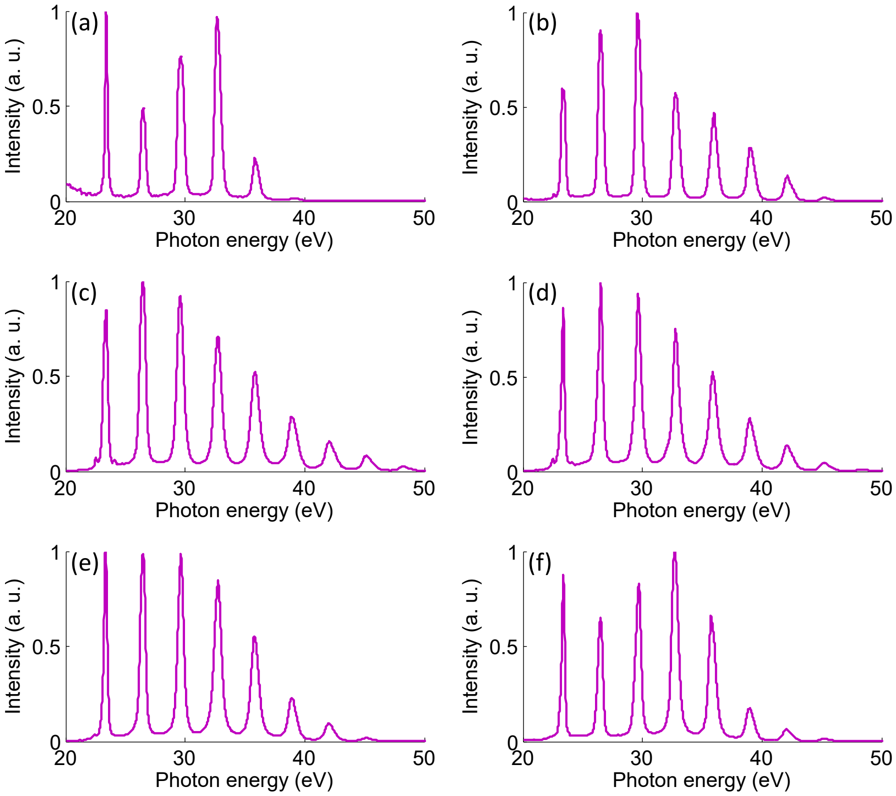

Figure 1.41: Normalized high-harmonic spectra generated with different iris diameters: (a) 17 mm, (b) 19 mm, (c) 21 mm, (d) 25 mm, (e) 29 mm, and (f) 33 mm.

The average energy of a harmonic pulse as a function of the diameter can be seen in figure 1.42. Apertures smaller than $19\,\mathrm{mm}$ lead to low-energy harmonic pulses. Further increasing the aperture leads to a steep increase in energy, which then stays almost constant in the range from $21\,\mathrm{mm}$ to $29\,\mathrm{mm}$ before decreasing again. Using smaller apertures within that range, however, yields higher intensities due to the smaller beam size. Figure 1.43 shows the evolution of the harmonic intensity distribution with the iris diameter.

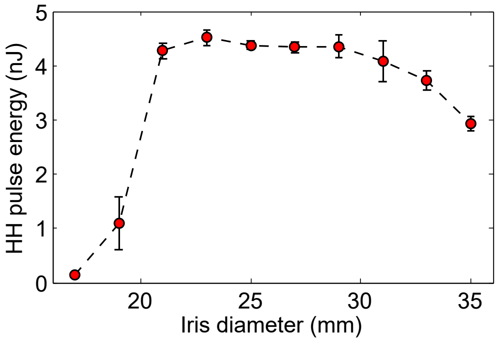

Figure 1.42: Energy of a high-harmonic pulse as a function of iris diameter.

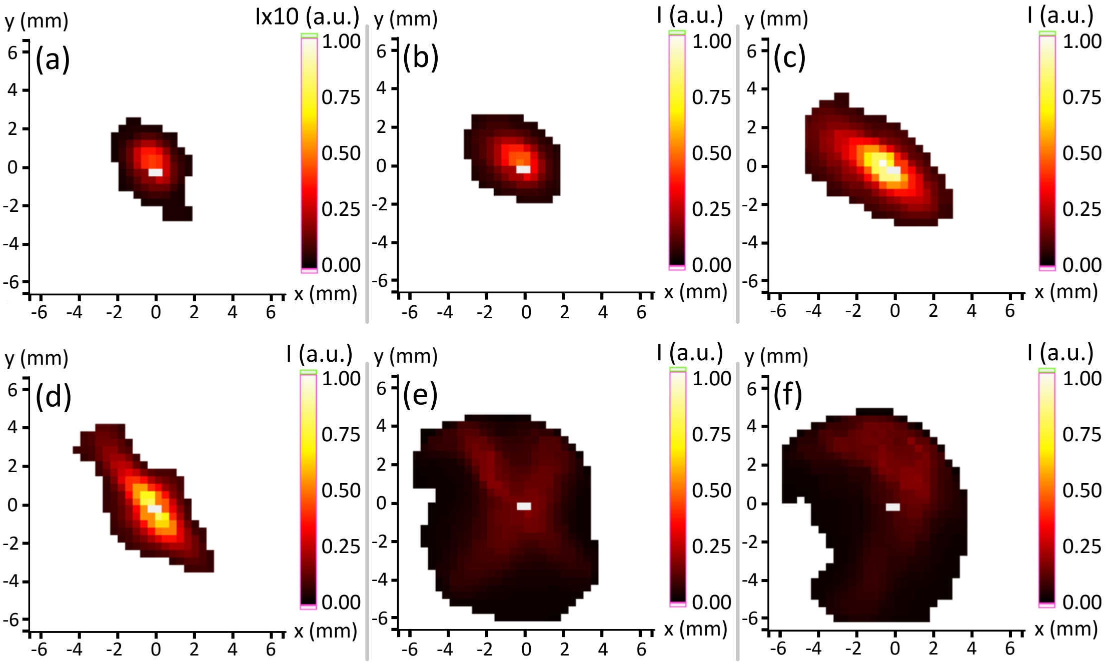

Figure 1.43: Single-shot high-harmonic intensity distributions for different iris diameters: (a) 17 mm, (b) 19 mm, (c) 21 mm, (d) 25 mm, (e) 29 mm, and (f) 33 mm. The scale was changed in (a) to make the beam more visible.

The aperture has a significant effect on the shape and size of the beam, which is small and almost circular for low aperture values and more elongated when it is increased. The largest apertures yield large and irregular pulses. The corresponding wavefronts can be seen in figure 1.44.

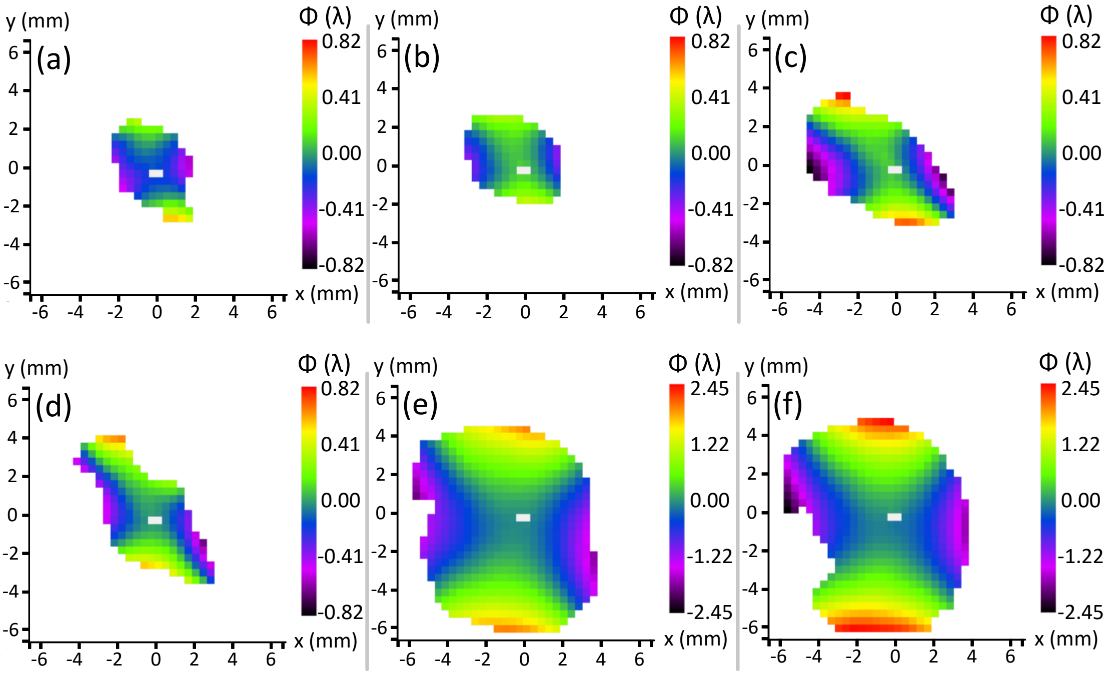

Figure 1.44: Single-shot high-harmonic wavefronts for different iris diameters: (a) 17 mm, (b) 19 mm, (c) 21 mm, (d) 25 mm, (e) 29 mm, and (f) 33 mm. Note the change of scale in (e) and (f).

Astigmatism at 0° is still the most prominent aberration in all cases, and the wavefront becomes increasingly aberrated when the diameter is increased. The overall spatial quality is worse for the largest apertures, where the beam is larger, with a more irregular intensity distribution and higher RMS and PV values, as shown in figures 1.45 (a) and (b). However, as seen in figures 1.45 (c) and (d), the residual wavefront RMS remains relatively constant for diameters above $21\,\mathrm{mm}$, while the residual PV has a maximum around $27\,\mathrm{mm}$.

The fact that the full wavefront is dominated by astigmatism can be easily seen by comparing figures 1.45 (a) and (e), with both curves having almost the exact same shape. While astigmatism is increasingly significant for higher diameters, figure 1.45 (f) demonstrates that its direction does change by more than 10° during the measurements, but is still close to 0°, with astigmatism at 45° not being very significant.

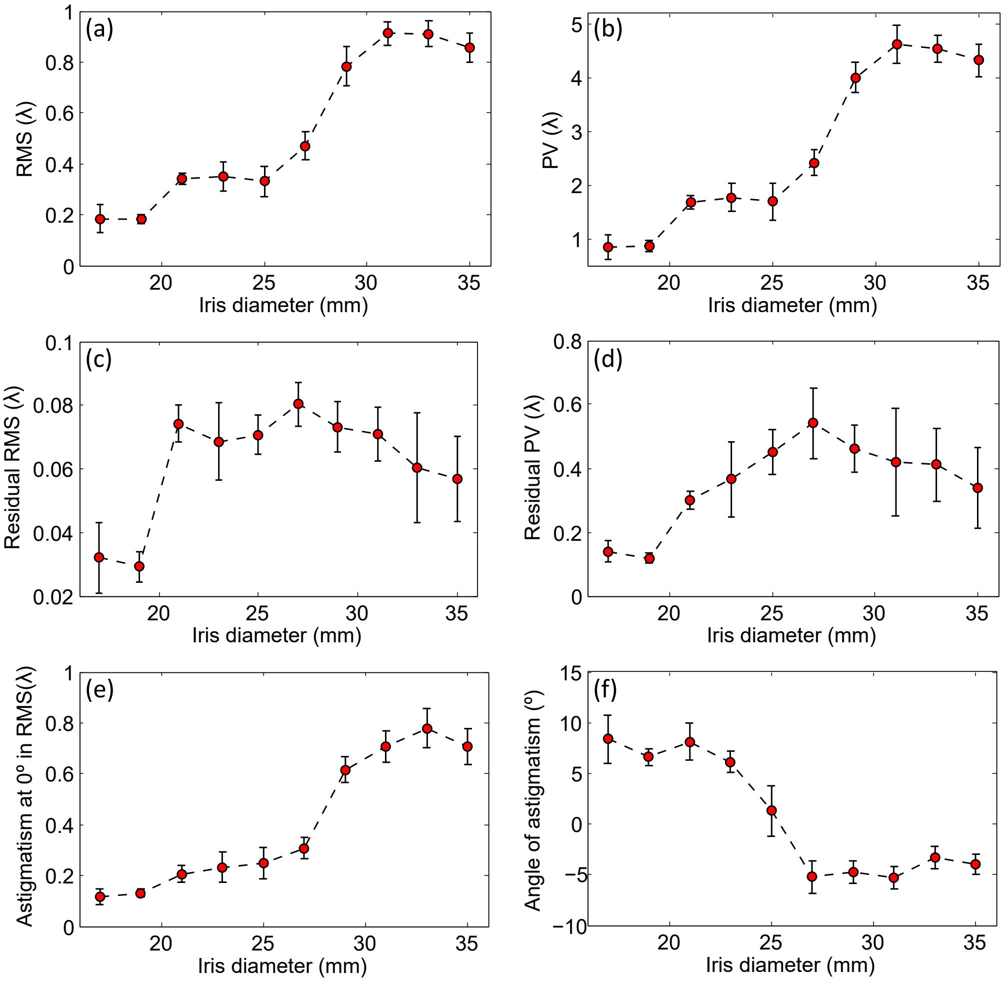

Figure 1.45: Evolution of several parameters describing the high-harmonic wavefront with respect to the iris diameter: (a) RMS, (b) PV, (c) residual RMS, (d) residual PV, (e) contribution of astigmatism at 0° to the wavefront RMS, and (f) angle of astigmatism.

The residual wavefronts seen in figure 1.46 confirm these trends, with the residual wavefronts at large diameters being slightly less aberrated than the one at $21\,\mathrm{mm}$, which, as seen in previous measurements, shows hints of coma at 0°.

The harmonic sources obtained after backpropagation of the above beams can be seen in figure 1.47. There is a clear trend in which increasing the iris aperture leads to more irregular shapes, being almost circular for low diameters, elliptical for intermediate values and more distorted for the largest diameters. These irregular harmonic sources could be caused by enhanced ionization of the gas due to more energy going through the aperture, as well as tighter focusing caused by a larger beam diameter.

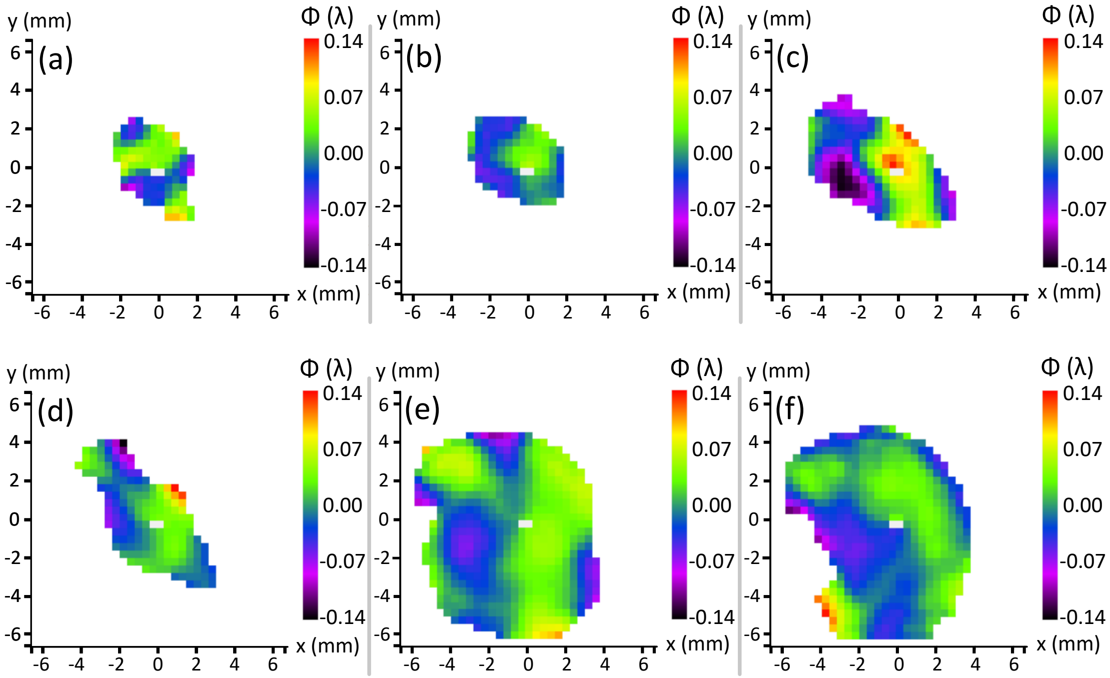

Figure 1.46: Residual high-harmonic wavefronts without astigmatism for different iris diameters: (a) 17 mm, (b) 19 mm, (c) 21 mm, (d) 25 mm, (e) 29 mm, and (f) 33 mm. The same scale is now used for all six cases.

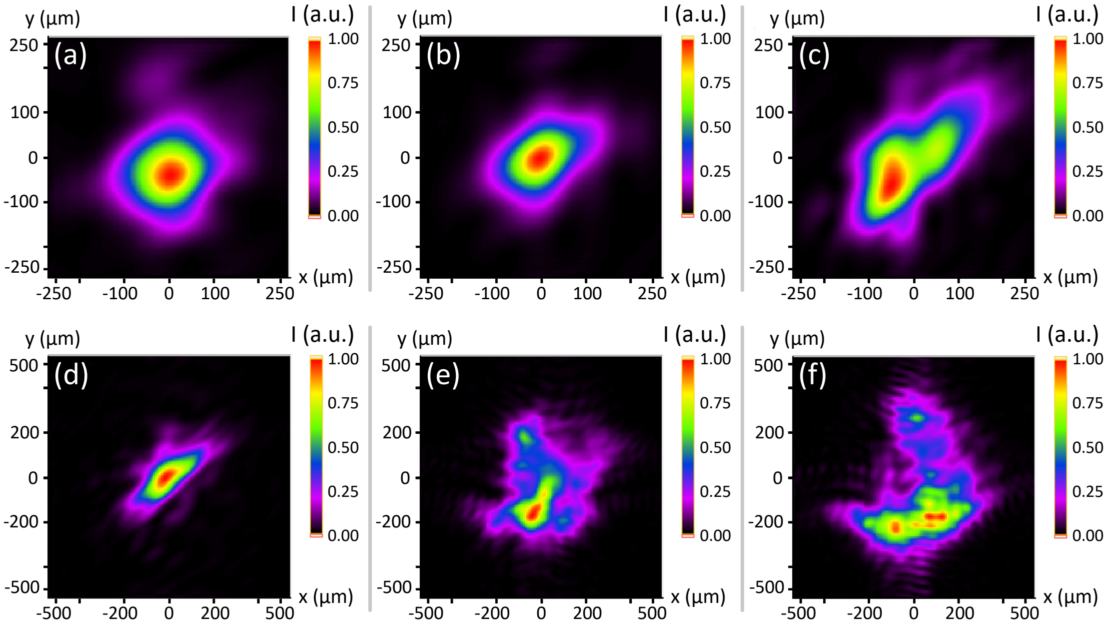

Figure 1.47: Calculated high-harmonic source for different iris diameters: (a) 17 mm, (b) 19 mm, (c) 21 mm, (d) 25 mm, (e) 29 mm, and (f) 33 mm. Note that two different lateral scales are used.

The source not only becomes larger with iris diameter, its size also becomes more unstable, as shown in figures 1.48 (a) and (b). The Strehl ratio is also seen in figure 1.48 (c) to decrease rapidly when the aperture is increased.

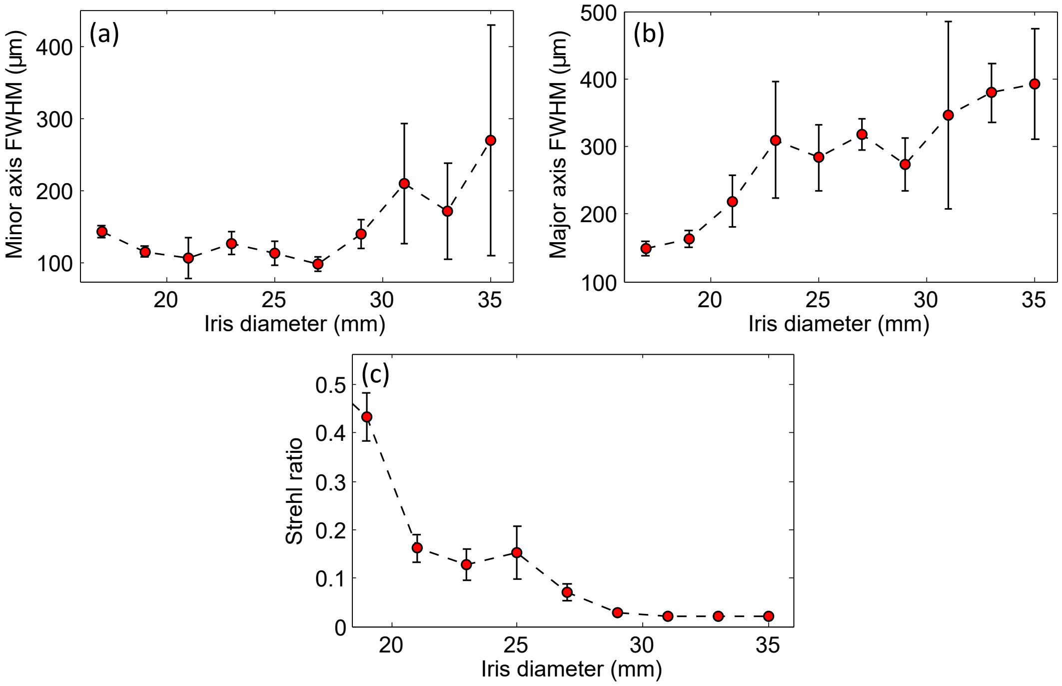

Figure 1.48: FWHM size of the calculated high-harmonic source along the minor (a) and major (b) axes, and (c) Strehl ratio as a function of iris diameter.

Chirp in the IR pulse

Another parameter that plays a role in the conversion efficiency of HHG is the chirp present in the driving pulse. Chirp, or group delay dispersion (GDD) is the quadratic component of its spectral phase. In the temporal domain, non-zero GDD leads to a stretched pulse in which the longer and shorter wavelengths that make up the pulse spectrum are found at different instants within its duration, thus making it longer and, as a consequence, less intense. A pulse with zero GDD is said to be Fourier transform-limited, since its duration is the shortest allowed by its spectrum.

Commercial femtosecond lasers are commonly based on chirped pulse amplification (CPA), so that the IR pulse is first stretched by adding GDD to it, then amplified, and then compressed again by adding to it the same amount of GDD of the opposite sign. Pulse compressors are based on pairs of diffraction gratings through which the pulse is propagated. The GDD introduced to the pulse by such devices depends on several parameters such as the pulse wavelength, the distance between the gratings, or the separation between their grooves.

Thanks to this, we used the compressor at the end of the IR laser chain to change the chirp of the driving IR pulses by changing the distance between the gratings. When changing the grating distance, the compressor used in this setup introduces a GDD of $4800\,\mathrm{fs}^2/\mathrm{mm}$. A total of eight GDD values were used for this series. In order to minimize the effect of the motor backlash, the gratings were first separated by steps of $0.1\,\mathrm{mm}$, i. e. $480\mathrm{fs}^2$, in one direction until the harmonic signal was too low. Then, they were moved back to zero GDD, and moved by the same steps in the other direction. In this case, IR pulse energy was $21.9\,\mathrm{mJ}$, the iris diameter was $22\,\mathrm{mm}$, and the gas pressure was kept at $188\,\mathrm{mbar}$.

The spectra obtained for six of the eight GDD values used for the measurements can be seen in figure 1.49. It can be seen that the 29^{th} harmonic is only non-negligible when the GDD is close to zero. These are also the only cases where the 31^{st} order is present, albeit with very low energy. Other than that, the overall spectrum does not change very significantly except for the fact that, for the lowest and highest values of GDD, the 15^{th} order becomes less intense, while intermediate orders become slightly more important. For the highest GDD values studied (figure 1.49 (e) and (f)), the peaks become wider, and for the highest value, only six orders are generated, with the highest one, the 25^{th}, being almost negligible.

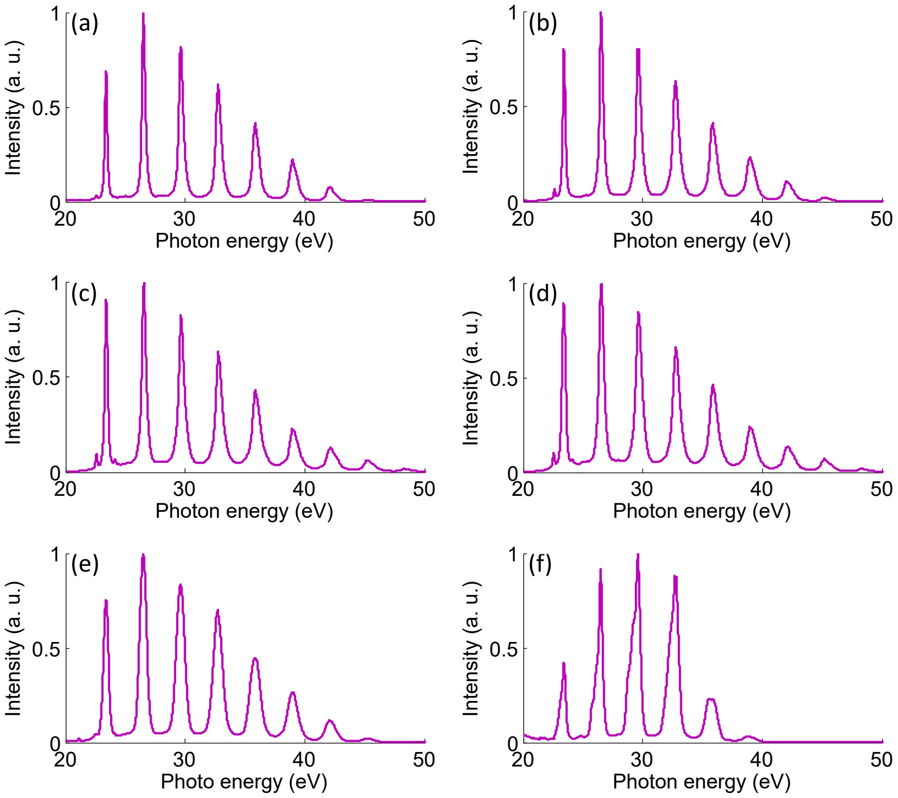

Figure 1.49: Normalized high-harmonic spectra generated with different values of GDD: (a) -960 fs^2, (b) -480 fs^2, (c) 0 fs^2, (d) +480 fs^2, (e) +1440 fs^2, and (f) +2400 fs^2.

The corresponding harmonic pulse energies and intensity distributions, seen in figures 1.50 and 1.51, respectively, follow a similar trend as seen in previous cases, in which the most intense harmonic pulses are also the most elliptical, being almost circular for the lowest energies. It is clear from the figures that Fourier transform-limited pulses provide the highest conversion efficiency. This is likely due to the fact that, for similar conditions, shorter driving pulses have been proven to be more efficient for HHG [31], and the fact that the compressed pulse is more intense than a stretched one.

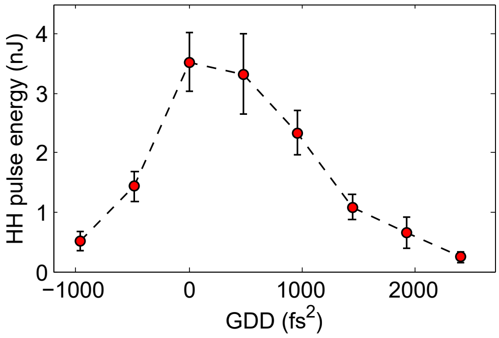

Figure 1.50: Energy of a high-harmonic pulse as a function of GDD.

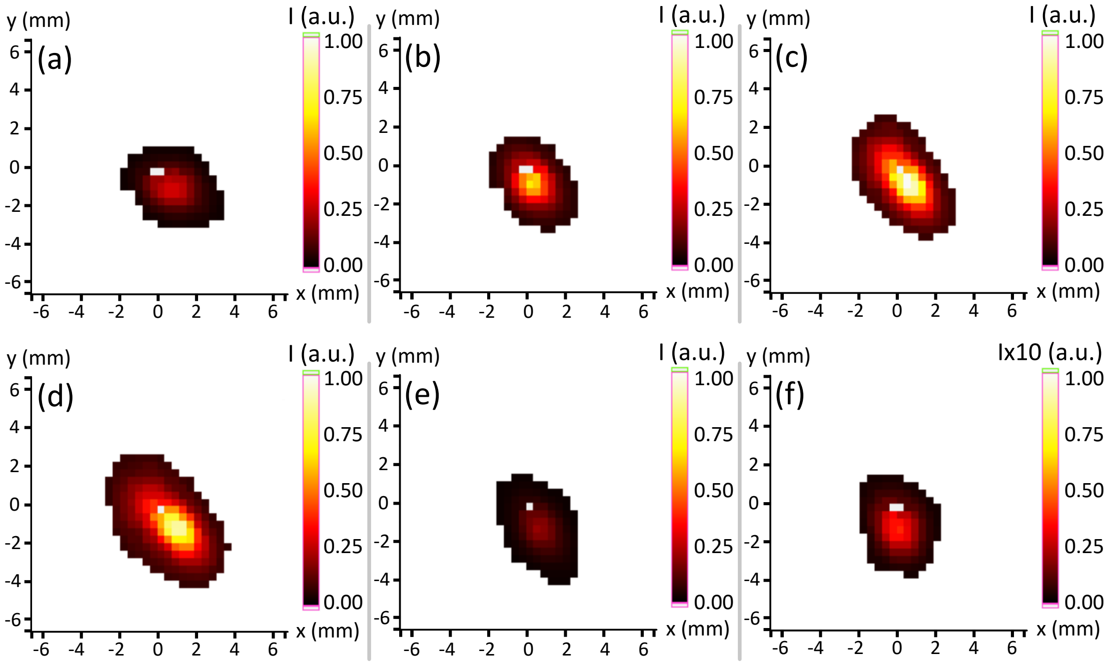

Figure 1.51: Single-shot high-harmonic intensity distributions for different values of GDD: (a) -960 fs^2, (b) -480 fs^2, (c) 0 fs^2, (d) +480 fs^2, (e) +1440 fs^2, and (f) +2400 fs^2. The scale was changed in (f) to make the beam more visible.

The corresponding measured wavefronts presented in figure 1.52 show that astigmatism at 0° is the dominant aberration, and that the wavefront is most aberrated for the conditions providing the highest harmonic energy. These two results are consistent with the previous series of measurements.

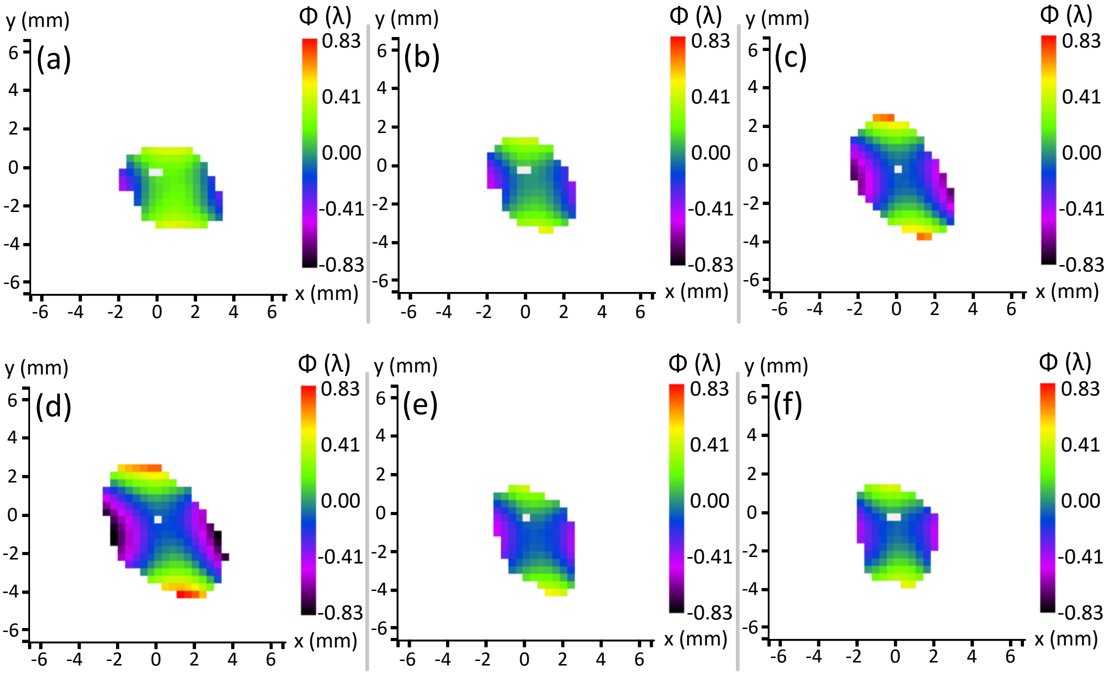

Figure 1.52: Single-shot high-harmonic wavefronts for different values of GDD: (a) -960 fs^2, (b) -480 fs^2, (c) 0 fs^2, (d) +480 fs^2, (e) +1440 fs^2, and (f) +2400 fs^2.

This can be seen in figures 1.53 (a) and (b) as well, where the highest RMS and PV values are found for low values of positive GDD. Both parameters are minimum for $-480\,\mathrm{fs}^2$ and $+1440\,\mathrm{fs}^2$. Additionally, a GDD of $+480\,\mathrm{fs}^2$ provides both the most aberrated wavefronts and the most unstable.

The residual RMS and PV, seen in figures 1.53 (c) and (d), show a more irregular trend, in which a GDD of $+480\,\mathrm{fs}^2$ still shows one of the most aberrated and unstable wavefronts. The contribution of astigmatism at 0° to the wavefront does not vary abruptly in the studied GDD range, and is also maximum for low values of GDD or Fourier transform-limited pulses, as seen in figure 1.53 (e). Lastly, figure 1.53 (f) shows that the angle of astigmatism is always kept between 0° and 5°, except for the most stretched pulse at $+2400\,\mathrm{fs}^2$, where it is also most unstable.

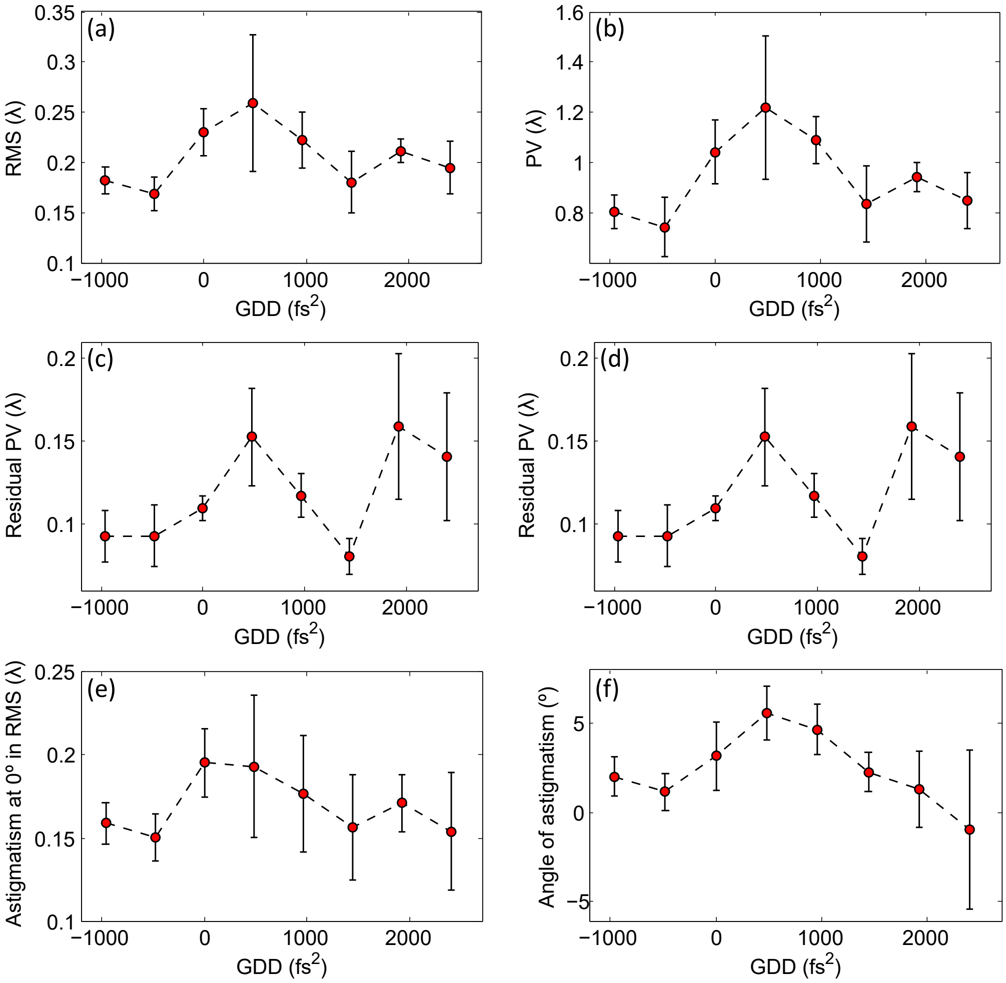

Figure 1.53: Evolution of several parameters describing the high-harmonic wavefront with respect to GDD: (a) RMS, (b) PV, (c) residual RMS, (d) residual PV, (e) contribution of astigmatism at 0° to the wavefront RMS, and (f) angle of astigmatism.

The residual wavefronts, in figure 1.54, confirm these trends, with the highest aberrations being present in the Fourier transform-limited case and for $+480\,\mathrm{fs}^2$, with the wavefronts having similar shapes in both cases. Some coma at 0° is present as well.

The calculated harmonic source does not change significantly with GDD, as seen in figure 1.55. Figures 1.56 (a) and (b) reveal that it has a similar size in all cases. The shape is slightly more circular for the least intense harmonic pulses, when the IR pulse is most stretched. Figure 1.56 (c) confirms this trend, as those cases lead to the highest Strehl ratio.

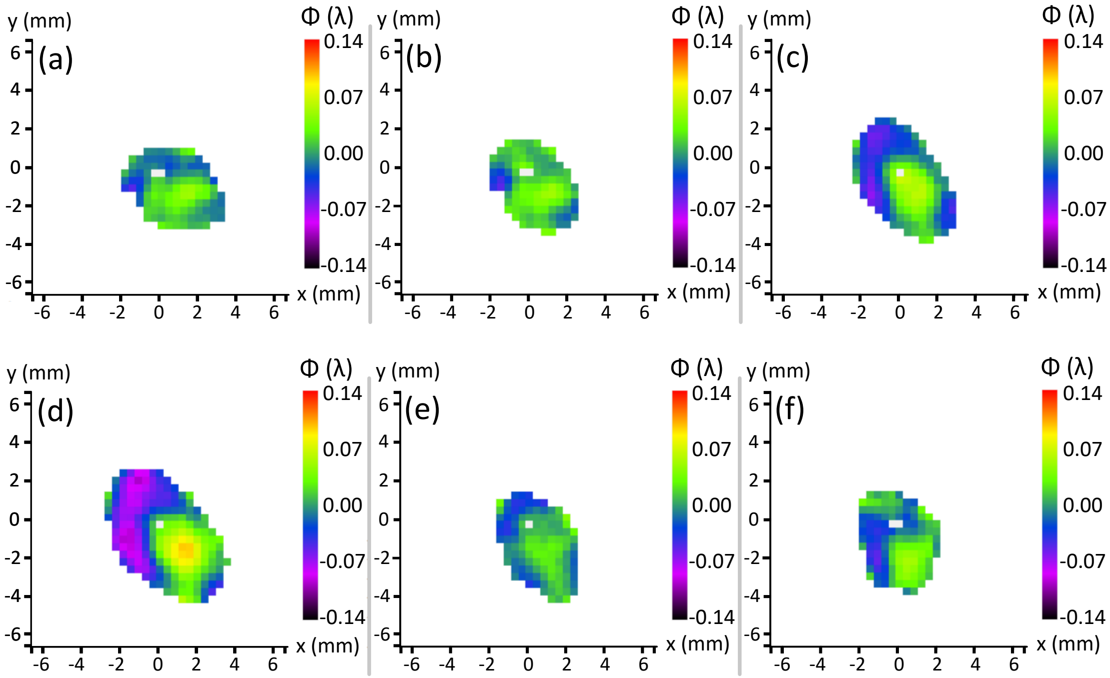

Figure 1.54: Residual high-harmonic wavefronts without astigmatism for different values of GDD: (a) -960 fs^2, (b) -480 fs^2, (c) 0 fs^2, (d) +480 fs^2, (e) +1440 fs^2, and (f) +2400 fs^2.

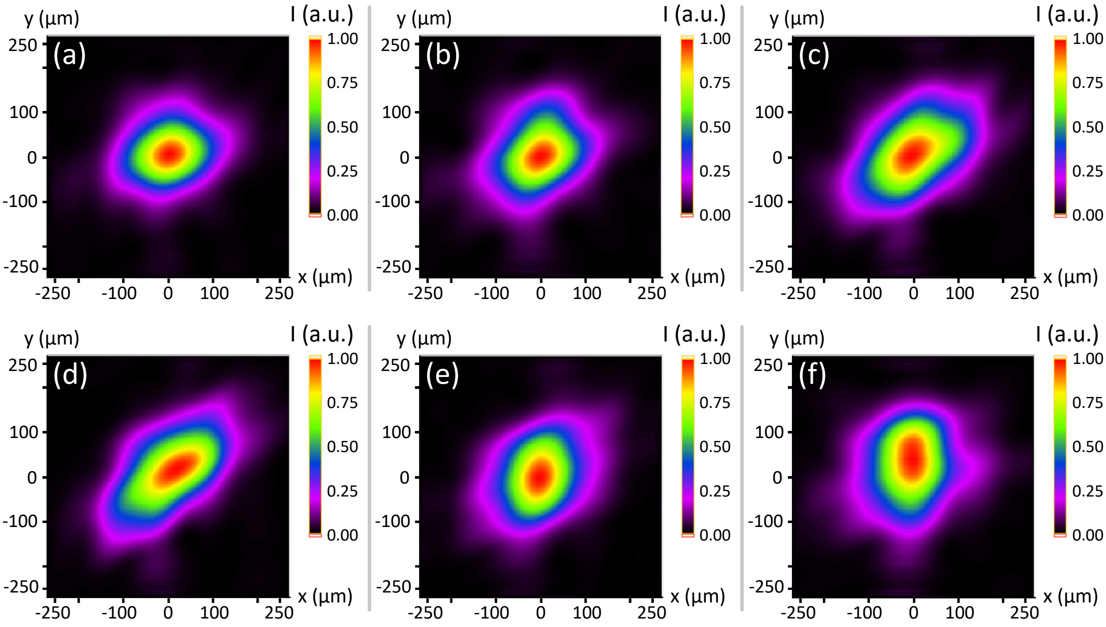

Figure 1.55: Calculated high-harmonic source for different values of GDD: (a) -960 fs^2, (b) -480 fs^2, (c) 0 fs^2, (d) +480 fs^2, (e) +1440 fs^2, and (f) +2400 fs^2.

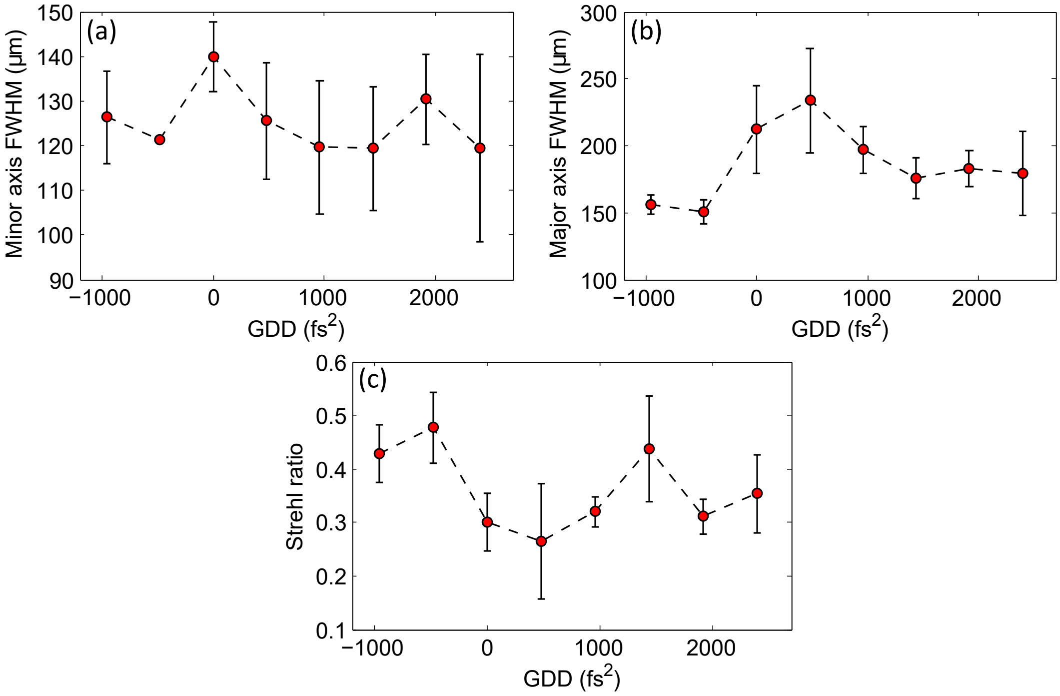

Figure 1.56: FWHM size of the calculated high-harmonic source along the minor (a) and major (b) axes, and (c) Strehl ratio as a function of GDD.

Direction of IR polarization

In all previous measurements, astigmatism was always observed to be dominant in the harmonic beam, and was always directed towards similar directions with only slight variations. However, it is not clear what defines this particular direction physically, since we have shown at the beginning of the experiment that it is not caused by the optics in the setup. There is a possibility that this direction is defined by the polarization of the IR beam, so we carried out another series of measurements, for three different polarization angles: the initial s-polarization, p-polarization, and $45°$. For these measurements, the gas pressure was kept at $180\,\mathrm{mbar}$, the aperture diameter was $22\,\mathrm{mm}$, and the IR pulse energy was $21.9\,\mathrm{mJ}$. Additionally, the compressor was moved back zero GDD after the previous measurements.

Figure 1.57 shows the spectra measured in the three cases. It must be noted, however, that the beam arrived at the spectrometer after being reflected by the silica plate and the rotating gold-coated mirror that directs it towards the spectrometer. These optics have slightly different reflective properties depending on the polarization of the incident light, which is most likely the cause for the differences in the spectra, rather than the HHG process itself. Their reflectivities can be found in appendix B. This can also be seen in figure 1.58, where the measured pulse energy is much lower for $45°$ than for s- and p-polarization.

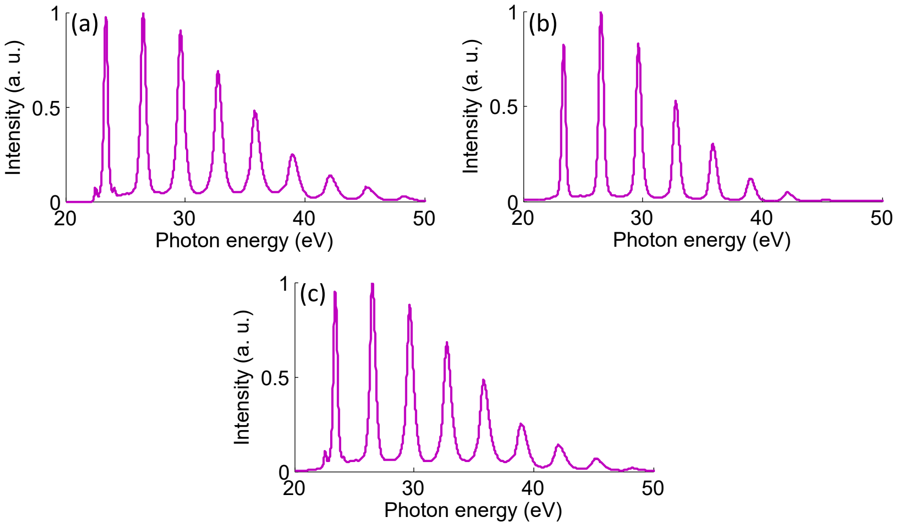

Figure 1.57: Normalized high-harmonic spectra generated with different IR polarization angles: (a) s-polarization, (b) 45° polarization, and (c) p-polarization.

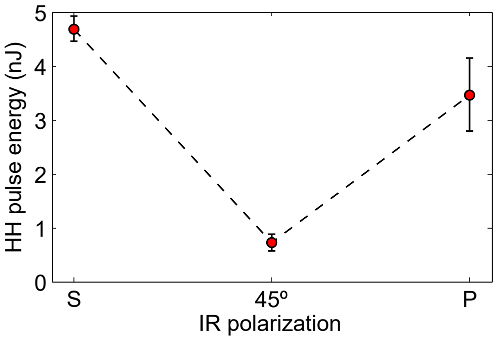

Figure 1.58: Energy of a high-harmonic pulse as a function of the IR polarization angle.

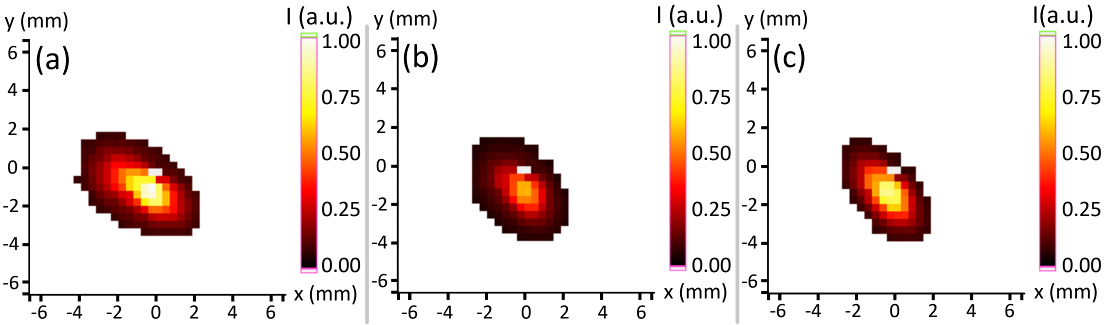

Figure 1.59: Single-shot high-harmonic intensity distributions for different IR polarization angles: (a) s-polarization, (b) 45° polarization, and (c) p-polarization.

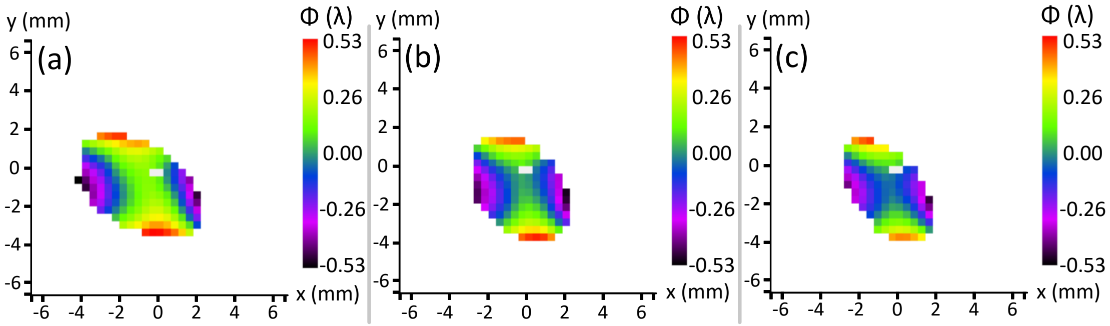

Figure 1.60: Single-shot high-harmonic wavefronts for different IR polarization angles: (a) s-polarization, (b) 45° polarization, and (c) p-polarization.

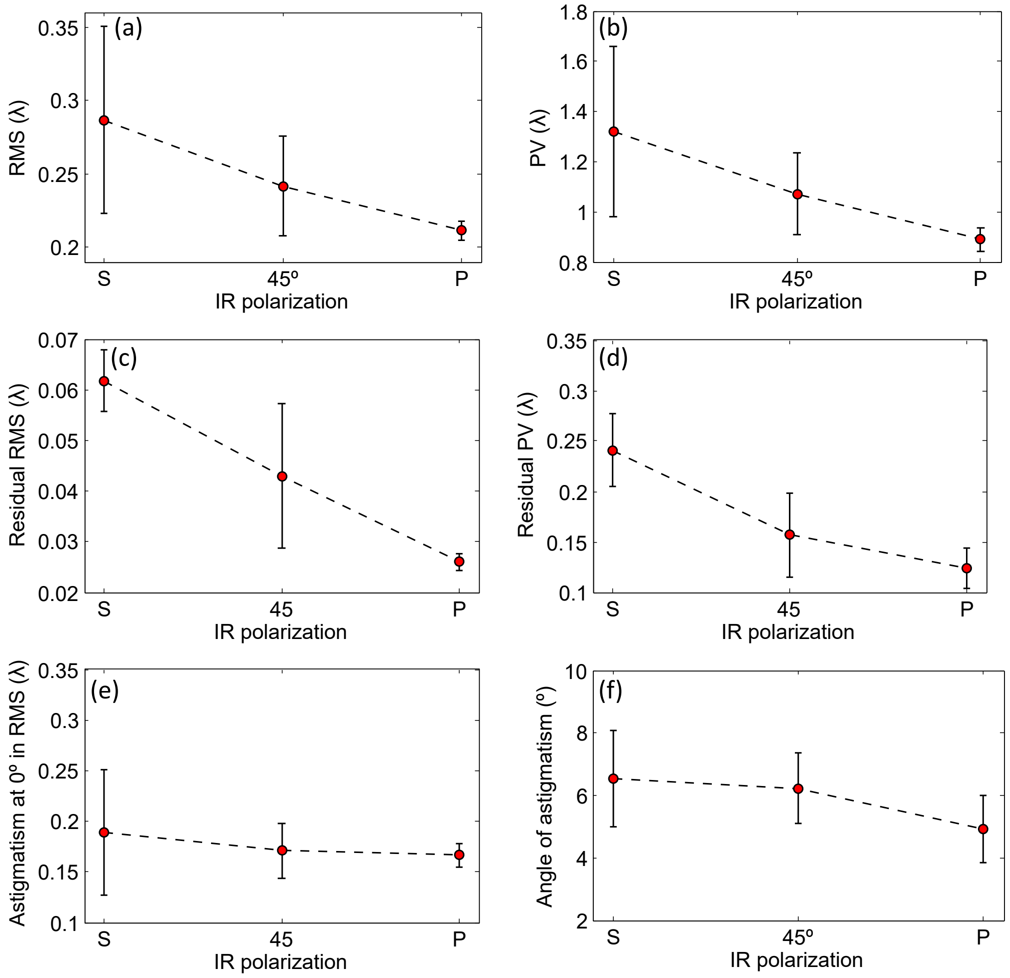

Figure 1.61: Evolution of several parameters describing the high-harmonic wavefront with respect to the IR polarization: (a) RMS, (b) PV, (c) residual RMS, (d) residual PV, (e) contribution of astigmatism at 0° to the wavefront RMS, and (f) angle of astigmatism.

Additionally, the intensity distribution of the harmonic pulse is not seen to change significantly with polarization beyond the intrinsic instability of HHG, as seen in figure 1.59. A slight difference in the orientation of the elliptical beam can be seen, as well as some differences in size. 45° polarization yields the least energetic pulses of the three cases studied. As mentioned above, this effect is most likely due to the optics and not to the generation itself.

Figure 1.60 demonstrates that the angle of astigmatism does not depend on the polarization of the IR pulse, which is also shown in figure 1.61 (f). As presented in figure 1.61 (e), even the magnitude of the astigmatism is almost constant regardless of polarization. However, figures 1.61 (a) to (d) indicate that the overall wavefront does seem to be better for p-polarization due to the residual wavefronts being better. This can be observed in more detail with the residual wavefronts included in figure 1.62, in which the coma at 0°, already mentioned in previous cases, can be seen to be less significant for p-polarization.

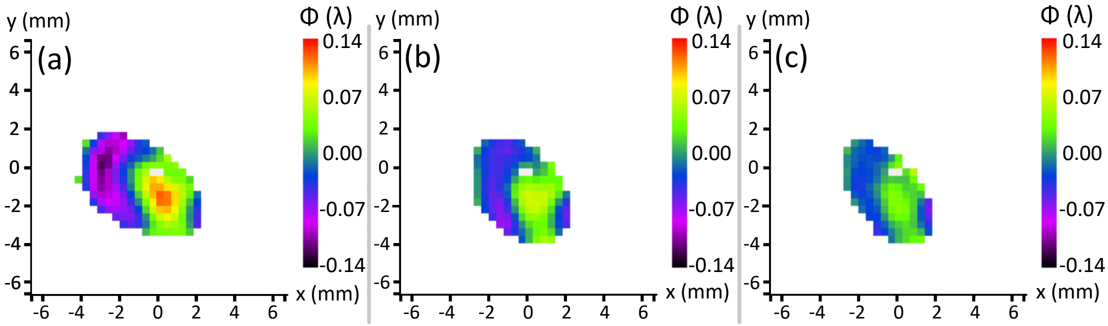

Figure 1.62: Residual high-harmonic wavefronts without astigmatism for different IR polarization angles: (a) s-polarization, (b) 45° polarization, and (c) p-polarization.

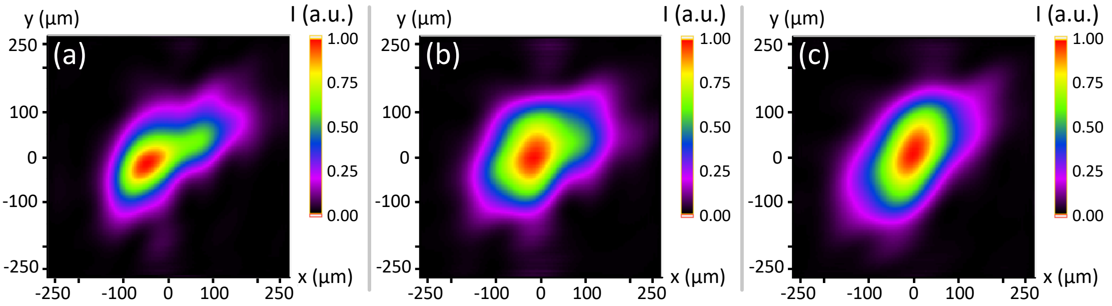

Figure 1.63: Calculated high-harmonic source for different IR polarization angles: (a) s-polarization, (b) 45° polarization, and (c) p-polarization.

The overall shape of the calculated harmonic source, shown in figure 1.63, changes slightly with the polarization, while being always elliptical. Its size does not change significantly either, as seen in figures 1.64 (a) and (b). The Strehl ratio, in figure 1.64 (c), is found to increase when the polarization approaches p, consistent with the less-aberrated wavefronts obtained for p-polarization. Overall, polarization does not affect the HHG process significantly, in terms of energy or spatial quality. More importantly, the direction of polarization of the driving pulse is unrelated to the direction of astigmatism found in the harmonic wavefronts.

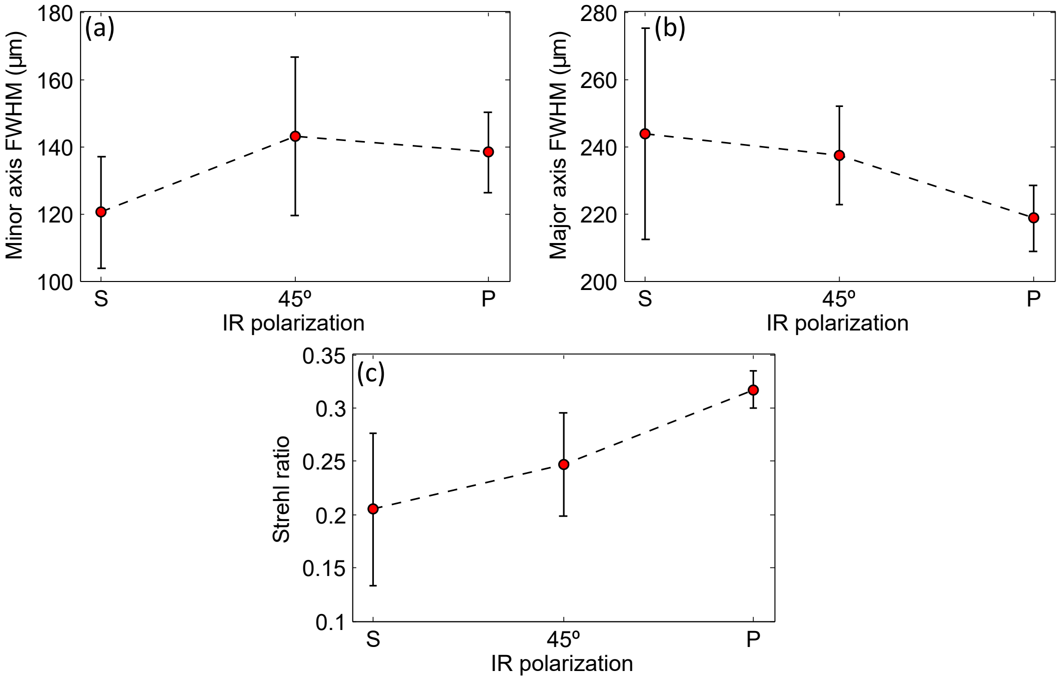

Figure 1.64: FWHM size of the calculated high-harmonic source along the minor (a) and major (b) axes, and (c) Strehl ratio as a function of the IR polarization angle.

Position of the IR focal plane

The position of the IR focal plane with respect to the generating medium has a very large influence on the phase matching of HHG, and thus on the conversion efficiency and the harmonic pulse energy (see section 1.1.2). So far throughout this experiment, this parameter was not changed, keeping the optimal configuration in which the focal plane is located $25\,\mathrm{cm}$ after the cell. Since this parameter has such high impact on efficiency, it is also interesting to observe how it can affect the generated wavefronts. It is changed by moving the lens along the propagation axis of the driving beam. Aside from the initial position used up to this point, two other positions were used, moving the lens both towards the lens and away from it. Due to the different focusing, the generation conditions had to be changed as well to optimize the signal. The parameter values are included in table 1.3. Moving the lens towards the cell is defined as the positive direction.

Relative lens position (cm)	*Cell-focus distance (cm)*	*IR pulse energy (mJ)*	*Iris diameter (mm)*	*Argon pressure (mbar)*
-32	-7	29.7	26	147
0	+25	24.2	21	186
+22	+47	15.8	19	190

Table 1.3: Generation parameters used for the different positions of the lens.

The harmonic spectra measured for all three cases are presented in figure 1.65, showing significant variations in the amount and relative intensities of the generated orders. Indeed, only five orders are generated when the IR focal plane is moved farther after the cell, with the 15^{th} and 23^{rd} being much less dominant than in other cases.

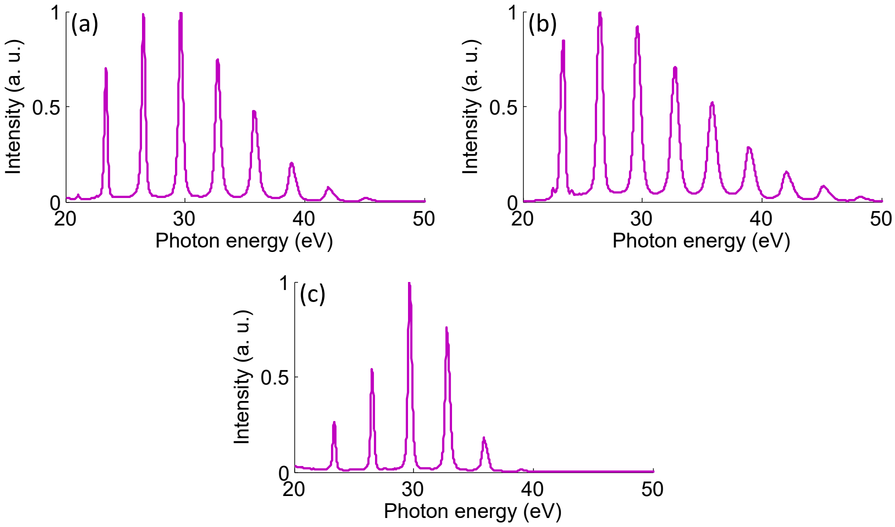

Figure 1.65: Normalized high-harmonic spectra generated with different positions of the IR focal plane: (a) 7 cm before the cell, (b) 25 cm after the cell, and (c) 47 cm after the cell.

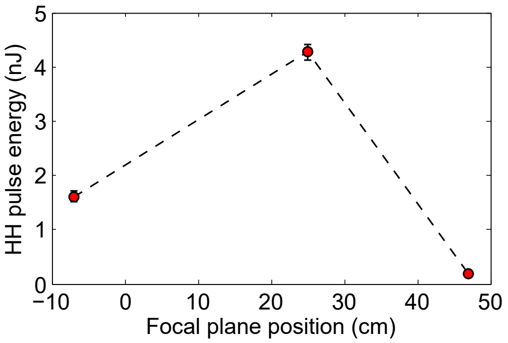

Figure 1.66: Energy of a high-harmonic pulse as a function of the focal plane position.

Figure 1.66 shows the effect of the lens position on harmonic pulse energy. As mentioned above, the initial position provided the best conversion efficiency, so naturally the other two cases present significantly lower energies. The energy drop in the new positions was so significant that single-shot wavefront measurements could no longer be acquired. Instead, those measurements required accumulating ten harmonic shots. The resulting intensity distributions for each case can be seen in figure 1.67, where significant differences in shape and size can be observed. As expected given the IR beam divergence around the focus, moving the lens away from the cell creates a larger beam, with a similar elliptical shape as the one observed throughout the experiment, albeit with a different direction. The opposite is observed then the lens is moved towards the cell, which produces a very small, fairly circular beam, with even lower energy.

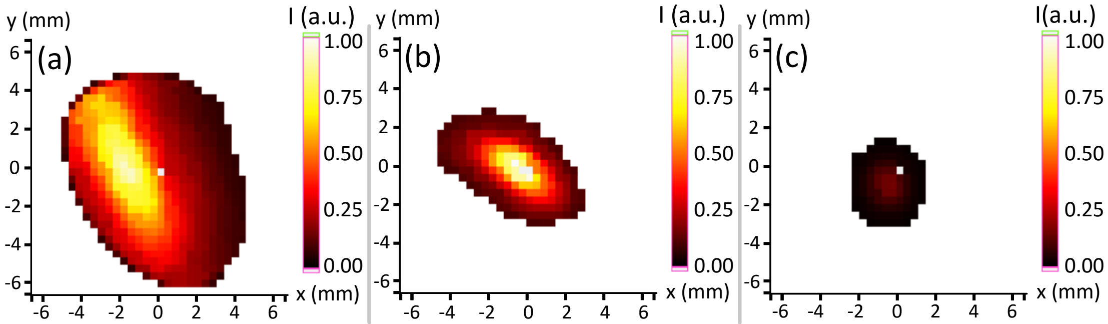

Figure 1.67: High-harmonic intensity distributions for different positions of the IR focal plane: (a) 7 cm before the cell, (b) 25 cm after the cell, and (c) 47 cm after the cell. For (a) and (c), ten shots were accumulated, while (b) was obtained from a single shot.

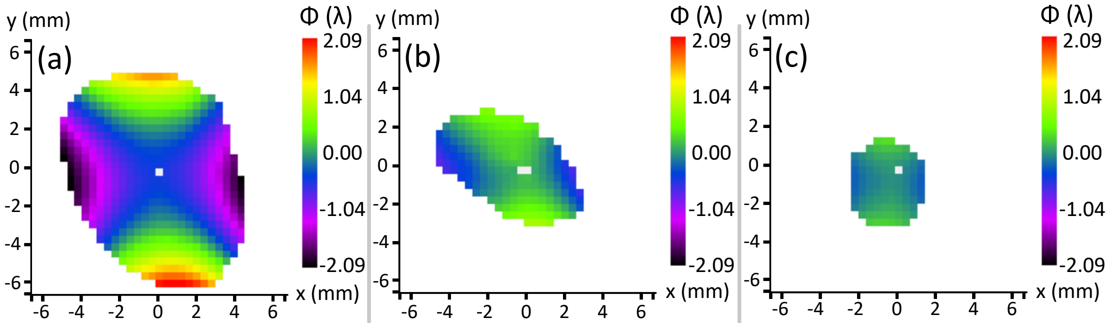

Figure 1.68: High-harmonic wavefronts for different positions of the IR focal plane: (a) 7 cm before the cell, (b) 25 cm after the cell, and (c) 47 cm after the cell. For (a) and (c), ten shots were accumulated, while (b) was obtained from a single shot.

The measured wavefronts, seen in figure 1.68, present high astigmatism at $0°$ in all cases as expected, significantly higher for the distance of $-7\,\mathrm{cm}$. For the case where the distance is $+47\,\mathrm{cm}$, the wavefront is much less aberrated, with astigmatism at $0°$

still being the dominant aberration. The details of the obtained wavefronts as a function of the focal plane position are included in figure 1.69. The evolution of RMS and PV with respect to the focal plane position is presented in figures 1.69 (a) and (b), where it can be seen that the farther the focal plane is after the cell, the less aberrated the harmonic wavefront is, at the cost of a large drop in energy with respect to the initial position as described above. Interestingly, the residual RMS and PV values presented in figures 1.69 (c) and (d) do not change significantly when moving the lens away from the cell, so the highly aberrated wavefront observed in the latter case is almost solely due to an increase in astigmatism at 0°, as seen in figure 1.69 (e). As observed in all measurements carried out so far, figure 1.69 (f) shows that the angle of astigmatism stays close to 0° for all cases. The variation of the residual wavefronts is shown in more detail in figure 1.70.

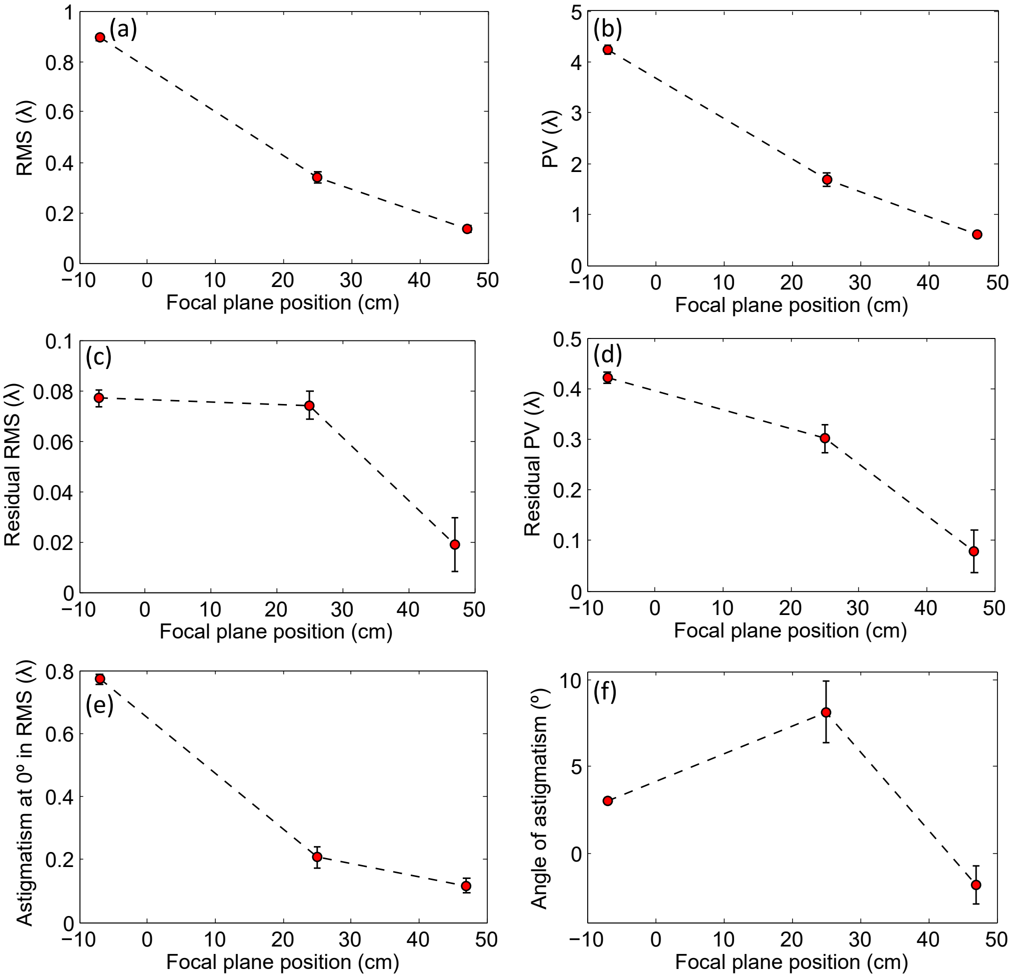

Figure 1.69: Evolution of several parameters describing the high-harmonic wavefront with respect to the position of the IR focal plane: (a) RMS, (b) PV, (c) residual RMS, (d) residual PV, (e) contribution of astigmatism at 0° to the wavefront RMS, and (f) angle of astigmatism.

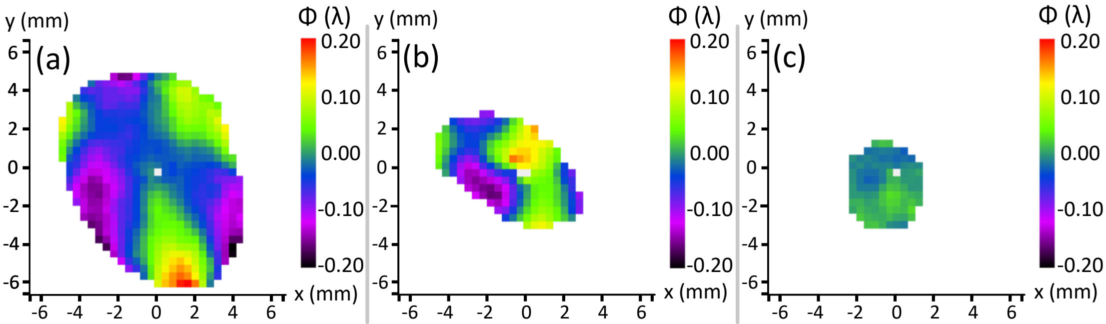

Figure 1.70: Residual high-harmonic wavefronts without astigmatism for different positions of the IR focal plane: (a) 7 cm before the cell, (b) 25 cm after the cell, and (c) 47 cm after the cell. For (a) and (c), ten shots were accumulated, while (b) was obtained from a single shot.

The harmonic sources obtained via backpropagation can be seen in figure 1.71 and are significantly different from one another in both shape and size. For the cell-focus distance of $-7\,\mathrm{cm}$, the source is the biggest and most distorted, while the initial position provides the smallest size, but not the best shape. The longest distance, $+45\,\mathrm{cm}$, provides the best shape, consistent with the lower aberrations found in this case.

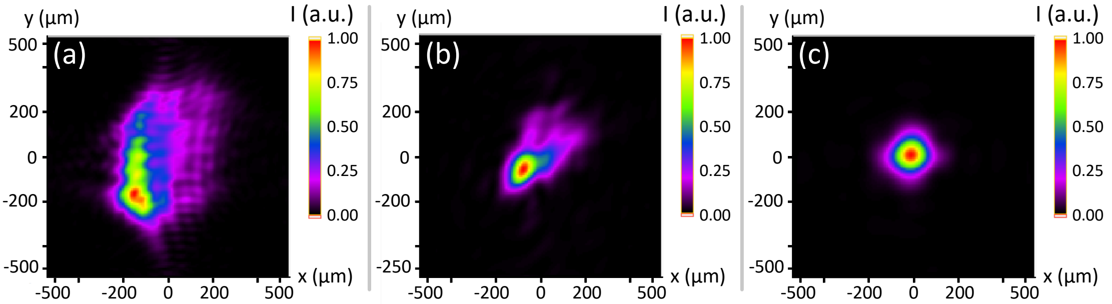

Figure 1.71: Calculated high-harmonic source for different positions of the IR focal plane: (a) 7 cm before the cell, (b) 25 cm after the cell, and (c) 47 cm after the cell. For (a) and (c), ten shots were accumulated, while (b) was obtained from a single shot.

The changes in size with the position of the focal plane are presented in figures 1.72 (a) and (b). The Strehl ratio, in figure 1.72 (c), shows a significant increase when the IR focal plane is moved farther away after the cell. However, the increase in spatial quality is not as significant as the large drop in pulse energy seen above.

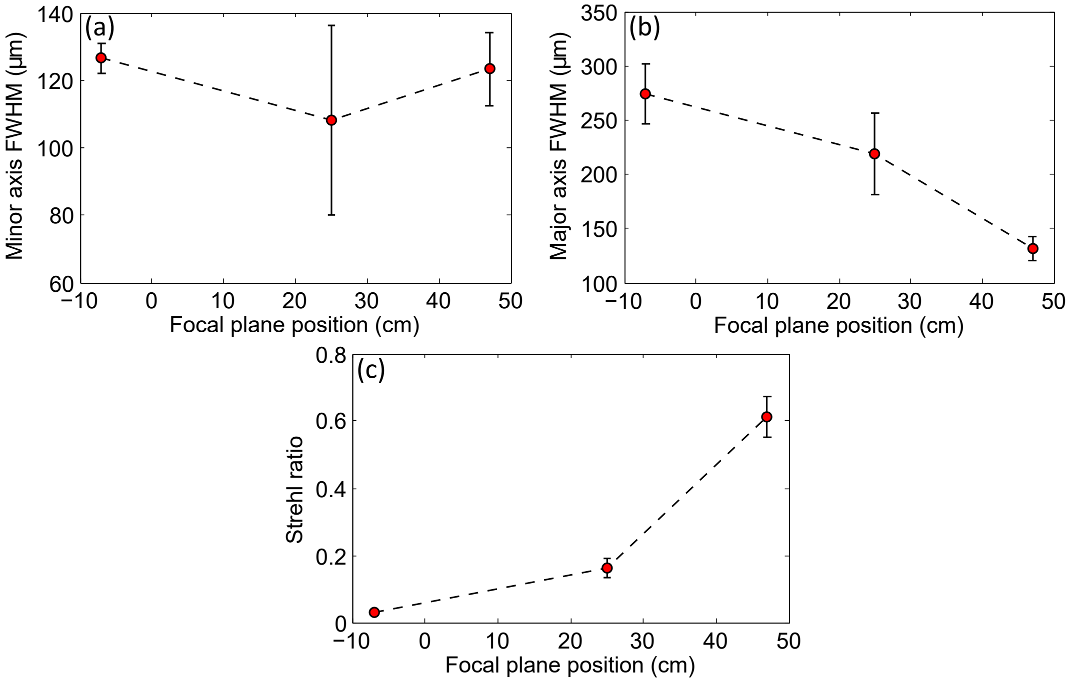

Figure 1.72: FWHM size of the calculated high-harmonic source along the minor (a) and major (b) axes, and (c) Strehl ratio as a function of the position of the IR focal plane.

1.3.2.4 Wavefronts of single harmonic orders

It is also interesting to measure the wavefronts corresponding to single harmonic orders in different parts of the spectrum and compare them to each other and to the full beam. Three dielectric multilayer mirrors with different peak reflectivities were used for this purpose. They were placed before the silica plate, and the XUV Hartmann WFS was moved to a new position, as seen in figure 1.73. Since the silica plate is no longer used to filter the IR beam, a beam splitter is placed instead shortly before the mirrors, consisting on two flat silicon mirrors at Brewster's angle.

The multilayer mirrors were mounted on a translation stage which allowed them to be moved away from the beam, so that it could be directed to the spectrometer and the CCD as usual. The three mirrors consist on layers of Al/Mo/SiC on fused silica substrates. Each of them has different layer thickness and number, which determine its reflected wavelength. They are all made for optimal use at 45° incidence, providing reflectivities around 35%. A 200-nm-thick aluminum filter is placed before the WFS.

Although only one harmonic order was reflected by each mirror, the pulses had enough energy to allow for single-shot wavefront acquisitions, mostly due to the higher reflectivities of the involved optics, as well as the beam being smaller on the sensor due to the shorter distance to the cell, close to $7\,\mathrm{m}$. As was done previously, five single-shot measurements were taken and averaged, to account for instabilities. It must be noted, however, that the setup did not allow for calibration of the aberrations that these mirrors introduce in the harmonic wavefront, given their placement. For this reason, they were taken to LOA for calibration after the experiment was finished, using the same method described in section 1.3.2.3, based on reflecting a reference beam on the mirror under test. The details and results of the calibration procedure can be found in appendix C.

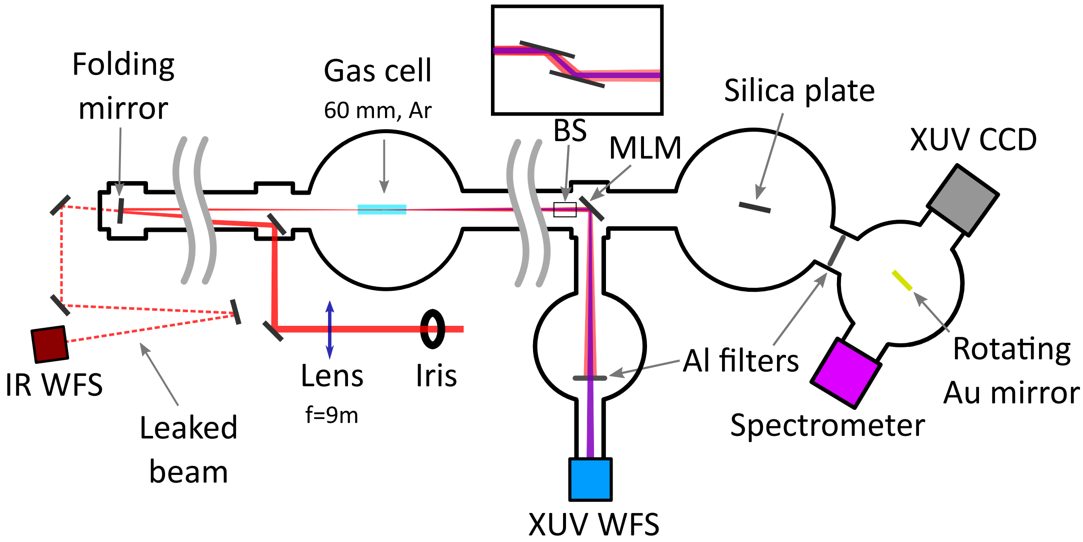

Figure 1.73: Variation of the experimental setup for the measurement of single harmonic orders with the use of multilayer mirrors, showing the new placement of the XUV WFS. BS: beam splitter. MLM: multilayer mirror.

The characteristics of the three mirrors are summarized as follows:

- Mirror 1 consists of $\mathrm{N} = 7$ layers with a thickness of $\mathrm{d} = 34.32\,\mathrm{nm}$. Its reflectivity is maximum at $41.4\,\mathrm{nm}$, corresponding to the 19^{th} harmonic order, found in the plateau. Two sets of generation parameters were used with this mirror.
- Mirror 2, consisting of $\mathrm{N} = 10$ layers of thickness $\mathrm{d} = 27.5\,\mathrm{nm}$, has its maximum reflectivity at $35\,\mathrm{nm}$, corresponding to the 23^{rd} harmonic order. Again, two sets of generation parameters were used with this mirror.
- Mirror 3 contains $\mathrm{N} = 20$ layers of thickness $17.7\,\mathrm{nm}$, for a maximum reflectivity at $23.9\,\mathrm{nm}$, the 33^{rd} harmonic order. This harmonic order is not usually obtained in this setup, as seen in the spectra shown in the previous section. For this reason, the generation conditions had to be heavily modified in order to generate it, so only one set of parameters was used.

The generation parameters used with each of the mirrors are listed in table 1.4.

Harmonic order	*Wavelength (nm)*	*Pressure (mbar)*	*IR energy (mJ)*	*Iris (mm)*
19th (Case 1)	41.4	144	18.8	20
19th (Case 2)	41.4	176	26.6	25
23rd (Case 1)	35	147	24.2	23
23rd (Case 2)	35	182	21.1	21
33rd	23.9	244	29.6	27

Table 1.4: High-harmonic generation parameters when using the multilayer mirrors.

The intensity profiles obtained with the three mirrors are presented in figure 1.74. In general, the beam profile is very similar for single harmonics and for the full beam measured earlier, except for the 33rd order, which is more elongated. This might be caused by its proximity to the cutoff, as well as the high pressure required to generate it. Little variation is observed between the two cases measured for the 19th and for the 23rd orders. Note that the images have been flipped horizontally to account for the fact that the beam was reflected by two mirrors in the previous setup, but only by one multilayer mirror for the current measurements.

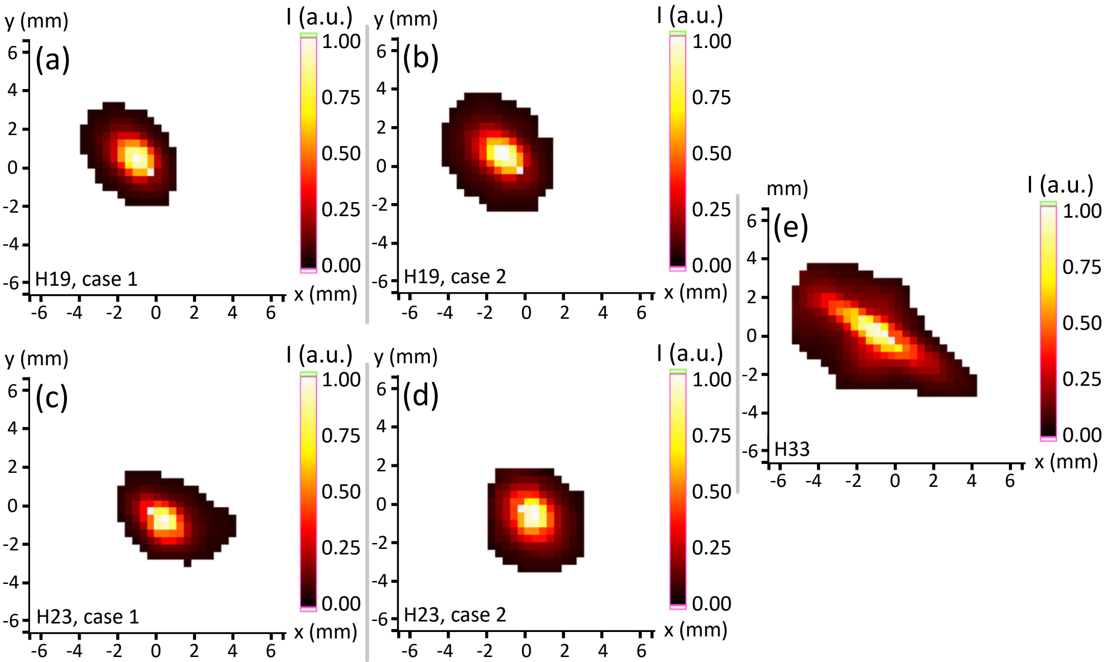

Figure 1.74: Single-shot high-harmonic intensity distributions for the 19th (a and b), 23rd (c and d), and 33rd (e) harmonic orders.

The corresponding wavefronts are presented in figure 1.75. It can be clearly seen that the 19^{th} order presents no astigmatism, in contrast with the full beam measured earlier where astigmatism at $0°$ was always present. Slight astigmatism appears in the 23^{rd} order, but it is still very low compared to the full beam. The wavefronts of these two orders vary slightly between the two cases measured. The 33^{rd} order, on the other hand, is completely dominated by astigmatism at $0°$. In particular, its angle of astigmatism is $8.0 \pm 1.9°$, very close to the typical values observed in the direct beam. While the generation conditions for this order do differ from the previous two, this result suggests that the wavefront aberrations found in the full high-harmonic beam are dictated by the cutoff harmonic orders, despite them being the least intense.

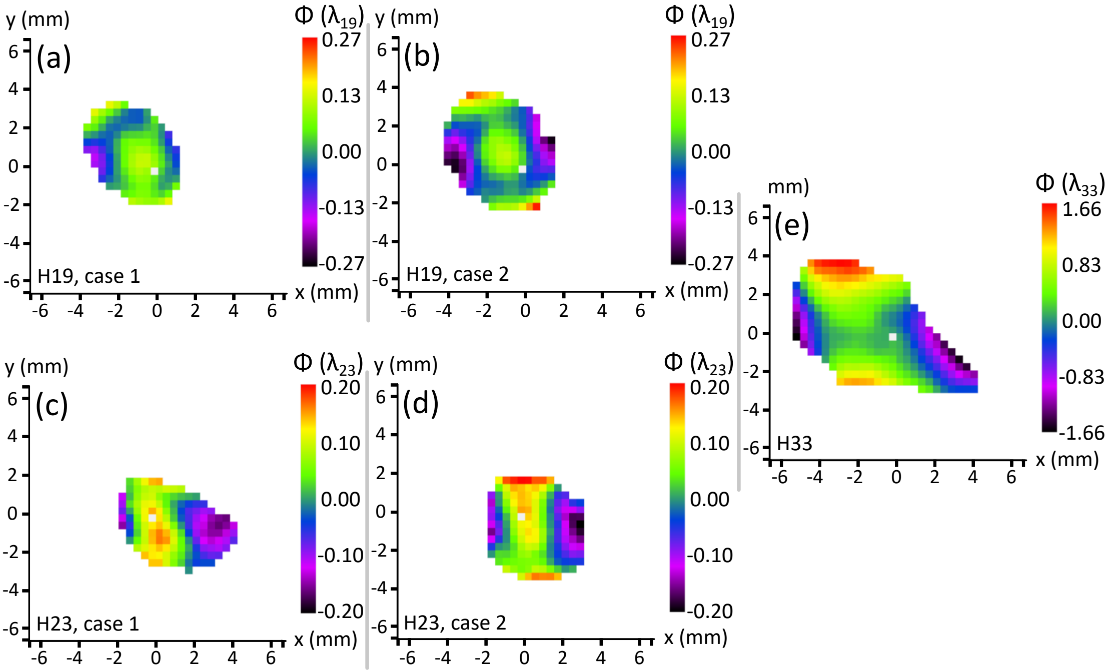

Figure 1.75: Single-shot high-harmonic wavefronts for the 19^{th} (a and b), 23^{rd} (c and d), and 33^{rd} (e) harmonic orders. Each of them is expressed in terms of its particular wavelength, and the calibration wavefronts presented in the appendix have been subtracted.

The RMS and PV values corresponding to the three orders can be seen in figure 1.76, both in relative and absolute terms, that is, in terms of their respective wavelengths and in units of length. In all plots, only the first cases for the 19^{th} and 23^{rd} orders are shown for the sake of visualization. The RMS and PV are almost equal for the 19^{th} and 23^{rd}. However, the RMS increases by a factor of 11 for the 33^{rd} order with respect to the former two when expressed in units of λ. This contrast is smaller when expressed in units of length, where the absolute RMS of the 33^{rd} order is 6 times higher. These results further support the idea that higher orders dictate the aberrations observed in the full harmonic beam. The relative standard deviation of the RMS is close to 10% in all cases.

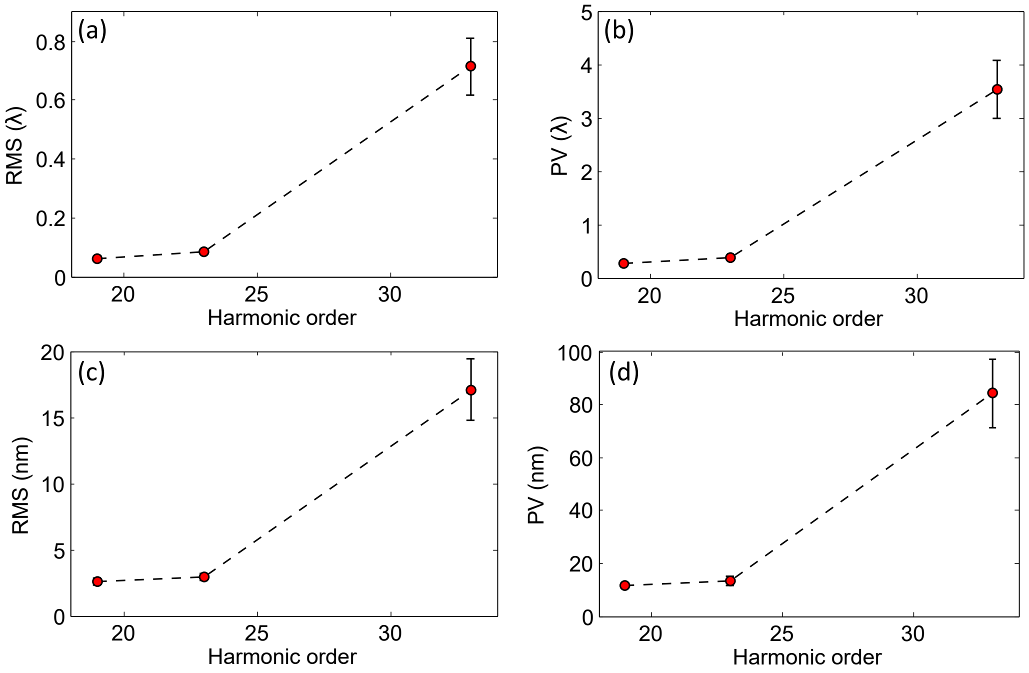

Figure 1.76: Average wavefront RMS and PV values for the 19^{th}, 23^{rd}, and 33^{rd} harmonic orders, expressed in units of their respective wavelengths (a and b) and in units of length (c and d). Only the first cases of the 19^{th} and 23^{rd} orders are shown, since the values of the second cases are almost identical.

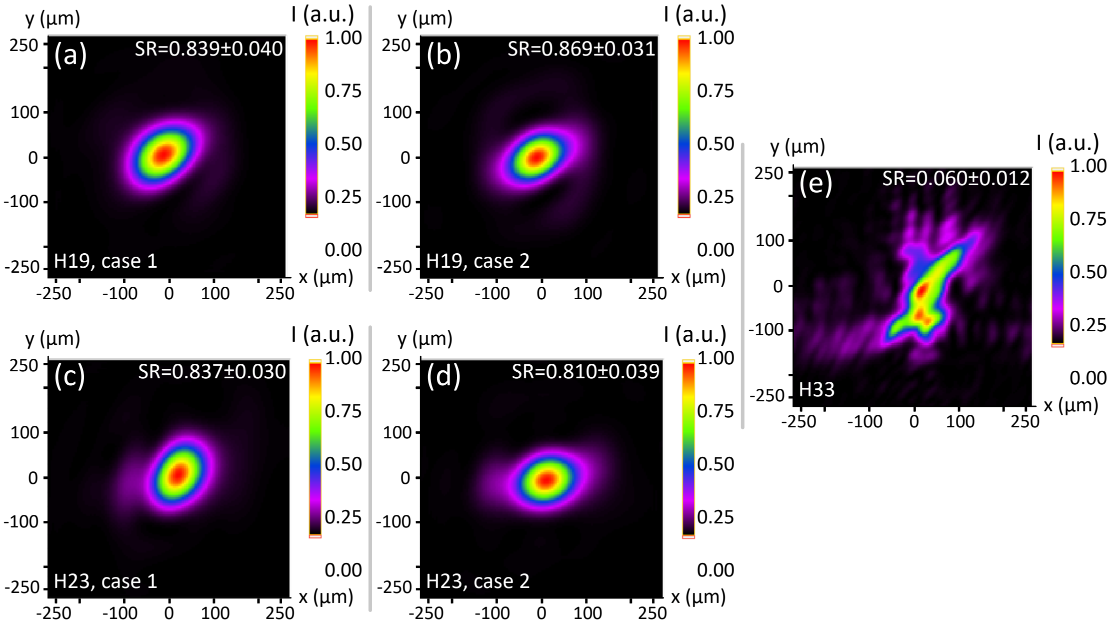

Figure 1.77: Calculated high-harmonic source for the 19^{th} (a and b), 23^{rd} (c and d), and 33^{rd} (e) harmonic orders. SR: Strehl ratio.

Lastly, the harmonic sources for each harmonic order, obtained via backpropagation, are presented in figure 1.77. Their Strehl ratios are included in the images as well. As expected from the measured wavefronts, the calculated sources for the 19^{th} and 23^{rd} orders are regular and slightly elliptical, and similar to the best cases measured earlier for the full harmonic beam, albeit somewhat smaller. For the case of the 33^{rd} order, however, the source is slightly larger and highly distorted. Comparing these results with previous measurements involving the full beam, it is clear that the shape of the harmonic source is the superposition of the sources of every individual harmonic order. In general, the measurements reported here strongly suggest that the wavefront of a high-harmonic beam can be largely improved, in particular removing its astigmatism, by filtering out the cutoff harmonic orders.

1.3.2.5 Relationship between high-harmonic and infrared wavefronts

Throughout the experiment, we have studied the effect that different generation parameters have on the wavefronts of the resulting high-harmonic pulses, both for the cases of the full spectrum and for individual harmonic orders. Being a secondary source of radiation, the spatial properties of harmonic radiation are also heavily influenced by those of the driving pulse. In order to learn more about the relation between the IR and harmonic beams, both wavefronts were measured.

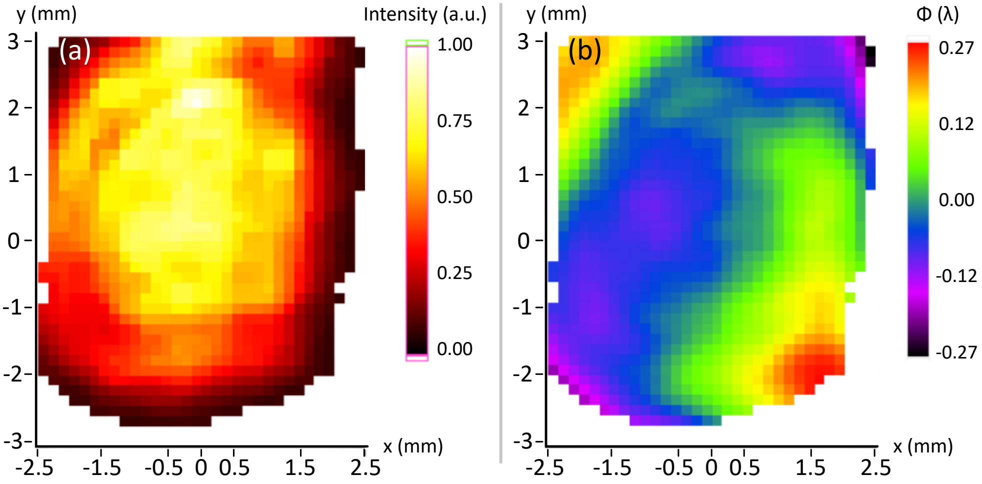

Figure 1.78: Intensity distribution (a) and wavefront (b) of the direct IR beam. Note that the WFS had to be rotated by 90° due to experimental constraints, hence why the pictures are vertically oriented.

The IR wavefront was first measured by placing the Shack-Hartmann sensor described in section 1.3.2.2 $1.5\,\mathrm{m}$ after the gas cell, before the silica plate. This step was carried out without vacuum and without argon in the gas cell. Several neutral-density filters were used to both protect the sensor and to avoid ionizing the air around the focus, which would affect the beam propagation. The total optical density used was 9.1. As was done with the high harmonics, a total of five single-shot measurements were taken and averaged. One of them is shown in figure 1.78, including the measured intensity distribution and the wavefront obtained with zonal reconstruction. After these measurements, the sensor is placed in its final position, shown previously in figure 1.17, for the rest of the experiment, in order to monitor the IR wavefront during the XUV wavefront measurements by means of a leak in a mirror.

The IR beam is also slightly elliptical, and the measured wavefront has an average RMS error of $(0.095 \pm 0.003)\lambda$, better than $\lambda/10$, and a PV of $(0.531 \pm 0.026)\lambda$. Table 1.5 includes the average Zernike coefficients corresponding to low-order aberrations. Contrary to the case of the high-harmonic beam, astigmatism at 45° is the dominant aberration in the IR wavefront, along with some coma at 0°. Astigmatism at 0°, the main aberration present in every high-harmonic wavefront measured throughout the experiment, is much less significant.

N	*Aberration*	*Average Zernike coefficient (λ)*
4	Astigmatism at 0°	0.0168
5	Astigmatism at 45°	-0.0948
6	Coma at 0°	0.0560
7	Coma at 90°	-0.0086
8	Spherical aberration	-0.0182

Table 1.5: Lowest-order Zernike coefficients (standard normalization) obtained via modal wavefront reconstruction of the IR beam, for a pupil of radius 2.3 mm.

The IR focal spot on the gas cell, obtained via backpropagation of one of the measured far-field wavefronts, can be seen in figure 1.79 (a). It has an elliptical shape and high shot-to-shot stability, with an average Strehl ratio of 0.774 ± 0.006. The beam profiles along the axes of the ellipse are also shown in the figure, and the average FWHM size was $238.55 \pm 0.67\,\mu\mathrm{m}$ along the major axis and $177.82 \pm 0.50\,\mu\mathrm{m}$ along the minor axis.

A direct comparison between the IR focal spot and an example of a calculated high-harmonic source is presented in figure 1.80. Both images are very similar in terms of shape and size. This seems to indicate that, while the far-field high-harmonic wavefront does not replicate the IR wavefront, the shape of the high-harmonic source is heavily influenced by the IR intensity distribution at focus, with the generation parameters playing a significant role on it as well.

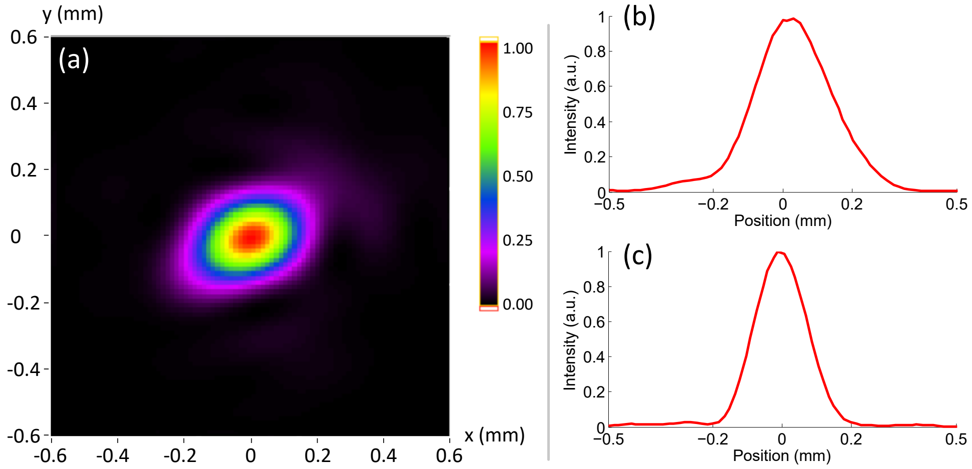

Figure 1.79: Calculated focal spot of the IR beam (a), measured directly after the gas cell and beam profiles along the major (b) and minor (c) axes of the ellipse.

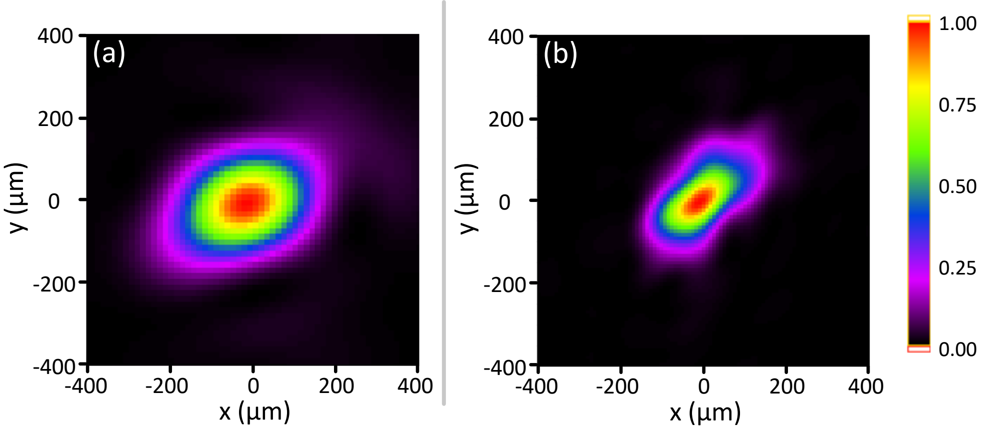

Figure 1.80: Side by side comparison between the calculated infrared focus (a) and high-harmonic source (b), taken from figure 1.39 (d).

The size of the harmonic source was observed to be variable depending on the generation conditions used, being almost always smaller than the IR focal spot. This can be explained by considering that the least intense parts of the IR beam are not intense enough to generate harmonics. Only in two cases was the harmonic source seen to be larger than the IR focus presented above (see figures 1.47 (e) and (f)). These were obtained when using large apertures, and thus tighter focusing on the gas, causing higher ionization than in the rest of the cases hindering phase matching as well as affecting the propagation of the IR beam in the medium.

1.3.2.6 Discussion

The wavefronts of the high-harmonic pulses measured in this experiment had typical RMS values of the order of $\lambda/4$. The high conversion efficiency of this beamline allowed us to take single-shot high-harmonic wavefront measurements, in turn allowing for the study of the shot-to-shot wavefront stability. The relative standard deviation for the wavefront RMS takes values between 15% and 20% in most cases, thus revealing a relatively good source stability, except for the most extreme cases such as those where the pressure was too high, or the iris was fully open. It is also interesting to note that high pulse energies are often paired with higher wavefront aberrations.

The results of our single-shot wavefront measurements are similar to previously published studies involving multishot measurements in beamlines with high repetition rates in that the high-harmonic wavefront always presents a very significant astigmatism at 0°. Since this astigmatism was not found in the IR wavefront, it is not yet known what causes it in the high-harmonic beam, and in particular what defines its direction. After making sure that it is not caused by the optics used in the beamline, we have confirmed that the polarization direction of the driving IR pulse does not have any influence on it. Other aberrations such as coma or spherical aberration are much less significant than astigmatism. In fact, if the latter is corrected, for example by focusing the beam with curved mirrors, RMS values lower than $\lambda/10$ can be obtained, even diffraction-limited beams in some of the cases reported here.

Additionally, the study of single harmonic orders by means of multilayer mirrors revealed that not all orders carry that astigmatism. In fact, it was observed to be present only for the highest measured order, the 33^{rd}, suggesting that the cutoff orders might determine the aberrations present in the full beam.

From the IR wavefront measurements, it is clear that there is not a direct wavefront transfer from the driving pulse to the high-harmonics. The wavefronts, however, are not unrelated. In particular, we have seen through backpropagation calculations that the high-harmonic source has a very similar size and shape as the focal spot of the IR laser, suggesting that the former is dictated by the latter. However, significant changes in the high-harmonic wavefront, shape, and size were found when changing the generation conditions with a constant IR wavefront. More insight on the influence of the IR wavefront on the HHG process could be gained with further experiments involving adaptive optics.

1.3.3 Modifying the harmonic wavefront with adaptive optics for the infrared driving laser

Shortly after the experiment reported in the previous section, a deformable mirror (DM) was installed in the beamline in order to modify the wavefront of the driving pulses, along with a Shack-Hartmann WFS to monitor it in real time. A second experiment was carried out as a follow-up, in which we studied how the spatial properties of the high-harmonic beam, as well as the conversion efficiency, could be influenced by modifying the IR wavefront.

DMs have been used in the past to modify the wavefront of the driving beam for HHG in setups with high repetition rate. This has been done to modify the astigmatism in the harmonic wavefront [20], and also to improve phase matching and thus harmonic energy [95]. However, the experiment reported in this section is, to the best of our knowledge, the first to measure the influence of the IR wavefront the spatial properties of single high-harmonic pulses, allowing us to account for shot-to-shot instabilities.

1.3.3.1 Experimental setup

The experimental setup, presented in figure 1.81 is largely the same from the previous experiment. The main difference is the DM introduced in the setup, placed before the lens. A new Shack-Hartmann WFS, connected to the DM, is used to measure the IR beam through the same leak as before. Two lenses, not shown in the figure, are used to form the image of the DM surface on the IR sensor.

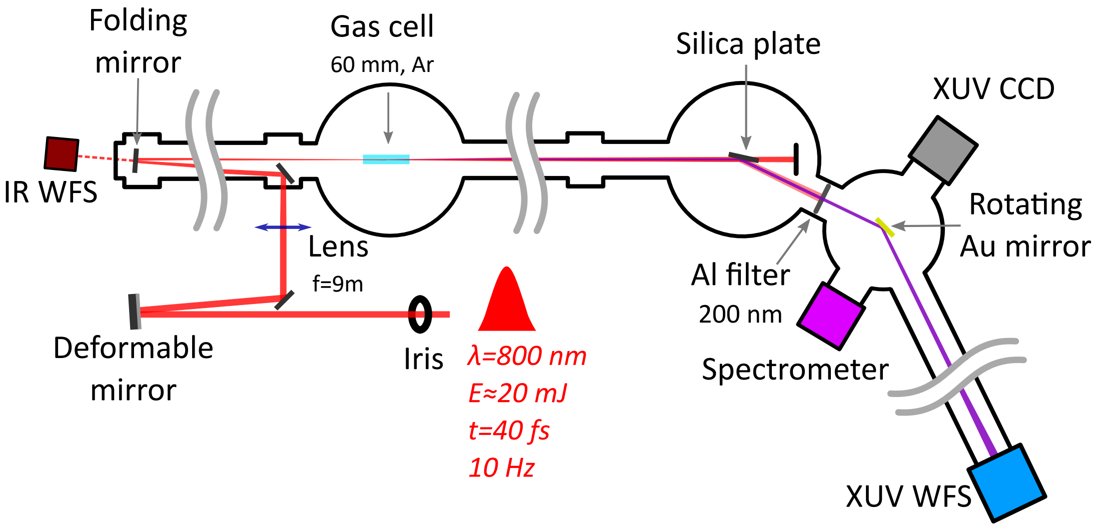

Figure 1.81: Schematic drawing of the experimental setup for the measurement of single-shot harmonic wavefronts using the deformable mirror for the infrared beam.

The deformable mirror

The DM used in this experiment, manufactured by AKA Optics, is a multilayered, circular mirror with 32 actuators to modify its surface. The actuators, based on the piezoelectric effect, are laid out as three rings consisting on 6, 10 and 14 actuators around a central one, and an additional actuator for defocusing, as seen in figure 1.82. The size of the piezo actuators is changed by applying voltage to them, at a rate of $10\,\mathrm{nm/V}$. The dielectric multilayer coating allows for $\mathrm{R} > 99.85\%$ for $800 \pm 50\,\mathrm{nm}$ wavelength at normal incidence. Other mirror parameters are presented in table 1.6. It must be noted that the actuators present some hysteresis, which means that applying a particular voltage to an actuator does not necessarily lead to the exact same position every time.

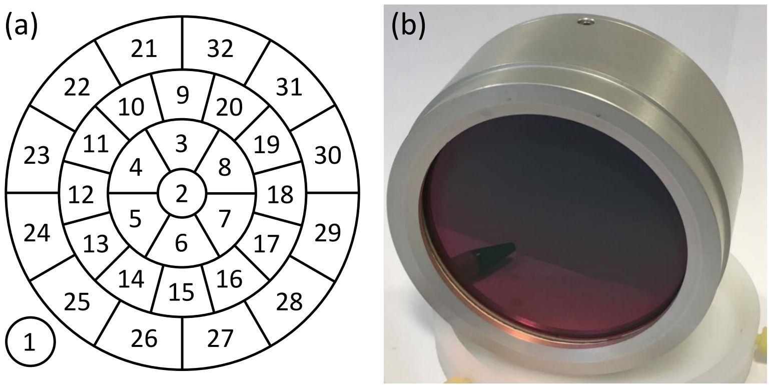

Figure 1.82: (a) Layout of the actuators and (b) photograph of the deformable mirror. Actuator 1 controls defocus.

Active aperture diameter	70 mm
Clear aperture diameter	80 mm
Single actuator stroke	$>$+3 µm/-2.5 µm
Maximal defocus stroke	± 20 µm
Maximal astigmatism stroke	± 4 µm
Maximal coma stroke	± 4 µm
Maximal spherical aberration stroke	± 1.5 µm
Flatness (voltages $< 20\%$ of maximum)	$<$20 nm RMS
Laser-induced damage threshold	2 J/cm ^{2}

Table 1.6: Parameters describing the deformable mirror.

The DM is connected to a Shack-Hartmann WFS, allowing for live control of the IR wavefront. This sensor has an array of $45\text{x}33$ microlenses, for an aperture of $6.1\text{x}4.6\,\mathrm{mm}^2$, with a $1/2$" CMOS camera. It can measure wavefronts with an accuracy of $20\,\mathrm{nm}$ RMS, on a wavelength range of $400\text{-}1100\,\mathrm{nm}$.

1.3.3.2 Results

The first step before the measurements take place is to quantify the aberrations introduced in the IR wavefront by the folding mirror and the window. This was simply done by removing those elements and recording the IR wavefront, and then putting them back in place and measuring the wavefront again. The calibration data are the difference between those wavefronts. The resulting aberrations are actually negligible compared to the typical wavefront RMS values measured during the experiment, and smaller than the shot-to-shot variations of the IR beam.

Before starting the experiment, the DM was configured to optimize the high-harmonic wavefront and energy. The energy was increased so much by the addition of the DM that two 200-nm-thick aluminum filters were needed to prevent saturation of the sensor, instead of one as in the previous experiment. During the experiment proper, five single-shot high-harmonic wavefronts were measured for several different DM configurations, while keeping all other generation parameters, such as IR pulse energy or gas pressure, constant. Two different series of wavefront measurements were carried out.

First series: astigmatism at 0° and defocus

The harmonic and IR wavefronts were first measured for the DM configuration providing maximum conversion efficiency, labeled *DM1*. For this series of measurements, the harmonics were generated in argon pumped at $195\,\mathrm{mbar}$ by IR pulses with energy $25.5\,\mathrm{mJ}$, and an iris diameter of $23\,\mathrm{mm}$. The initial IR and high-harmonic wavefronts, as well as the harmonic intensity distribution can be seen in figures 1.83 (a), (d), and (g), respectively. Each wavefront is represented in units of its corresponding wavelength: $\lambda_{\mathrm{IR}} = 800\,\mathrm{nm}$ and $\lambda_{\mathrm{XUV}} = 42\,\mathrm{nm}$. The intensity distribution is smaller and less elliptical than previously observed. Despite the two wavefronts not being identical, some similarities can indeed be found between them. Consistent with the previous experiment, the harmonic wavefront is mainly astigmatic at $0°$, whereas the IR wavefront presents more astigmatism at $45°$. The Zernike coefficients of the IR wavefront, shown in table 1.7 for all configurations in this series of measurements, confirm this in more detail. The values are averaged over five separate acquisitions, and the standard deviation is also included.

Aberration	*DM1*	*DM2*
Astigmatism at 0°	-0.0482 ± 0.0118	-0.0918 ± 0.0090
Astigmatism at 45°	0.0818 ± 0.0145	0.0741 ± 0.0120
Coma at 0°	-0.0177 ± 0.0053	-0.0119 ± 0.0065
Coma at 90°	0.0070 ± 0.0036	-0.0193 ± 0.0030
Spherical	-0.0050± 0.0013	-0.0021 ± 0.0025

Aberration	*DM3*	*DM4*
Astigmatism at 0°	0.0251 ± 0.0100	0.0025 ± 0.0108
Astigmatism at 45°	-0.0011 ± 0.0150	0.0592 ± 0.0065
Coma at 0°	-0.0117 ± 0.0034	-0.0460 ± 0.0076
Coma at 90°	-0.0172 ± 0.0030	-0.0563 ± 0.0077
Spherical	-0.0045 ± 0.0022	-0.0156 ± 0.0014

Table 1.7: Zernike coefficients for the five most prominent aberrations in the IR wavefronts corresponding to DM configurations 1 through 4, in units of λ_{IR}.

In order to modify the astigmatism at $0°$ present in the IR wavefront, a voltage of $+50\,\mathrm{V}$ was applied to actuators 21, 32, 26, and 27 from the *DM1* configuration, and $+100\,\mathrm{V}$ on actuators 7 and 11. The measured Zernike coefficients show a large increase in said aberration, with smaller variations on the rest of them. The IR and harmonic wavefronts obtained with this configuration, *DM2*, along with the harmonic beam shape, are shown in figures 1.83 (b), (e), and (h), respectively. As observed with the previous case, while both wavefronts are astigmatic, this astigmatism is not directed along the same direction. In fact, the dominant aberration in the harmonic wavefront is now astigmatism at 45°, unlike any other previous case. The beam is also much larger and less energetic than before.

For the *DM3* configuration, the positions of several actuators were tweaked in order to create a flatter IR wavefront, shown in figure 1.83 (c). Astigmatism at 45° is the lowest of this series, with a very small coma and some astigmatism at 0° present as well. However, as seen in figures 1.83 (f) and (i), the least aberrated IR wavefront did not lead to the least aberrated harmonic wavefront or the most circular beam, but the harmonic pulse energy is increased again and only slightly lower than for *DM1*.

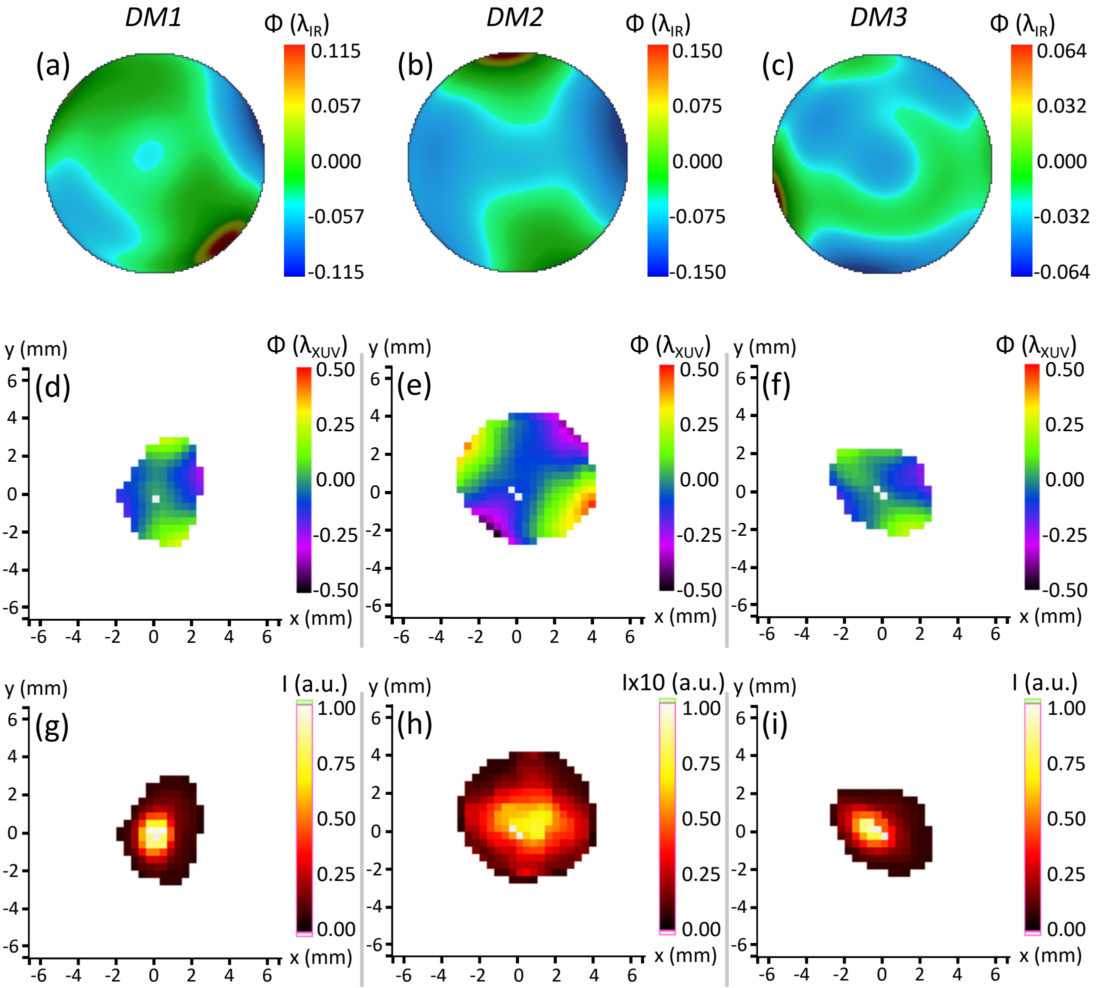

Figure 1.83: Direct comparison between the IR wavefronts measured with DM configurations 1, 2, and 3 (a, b, and c, respectively) with the single-shot high-harmonic wavefronts (d, e, and f) and intensity distributions for each case (g, h, and i). Note that the intensity scale was changed in (h) to make the beam more visible due to its lower energy.

As the next step, we used actuator 1 to change the curvature of the DM to move the position of the focal plane along the propagation axis. For *DM4*, a voltage of $-30\,\mathrm{V}$ was applied, moving the focal plane some centimeters before the cell. The IR wavefront in this case has some coma, both at 0° and 90°, and some astigmatism at 45°. For *DM5* and *DM6*, voltages of $0\,\mathrm{V}$ and $+15\mathrm{V}$ were applied to the same actuator, respectively, moving the focal plane after the lens. The IR wavefront was measured only for *DM4*. It can be assumed that it stays fairly constant in these three cases, since actuator 1 only affects the sphericity of the mirror, which is not accounted for in the presented wavefronts. This IR wavefront can be seen in figure 1.84 (a).

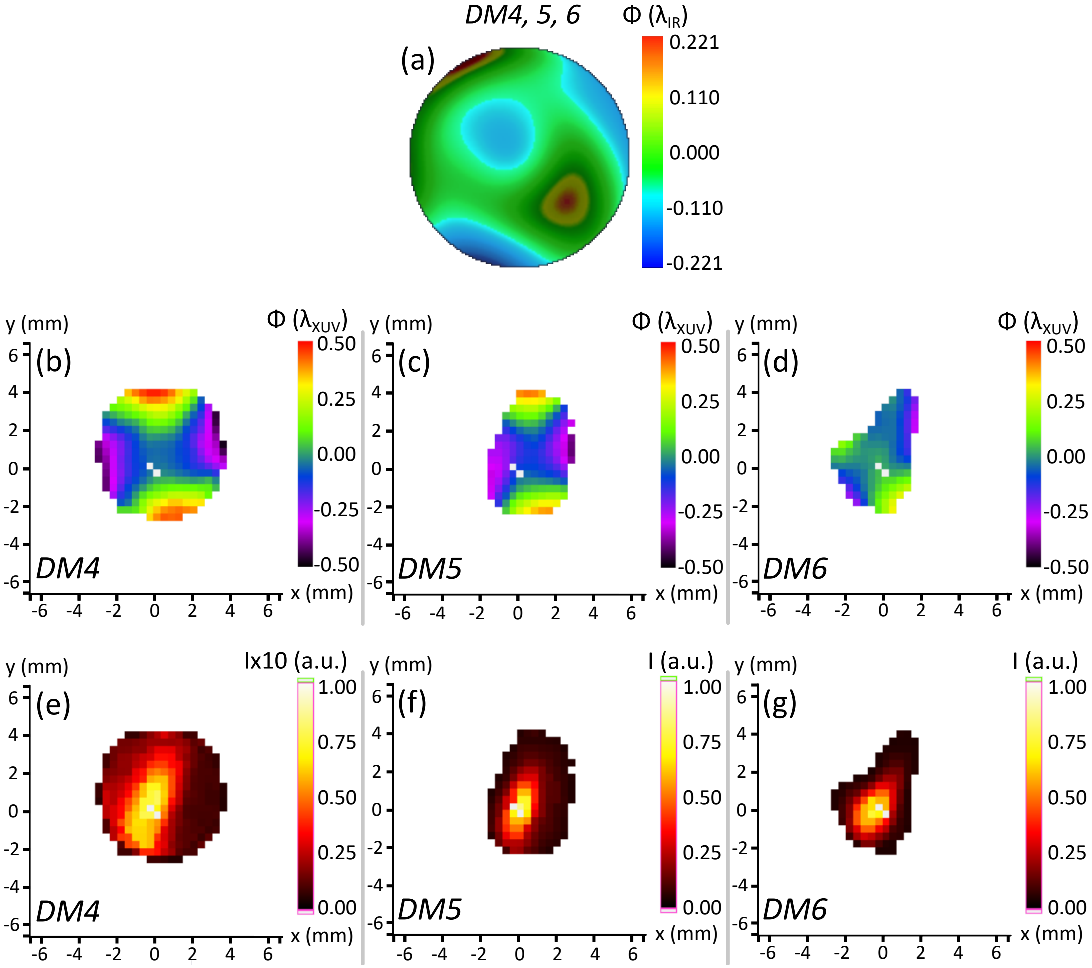

Figure 1.84: Direct comparison between the IR wavefront measured with DM4 configuration (a) with the single-shot high-harmonic wavefronts (b, c, and d) and intensity distributions for DM configurations 4, 5 and 6 (e, f, and g). The intensity scale is the same as in the previous figure for easier comparison. Note that the scale was changed in (e) to make the beam more visible due to its lower energy.

The three harmonic wavefronts measured for these DM configurations can be seen in figures 1.84 (b), (c), and (d), and the intensity distributions are presented in figures 1.84 (e), (f), and (g). It can be clearly seen that the coma dominating the IR wavefront is not present in the harmonics, which are, as usual, dominated by astigmatism, at 0° for *DM4* and *DM5*, but at 45° for *DM6*. The variations in both shape and size of the harmonic beams are similar to what was obtained in the previous experiment when moving the lens (see figure 1.67).

Up to this point, only the shapes of the IR and harmonic wavefronts were compared. A direct comparison between their RMS and PV values is presented in figure 1.85. All data points are obtained by averaging five separate single-shot measurements, with the error bars representing the standard deviation.

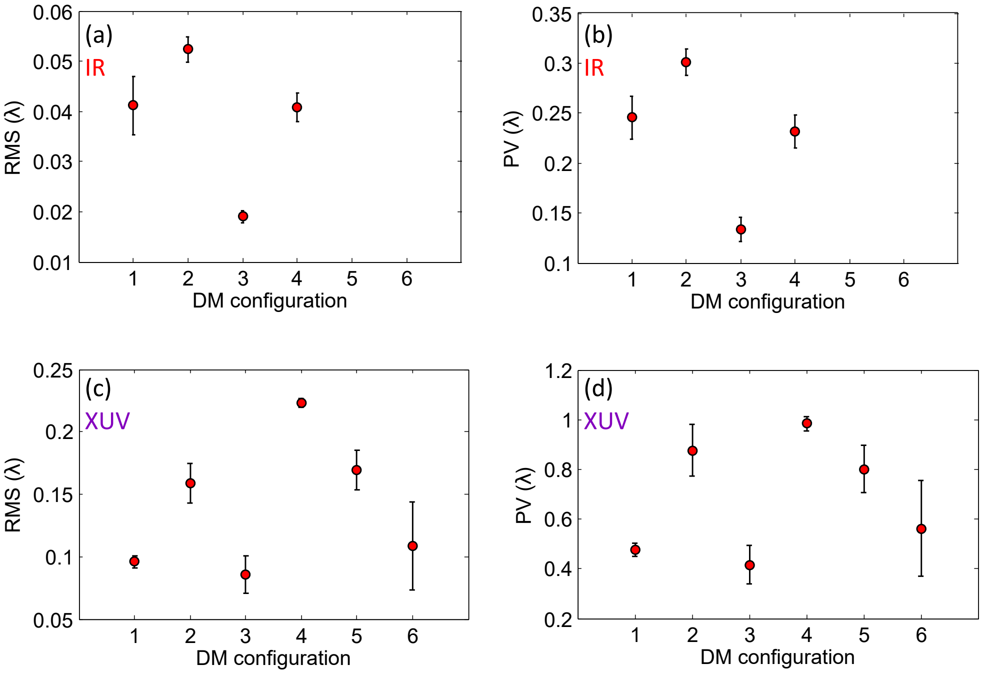

Figure 1.85: Direct comparison between the RMS and PV values of the IR (a and b) and harmonic wavefronts (c and d) for DM configurations 1 through 6. The IR wavefront in configurations 4, 5, and 6 is assumed to be the same.

The figure shows the intuitive result that increasing the aberrations of the driving beam has the same effect on the harmonic wavefront. It is however important to note that configurations *DM1* and *DM3* provide IR pulses with RMS errors differing by a factor of 2, while generating harmonic wavefronts with a similar RMS, slightly lower than $\lambda_{\mathrm{XUV}}/10$, albeit with a different direction of astigmatism. Despite the harmonic wavefronts being very similar to one another, the IR wavefronts that generate them are vastly different for both cases, both in their overall shapes and in their RMS and PV values. These results clearly demonstrate that, while the IR wavefront does have a very large impact on the HHG process in terms of aberrations, beam shape, size, and energy, it is is not directly transferred to the harmonic beam. This is consistent with the results of the previous experiments, in which the generation conditions were observed to significantly alter the harmonic spatial profile for a constant IR wavefront. Additional information about the harmonic wavefronts can be found in figure 1.86.

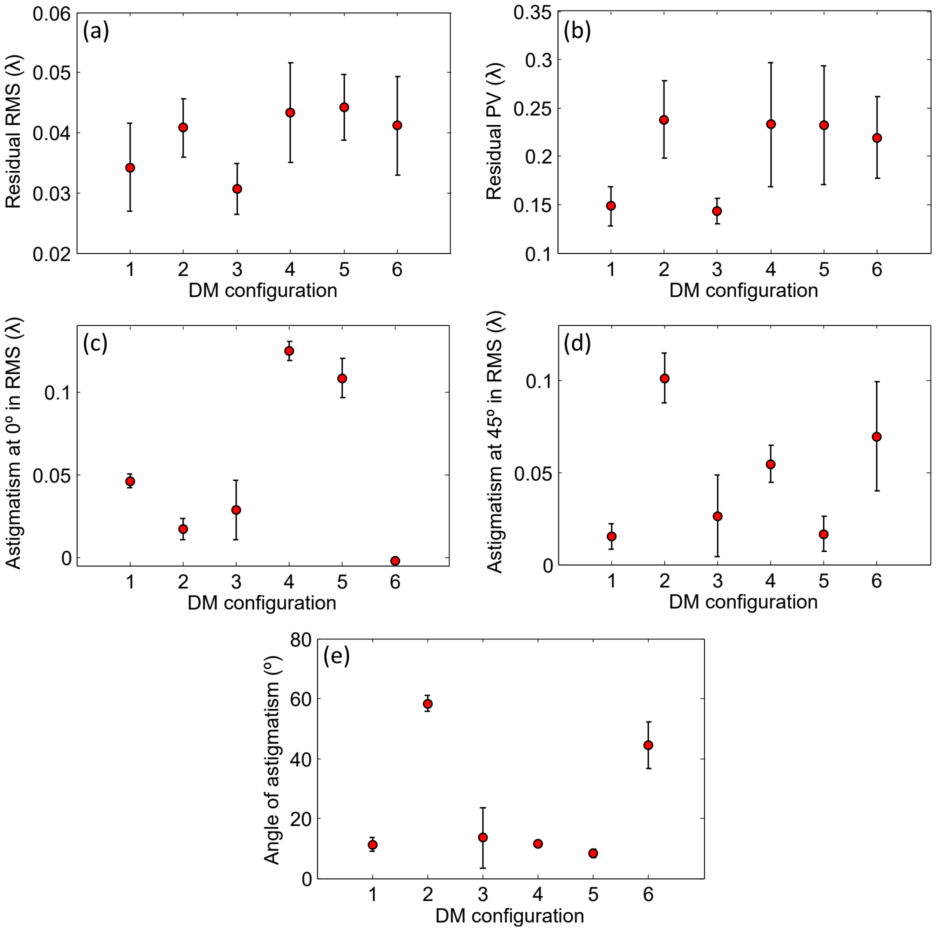

Figure 1.86: Parameters describing the high-harmonic wavefronts for DM configurations 1 through 6: (a) residual RMS, (b) residual PV, (c) contribution of astigmatism at 0° and (d) 45° to the wavefront RMS, and (e) angle of astigmatism.

Figures 1.86 (a) and (b) show the residual RMS and PV, when astigmatism is filtered out of the harmonic wavefronts. They show smaller variation than the full wavefronts, meaning that the large variations observed in these measurements are mostly due to changes in the astigmatism present in the wavefront, which can be seen for 0° and 45° in figures 1.86 (c) and (d), respectively. It can be seen that both components vary differently with the DM configuration. This leads to the angle of astigmatism varying significantly throughout these measurements, as seen in figure 1.86 (e), with values of 58.3° and 44.3° for configurations 2 and 6, respectively. However, in all other cases, the angle of astigmatism is close to 10°, as observed in the previous experiment.

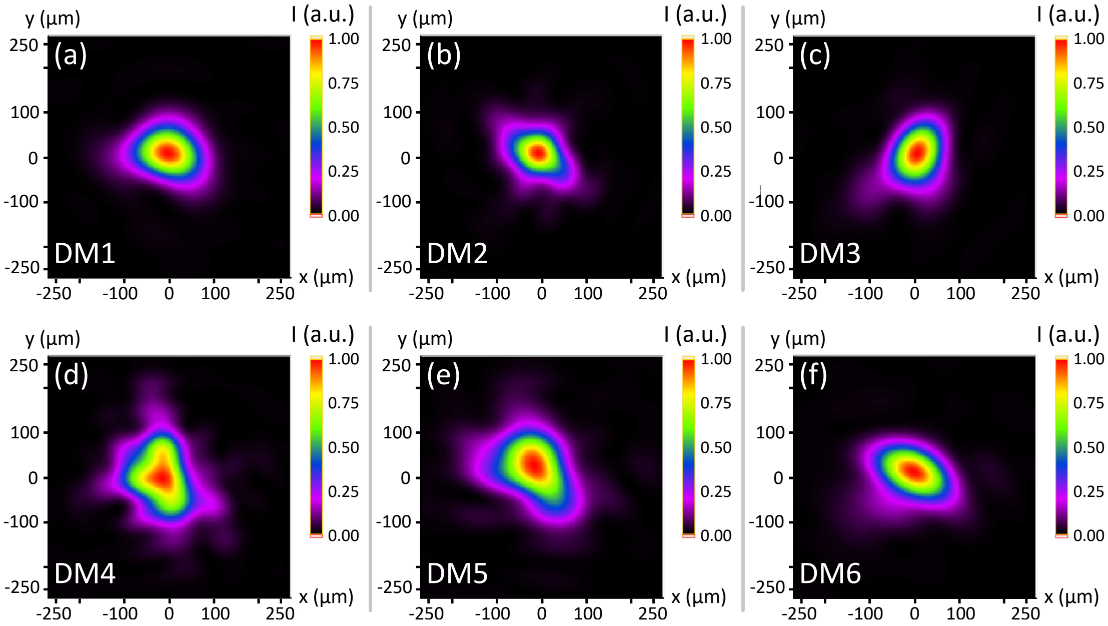

Figure 1.87: Calculated high-harmonic sources for DM configurations 1 through 6.

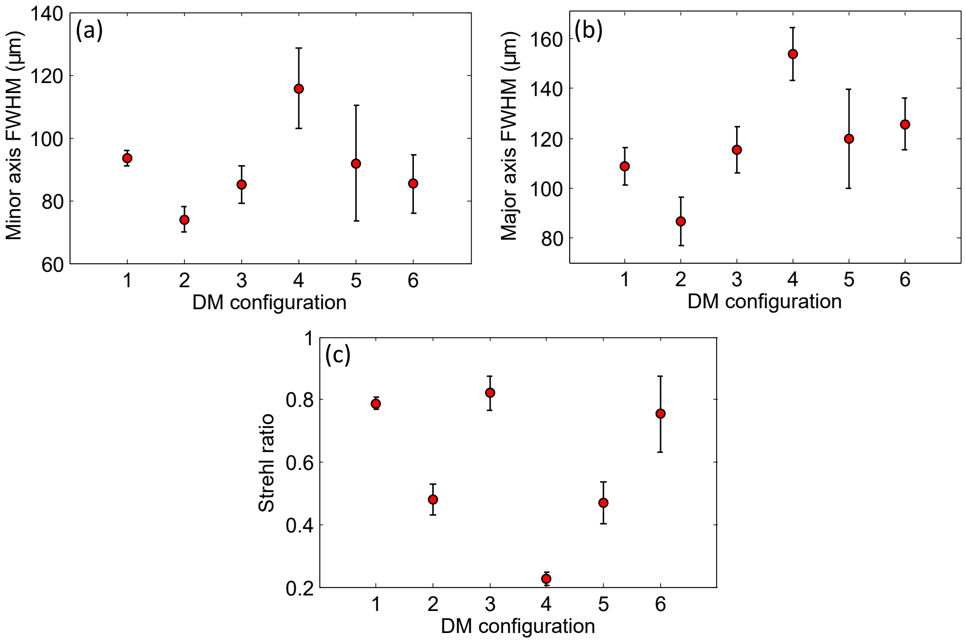

Figure 1.88: FWHM size of the calculated high-harmonic source along the minor (a) and major (b) axes, and (c) Strehl ratio for DM configurations 1 through 6.

Figure 1.87 presents the high-harmonic sources for each DM configuration, obtained by backpropagation. The many different IR wavefronts used so far lead, of course, to many different IR focii. As a consequence, significant variations are observed in the high-harmonic source in terms of shape, size, and orientation. Interestingly, it was seen in a previous figure that the intensity and wavefronts for configurations 1 and 3 are very similar, albeit with a different orientation, observed here as well. Configurations 4 through 6, where the position of the IR focus was moved along the propagation axis, lead to shape and size variations similar to those observed when moving the focal lens, albeit at a smaller scale.

The FWHM size of the source, along with its Strehl ratio, is presented in figure 1.88 for each configuration. In terms of stability and spatial quality, the initial position *DM1* is the optimal, with *DM3* being very similar, only slightly less stable. These results support the aforementioned conclusion that, while both wavefronts are very clearly related, a better IR wavefront does not always lead to a better harmonic wavefront or higher harmonic energy, since HHG is affected by many different parameters.

Second series: outermost actuators

Another series of measurements was carried out in order to further explore the influence of the IR wavefront on the harmonic pulses. In this case, we used only actuators placed in the outermost ring of the DM, significantly changing the magnitude and direction of astigmatism, as well as coma. The generation conditions were slightly different for this series of measurements, with iris diameter $22\,\mathrm{mm}$, IR pulse energy $24.3\,\mathrm{mJ}$, and argon pressure $200\,\mathrm{mbar}$. Two 200-nm-thick aluminum filters were in use at the beginning of the series, with one of them being removed later on due to the lower harmonic signal generated in some cases. Five more DM configurations were used, producing IR wavefronts with the Zernike coefficients included in table 1.8.

Aberration	*DM7*	*DM8*	*DM9*	*DM10*	*DM11*
Astigmatism at 0°	0.0729 ± 0.0220	0.0973 ± 0.0290	0.0363 ± 0.0138	0.0105 ± 0.0137	-0.0304 ± 0.0180
Astigmatism at 45°	0.0497 ± 0.0166	-0.0188 ± 0.0134	0.0194 ± 0.0258	-0.0873 ± 0.0187	0.0464 ± 0.0069
Coma at 0°	-0.0245 ± 0.0060	-0.0108 ± 0.0093	-0.0266 ± 0.0131	-0.0106 ± 0.0110	-0.0184 ± 0.0052
Coma at 90°	-0.0180 ± 0.0035	-0.0198 ± 0.0047	-0.0183 ± 0.0087	-0.0226 ± 0.0055	-0.0212 ± 0.0146
Spherical	-0.0083 ± 0.0031	0.0034 ± 0.0037	0.0045 ± 0.0032	0.0024 ± 0.0028	-0.0025 ± 0.0024

Table 1.8: Zernike coefficients for the five most prominent aberrations in the IR wavefronts corresponding to DM configurations 7 through 11, in units of λ_{IR}.

The *DM7* configuration was obtained by applying $-200\,\mathrm{V}$ to actuator 22. The IR and harmonic wavefronts can be seen in figures 1.89 (a) and (d), creating significant astigmatism at $0°$, and less prominent at $45°$. The harmonic wavefront is dominated by astigmatism at $0°$, as usual, and the intensity distribution, seen in figure 1.89 (g), is not very elliptical, compared to the first series.

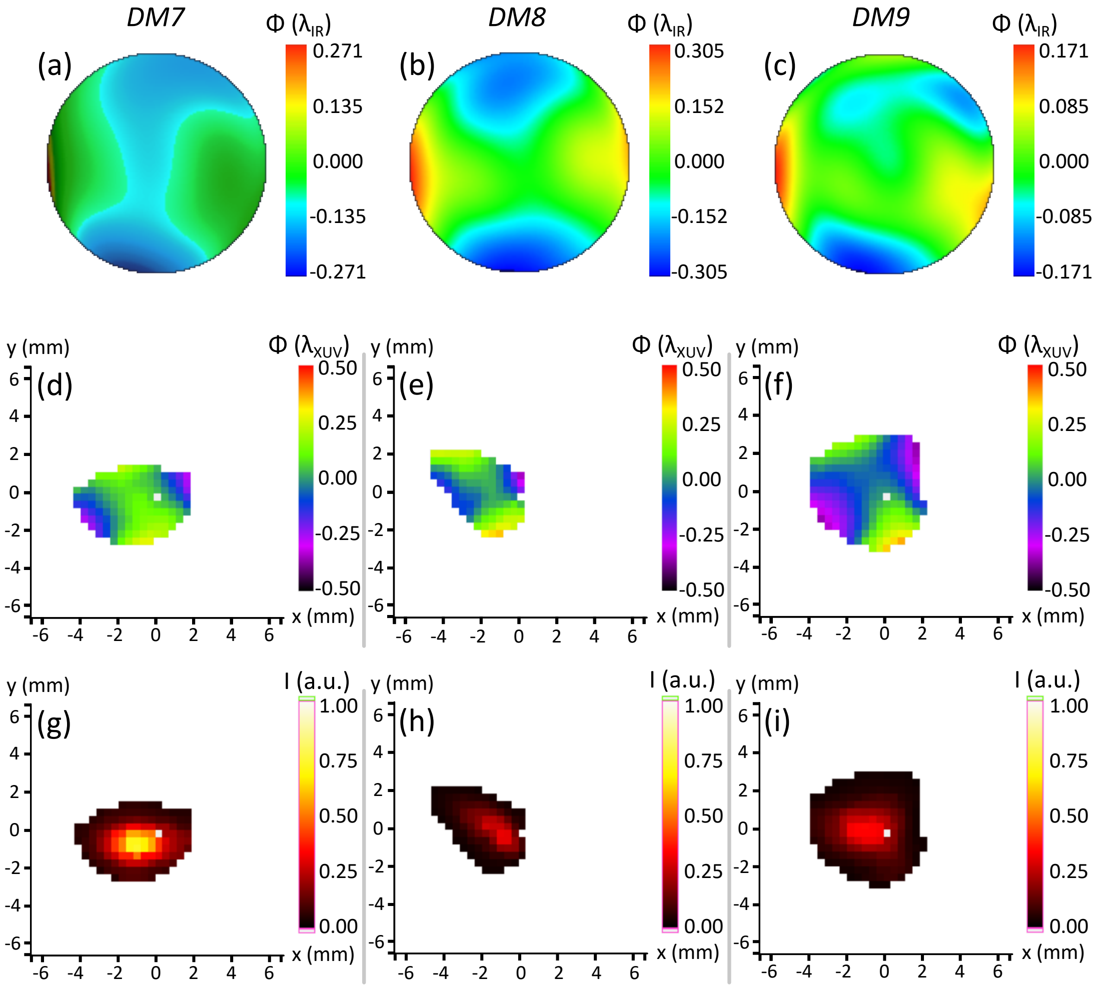

Figure 1.89: Direct comparison between the IR wavefronts measured with DM configurations 7, 8, and 9 (a, b, and c, respectively) with the single-shot high-harmonic wavefronts (d, e, and f) and intensity distributions for each case (g, h, and i).

Afterwards, configuration *DM8* was created by using actuator 28, symmetric with respect to 22, in order to affect astigmatism at $45°$. The applied voltage was $-120\,\mathrm{V}$, leading to the IR wavefront shown in figure 1.89 (b). This made astigmatism at $0°$ far more prevalent than $45°$. However, while the IR wavefront is significantly different from *DM7*, figure 1.89 (e) shows that the high-harmonic wavefront is not much different, albeit with a higher component of astigmatism at $45°$. However, the harmonic pulse has much less energy, as observed in figure 1.89 (h).

A voltage of $-120\,\mathrm{V}$ was applied next to actuator 30, creating the IR wavefront seen in figure 1.89 (c), corresponding to the *DM9* configuration, which is significantly less aberrated than the previous two cases. Interestingly, the general shape of the high-harmonic wavefront shown in figure 1.89 (f) has not varied much, with astigmatism being directed towards the same direction in all three cases. Additionally, the intensity distribution shown in figure 1.89 (i) shows significant differences in terms of shape and size. The energy also decreased significantly despite the IR wavefront being better. In fact, one of the filters had to be removed to increase the signal on the sensor. Doing this increased the counts by a factor of 3.

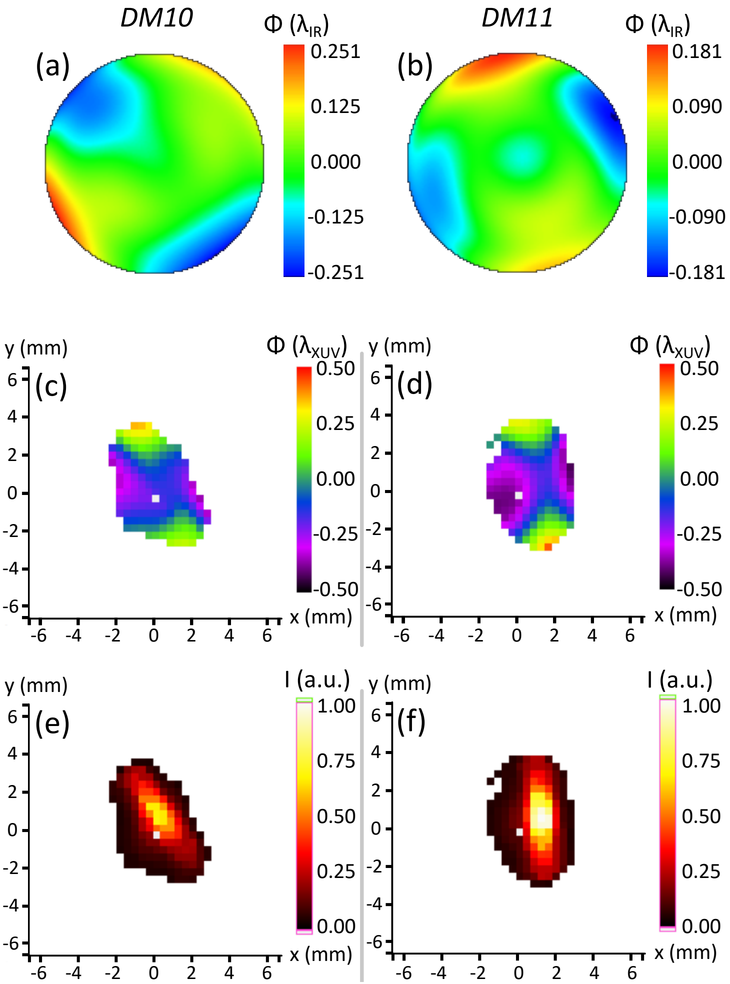

Figure 1.90: Direct comparison between the IR wavefronts measured with DM configurations 10 and 11 (a and b, respectively) with the single-shot high-harmonic wavefronts (c and d) and intensity distributions for each case (e and f).

Next, for the *DM10* configuration, we applied $-220\,\mathrm{V}$ to actuator 26, further rotating the direction of astigmatism towards 45°, presented in figure 1.90 (a). The high-harmonic wavefront, however, is still dominated by astigmatism at 0°, which can be seen in figure 1.90 (c). The pulse shape, in figure 1.90 (e), varied significantly, becoming much more elongated and increasing its energy.

The final configuration, *DM11*, was obtained by applying a voltage of $-210\,\mathrm{V}$ to actuator 24. This led to a less aberrated IR wavefront, seen in figure 1.90 (b). This, in turn, led to a more aberrated harmonic wavefront as shown in figure 1.90 (d). Additionally, figure 1.90 (f) shows that, despite the wavefront being worse, the pulse energy was increased, with the pulse shape being still elongated, but directed towards the vertical axis.

Figure 1.91 compares the RMS and PV values of the IR and harmonic wavefronts obtained in this second series of measurements. It can be seen that, in this case, the best harmonic wavefronts are generated with the worst IR wavefronts, in contrast with what was seen in the first series, further proving that there is no direct wavefront transfer from one pulse to the other, and that the relation between their spatial properties is far more complex, and also highly dependent on the generation parameters.

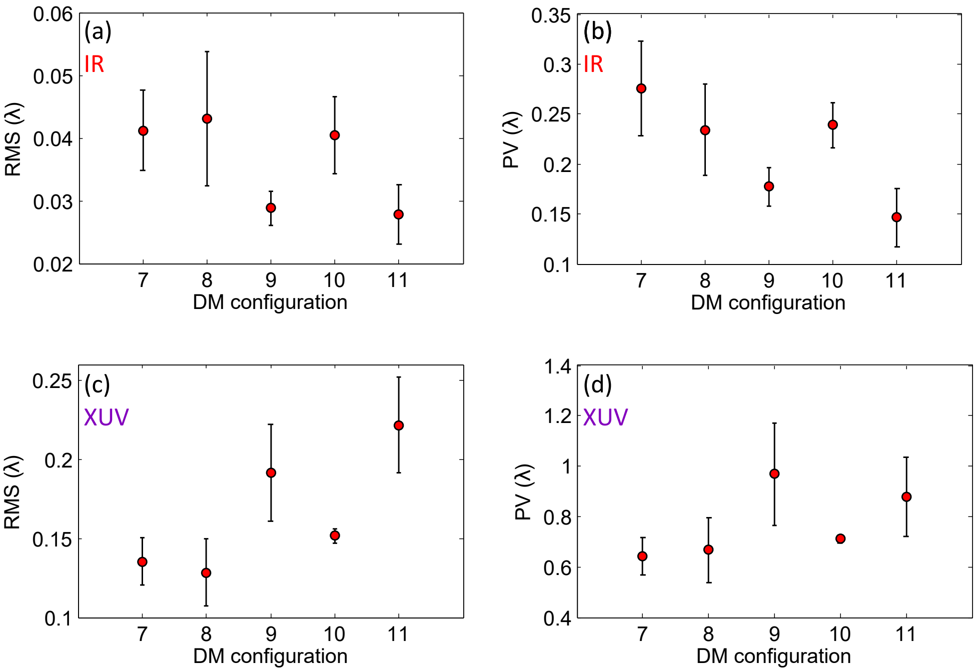

Figure 1.91: Direct comparison between the RMS and PV values of the IR (a and b) and harmonic wavefronts (c and d) for DM configurations 7 through 11.

The RMS and PV values for the residual wavefronts are shown in figures 1.92 (a) and (b), with very similar trends as the values obtained from the full wavefront. The contributions of astigmatism at 0° and 45°, in figures 1.92 (c) and (d), show a wide range of variation for both of them, due to large variations of the angle of astigmatism seen in figure 1.92 (e), where the angle can be seen to vary by more than 20°.

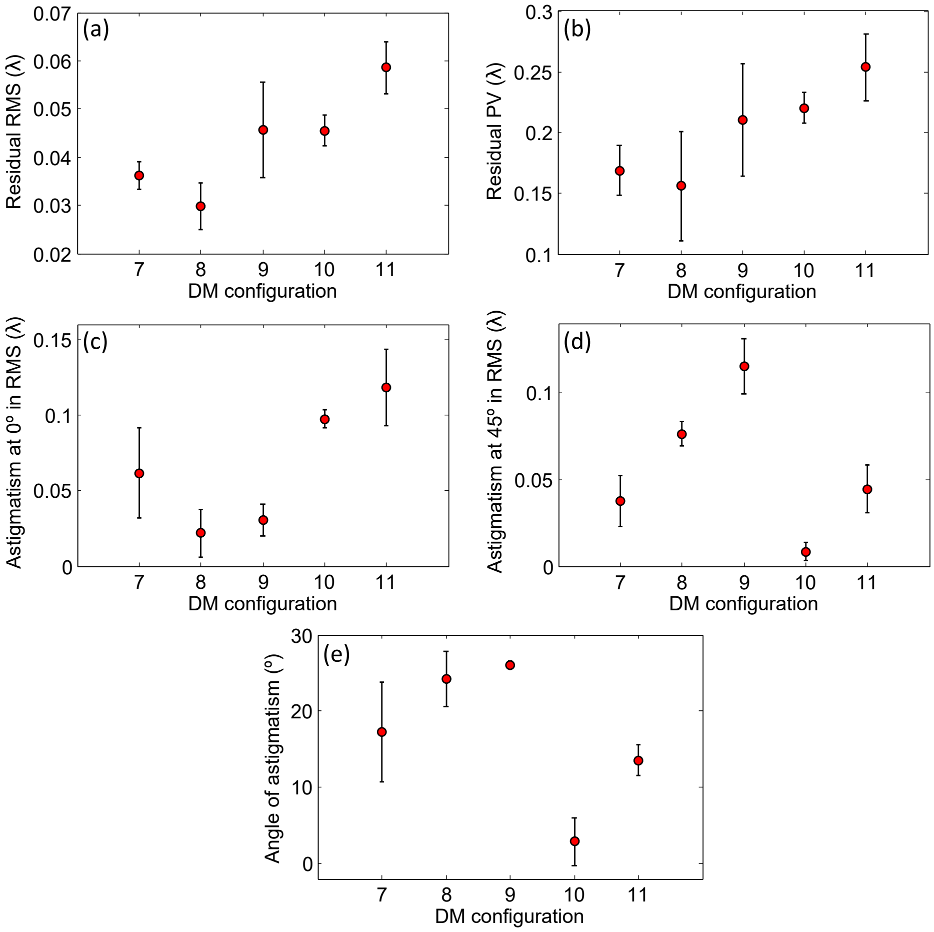

Figure 1.92: Parameters describing the high-harmonic wavefronts for DM configurations 7 through 11: (a) residual RMS, (b) residual PV, (c) contribution of astigmatism at 0° and (d) 45° to the wavefront RMS, and (e) angle of astigmatism.

The calculated high-harmonic source shapes are presented in figure 1.93 for all five configurations in the second series. As in the first series, the shape is seen to change significantly with each change made to the DM. Except for *DM9*, it has an elliptical shape, with variable orientation. The FWHM size and Strehl ratio for each case are included in figure 1.94.

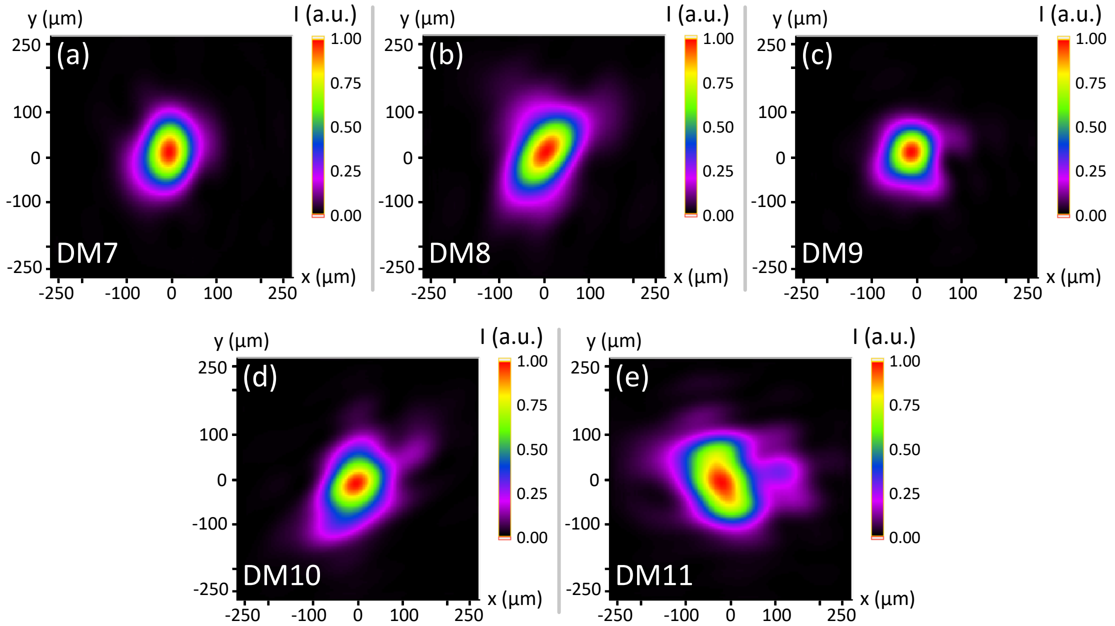

Figure 1.93: Calculated high-harmonic sources for DM configurations 7 through 11.

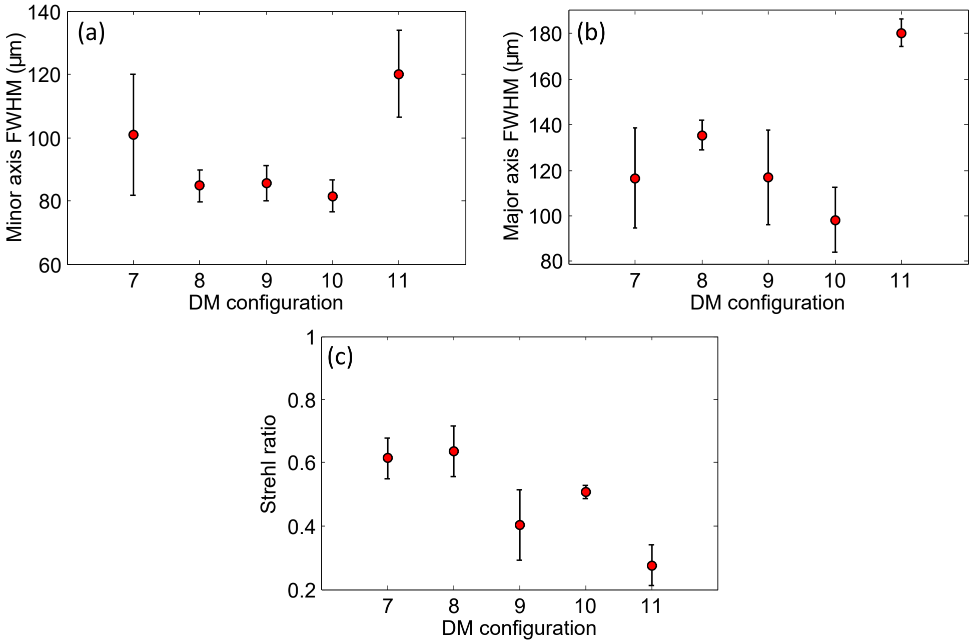

Figure 1.94: FWHM size of the calculated high-harmonic source along the minor (a) and major (b) axes, and (c) Strehl ratio for DM configurations 7 through 11.

1.3.3.3 Discussion

The results presented here showcase the important influence that the IR wavefront has on the HHG process, since it affects not only the high-harmonic pulse wavefront, but also its shape and size, as well as the conversion efficiency, if all other generation conditions are kept unchanged. High-harmonic wavefronts with $\mathrm{RMS} < \lambda/11$ were obtained thanks to the implementation of the DM, representing a very significant improvement with respect to the values of $\lambda/4$ typically found in the previous experiment, in absence of the DM. As observed before, it is clear that there is no direct wavefront transfer from the driving beam to the harmonics. This is supported by the fact that astigmatism at 0° is still the dominant aberration in most cases, even when this aberration is almost nonexistent in the IR wavefront. However, higher astigmatism angles close to 30° were also found. Interestingly, it seems that those cases are the ones where generation is the least efficient. Furthermore, the first DM configuration provides the highest efficiency, as well as a small, circular harmonic beam, but does not provide the best wavefront. A similar effect was observed in the previous experiment as well.

This experiment demonstrates that the spatial properties of the high-harmonic beam can be manipulated to a great extent by using IR adaptive optics. This scheme allowed us to change the shape of the harmonic pulse from circular to elliptical, as well as its orientation. Being able to tailor the spatial properties of the harmonics with this method provides a useful alternative to the use of a more expensive DM for the XUV domain, which would also provide lower reflectivity. Furthermore, a computerized closed-loop program could eventually be implemented in the beamline, which would use data from the XUV sensor to find the DM configuration which provides the best harmonic wavefront, the highest energy, or the most circular beam shape.

1.4 Summary

The XUV Hartmann sensor provides a powerful tool for spatial metrology of XUV pulses. The sensor was extensively used in the two experiments carried out at LLC reported in this chapter, aimed at studying how the wavefronts of high-harmonic pulses are affected by the generation parameters, as well as the wavefront of the driving IR pulse. In both cases, the high-harmonic pulse energy was high enough to allow for single-shot wavefront measurements.

In the first experiment, the IR wavefront was kept constant, with an RMS error of $\lambda_{\mathrm{IR}}/10$. The typical high-harmonic wavefront had an RMS value close to $\lambda_{\mathrm{XUV}}/4$, with good shot-to-shot stability, represented by a relative standard deviation usually lower than 25% when considering five independent measurements. The high-harmonic wavefronts were observed to always have significant astigmatism at 0°, an aberration that seems to be absent from the driving pulse. This, along with the large difference in RMS values, indicates that there is no direct wavefront transfer from the driving beam to the harmonics. All other aberrations, such as coma or spherical aberration, are much less relevant. This is particularly useful for focusing the harmonic beam, since astigmatism can be corrected when using curved optics. The use of multilayer mirrors allowed us to measure the wavefronts of single harmonic orders, revealing that the astigmatism is caused by the highest ones, being almost entirely absent from plateau harmonics. As a consequence, the full wavefront could also be improved by filtering the cutoff harmonics from the beam.

Backpropagation calculations suggest that the shape of the IR beam at focus largely dictates the shape of the harmonic source, with the different generation parameters, such as pressure in the gas cell, having a large influence on the wavefront RMS in general, and astigmatism in particular. Additionally, we found that the HHG parameters leading to the highest conversion efficiencies do not yield the best wavefronts. In fact, the opposite is usually observed.

For the second experiment, adaptive optics were installed in the IR beam path in order to obtain further information about how changing the driving pulse wavefront can affect HHG. It was found to have a very significant influence on the wavefront, shape, and size of the harmonic pulses, as well as on the conversion efficiency. With the use of the DM, IR wavefronts with RMS lower than $\lambda_{\mathrm{IR}}/20$ could be obtained, leading to the generation of harmonics with $\mathrm{RMS} < \lambda_{\mathrm{XUV}}/11$, a significant improvement from the results of the previous experiment. When using the DM, the harmonic pulses with the best wavefront were also the ones with the highest pulse energy, as well as the most circular shape.

These measurements highlight the importance of using a driving beam with good spatial quality to obtain high harmonics not only with good wavefronts, but also with circular beam profiles and high energy. Furthermore, the use of DM for the driving laser allows for some degree of control over the shape of the harmonic pulses, mainly their ellipticity and orientation.

CHAPTER 2

Spatial metrology of XUV optics using high-harmonic beams

Contents

The diffraction-limited resolution of an imaging system with numerical aperture NA, when using a source with wavelength λ, is given by the Rayleigh criterion as $\mathrm{Res} = \frac{0.61\lambda}{\mathrm{NA}}$ [96]. As a consequence, XUV and X-ray sources can provide finer resolutions than IR or visible sources. In fact, resolutions under $50\,\mathrm{nm}$ have been achieved with reflective microscopes, using tabletop XUV illumination [97].

For nanoimaging with XUV sources, high-quality optics are also required for the best resolutions. The same occurs for other applications such as EUV litography, where better optics are able to produce smaller features [98]. XUV wavelengths, of the order of tens of nanometers, are sensitive to smaller surface defects than visible or IR light. For this reason, the surface quality requirements for XUV optics are much more strict. Visible light sources such as He-Ne lasers ($\lambda = 632.8\,\mathrm{nm}$), often used for optics metrology due to their simplicity [99, 100, 101], are not always sufficiently precise for the case of XUV optics, which might benefit from *at-wavelength* tests. These tests are usually time-consuming since they must be carried out in synchrotrons [102], where beamline access is limited, due to the high XUV flux required. Being able to perform these tests in tabletop setups would be extremely beneficial for the manufacturing process.

This chapter reports the use of our XUV Hartmann wavefront sensor with two XUV optical systems used with high-harmonic radiation. In section 2.1, the main concepts of characterization of XUV optics are presented. Section 2.2 reports the use of HHG and the XUV Hartmann WFS for tabletop characterization of the primary multilayer mirror of an XUV Schwarzschild objective, as well as the optimization of its alignment in the Salle Orange beamline of LOA. Finally, section 2.3 presents the use of the sensor to quickly and efficiently optimize the focusing of an XUV Wolter-like telescope for high harmonics, made up of two toroidal mirrors.

2.1 Surface metrology of XUV optics

The lateral resolution of an imaging system is defined as the minimum necessary distance between two points so that they can be distinguished, and it is limited by two factors: diffraction and aberrations. The diffraction limit is imposed by the laws of nature, and it leads to the minimum possible size of a focused beam having a similar order of magnitude as its wavelength. On the other hand, a focused beam can only achieve said minimum size if its wavefront is not aberrated. If it is, the resolution is said to be limited by aberrations. This limit is caused by technology rather than nature, and can be minimized or fully suppressed by using aberration-free optics, or using adaptive optics to further reduce any aberrations a beam may have. An imaging system is said to be *diffraction-limited* or *aberration-limited* depending on which phenomenon is more prominent. When using short-wavelength illumination sources, aberrations usually play a larger role than diffraction [103].

According to the Maréchal criterion, a beam is considered diffraction-limited if the RMS error of its wavefront is lower than $\lambda/14$ [83]. For example, for a Ti:Sapphire IR laser emitting at $\lambda_{\mathrm{IR}} = 800\,\mathrm{nm}$, this means an RMS of $\lambda_{\mathrm{IR}}/14 = 57.14\,\mathrm{nm}$. However, for its 25^{th} harmonic, with a wavelength of $\lambda_{\mathrm{HH}} = 32\,\mathrm{nm}$, a diffraction-limited beam requires an RMS lower than $\lambda_{\mathrm{HH}}/14 = 2.29\,\mathrm{nm}$. As a consequence, while manufacturing diffraction-limited optics for the IR range is fairly easy, it is challenging in the XUV range, so high-accuracy surface metrology is more demanding as well.

The main reason for metrology of multilayer mirrors is to identify and quantify any defects they may have, which will hinder their performance during experiments. Those defects can include the so-called *amplitude defects*, like particles or clusters on the mirror surface which cause scattering, and *phase defects*, deviations of the mirror shape with respect to the design, such as swellings or depressions on the layers [102]. Some defects can be caused during the fabrication process, such as the layers being deposited over a defect on the substrate, and others can happen during normal operation, such as particles being deposited on the multilayer surface. XUV radiation can also cause damage on the multilayer coatings during experiments, as well as morphological changes like the appearance of blisters [104]. Shack-Hartmann sensors can be used to characterize XUV optics with visible light [99].

There are two main reasons why at-wavelength characterization is preferred over more conventional characterization with visible light. Firstly, there is the fact that XUV light is sensitive to defects of nanometer scale, unlike visible light, where wavelengths are tens of times longer. Secondly, the response of multilayer mirrors to incident light is extremely wavelength-dependent, due to their working principle being based on interference inside the layers. For example, if a mirror uses a metallic coating, such as molybdenum and silicon (Mo/Si), an XUV beam used for an experiment will penetrate several layers, and thus be affected by any internal defect [102], while visible light will be completely reflected by the top layer. As a consequence, using a visible beam for metrology cannot reveal internal defects that will affect the performance of a multilayer mirror under working conditions.

Point-diffraction interferometry (PDI) is often used for at-wavelength characterization of XUV optics [105, 106]. In this technique, the beam is reflected by the optics under test and carries wavefront aberrations produced by it. Then, it is sent through a partially transmitting membrane which contains a pinhole. The pinhole produces a spherical reference wavefront by means of diffraction, which interferes with the attenuated wavefront transmitted though the membrane [107]. The pinhole diameter must be chosen with respect to the NA of the optical system under test, in order to provide a beam with a sufficiently large diameter. Due to the short wavelengths of the XUV region, diameters smaller than one micron are often necessary, which in turn leads to very low transmitted energy, thus requiring high average powers such as those provided by synchrotrons, to allow for short acquisition times [97].

2.2 Tabletop at-wavelength characterization and alignment of an XUV Schwarzschild objective

While at-wavelength characterization of XUV optics is important to accurately characterize any possible defect, the high flux needed for techniques like PDI means that the tests must be conducted in synchrotron radiation facilities, where access to beamtime is limited, since tabletop XUV sources such as HHG do not provide enough power.

This section describes two experiments carried out in LOA, which showcase the possibility of using HHG for tabletop, at-wavelength metrology of multilayer mirrors, thanks to the use of the XUV Hartmann sensor described in section 1.3.1.2. This WFS is also used for tabletop and at-wavelength alignment of an XUV Schwarzschild microscope objective designed and built by the Optical Microanalysis group of the Swiss Federal Laboratories for Materials Science and Technology (abbreviated by its German acronym, Empa), in Switzerland, for its use in nanoimaging. By being able to carry out these steps with HHG, XUV optics can be tested, and XUV optical systems can be analyzed in the same laboratory where they will be later used, without the need for an external beamtime.

2.2.1 The XUV Schwarzschild objective

A Schwarzschild objective is made of two concentric spherical mirrors: a concave primary mirror (PM) and a convex secondary mirror (SM) [108]. It is widely used in the field of astronomy, and known also as Cassegrain telescope. It is interesting for microscopy in the XUV range due to its simplicity [109], since it is made up of only two optical elements, as well as its low geometrical aberrations [103]. It has been shown that his type of objective can be free of third and fifth order aberrations if certain geometrical conditions are met. They involve the relationship between the radii of curvature, and between object position and the radius of the SM. In these conditions, the Schwarzschild objective is aplanatic, meaning that it is free of third-order spherical aberration, coma and astigmatism.

This type of objective can be used in different configurations which are shown schematically in figure 2.1, depending on the relative positions of the mirrors and the aperture of the used illumination:

- **Classical or concentric Schwarzschild**: In this configuration, both mirrors have the same center of curvature Q, and they are parallel to one another. This configuration allows for compensation of third-order spherical aberration, coma and astigmatism. To fully utilize the whole NA of the objective, a divergent, non-coherent source must be used, or, in the case of a collimated beam, a condenser must be used instead.

- **Eccentric or non-concentric Schwarzschild**: In this variation of the classical Schwarzschild, there is an offset $\Delta\mathrm{Q}$ between the centers of curvature Q_1 and Q_2 of the mirrors, optimized for better imaging performance by further reducing spherical aberration.

- **Partial Schwarzschild**: In this case, the mirrors share their center of curvature, but there is a lateral offset between them to reduce the obscuration caused by the SM. The PM is also tilted by an angle α, in order to reflect the incoming light towards the SM.

- **Off-axis Schwarzschild**: This configuration is a particular case of the classical setup, for cases where low-NA sources are used for illumination. As with the partial configuration, only a part of the PM is used.

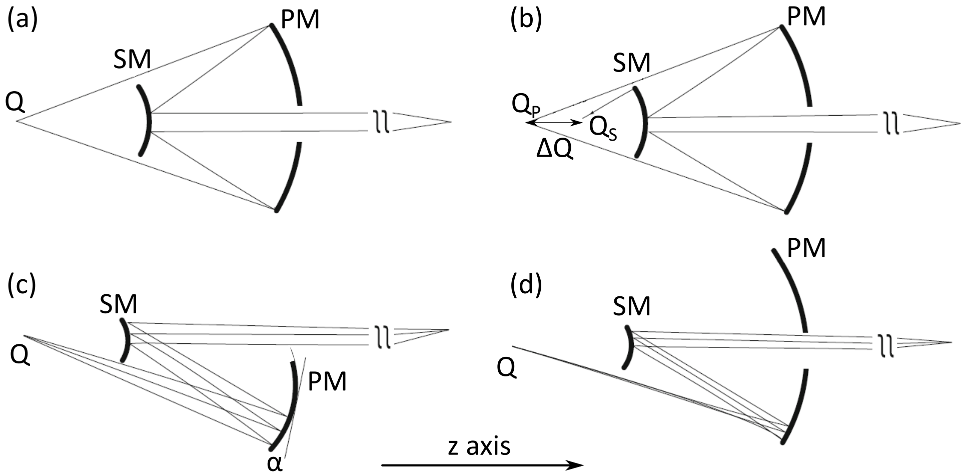

Figure 2.1: Schematic drawings showing the different configurations in which the objective can be used, depending on the relative positions of the mirrors: (a) classical Schwarzschild objective, (b) eccentric Schwarzschild, (c) partial Schwarzschild, and (d) off-axis Schwarzschild. Taken from [110].

The XUV Schwarzschild objective presented in this section [110, 111] has a PM with external and internal diameters of $38.1\,\mathrm{mm}$, and $17\,\mathrm{mm}$, respectively, and a radius of curvature of $100\,\mathrm{mm}$. The SM has a diameter of $8.6\,\mathrm{mm}$ and a radius of curvature of $36\,\mathrm{mm}$. Thus, the distance between the mirrors must be $64\,\mathrm{mm}$ in the classical configuration. The objective provides $30\mathrm{X}$ magnification, with numerical aperture $\mathrm{NA} = 0.15$. We tested and aligned this objective in the Salle Orange HHG beamline of LOA.

Due to the fact that most materials do not reflect XUV radiation efficiently, more so when approaching normal incidence, multilayer mirrors are used. Both mirrors consist on 70 alternating layers of ruthenium and boron carbide (Ru/B_4C) deposited on fused silica substrates. The layer period is $6.28\,\mathrm{nm}$ for the PM and $6.205\,\mathrm{nm}$ for the SM, consisting in both cases on 29% Ru and 71% B_4C. The layer deposition was performed in the Fraunhofer Institute, using the Nessy-3 DC magnetron sputtering system. The mirrors were designed and fabricated so that their reflectivity is maximum at $12\,\mathrm{nm}$ wavelength. This particular working wavelength was chosen because it is the central wavelength emitted by the plasma-based XUV light source in the BeAGLE (Bern Advanced Glass Laser for Experiments) facility in Switzerland, which uses a tin target [112]. The NA of the system was chosen in order to provide optimal resolution at this wavelength, considering both diffraction and aberration-limited resolutions.

The reflectivities of both mirrors as a function of the angle of incidence, as well as pictures of the mirrors themselves, are presented in figure 2.2, for the working wavelength, and figure 2.3 shows the reflectivity as a function of wavelength, assuming incidence angles of 2° on the PM and 5° on the SM. It must be noted that, in classical Schwarzschild configuration, the SM prevents part of the radiation from reaching the PM, causing an obscuration of 17%. Taking mirror reflectivities and obscuration into account, the total transmission of the objective is 17.2%.

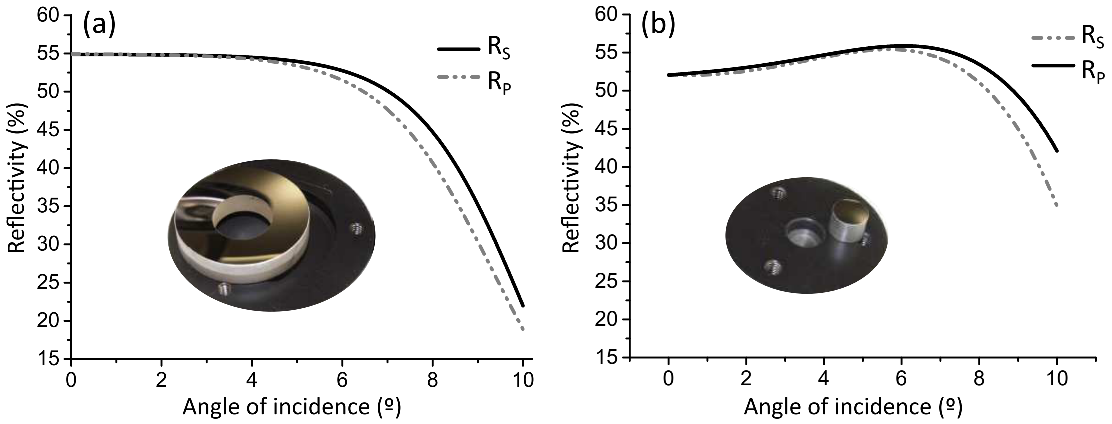

Figure 2.2: Reflectivity of the two multilayer mirrors as a function of the angle of incidence, for 12-nm radiation and for s- and p-polarization. (a) Primary mirror and (b) secondary mirror. Taken from [111].

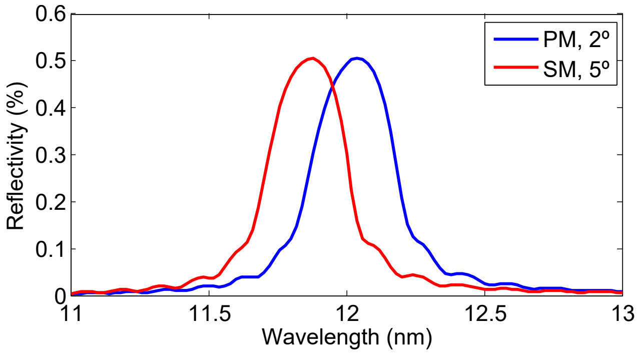

Figure 2.3: Theoretical spectral reflectivity of the multilayer mirrors that make up the Schwarzschild objective. S-polarization is assumed. Data from the CXRO [61].

Parameter	*Primary mirror*	*Secondary mirror*
Radius of curvature (mm)	100, concave	36, convex
Diameter (mm)	Ext.: 38.1 ± 0.1 Int.: 17.0 ± 0.1	8.6 ± 0.1
Angle of incidence (°)	1.2 to 2.5	3.0 to 7.0
Thickness (mm)	8.00 ± 0.10	6.35 ± 0.10
Reflectivity for 12 nm (%)	50-55	50-55
Surface roughness (nm RMS)	Central: 0.10 15 mm from center: 0.13	Central: 0.12 Outer: 0.13

Table 2.1: Parameters of the multilayer mirrors used in the Schwarzschild objective.

Table 2.1 summarizes the features of the two mirrors that make up the Schwarzschild objective. The roughness of the mirror surfaces was characterized in the BESSY II synchrotron, in Germany, by measuring scattered radiation when using the mirrors in normal incidence, a technique called scatterometry [113].

If the mirrors are accurately aligned, the aberrations are kept to a minimum, so the resolution is limited by diffraction instead. The resolution is then given by the Rayleigh criterion as $\mathrm{Res} = \frac{0.61\lambda}{\mathrm{NA}}$ [96]. In the case of the XUV Schwarzschild objective, $\mathrm{Res} \simeq 50\,\mathrm{nm}$. To achieve this, the mirrors are encased in the shell shown in figure 2.4.

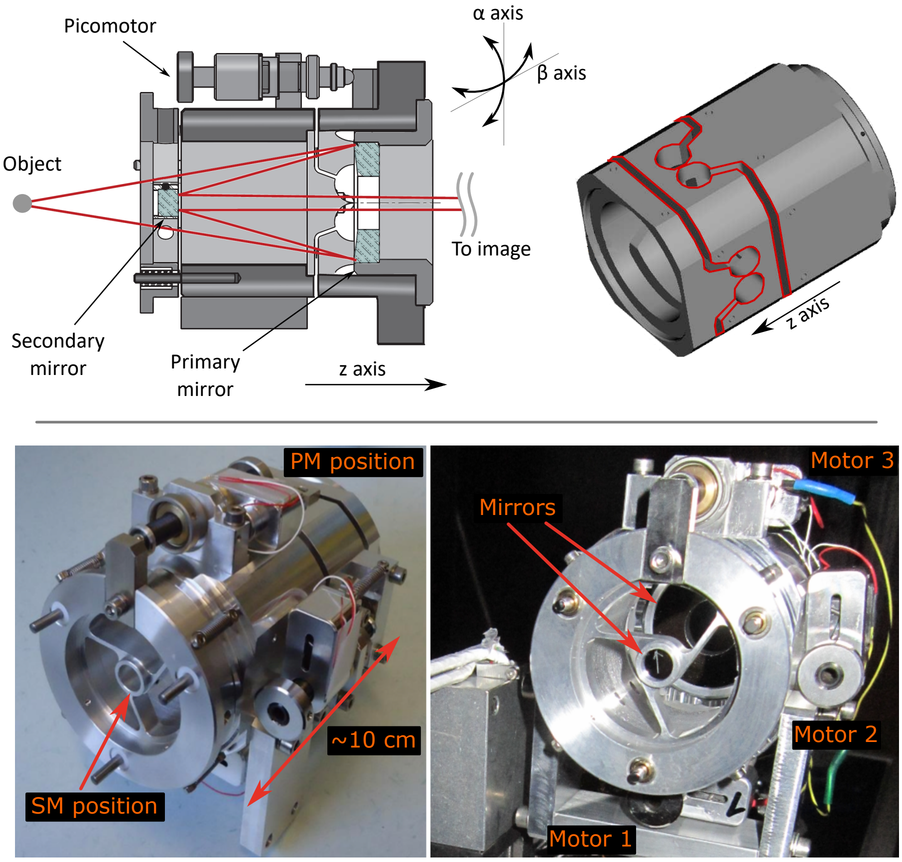

Figure 2.4: Drawings (top) of the Schwarzschild microscope objective, taken from [111]. The flexure gimbal, marked in red, allows for flexibility on the shell. Photographs of the shell are also presented (bottom), showing the mirrors and the picomotors.

Three piezoelectric picomotors, with a resolution of $30\,\mathrm{nm}$, allow for precise tuning of the relative positions of the mirrors in vacuum, as well as the use of the different mirror configurations presented above. Motors 1 and 2 are used to tilt the PM along the α and β axes, respectively, with motor 3 being used to modify the distance between both mirrors along the z axis. As mentioned above, this distance must be $64\,\mathrm{mm}$ in the classical configuration, and the object must be placed $65.03\,\mathrm{mm}$ before the surface of the SM.

The shell contains two flexure gimbals, highlighted in the figure, to allow for the tilting movement. They consist of two hollow circles each, with a diameter of $12.1\,\mathrm{mm}$ and a gap dividing the shell in two sections. The circles are separated by a bridge of thickness $0.5\,\mathrm{mm}$.

Figure 2.5 shows how misalignments affect the resolution provided by the objective. In particular, to provide $\mathrm{Res} < 100\,\mathrm{nm}$, the angular tolerance is $\pm 0.15^\circ$ around 0°, while the spatial tolerance is $\pm 20\,\mu\mathrm{m}$ around the nominal distance of $64\,\mathrm{mm}$. When the alignment is optimum, resolution is limited by diffraction, to $50\,\mathrm{nm}$.

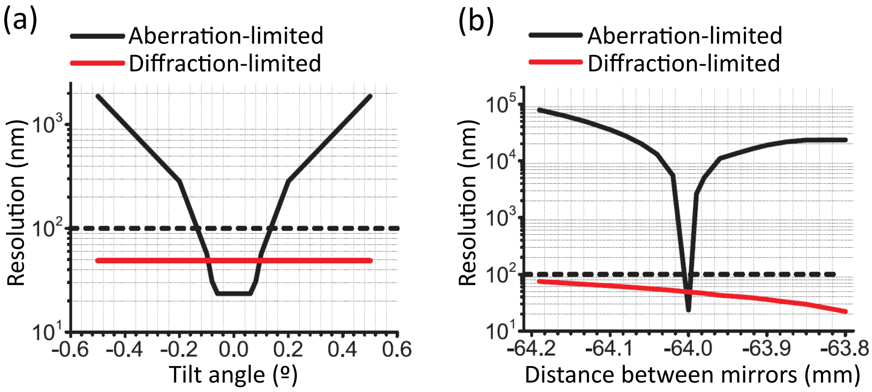

Figure 2.5: Diffraction and aberration-limited resolution provided by the Schwarzschild objective as a function of (a) mirror tilt and (b) distance between mirrors, around the design values. Taken from [111].

2.2.2 Characterization of the primary mirror with high harmonics

Prior to mounting the mirrors inside the shell, they were brought to LOA for testing using high harmonics. The XUV Hartmann sensor described in section 1.3.1.2 was used for this experiment, shortly after its calibration. In this experiment, carried out in the Salle Orange beamline, a high-harmonic beam with a reference wavefront was reflected on the mirror surface at an angle of 22.5°, and the reflected wavefront was measured with the Hartmann WFS in order to check for mirror defects. Due to time constraints, only the PM was characterized.

2.2.2.1 Experimental setup

The experimental setup is presented in figures 2.6 and 2.7. The harmonics were generated by focusing the 800-nm driving laser into a 15-mm-long cell filled with argon at $30\,\mathrm{mbar}$. The IR beam was apertured down to $15.4\,\mathrm{mm}$.

High-harmonic beams are known to be less aberrated in the center, so the beam was clipped by a 870-mm pinhole in order to obtain a spherical wavefront on the probe beam. Considering the distance between the pinhole and the mirror, as well as the beam divergence, its diameter on the mirror surface is approximately $1\,\mathrm{mm}$.

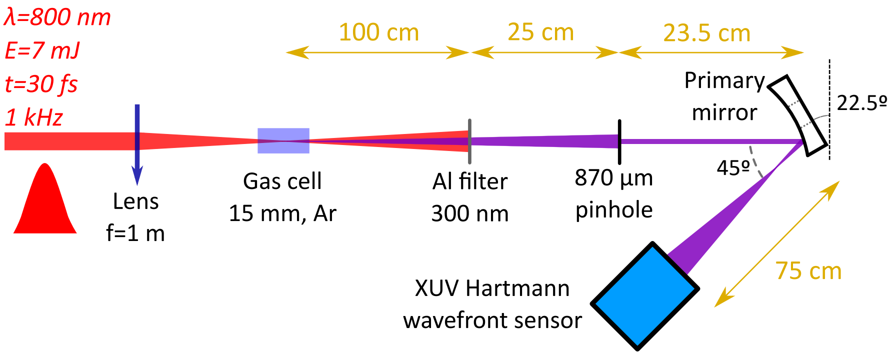

Figure 2.6: *Schematic drawing of the setup used for the at-wavelength testing of the PM with high harmonics.*

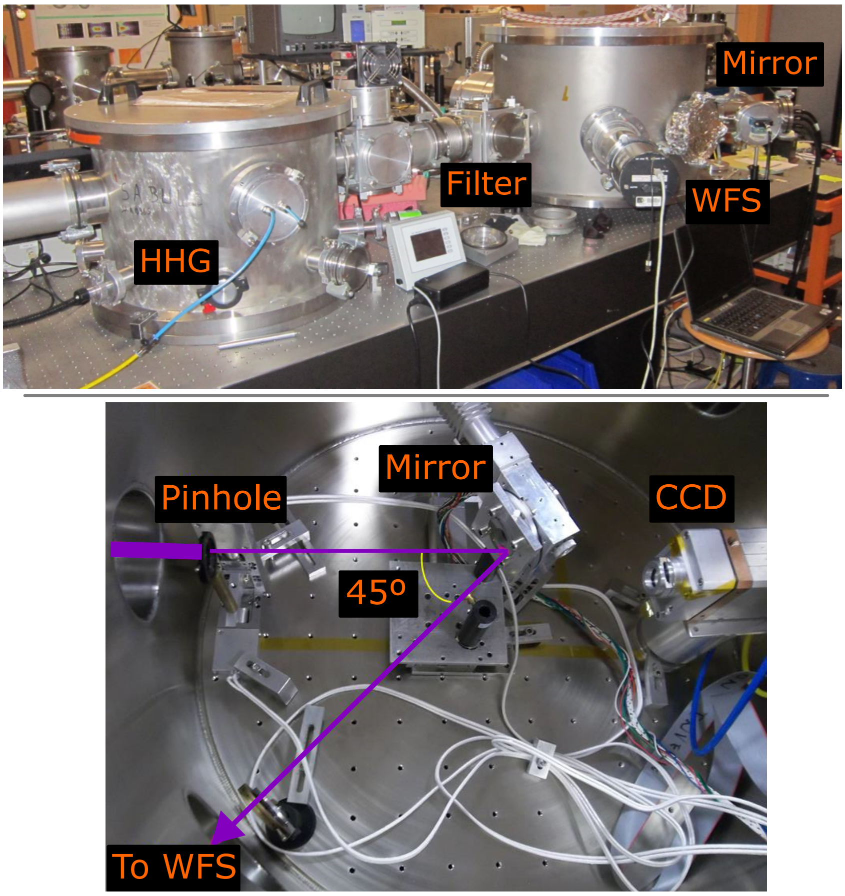

Figure 2.7: *Picture of the vacuum chamber layout (top), showing the sensor, and picture of the interior of the main chamber (bottom), showing the spherical mirror mounted on the rotation stage. The CCD placed after the rotation stage is used for alignment of the harmonic beam and optimization of the pinhole position under vacuum.*

The mirror was mounted on a rotation stage, used to rotate the mirror by 3° between consecutive measurements. This was done to ensure that the probing beam covered a full circumference around the center of the mirror, at $28\,\mathrm{mm}$ from it. Although the proper working wavelength for the mirrors is $12\,\mathrm{nm}$, such a short wavelength could not be efficiently generated in Salle Orange. This is due to neon, the gas generally used to generate shorter wavelengths, being less efficient for HHG and due to the available Al filters completely blocking radiation under $\lambda = 17\,\mathrm{nm}$. For those reasons, $\lambda = 32\,\mathrm{nm}$ was used instead, which corresponds to the 25^{th} harmonic order. At this wavelength, the sensor provides a sensitivity of $\lambda/50\ \mathrm{RMS}$.

2.2.2.2 Results and discussion

An example of reflected wavefront is shown in figure 2.8. The beam is first focused less than $5\,\mathrm{cm}$ away from the mirror, and it then diverges again when propagating towards the WFS. Given that it is a spherical mirror in non-normal incidence, the measured wavefront is, as expected, mainly astigmatic at 0°, with some astigmatism at 45° also present. The wavefront resulting from ruling out both astigmatism is also included, and shows some spherical aberration. The RMS and PV values are given in the figure for each case.

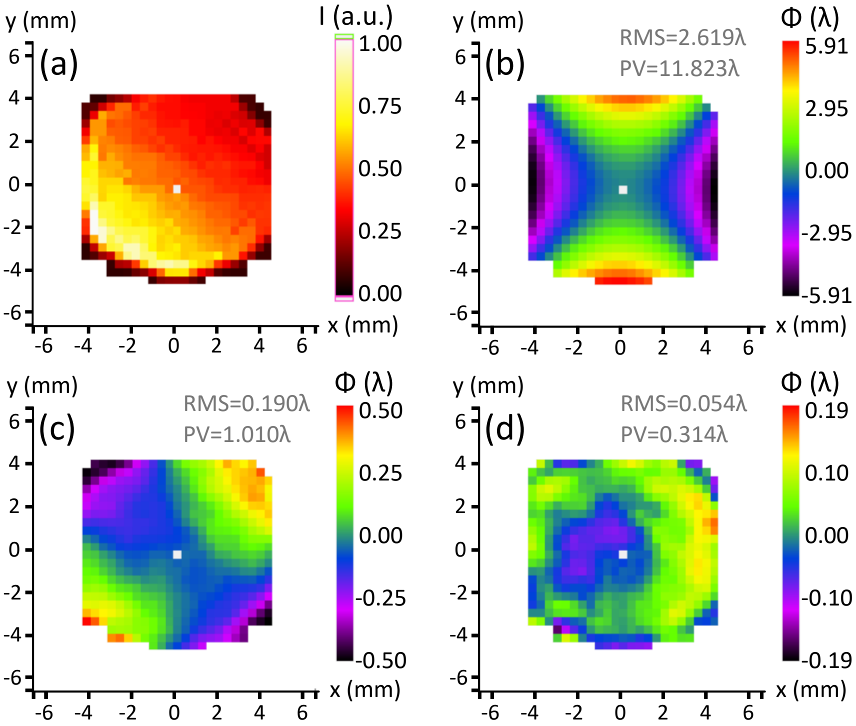

Figure 2.8: Far field of the high-harmonic beam reflected by the primary Schwarzschild mirror at 22.5° incidence: (a) intensity distribution, (b) corresponding wavefront, (c) wavefront after ruling out astigmatism at 0°, and (d) residual wavefront after ruling out astigmatism at 0° and at 45°. 10000 shots were accumulated for this acquisition.

Maps of aberrations at different positions on the mirror surface can be traced with these measurements. Figure 2.9 presents a map of astigmatism at 0° around the full circle, as well as several consecutive harmonic wavefronts.

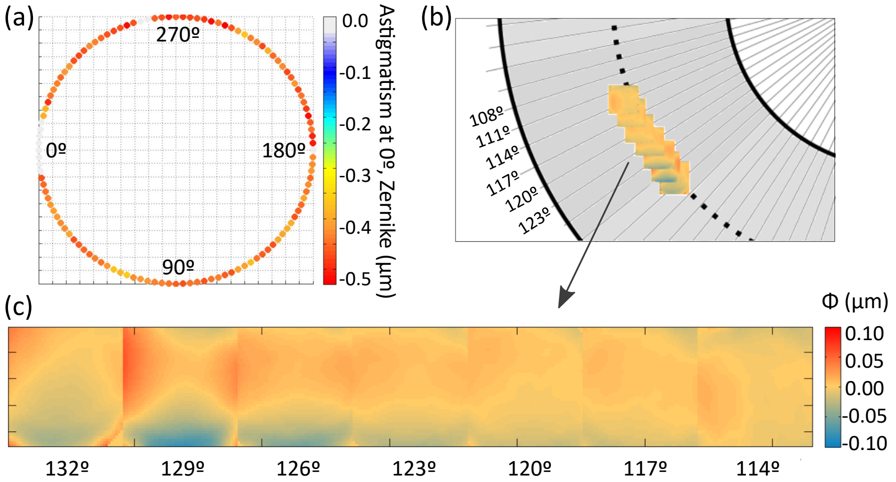

Figure 2.9: Maps made from high-harmonic wavefronts: (a) Zernike coefficients for astigmatism at 0° for all measured positions, (b) portion of a map showing the wavefronts at several points, and (c) the same wavefronts in more detail. Taken and adapted from [111].

The Zernike coefficients corresponding to the main aberrations were also studied. The measured values were compared to the theoretical values corresponding to the mirror and setup parameters, calculated through a simulation in the OSLO ray-tracing software, as seen in figure 2.10. As expected, astigmatism at 0°, caused by the angle of incidence, is the most prominent aberration, while the rest of them are very low in comparison. We find very good agreement between theoretical and experimental values.

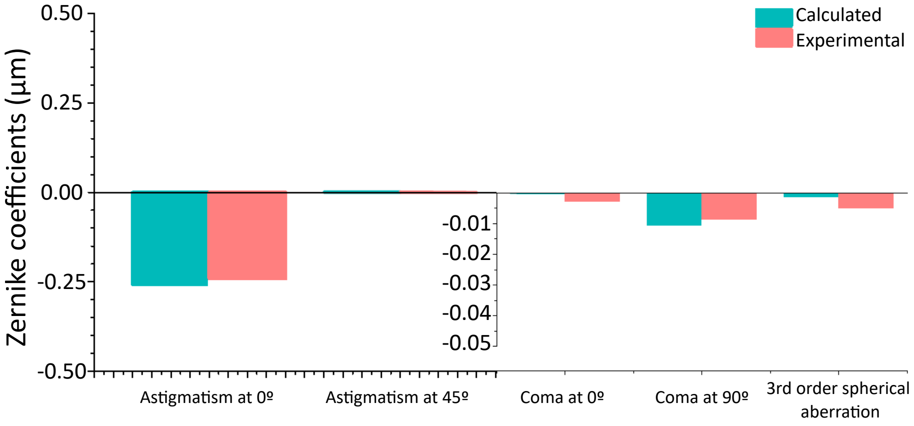

Figure 2.10: Comparison of the measured and calculated Zernike coefficients for the main aberrations. Taken from [111].

Higher-order aberrations, in particular those with Zernike coefficients over the 8^{th} mode, were seen to have peak-to-valley values close to only $20\,\mathrm{nm}$, much smaller than the theoretical diffraction-limited resolution of the Schwarzschild objective, $50\,\mathrm{nm}$. All these results demonstrate the high optical quality of the PM. Furthermore, this test showcases the potential of HHG and XUV Hartmann wavefront sensors for tabletop, non-contact, and at-wavelength metrology of multilayer optics for the XUV range. This, in turn, implies that XUV optics can be characterized in the same laboratory where they will be used for experiments, without the need to resort to a synchrotron.

2.2.3 Optimizing the alignment of the objective with visible and XUV wavefront metrology

Once the mirrors had been mounted in the shell, the completed Schwarzschild objective was brought again to LOA for alignment, again using HHG and the Hartmann WFS. The mirrors were mounted in the so-called classical configuration, in which both mirrors are parallel and the have the same center of curvature. Given the radii of $100\,\mathrm{mm}$ and $36\,\mathrm{mm}$, this leads to a distance of $64\,\mathrm{mm}$ between the mirrors.

The main idea behind the experiment, carried out in Salle Orange, is to send a high-harmonic beam with a spherical wavefront through the objective, and then change the relative position of the mirrors with the picomotors built into the shell in order to optimize the focal spot. Since the beam sent through the objective has a perfect spherical wavefront, any defect of the focusing is solely due to misalignment, and can thus be corrected.

2.2.3.1 Experimental setup

The experimental setup is presented in figure 2.11, which also includes a zoom on the Schwarzschild objective. The reference beam is created by diffraction of the high harmonics with a small pinhole, as it was done for the sensor calibration (see section 1.3.1.2). The beam has to cover the full diameter of the PM, $38.1\,\mathrm{mm}$ at a distance of $129.03\,\mathrm{mm}$. The central harmonic order generated in Salle Orange was the 25^{th}, corresponding to $\lambda = 32\,\mathrm{nm}$, so the pinhole diameter must be smaller than $0.3\,\mu\mathrm{m}$ in order to produce a beam with enough aperture. Both the pinhole and the Schwarzschild objective are mounted on 3D translation stages for precise alignment under vacuum.

Considering that the direct harmonic beam had a diameter of several millimeters, the energy would be decreased by several orders of magnitude due to the small diameter of the pinhole, in turn leading to hours-long acquisition times on the WFS. This is also the reason why $\lambda = 32\,\mathrm{nm}$ is preferred instead of the mirror's working wavelength of $\lambda = 12\,\mathrm{nm}$, which would require a reduction in pinhole diameter of a factor of 3 in order to obtain a beam with the same aperture.

To increase the energy transmitted through the pinhole, the harmonic beam is focused on it with two fused silica spherical mirrors placed in grazing incidence, in the Kirkpatrick-Baez (KB) configuration [114]. They are placed perpendicularly to one another, so that each one focuses the beam in one direction, and their incidence angles are chosen so that their focal planes overlap. Of course, the KB mirrors change the direction of propagation upon reflection of the beam, so a pair of flat mirrors are used to compensate for the vertical offset.

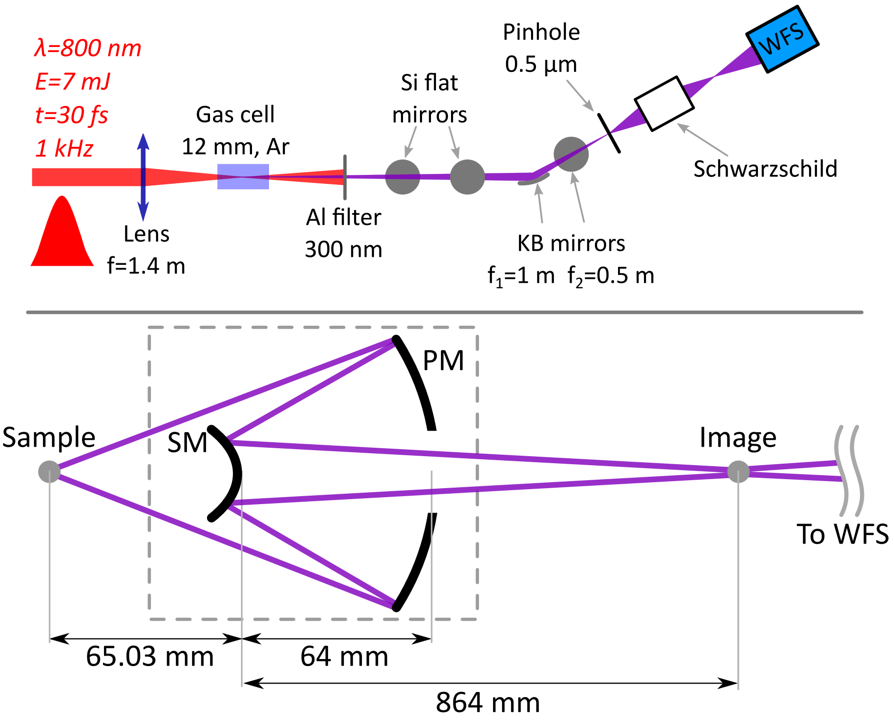

Figure 2.11: (Top) Schematic drawing of the experimental setup used for the at-wavelength optimization of the Schwarzschild microscope and (bottom) additional drawing showing the relevant distances. In this case, the pinhole constitutes the sample to be imaged.

After the reference beam is propagated through the objective, it is focused and then propagated to the Hartmann WFS. The focal spot is then calculated through backpropagation of the far-field beam. The sensor is placed at approximately $1.5\,\mathrm{m}$ from the objective, so that the beam covers as many subpupils as possible.

2.2.3.2 Results

As a first step, a coarse prealignment of the objective was performed using a green laser diode, emitting continuously at $\lambda = 532\,\mathrm{nm}$, and a 500-$\mu\mathrm{m}$ pinhole as the object. The setup used for this step is presented in figure 2.12. A beam expander providing a magnification of 6 is used, in order to ensure that the focal spot is smaller than the pinhole, which provides spatial filtering and improves the wavefront. The filtered beam is then sent to the objective, and the mirrors are aligned with the picomotors, until an image of the pinhole is formed on the screen.

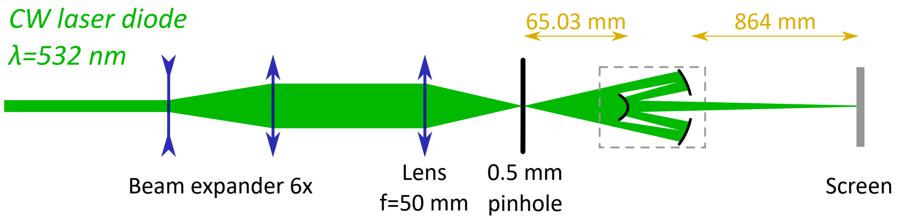

Figure 2.12: Schematic drawing of the setup used to prealign the objective with a green laser diode.

Once this simple prealignment was finished, the objective was placed after the pinhole for the alignment proper. However, the small pinhole diameter required for the high harmonic beam leads to long acquisition times for each wavefront. In order to reduce the number of acquisitions necessary to find the optimal mirror position, a finer alignment was performed by using a 2ω beam produced via second-harmonic generation (SHG) and a visible Shack-Hartmann WFS.

The second harmonic of the Ti:Sapphire laser was generated by placing a 100-μm-thick BBO (beta barium borate) crystal $70\,\mathrm{cm}$ after the lens and filtering out the remaining IR energy with a bandpass filter. The Shack-Hartmann WFS was placed $1.5\,\mathrm{m}$ after the objective. The sensor, provided by Imagine Optic, has an array of 40x32 microlenses, spaced by $114.023\,\mu\mathrm{m}$, with focal distance $2841\,\mu\mathrm{m}$.

Given that the wavelength is, in this case, $400\,\mathrm{nm}$, a pinhole with a 3-μm diameter was used, since it is small enough to provide the necessary aperture for the reference beam. The energy transmitted through the pinhole was sufficient to allow for real-time monitoring of the pinhole image formed by the objective by backpropagating the measured wavefront, thus enabling fast and precise optimization of the mirror positions. Figure 2.13 shows the far-field intensity distributions and wavefronts measured for three different configurations of the objective: at the starting point, during the optimization and at the end. The trefoil-like shape of the beam is due to the obscuration of the SM holder, visible in figure 2.4. The different sizes and pointings are due to the different mirror distances and tilt, respectively.

The images of the pinhole formed by the objective in each case, obtained through backpropagation, are presented in figure 2.14. This showcases how important mirror alignment is in order to achieve the optimal imaging performance of the system, as well as the usefulness of wavefront sensors for real-time optimization. The use of cameras to monitor the focusing of an optical system is not always possible for several reasons. For example, it is not always possible to place a camera at the image or focal planes, especially when working in vacuum, where it cannot be accessed during operation with high harmonics. In other cases, the camera could be damaged due to the intensity at focus. And lastly, and most importantly in this case, sometimes the image or focus is too small to be accurately resolved by a CCD due to the pixel size. A common pixel size in CCD cameras with Si chips is $13.5\,\mu\mathrm{m}$, and the image of the 3-μm pinhole, after the 30X magnification provided by the Schwarzschild, will have a diameter of $90\,\mu\mathrm{m}$,

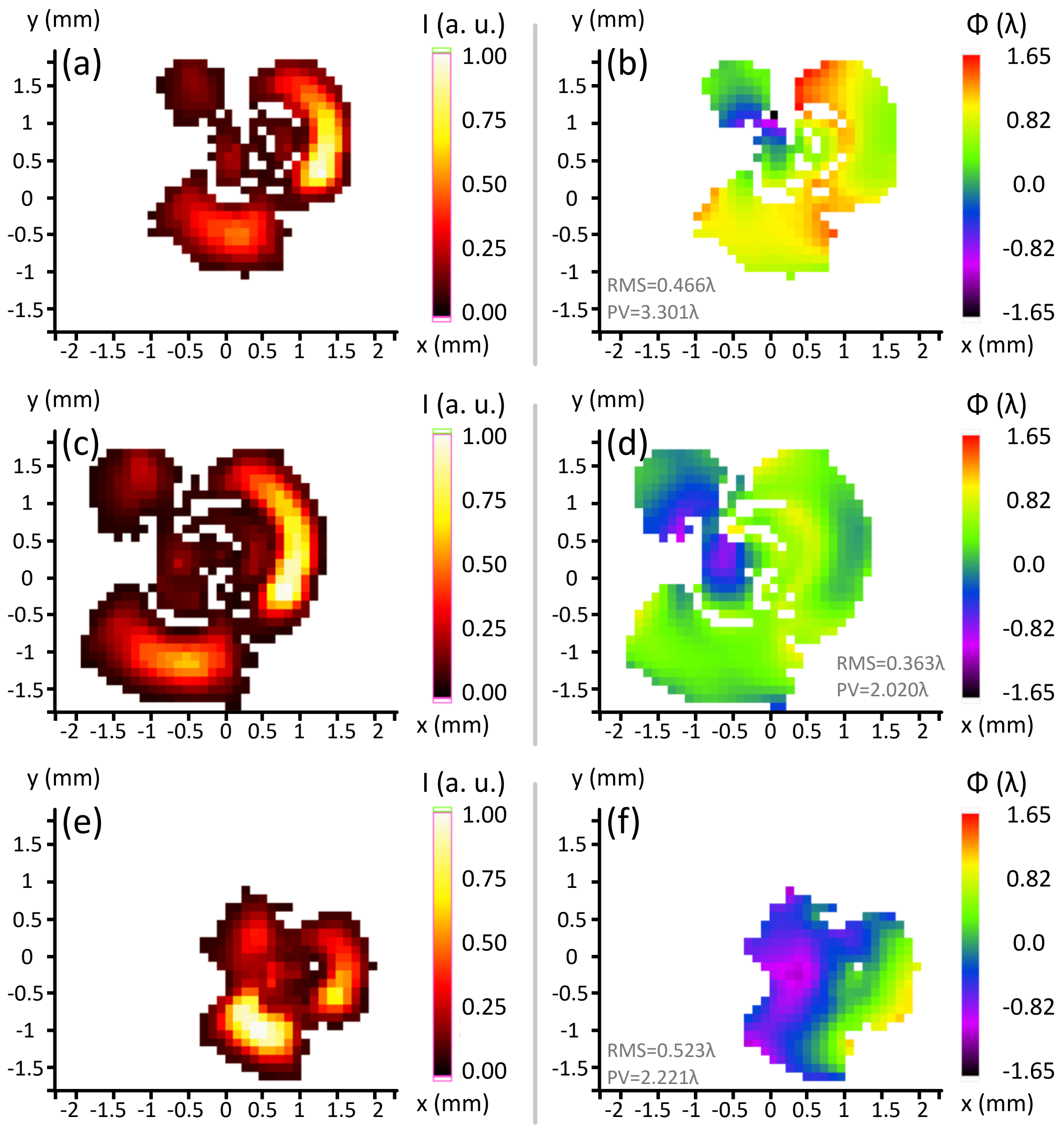

Figure 2.13: Intensity distributions and wavefronts of the blue beam after being focused by the Schwarzschild objective, measured in the far field at three stages of the alignment: at the beginning (a and b), during alignment (c and d), and at the end (e and f).

corresponding to only 6 pixels. Measuring the far-field wavefront and backpropagating it can provide higher resolution. This $90\,\mu\mathrm{m}$ size can be seen in figure 2.14 (c).

With the objective aligned with 400-nm light, the remaining step is to align it with XUV light. This, however, was put on hold due to the low energy available after the pinhole. This was due, firstly, to the small diameter of the pinhole instead, and secondly, due to the bad focusing of the KB mirrors (see figure 2.15), which would lead to hour-long acquisition times for each step of the alignment. The final alignment will be carried out in the Salle Corail laboratory, introduced in section 1.2.

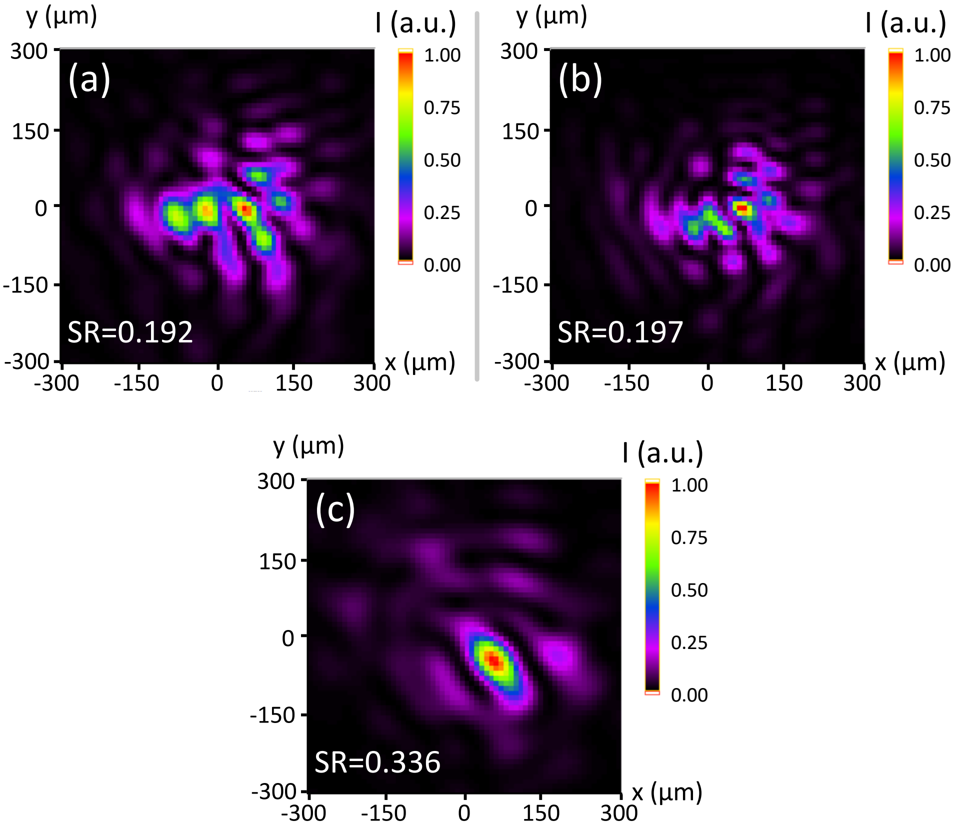

Figure 2.14: Calculated image of the pinhole illuminated with 400-nm light, at the initial position (a), during alignment (b), and at the end (c). The Strehl ratio for each case is also shown.

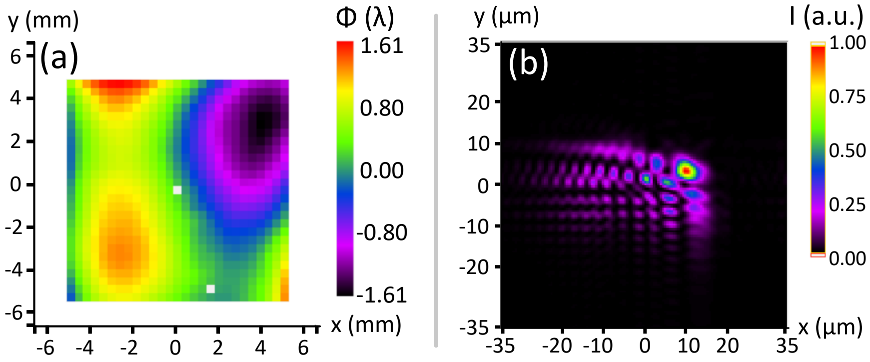

Figure 2.15: (a) Wavefront of the harmonic beam measured after focusing by the KB and (b) its calculated focal spot, with a Strehl ratio of 0.066. The wavefront has RMS and PV values of 0.794λ and 3.228λ, respectively.

2.2.3.3 Future work

The alignment of the objective is scheduled to be finished with high-harmonic radiation in the Salle Corail beamline of LOA during the year 2017. We observe that high-harmonics are generated much more efficiently in the new beamline, with more than three times the average power obtained in Salle Orange. This is mainly due to the fact that the new Ti:Sapphire laser provides an average power of $15\,\mathrm{W}$, more than twice the power provided by the old one, added to a better spatial quality. Thanks to this, the long acquisition times due to the energy losses caused by the pinhole will be significantly reduced.

Another way of increasing the harmonic energy arriving at the mirror is to use a bigger pinhole to create the reference beam. This can be done by turning the Schwarzschild around, so that the convex mirror (the SM) will be illuminated instead of the concave (the PM). In that case, the beam must have a 8.6-mm FWHM diameter at $864\,\mathrm{mm}$ from the pinhole, instead of $38\,\mathrm{mm}$ at a distance of $129\,\mathrm{mm}$. As a consequence, the maximum pinhole diameter required is now $4\,\mathrm{\mu m}$. In order to make sure that the SM is illuminated only by the central part of the Airy disk, a $2\text{-}\mathrm{\mu m}$ pinhole will be used, which transmits more than 40 times more energy than the previously used pinhole of diameter $0.3\,\mathrm{\mu m}$. Thanks to higher efficiency and larger pinhole diameter, the harmonic beam will not be focused on it, in order to reduce the number of optics and thus to simplify alignment.

Since the Schwarzschild objective is going to be inverted, the output beam is much more divergent than before. However, such a beam cannot be measured with the Hartmann WFS used so far, for two reasons: first and foremost, its low numerical aperture of $\mathrm{NA} = 0.01$ does not allow for measurement of highly divergent beams, and secondly, it must be attached to the vacuum chambers from the outside, so it cannot be approached to the objective as much as necessary.

Both problems are solved by the use of a new Hartmann XUV wavefront sensor recently prepared by LOA and Imagine Optic, which was calibrated in Salle Corail. This new sensor has a higher numerical aperture of $\mathrm{NA} = 0.1$, allowing for measurement of divergent XUV beams. Additionally, it can be put inside vacuum chambers, so it can be approached to the Schwarzschild as much as necessary in order to optimize the beam diameter on the Hartmann plate. The High-NA WFS is presented in figure 2.16. It is mounted on several motorized stages controlling position and tilt for under-vacuum alignment.

This sensor consists on a Hartmann plate attached to a Princeton Instruments PI-MTE 2048B CCD camera, with a resolution of $2048\mathrm{x}2048$ square pixels of side $13\,\mathrm{\mu m}$. The circular Hartmann plate, made of Ni, has a diameter of $32.5\,\mathrm{mm}$. It is placed $50\,\mathrm{mm}$ in front of the chip, and contains an array of square holes of side $50\,\mathrm{\mu m}$, separated by $150\,\mathrm{\mu m}$, and tilted by 25°.

The proposed setup for the alignment of the Schwarzschild objective in Salle Corail is presented in figure 2.17. The chambers will be slightly rearranged with respect to what was shown in section 1.2 to allow for the required pinhole-mirror distance. Additionally, the ceramic pinhole will block most of the IR radiation, and any IR passing through it will be filtered out with an Al filter.

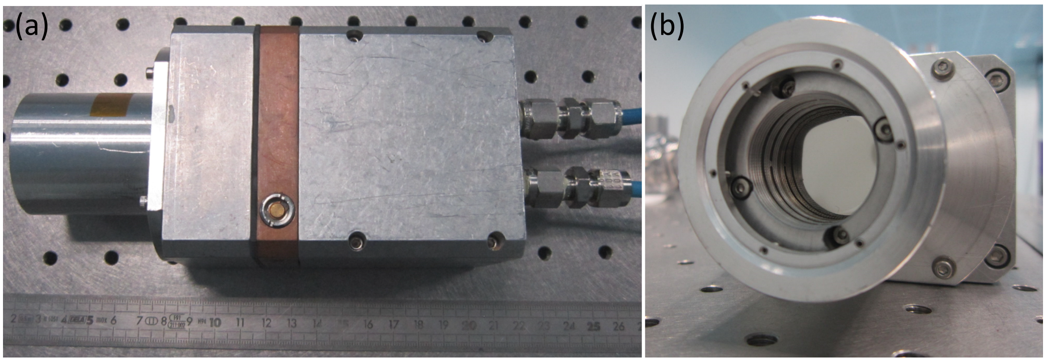

Figure 2.16: Pictures of the new high-NA wavefront sensor: (a) the complete sensor and (b) close-up of the Hartmann plate.

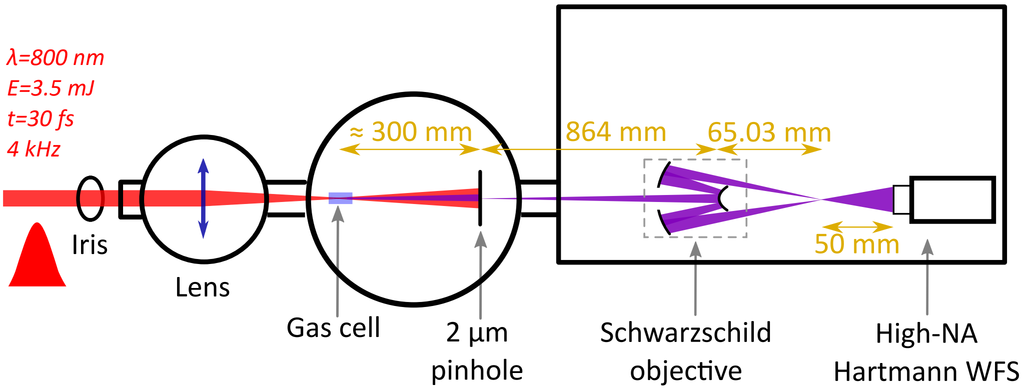

Figure 2.17: Schematic drawing of the setup for the future at-wavelength alignment of the Schwarzschild objective in the Salle Corail high-harmonic beamline.

2.3 Alignment of an XUV Wolter-like telescope by means of high -harmonic wavefront metrology

High-harmonic sources provide coherent, ultrashort pulses in the XUV and soft-X-ray spectral ranges. The average power obtained with HHG, however, is much lower than the one obtained in FELs. This higher power comes at the cost of much larger facilities, with high economic costs, and where beamtime is not as available for users. For these reasons, efforts have been made to improve the conversion efficiency of high-harmonic sources, which will in turn allow for research requiring high intensities to be carried out in tabletop setups.

One method of obtaining high intensity with a high-harmonic beam is using tight and efficient focusing. In this section, an experiment is reported in which our Hartmann wavefront sensor was used to optimize the focusing of the XUV Wolter-like telescope installed in the high-harmonic beamline at the LLC in Sweden (presented in section 1.3.2), vastly increasing the intensity at focus.

2.3.1 The XUV Wolter-like telescope

Traditional Wolter telescopes consist on a hyperboloidal and an ellipsoidal surface with the same axis of revolution [115], and are commonly used for X-ray astronomy due to the high theoretical resolution they can provide. The system described in this section is a Wolter-like telescope consisting instead on two toroidal mirrors, which are easier to polish [116, 117].

The Wolter-like telescope installed in this beamline, manufactured by Thales SESO, consists of two gold-coated toroidal mirrors used with a grazing angle of 10° to focus the high-harmonic beam. The mirrors are rectangular, with a size of $10\text{x}50\,\text{mm}^2$ each, providing $\text{NA} = 0.015$. The focal lengths of the mirrors are $\text{f} = 265\,\text{mm}$ for the first one and $\text{f} = 545\,\text{mm}$ for the second one, and their focal plane is located $164\,\text{mm}$ after the center of the second mirror. The mirrors are mounted on five motorized translation and rotation stages, allowing for alignment in vacuum. A drawing and a picture of the telescope are presented in figure 2.18, with the axes of movement highlighted as well. The axes will be referred to as follows:

- **X-Y movement**.
- **Rotation**: Changes the angle of incidence.
- **Twist**: Ensures that the mirrors are placed horizontally.
- **Tilt**: Ensures that the plane of incidence is kept horizontal.

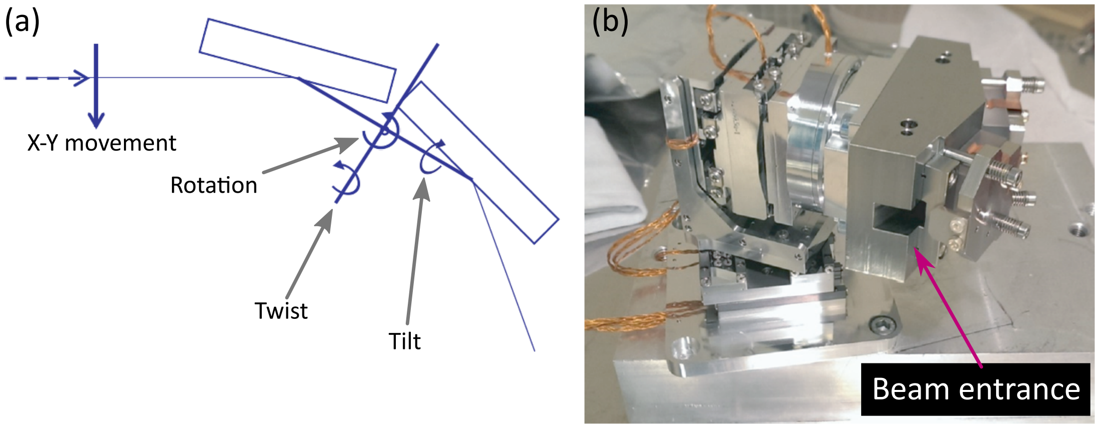

Figure 2.18: Schematic drawing (a) and picture (b) of the Wolter telescope used in this beamline. The motors responsible for the movement and rotation of the mirrors can be seen as well. The mirrors themselves are inside the metal casing.

2.3.2 Alignment optimization with the Hartmann wavefront sensor

In this experiment, the high-harmonic wavefront is measured with the XUV Hartmann sensor after the pulse is focused by the Wolter-like telescope. Then, the system is moved along each one of its axes in order to identify how each axis affects the pointing, beam shape and aberrations in its wavefront. Finally, the position along all axes is optimized to reduce those aberrations and, as a consequence, improve the focusing. This will lead to an improvement in the beam intensity at focus.

2.3.2.1 Experimental setup

The experimental setup used for these measurements is mostly the same used in the experiments reported in the previous chapter (see section 1.3.2.2). However, in this case the gold-coated mirror is rotated in such a way that the beam is propagated into the next chamber, where the telescope is located. The Hartmann sensor is now placed after its focal plane so that the focal spot can be studied by backpropagating the measured wavefronts. The setup is presented in figure 2.19. It must be noted that, due to experimental constraints caused by the vacuum chambers, the sensor had to be rotated by 18°. Nevertheless, this does not hinder the optimization.

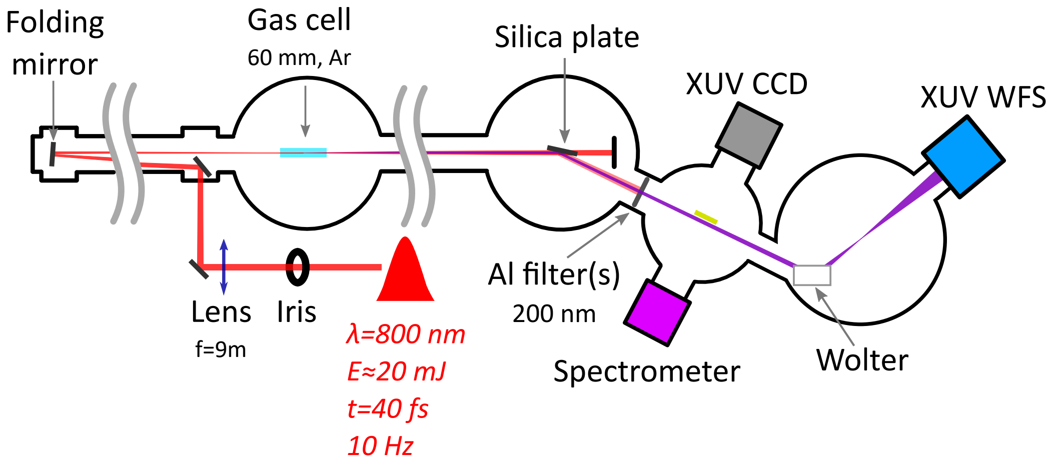

Figure 2.19: Schematic drawing of the experimental setup for the optimization of the Wolter-like telescope with the XUV Hartmann sensor.

2.3.2.2 Results of the optimization

As mentioned above, the idea behind the optimization is simply to measure the wavefront of the high-harmonic beam after it is focused by the Wolter-like telescope and adjust its position accordingly. If the wavefront is aberrated, the focusing will not be optimal, in which case the mirrors are moved or rotated in order to reduce said aberrations. Backpropagation allows for direct monitoring of the calculated focal spot, providing its size and its overall quality by means of its Strehl ratio. Five high-harmonic pulses are accumulated for every acquisition in order to mitigate the effects of shot-to-shot pulse variations, thus highlighting the wavefront changes induced solely by the optics.

The first wavefront, measured at the beginning of the experiment, is presented in figure 2.20. The beam was generated with an IR pulse energy of $28.2\,\mathrm{mJ}$, an iris diameter of $21.7\,\mathrm{mm}$ and a gas pressure of $192\,\mathrm{mbar}$, and one 200-nm thick Al filter is used. $\lambda = 42\,\mathrm{nm}$ is used for the wavefront reconstruction, and no intensity threshold is applied.

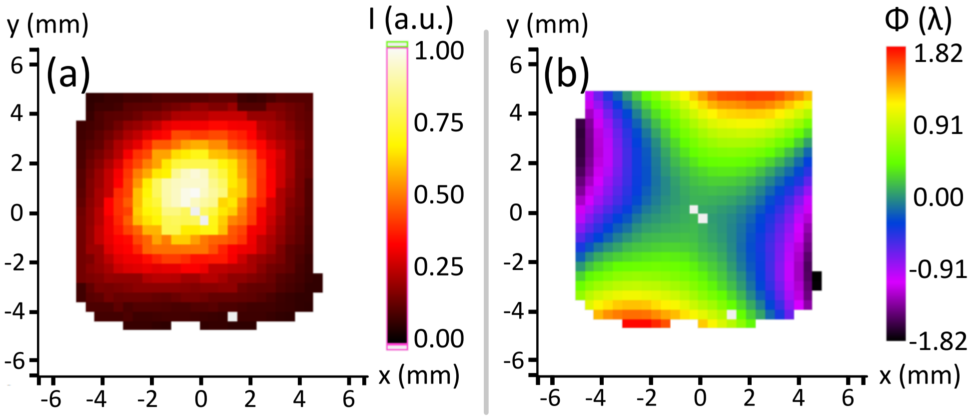

Figure 2.20: Intensity distribution (a) and wavefront (b) of the high-harmonic beam after being focused by the Wolter-like telescope, before optimizing its alignment.

The wavefront can be seen to be mainly astigmatic, with the angle of astigmatism being 14.5°. This angle is very close to the angle of 18° by which the sensor had to be rotated due to the vacuum chamber, which means that the most significant aberration is astigmatism at 0°. Its RMS and PV values are 0.752λ and 3.656λ, meaning that it is highly aberrated.

From this wavefront, we obtain that the sagittal focal plane is placed $631.0\,\mathrm{mm}$ before the WFS, with the tangential focal plane being placed at $635.5\,\mathrm{mm}$ before the WFS. The offset between them is thus $4.5\,\mathrm{mm}$. Both focii can be seen in figures 2.21 (a) and (b). Their shapes are lines with $48\,\mu\mathrm{m}$ length and $3\,\mu\mathrm{m}$ thickness (FWHM). In figure 2.21 (c), the beam is shown at $2.25\,\mathrm{mm}$ from both planes, with a Strehl ratio of only 0.026. The profiles, taken along the axes defined by the (a) and (b), reveal a FWHM size of $16.0\,\mu\mathrm{m}$ along one axis and $17.9\,\mu\mathrm{m}$ along the other.

Astigmatism at 0° is frequently obtained when a beam is focused with curved mirrors. Spherical mirrors, for example, create astigmatism in the direction of the plane of incidence whenever used out of normal incidence, since they only provide focusing in that direction. Toroidal mirrors, however, provide focusing in both directions. The offset between sagittal and tangential plane is thus caused by a misalignment of the system, and can be corrected. The system is moved along all five axes in order to verify how they affect the beam in terms of pointing, shape and wavefront.

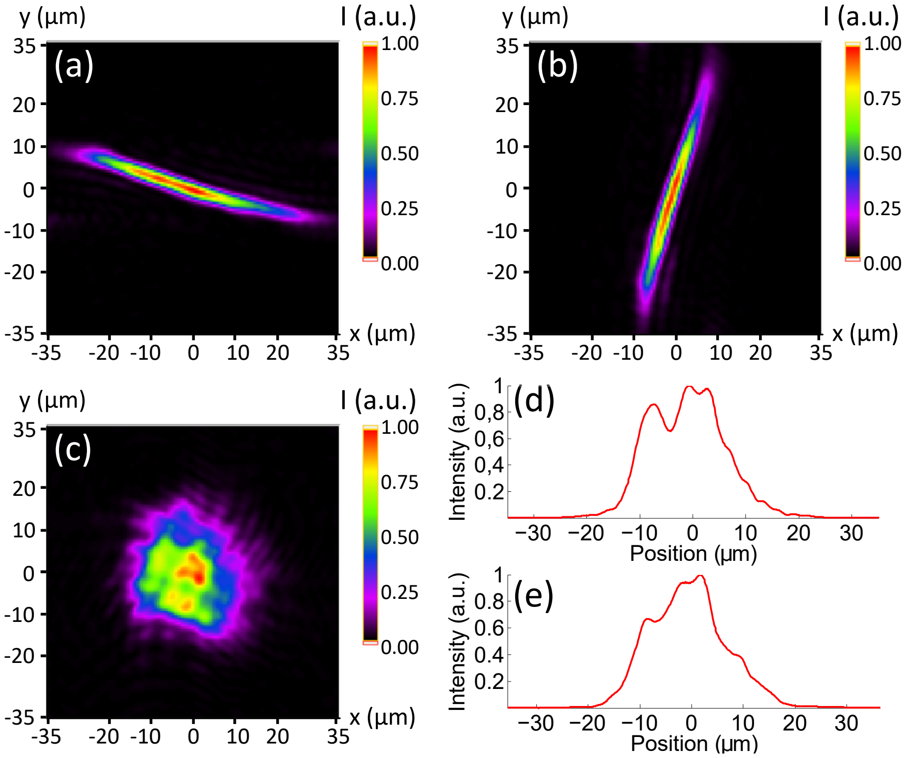

Figure 2.21: Focus of the system prior to optimization, calculated by backpropagating the wavefront measured before optimization: sagittal (a) and tangential (b) focii, and (c) focal spot between the previous two, including its profiles along both axes (d and e).

The system was first moved along its *tilt* axis. At each position, five wavefronts were measured, each of them after accumulating five harmonic pulses. In this scan, the stage was moved by 30 *steps* between measurements. Unfortunately, the motorized stages in charge of moving the optical system are open-loop systems, which means that there is not a constant step-to-angle equivalence or absolute positions, so the exact angle by which the telescope was rotated is not known. For this reason, the x axes of the curves shown in the following consist of numbered *positions* instead of steps. Increasing numbers always indicate movement along the same direction.

Figure 2.22 shows how moving the tilt axis affects several parameters of the wavefront. All data points and error bars represent average values and standard deviation, respectively, over the five independent wavefront acquisitions. Tilting the mirrors affects the beam pointing significantly, mostly in the vertical direction. This limits the range of movement, since the beam can easily be moved outside the WFS. This is the reason why only four positions were recorded before moving on to other axes of movement. In this range, the far-field beam shape does not change visibly, and is always slightly elliptical, similar to what was shown above (see figure 2.20).

The average RMS and PV values of the measured wavefronts are presented in figures 2.22 (a) and (b). Both values decrease by approximately 30% in the range of movement studied. Figures 2.22 (c) and (d) present the RMS and PV values of the *residual* wavefront, with astigmatism at $0°$ and $45°$ ruled out. These parameters show smaller variation, which means that aberrations like coma and third order spherical aberration are also affected by the mirror tilt, albeit more slightly. Additionally, they only cause an RMS error of approximately $\lambda/11$, with astigmatism being the main aberration present on the focused beam. Some slight coma at $0°$ is also present. The evolution of astigmatism with tilt can be seen in figure 2.22 (e), and is responsible for 90% of the RMS error present in the wavefront. The angle of astigmatism is shown in figure 2.22 (f), and its values being so close to $0°$ indicate that astigmatism at $45°$ is negligible compared to $0°$. The small variation of this angle with tilt indicates that astigmatism at both $0°$ and $45°$ are reduced by a similar factor by moving the tilt in the studied range. Note that the angle by which the Hartmann WFS was rotated when installed in the setup has been taken into account when calculating the angle of astigmatism.

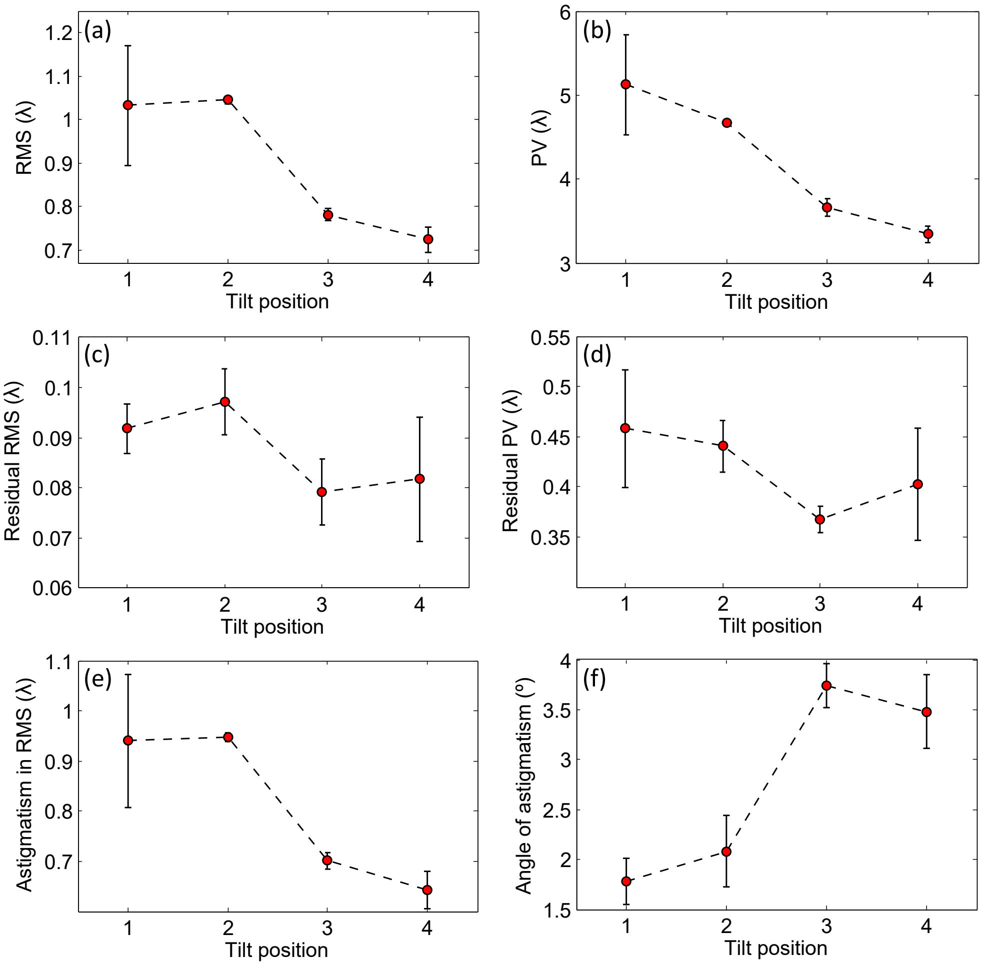

Figure 2.22: Evolution of the harmonic wavefront when the system is moved along the tilt axis: (a) wavefront RMS, (b) wavefront PV, (c) residual RMS, (d) residual PV, (e) contribution of astigmatism to the overall wavefront RMS, and (f) angle of astigmatism.

When optimizing the Wolter-like telescope, it is important to pay attention not only to the wavefront, but also to the parameters describing the focal spot calculated by back-propagation. Some of this parameters, and its variations with the tilt of the system, are included in figure 2.23. In particular, the FWHM size of the focal spot is presented in figures 2.23 (a) and (b). Before the focusing is optimized, the spot is visibly elliptical, and its size is reduced in both its minor and major axes when the wavefront is improved. This also involves an improvement of its Strehl ratio, as shown in figure 2.23 (c). While the Strehl ratio values are still quite low, an improvement of a factor of 2.5 was achieved by moving the tilt. Another key parameter to look at when optimizing the focus is the distance between the sagittal and tangential focal planes, presented in figure 2.23 (d), which should be as close as possible to $0\,\mathrm{mm}$, in the optimal case. All these parameters are good indicators that the focusing quality has been improved after the tilt was changed.

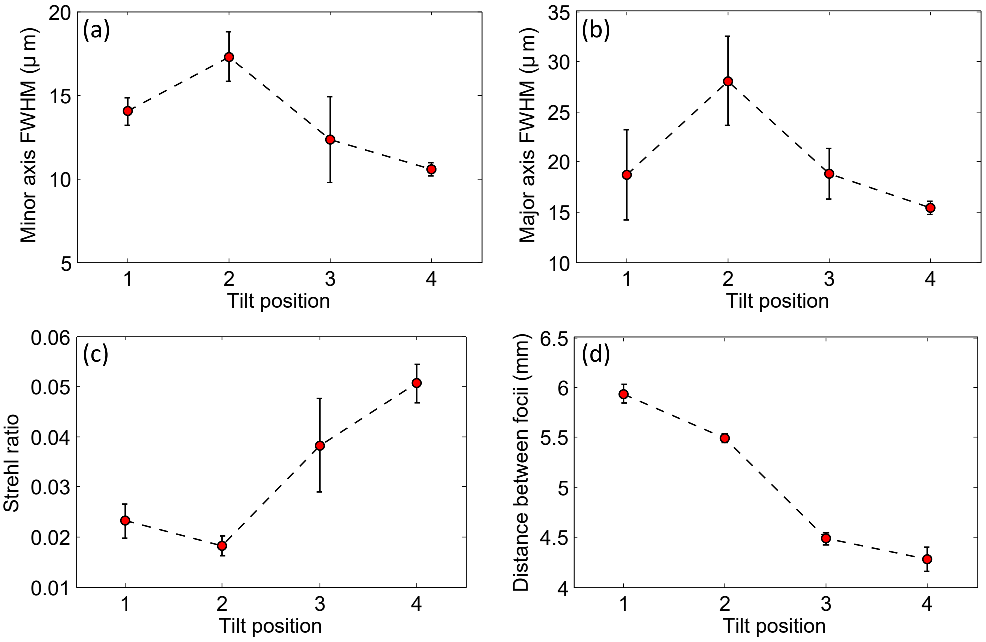

Figure 2.23: Evolution of the focal spot when the system is moved along the tilt axis: (a) FWHM diameter along the minor and (b) major axes, (c) Strehl ratio, and (d) distance between the sagittal and tangential focal planes.

Next, the *rotation* movement is optimized. This axis has a very large effect on the beam shape, its ellipticity in particular, and its wavefront, mainly its astigmatism, even for small movements that have very little effect on the beam pointing. Unfortunately, the positioner that provides this movement suffers high backlash, so a particular position is not easily retrieved again after moving the telescope away from it.

The effect of this movement on several wavefront parameters can be seen in figure 2.24, again averaged over five acquisitions for each case. It is clear from the RMS and PV curves, in figures 2.24 (a) and (b), that this movement has a very significant impact on the reflected wavefront, with both parameters being reduced by a factor of 6 between the worst position and the optimal one. The RMS and PV values of the residual wavefronts are presented in figures 2.24 (c) and (d), and show that, while it is expected to affect astigmatism, it also has a noticeable effect on other aberrations, with the RMS varying by a factor of 2.5 on the studied movement range. Coma at 0° is still present, even in the best case. From figure 2.24 (e), astigmatism can be seen to be much more significant than all the other aberrations. As with the tilt scan shown above, the variation of RMS with movement is essentially due to the variation of astigmatism, with the other aberrations playing a much smaller role. Figure 2.24 (f) presents the angle of astigmatism, which also shows large variations when rotating the telescope, with the angle being changed by almost 70° in the studied range. From the curve, it is also apparent that the least aberrated wavefront also presents very little astigmatism at 45°.

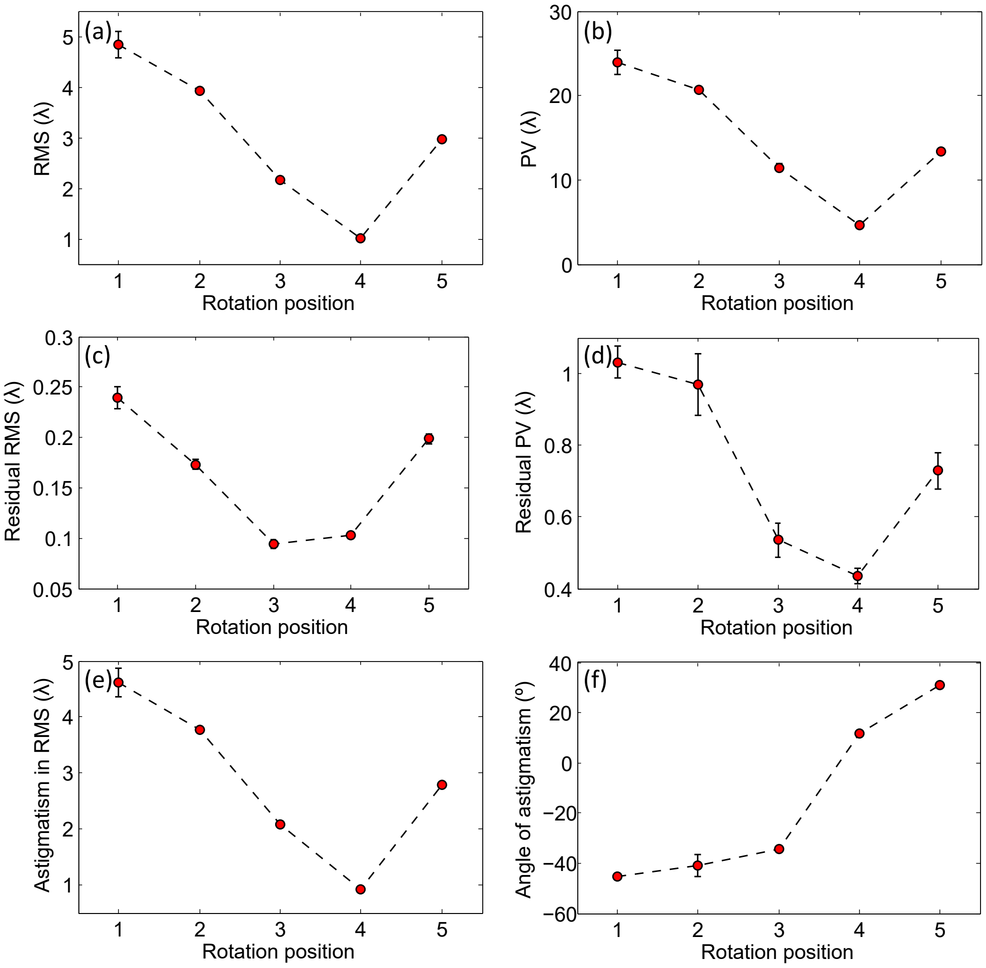

Figure 2.24: Evolution of the harmonic wavefront when the system is moved along the rotation axis: (a) wavefront RMS, (b) wavefront PV, (c) residual RMS, (d) residual PV, (e) contribution of astigmatism to the overall wavefront RMS, and (f) angle of astigmatism.

The effect of the rotation movement on the focus properties can be seen in figure 2.25. The size of the focal spot, in figures 2.25 (a) and (b), is of course the smallest for the position providing the least aberrated wavefront. The diameter in both directions was changed by a factor of more than 4. These two curves are in fact very similar to those of RMS and PV. The Strehl ratio, in figure 2.25 (c), shows the opposite trend, but with a much higher variation, up to a factor of 10 between the best and worst cases. Figure 2.25 (d) presents the distance between focal planes with rotation, again showing a similar trend, with the lowest distance corresponding to the highest Strehl ratio and the smallest size at focus.

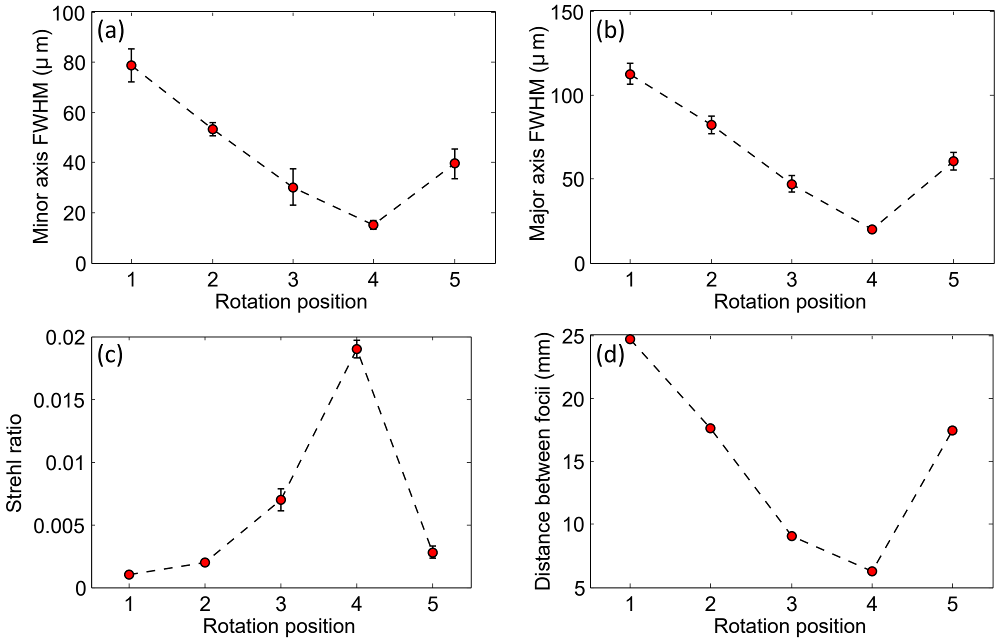

Figure 2.25: Evolution of the focal spot when the system is moved along the rotation axis: (a) FWHM diameter along the minor and (b) major axes, (c) Strehl ratio, and (d) distance between the sagittal and tangential focal planes.

After studying the effects of tilt and rotation, the *twist* movement is explored next. It was seen from the previous curves in both movement scans that the wavefront and focus parameters do not vary significantly between acquisitions, as shown by the small size of the error bars in most curves. Based on this, and in order to save time, only one five-shot wavefront was measured for each twist position. The beam pointing changed very slightly along the vertical direction during these measurements, and the beam shape remained almost circular as well.

The wavefront properties as a function of the twist movement are presented in figure 2.26. Figures 2.26 (a) and (b) show a similar trend for both RMS and PV. Although the twist axis does not have such a large impact on the wavefront RMS as the rotation movement does, the RMS was largely improved, from a value of 1λ to $\lambda/4$. However, the RMS and PV of the residual wavefront, in figures 2.26 (c) and (d), do not show a clear trend, and keep similar values throughout the scan. Astigmatism was almost entirely eliminated from the wavefront, as evidenced by figure 2.26 (e). In the cases where astigmatism is the lowest, the other aberrations are actually more important to the overall wavefront RMS. With astigmatism being so low, an angle of astigmatism cannot be calculated, hence why its values are not shown in this case.

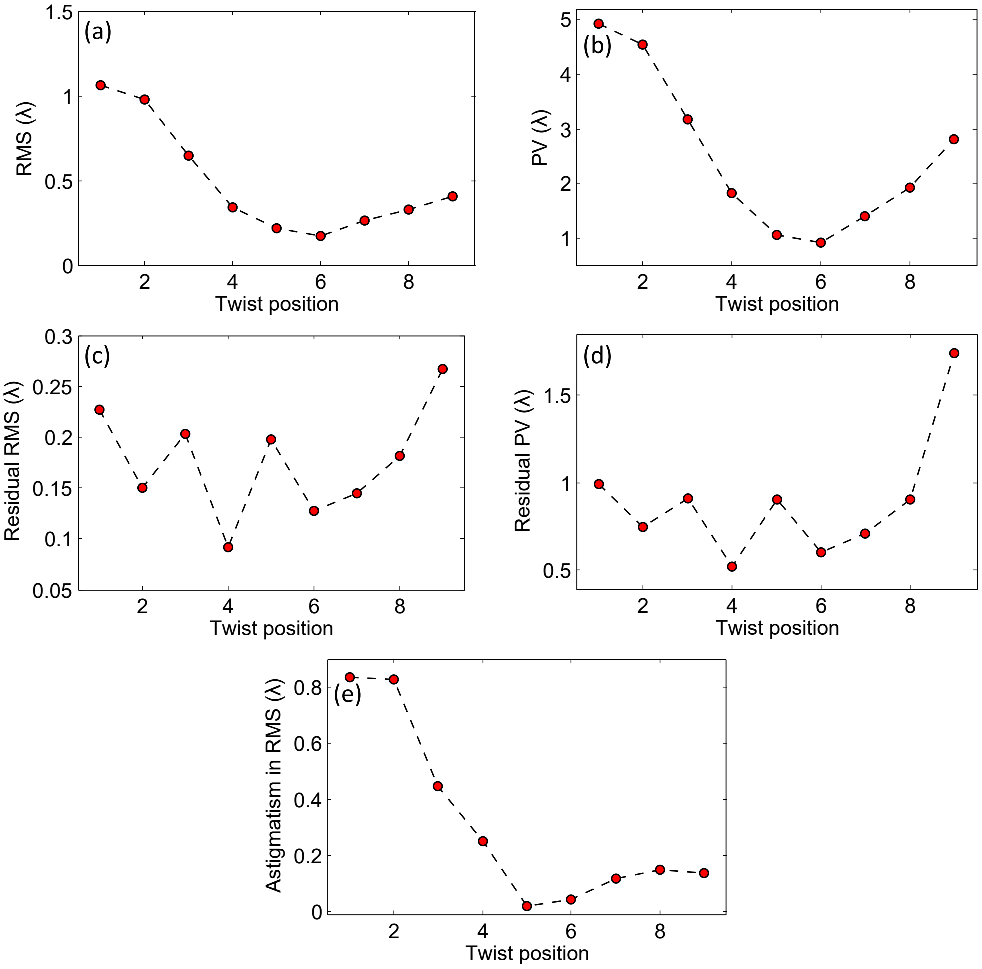

Figure 2.26: Evolution of the harmonic wavefront when the system is moved along the twist axis: (a) wavefront RMS, (b) wavefront PV, (c) residual RMS, (d) residual PV, (e) contribution of astigmatism to the overall wavefront RMS, and (f) angle of astigmatism.

Lastly, the effects of the twist movement on the focusing are summarized in figure 2.27. The FWHM size of the focus along both axes, presented in figures 2.27 (a) and (b), both follow similar trends to the RMS and PV shown above, as expected. Moreover, both values become very similar, indicating that the focal spot becomes circular. The Strehl ratio is also seen to improve very significantly in figure 2.27 (c), going from a starting value of 0.03 to a maximum of 0.687. The distance between focal planes is presented in figure 2.27 (d), and also shows significant improvements, with its lowest value being $0.93\,\mathrm{mm}$.

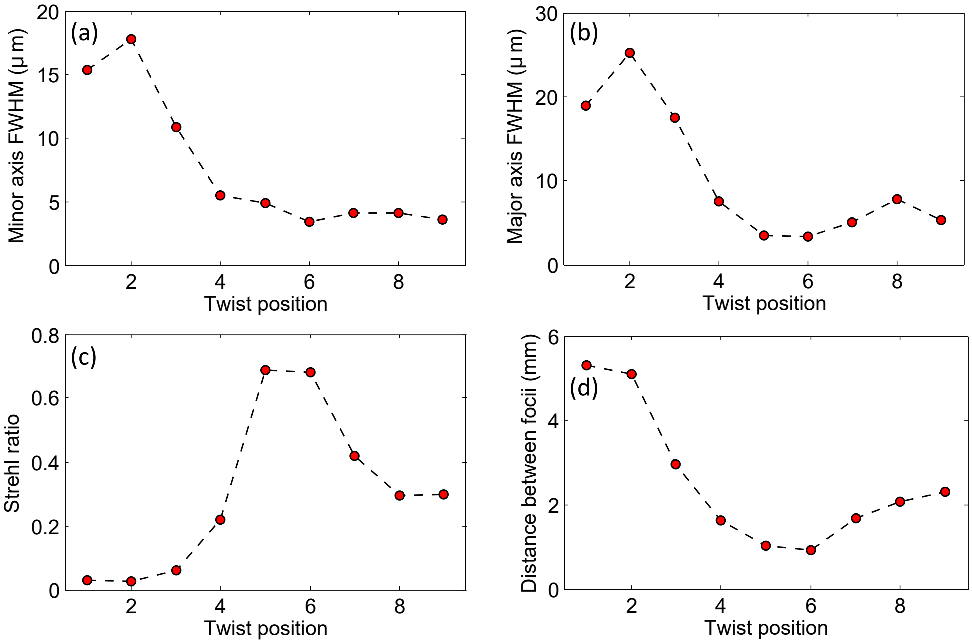

Figure 2.27: Evolution of the focal spot when the system is moved along the twist axis: (a) FWHM diameter along the minor and (b) major axes, (c) Strehl ratio, and (d) distance between the sagittal and tangential focal planes.

Moving the system along the X axis changes the pointing horizontally. The beam is easily moved out of the Hartmann WFS, with small changes to the wavefront. The Y axis has a similar behavior along the vertical direction. The intensity pattern, wavefront and calculated focal spot obtained after optimizing the system position along every axis is presented in figure 2.28. The wavefront has $\mathrm{RMS} = 0.119\lambda \simeq \lambda/9$ and $\mathrm{PV} = 0.547\lambda$. The calculated focal spot is now circular and Gaussian, and has a FWHM diameter of $3.39\,\mu\mathrm{m}$, and a Strehl ratio of 0.710. Some astigmatism is still present in the wavefront, but is low enough to not significantly hinder the focusing. The wavefront still has some coma at $0°$.

The spot size at focus was decreased approximately by a factor of 5 with respect to the initial measurement. This, in turn, means that the intensity at focus was increased 25 times after the alignment was optimized. Additionally, the Strehl ratio was increased 27 times, vastly improving the spatial quality of the focal spot. The focus, however, is still not perfectly Gaussian and shows some defects due to the remaining wavefront aberrations. These aberrations found after focusing are most likely caused by the aberrated wavefronts produced in the HHG process itself, studied in detail in section 1.3.2, which generally presented some coma as well. The high-harmonic beams generated in this beamline were shown to carry significant astigmatism at $0°$. Rotating the Wolter-like telescope along its three axes was shown to have a very large effect on the astigmatism of the reflected beam, which was effectively eliminated during the optimization. However, reducing other aberrations such as coma, third order spherical aberration and high-order aberrations is not as straightforward. Further improving the focal spot requires generating harmonic pulses with better wavefronts.

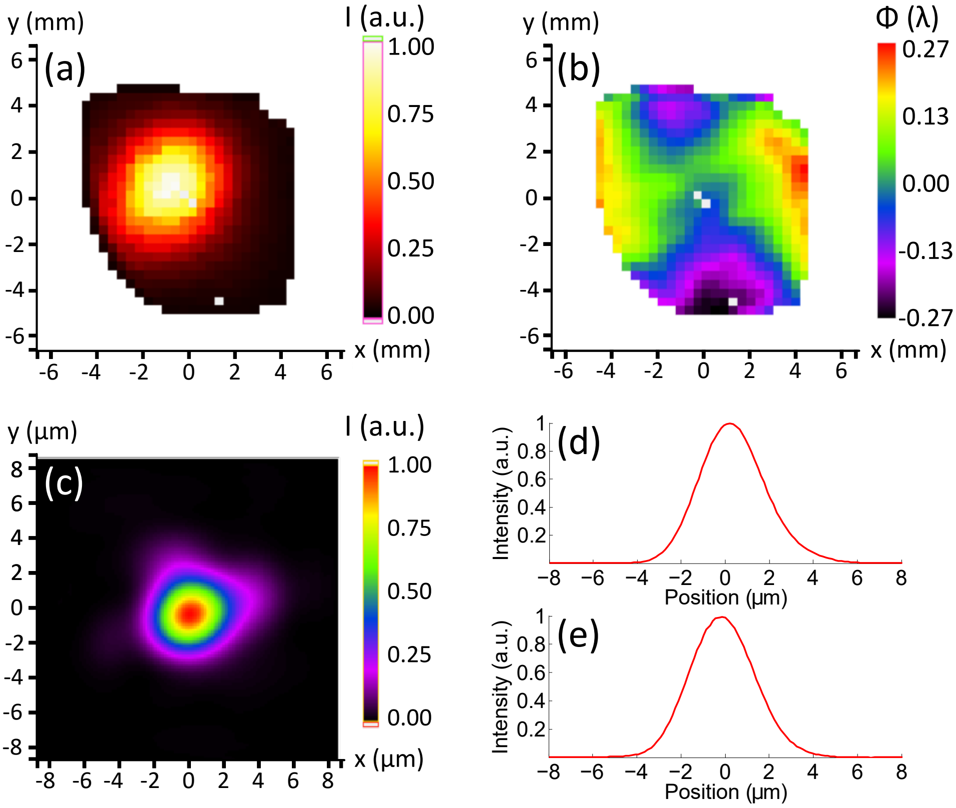

Figure 2.28: High-harmonic beam measured after optimizing the alignment. Intensity distribution (a), wavefront (b), and calculated focus (c), with its profiles along the axes defined in figure 2.21 (d and e). Five pulses were accumulated for this measurement.

2.3.3 Further optimization by using the deformable mirror for the driving laser

In section 1.3.3, an experiment was reported in which a deformable mirror was placed on the IR beam path in order to study the influence of the IR wavefront on the HHG process. Since the conditions for HHG were changed during that experiment due to the use of the DM, the alignment of the Wolter-like telescope was reoptimized after it was finished, in order to compensate for the changes in beam pointing, shape, and wavefront. The modified experimental setup is illustrated in figure 2.29, now including the DM and the Shack-Hartmann IR WFS connected to it. The Hartmann WFS is now correctly placed without any tilt, thanks to the use of different adapters on the vacuum chamber.

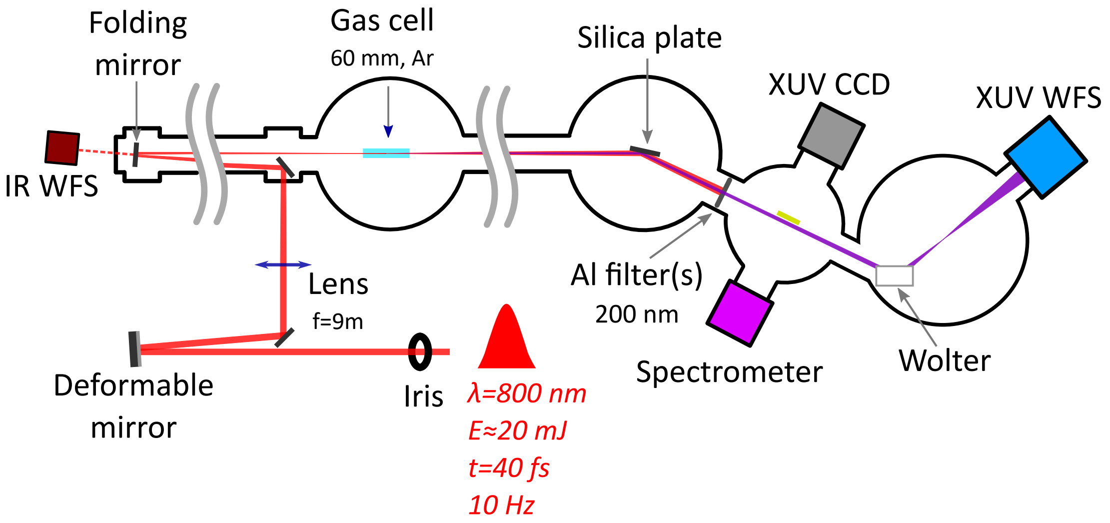

Figure 2.29: Schematic drawing of the experimental setup for the optimization of the focus of the Wolter-like telescope with the deformable mirror for the driving IR beam. The XUV Hartmann sensor is kept in the same position.

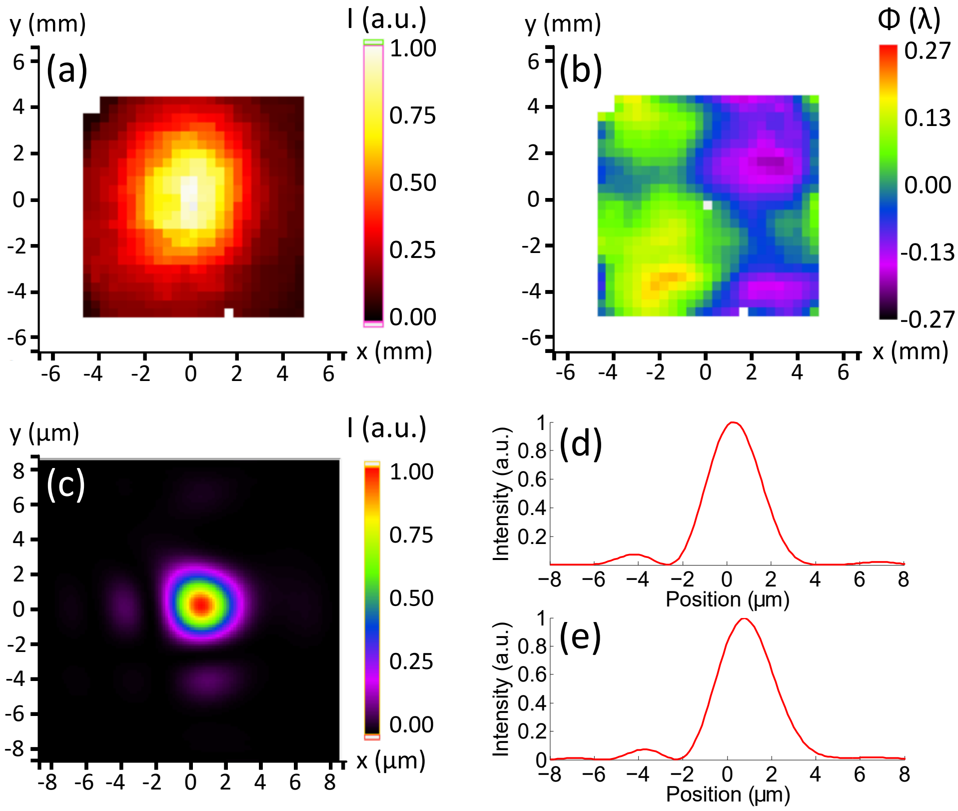

Figure 2.30: Single high-harmonic pulse measured after reoptimizing the alignment. Intensity distribution (a), wavefront (b), and calculated focus (c), with its profiles along the axes defined above (d and e).

Figure 2.30 presents the best single-shot wavefront and smallest focal spot obtained after reoptimizing the alignment along every axis of movement and using the DM to further reduce aberrations. The gas pressure was $196\,\mathrm{mbar}$, the IR energy was $30\,\mathrm{mJ}$, and the iris diameter was $20\,\mathrm{mm}$. A single 200-nm-thick Al filter was used. The measured wavefront has $\mathrm{RMS} = 0.091\lambda = \lambda/11$ and $\mathrm{PV} = 0.384\lambda$. It is almost completely free of astigmatism, and some coma at 0° can be seen. It is presented using the same color scale as the one shown in figure 2.28, for easier comparison. The focal spot has a Strehl ratio of 0.831, and its FWHM diameter is $2.84\,\mu\mathrm{m}$ along both axes, meaning that its area was further reduced by a factor of 1.5. Although some energy is found outside the main focal spot, it is smaller and of higher quality than the one achieved without the use of the DM.

In the previous section, it was shown how the Wolter-like telescope can be used to eliminate astigmatism both at 0° and at 45° fairly easily, but its effect on other aberrations such as a coma or third-order spherical aberration was not as straightforward, making them more difficult to correct with the optics. In this case, instead of using the optics to correct these aberrations, the DM was be used to generate high-harmonic beams with less aberrations, allowing for better focusing.

2.4 Summary

Development of high-quality XUV optical systems will lead to better resolution in nano-scale imaging applications, as well as lower data acquisition times thanks to higher efficiencies. In order to provide good reflectivity, imaging and focusing systems for XUV radiation must use mirrors in grazing incidence, such as the Wolter-like telescope shown here, or multilayer mirrors, such as the Schwarzschild microscope objective, where the mirrors are used close to normal incidence. At-wavelength defect characterization is important for multilayer XUV optics since it provides more resolution than characterization with, for example, He-Ne lasers. Synchrotrons are necessary in order to perform such measurements due to the high flux required by techniques such as PDI. In this chapter, the use of an XUV Hartmann wavefront sensor for at-wavelength measurement of the surface of the primary mirror of an XUV Schwarzschild microscope objective has been reported. Since this technique does not require high pulse energies, it can be performed in a tabletop setup with high-harmonic radiation. The measurement results show good agreement with ray-tracing simulations, thus confirming the high quality of the mirror under test.

The optical system, however, must be correctly aligned to provide its best imaging or focusing performance. A direct measurement of a focal spot with a diameter of a few microns cannot, in general, be taken by directly placing a CCD camera on the focal plane due to the focus being typically smaller than the pixel size, and the possibility of damaging the device if the intensity is too high. XUV focal spot measurements are commonly made by placing a scintillator crystal, such as Ce:YAG, in the focal plane. The crystal then emits visible light through fluorescence, and its image is taken with a microscope in order to measure the spot size. The accuracy of this scheme, however, is limited by the appearance of nonlinear effects in the crystal, as well as saturation.

Our XUV Hartmann sensor has been proven to be a useful tool for measurement of focused beams, by backpropagation of wavefronts measured some tens of centimeters after the focal plane. It can thus be used for optimizing the alignment of focusing optics in real time with excellent results. In this chapter, the sensor was used to optimize alignment of an XUV Wolter-like telescope based on two toroidal mirrors, reducing the focus diameter by a factor of more than 5, and thus the intensity at focus by almost 30, in a process that can take only a few minutes, depending on the initial alignment.

CHAPTER 3

Application of high harmonics to probing warm dense matter

Contents

One of the many applications of XUV pulses, and high harmonics in particular, is plasma diagnostics. Similarly, they can also be used to probe warm dense matter (WDM) states. WDM is a transient state of matter between condensed matter and hot plasma in terms of density and temperature [118, 119]. WDM states are typically defined as those with a solid density $(1-10\,\mathrm{g/cm^3})$ and a moderate electron temperature $(10-100\,\mathrm{eV})$ [120], thus simultaneously too cold and dense to be described by plasma physics, and too warm to be described condensed matter physics. It is present in fields such as astrophysics [121, 122], material science [123] or inertial confinement fusion [124].

In this chapter, an experiment is reported in which high harmonics were used to probe the absorption properties of warm dense aluminum at XUV wavelengths. In section 3.1, the general characteristics of WDM are briefly presented, then section 3.2 shows the obtained results, which have been published in [125].

3.1 General properties of warm dense matter

WDM is described by a combination of the Coulomb binding forces that describe solids and the thermal motion of particles that occurs in classical plasmas. The so-called *strong coupling parameter* is often used to characterize the state of a sample [119]. It expresses the ratio between the ion-ion Coulomb potential and the thermal energy within the sample:

$$\Gamma_{\mathrm{ii}} = \frac{(\mathrm{Z}^{*}\mathrm{e})^2}{\mathrm{R_i k T_i}}, \quad \mathrm{R_i} = \left(\frac{3\mathrm{Z}}{4\pi \mathrm{n_i}}\right)^{1/3}, \tag{3.1}$$

where $\mathrm{Z}^*\mathrm{e}$ is the average ionic charge, $\mathrm{R_i}$ is the average ion-ion separation, k is Boltzmann's constant, $\mathrm{T_i}$ is the ion temperature, Z is the atomic number of the ions, and $\mathrm{n_i}$ is the ion density. Three states can be defined depending on the value of Γ_{ii}:

- $\Gamma_{\mathrm{ii}} \gg 1$ indicates condensed matter, with strong ion bounds.
- $\Gamma_{\mathrm{ii}} \ll 1$ means weak ionic bounds, so that the thermal energy of the particles is much more prevalent.
- $\Gamma_{\mathrm{ii}} \simeq 1$ is found in a warm dense state, where both effects are similarly significant.

Figure 3.1 shows the different states of an aluminum sample as a function of its temperature and density. Several values of Γ are highlighted. Additionally, partial electron degeneracy can occur in WDM states with high density or low temperature. In such cases, the coupling parameter must be modified to include quantum effects which alter the Coulomb potentials present in the sample, stemming from Pauli exclusion principle, in turn due to the fermionic nature of the electrons. More information about this topic can be found in [118, 126].

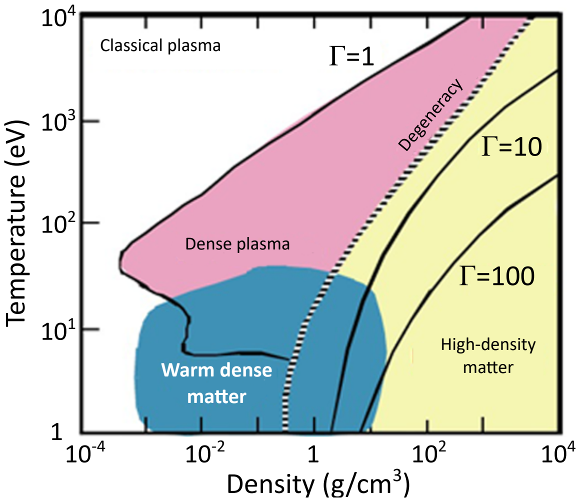

Figure 3.1: States of aluminum as a function of its temperature and density. Three values of the strong coupling diameter are highlighted. Quantum effects are significant in the region at the right of the degeneracy line. Taken from [126, 127].

Many of the properties of WDM can be observed experimentally, such as the equation of state [128], its electrical and thermal conductivity [129] or its microscopic structure [130]. Due to the short lifetimes of WDM states, optical methods provide a valuable tool for probing these properties. However, if the photon energy of a probe beam is lower than the plasma frequency of the sample, it will be reflected. For this reason, the use of XUV and X-ray pulses is required to penetrate a warm dense sample sample due to its high density. Plasma frequency is defined as:

$$\omega_p = \sqrt{\frac{n_e e^2}{m_e \epsilon_0}}, \tag{3.2}$$

where $\epsilon_0 = 8.854 \cdot 10^{-12}\,\mathrm{F/m}$ is the vacuum permittivity, and n_e, e, and m_e are the electron density, charge and mass, respectively. For example, for a warm dense sample with $n_e = 10^{22}\,\mathrm{cm}^{-3}$, a probe wavelength lower than $100\,\mathrm{nm}$ must be used.

The absorption of XUV light by a warm dense sample is another macroscopic property that can provide information about the behavior of its electrons. The *absorption coefficient* α provides the rate of attenuation of the intensity of light in the sample per unit length. Indeed, a probe beam with initial intensity I_0 traveling through a sample of width l will have a final intensity of $I = I_0 e^{-\alpha l}$. Photons are generally absorbed in electronic transitions within the material. Three types of electronic transitions can occur depending on the initial and final states of the electron: bound-bound transitions, in which the electron leaps between two bound states with different energies, bound-free transitions, i. e. ionization, or free-free transitions by means of *inverse bremsstrahlung*, also referred to as *collisional absorption*. The probability of each of these processes depends on the temperature, density and ionization state of the sample, and thus the value of α, which can be calculated from transmission measurements, may vary upon heating it to warm dense states [126]. In the experiment described in the following section, the probing wavelengths are chosen so that only free-free absorption occurs.

Furthermore, due to the short lifetimes of WDM states, any experiment designed to probe their properties must do so in a short time frame, typically below a few hundreds of picoseconds upon heating, after which the sample expands and cools. For this reason, producing a suitable warm dense sample requires rapid and homogeneous heating, which in turns leads to the need for small samples. Some methods to generate WDM are based in irradiation of the sample with energetic ions [131], compressing it with laser-driven shocks [132, 133] or heating it radiatively with hard X-ray radiation [120]. In the latter scheme, the X-rays are generated by a hot dense plasma with a high ionization state, created by irradiating a foil target with an intense laser pulse ($\mathrm{I} \simeq 10^{15}\,\mathrm{W/cm^2}$). The generated radiation has a similar duration as the driving pulse, and is used to homogeneously heat a sample to a warm dense state [126]. The energy conversion efficiency is typically a few percent [134, 135, 136].

3.2 Experimental measurements of collisional absorption of XUV radiation in warm dense aluminum

The study of collisional or free-free absorption of XUV radiation by a warm dense sample is a way of obtaining information about the microscopic processes occurring within it, such as the electron-ion collision rate. There are, however, several different numerical models describing free-free absorption of XUV radiation in WDM which provide different behaviors of absorption as a function of sample temperature. Two of those models are the weak scattering model by S. Vinko *et al.* [137] and the corrected classical model by C. A. Iglesias [138]. Experimental measurements of the absorption coefficient of WDM could help clarify which model is more accurate.

In this section, an experiment is reported in which HHG was used to measure the absorption of warm dense aluminum at XUV wavelengths, in order to compare the obtained result with previous experiments and the aforementioned numerical models. The experiment was carried out at the Vulcan laser system [139], at the Central Laser Facility (CLF) of the Rutherford Appleton Laboratory (RAL), in the United Kingdom, as the result of a collaboration between Queen's University Belfast (QUB) in the United Kingdom, the Instituto Superior Técnico (IST) in Portugal, and LOA.

3.2.1 Experimental setup

A pump-probe scheme is implemented in order to study the absorption of XUV photons with an energy of $25.88\,\mathrm{eV}$ by warm dense aluminum, heated to an electron temperature of $\mathrm{T_e} \simeq 1\,\mathrm{eV}$. The photon energy is higher than the plasma frequency of the heated targets ($\simeq 15$-eV photons), but lower than its L-edge ($72.6\,\mathrm{eV}$) [61]. As a consequence, free-free absorption is the dominant mechanism.

Figure 3.2 shows the experimental setup around the target. The aluminum sample foil is supported by a thin steel frame, and placed at a $45°$ angle between two 100-nm-thick palladium-coated CH plastic foils, at a 1-mm distance each.

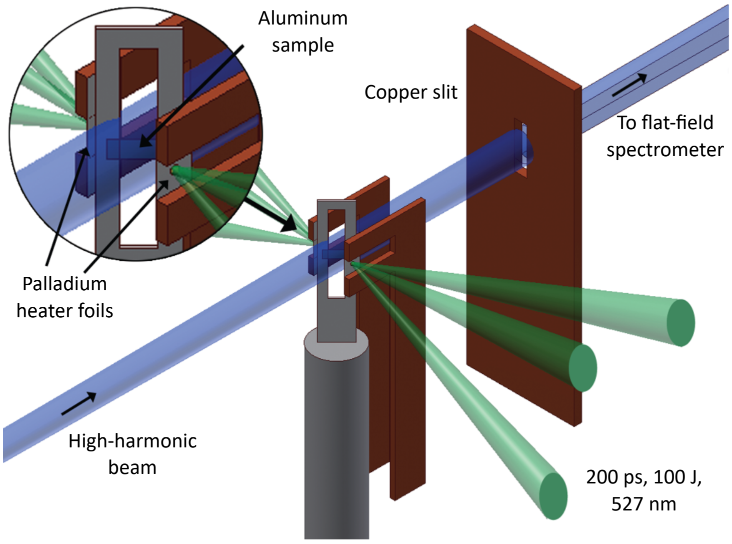

Figure 3.2: Experimental setup around the target. The two palladium-coated CH foils are placed at 1 mm from the aluminum sample, which is rotated by 45°. The sample is heated by laser-driven hard X-rays, produced by focusing three intense pulses in each target. Then, the high-harmonic probe pulse is propagated through the heated sample towards a spectrometer.

The target is heated by irradiating it with laser-generated hard X-rays [120]. In order to generate this radiation, three laser pulses (the *pump* pulses) are focused simultaneously on each of the palladium foils, to an intensity of $\sim 2 \cdot 10^{15}\,\mathrm{W/cm^2}$ in elliptical, flat top focal spots of size $220\text{x}200\,\mu\mathrm{m}$. They are produced by frequency doubling of the pulses from the Nd:glass laser at the Vulcan facility. Their wavelength, duration and energy are $527\,\mathrm{nm}$, $200\,\mathrm{ps}$, and $100\,\mathrm{J}$, respectively. The incident energy is converted into M-L band hard X-rays, with photon energies in the $3\text{-}3.5\,\mathrm{keV}$ range. The CH backing, placed in the non-irradiated side of the target, suppresses the lower-energy photons which would be primarily absorbed in the sample's surface, leading to inhomogeneous heating. The efficiency of the X-ray generation process in this setup is approximately 4% [120, 135].

It must be noted, however, that each aluminum sample has a uniform surface layer of a few nanometers of oxide, as well as a few nanometers of organic surface contamination that must be taken into account. Additionally, despite the rapid radiative heating, the outer edges of the sample will begin to decompress during heating. These surface factors are assumed to be identical for every sample, since they were all manufactured at the same time and in the same environment by the RAL Target Fabrication department. Thus, different sample thicknesses must be probed, since the differences in transmission will be due exclusively to the different thickness of warm aluminum. Two different thicknesses were used for the warm dense aluminum absorption measurements: 218 and $418\,\mathrm{nm}$. Cold, 838-nm-thick samples were also used for absorption measurements. The thickness of the samples is known to $\pm 5\,\mathrm{nm}$.

The volumetric heating creates a core of solid-density warm dense aluminum in the target, which is then *probed* by an ultrashort high-harmonic pulse, generated by a seventh laser pulse with a duration of $\sim 1.5\,\mathrm{ps}$. Upon entering the chamber, the pulse is apertured down to a 70-mm diameter and frequency-doubled with a KDP (monopotassium phosphate) crystal to a wavelength of $527\,\mathrm{nm}$. It is loosely focused on an argon gas jet with a spherical mirror with $\mathrm{f} = 5\,\mathrm{m}$. The generated harmonic beam is propagated through and around the sample, and then measured in a flat-field grating spectrometer [140]. The copper slit seen in the figure filters any incoming radiation that does not pass through the frame holding the aluminum sample. A 200-nm-thick aluminum filter is placed in front of the spectrometer to eliminate the remaining driving beam, and is destroyed and replaced after each shot.

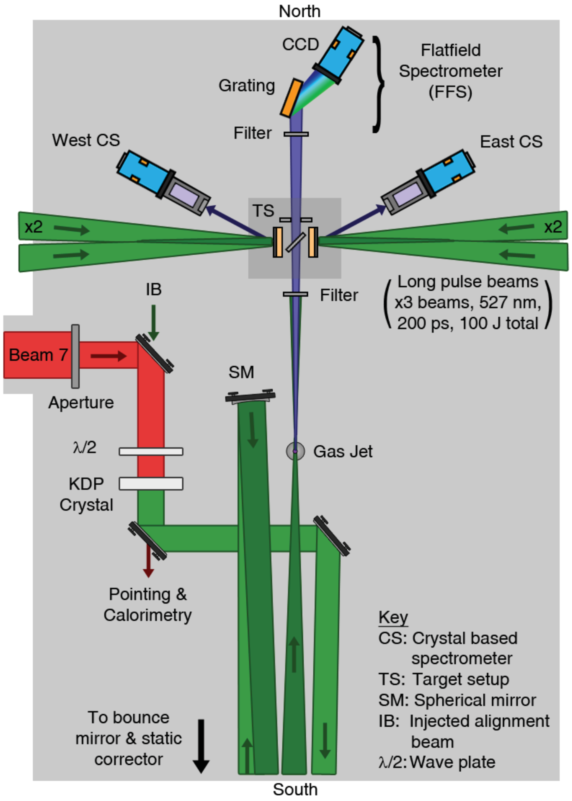

Figure 3.3: Schematic drawing of the complete setup inside the vacuum chamber at the Target Area West of the Vulcan laser facility. Three beams enter from each side of the chamber to produce hard X-rays to heat the aluminum sample. A seventh pulse is used as the driving beam for the generation of the probe beam. A dichroic mirror is used to separate the second harmonic from the fundamental infrared beam, and it is focused with a spherical mirror not included in the picture, located at the southernmost part of the setup.

Figure 3.3 presents the full experimental setup. A total of four crystal-based spectrometers were used to observe the hard-X-ray emission of each palladium target, two per target, each at different angles to measure the full emitted spectrum. Additionally, an X-ray streak camera was placed above the target setup (not pictured in the figure) to measure the duration of the emission with a resolution of $2\,\mathrm{ps}$, filtered by $8\,\mathrm{\mu m}$ of silver. Additionally, a pinhole camera (not pictured) with a 9-$\mathrm{\mu m}$ cadmium filter was used to measure the hard-X-ray source size mentioned above.

3.2.2 Calculation of the absorption coefficients

Data from a harmonic shot through a heated aluminum sample with a thickness of $418\,\mathrm{nm}$ are shown in figure 3.4 (a). In the measured spectra, three harmonic orders can be seen: the 13^{th}, the 11^{th}, and the 9^{th}. The 11^{th} is the most intense, by a factor of nearly 4. The presence of the target can be seen in the center of the spatial profile, causing the large drop in signal. Some additional spectral lines can be seen as well. They correspond to carbon emission lines from the CH backing of the heating targets and reflected on the aluminum sample's surface, and can be easily removed from the data.

Figure 3.4 (b) shows an averaged line-out profile along the spatial direction for the 11^{th} harmonic order, using a cold, 838-nm-thick aluminum sample. Note that the low signal found near $\mathrm{x} = 800\,\mathrm{\mu m}$ is due to an artifact of the CCD camera. Diffraction effects from the edges of the sample can be seen both inside and outside its shadow. These diffraction features have been simulated with a mathematical model based on the Fresnel laws for near-field diffraction. The transmission of this relatively thick foil is known to be effectively zero ($< 0.1\%$) at this photon energy, so all energy found inside the sample's shadow is due to said diffraction, providing a reference for the model. The figure also shows the results of the diffraction simulation, assuming a Gaussian spatial profile for the probe beam, effectively reproducing the experimental data.

A close-up of the sample's shadow region can be seen in figure 3.4 (c). The data and the simulation output match with 99.7% accuracy over the sample shadow. Also shown in the figure are data from a cold, 218-nm-thick sample which does have some transmission, around $\sim 2.9\%$. In this case, there is interference between the diffracted and transmitted parts of the beam.

The setup did not allow for simultaneous measurement of the beam profile and transmitted spectrum. However, several test shots taken with no aluminum sample showed that the spatial profile is typically Gaussian. The transmitted energy is found by first fitting a Gaussian curve to the signal outside the shadow of the sample, as seen in figure 3.4 (b). The total energy under the peak in the sample shadow region can be predicted within $\pm 15\%$. The error is estimated by comparing data from a test shot, without sample, to three different Gaussian fits: the best fit, and two fits deemed to be the worst-case scenarios for an over- and an underestimation. The total transmitted signal is calculated by integrating the total signal detected in the sample shadow region, and then subtracting the signal that would be found in the shadow region after diffraction from the edges of an opaque sample. By comparing the transmitted signal to the Gaussian fit, the transmission of the sample is found. The obtained values are given in table 3.1.

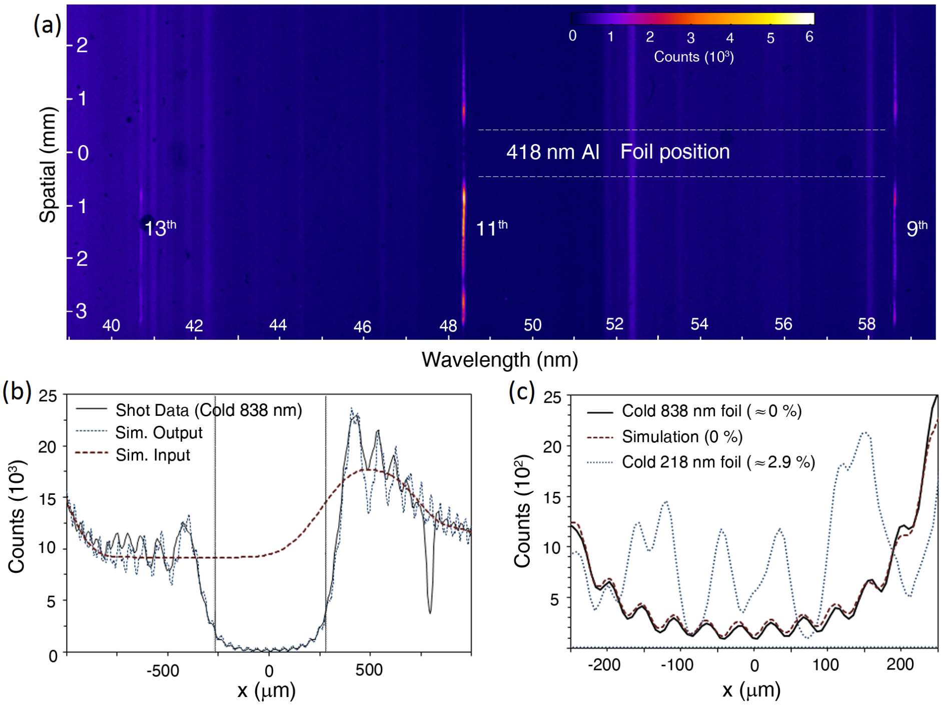

Figure 3.4: (a) Spectrometer data for a harmonic shot through a heated 418-nm aluminum sample. The position of the foil along the spatial axes is highlighted. Three harmonic orders can be seen, with the 11^{th} being the most intense. (b) Line-out along the spatial axis for the 11^{th} harmonic, from a shot through a cold 838-nm sample with effectively zero transmission, centered at x=0 (black solid line). The input (red dashed line) and output (blue dotted line) of the diffraction simulation are compared to these experimental data. The vertical lines indicate the position of the sample. (c) Close-up of the same data in the sample shadow region, compared to the output of the diffraction simulation (red dashed line). The shot data from a cold 218-nm sample are also included (blue dotted line) for comparison.

Al sample	*Harmonic order*	*Photon energy (eV)*	*Transmission* $(\%)$
Cold 218 nm	11	25.88	2.91 $\pm$ 0.43
Cold 218 nm	13	30.58	5.84 $\pm$ 0.90
Cold 418 nm	11	25.88	0.96 $\pm$ 0.15
Cold 418 nm	13	30.58	2.42 $\pm$ 0.36
Heated 218 nm	11	25.88	2.83 $\pm$ 0.40
Heated 418 nm	11	25.88	1.01 $\pm$ 0.15

Table 3.1: Measured transmission values for cold and heated aluminum samples. The errors are obtained by the change in transmission after estimating the maximum and minimum incident Gaussian profiles, combined with the error margin in the diffraction simulation.

The values summarized in the table include the effects of surface oxides and contamination mentioned above, which are extremely difficult to characterize, but must be accounted for nonetheless. We assume that all aluminum samples have identical surface layers and, as such, they have identical transmissions. The absorption coefficient α for a harmonic order of frequency ω is calculated as:

$$\alpha(\omega) = \frac{\ln[\mathrm{T_a}(\omega)/\mathrm{T_b}(\omega)]}{\mathrm{L_b} - \mathrm{L_a}}, \tag{3.3}$$

where $\mathrm{T_a}$ and $\mathrm{T_b}$ are the transmission of the samples with lengths $\mathrm{L_a}$ and $\mathrm{L_b}$, respectively. The lengths are the values of the optical path traveled by the high-harmonic probe pulse through the samples, accounting for the refraction of the signal by the sample, due to the real part of its refractive index, taken from the model by C. A. Iglesias [138] and with values close to unity. The absorption coefficients for cold aluminum were found to be $\alpha_{\mathrm{cold}}(\omega_{11}) = 2.47\,(\pm 0.69)\cdot 10^6\,\mathrm{m}^{-1}$ and $\alpha_{\mathrm{cold}}(\omega_{13}) = 2.44\,(\pm 0.68)\cdot 10^6\,\mathrm{m}^{-1}$. The errors come from the error margins in the transmission measurements (table 3.1) and in the optical path lengths. Unfortunately, it could not be accurately obtained for the 9^{th} harmonic order because the real part of the refractive index is much lower than the other orders, and the error margin in its value leads to a large fluctuation in the predicted absorption coefficient.

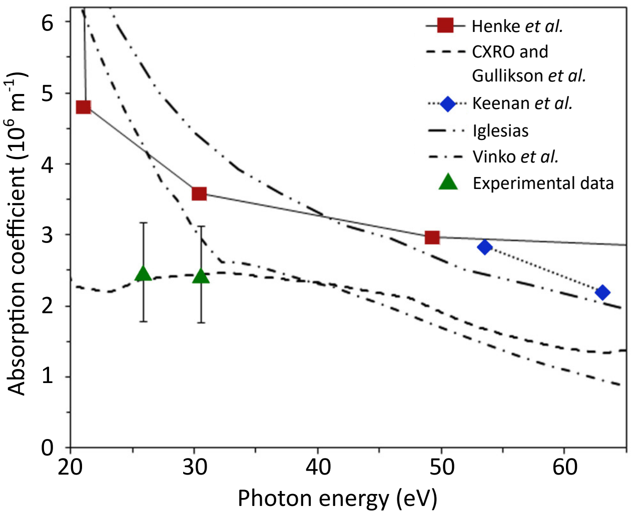

Figure 3.5: Measured absorption coefficient of cold aluminum samples for the 11^{th} and 13^{th} harmonic orders (green triangles), compared to other experimental data and the two aforementioned numerical models.

Figure 3.5 shows a comparison of the obtained results with the predictions of the theoretical models of S. Vinko *et al.* [137] and C. A. Iglesias [138], as well as existing experimental data from different teams: Keenan *et al.* [141], Gullikson *et al.* [142], Henke *et al.* [143] and the CXRO [61]. Although the error bars are large, remarkable agreement with the values of Gullikson *et al.* can be seen. However, both theoretical models predict much higher absorption coefficients. It must be noted, nonetheless, that these models are not designed specifically for the case of cold samples.

For the case of the heated aluminum samples, in addition to the aforementioned surface contamination, an expanded sub-solid density plasma in each face must be taken into account as well. Hydrodynamic simulations were performed in order to estimate the conditions of the samples, including the expansion, after heating by the hard X-rays generated on the palladium foils [135]. The heating was simulated by ray-tracing calculations, in which the X-rays coming from both palladium foils, characterized by the crystal-based spectrometer for each shot, are used as an photon-flux input for HYADES modeling [144].

The calculated density and electron temperature of two different shots can be seen in figures 3.6 (a) and (b), respectively: one shot with for a 418-nm sample, probed $104 \pm 5\,\mathrm{ps}$ after the pump, and one shot for a 218-nm sample, probed $108 \pm 5\,\mathrm{ps}$ after the pump. Note that the samples are tilted by $45°$ with respect to the probe beam. This is taken into account by increasing the thickness of the targets by a factor of $1/\cos(45°)$. The additional $283\,\mathrm{nm}$ of warm aluminum at that angle are highlighted in the plot. The heating in this region was found to be extremely uniform around $\mathrm{T_e} \simeq 1\,\mathrm{eV}$, and the sample remains at solid density at the time of the probing. The expansion of both samples at the edges is very similar, so any difference in transmission must be caused by the additional central material in the 418-nm sample.

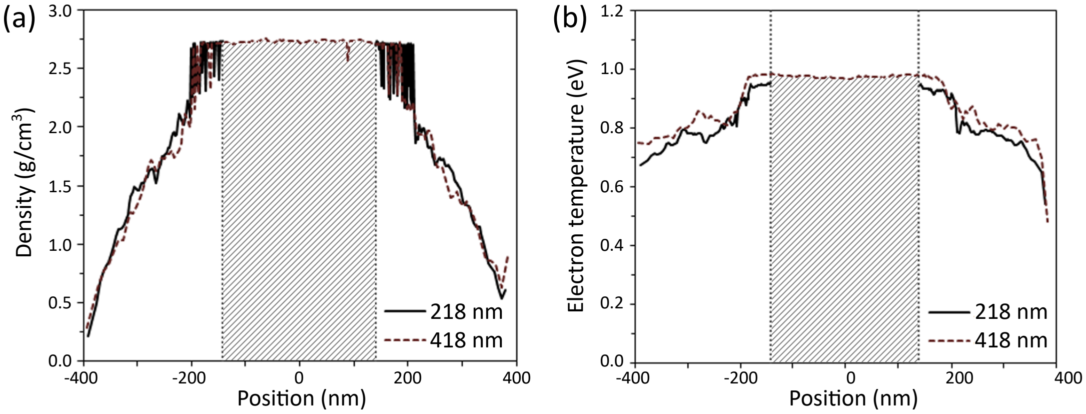

Figure 3.6: Conditions of heated aluminum samples. Comparison of the (a) density and (b) electron temperature of a 418-nm (dashed lines) and a 218-nm sample (solid lines). The data for the 218-nm foil has been split along its center and laterally shifted to match the edge position of the 418-nm target. The additional material in the latter case is represented in crosshatching.

The transmission values for both heated samples were found with the method described above for the cold samples, and are included in table 3.1. The same values of the real part of the refractive index were used to calculate the optical path of the probe beam inside the heated sample, since, according to C. A. Iglesias, it does not change upon heating below $T_e = 10\,eV$. Finally, the resulting absorption coefficient for the 11^{th} harmonic order was found to be $\alpha_{warm}(\omega_{11}) = 2.30\,(\pm 0.64) \cdot 10^6\,m^{-1}$, very similar to $\alpha_{cold}(\omega_{11})$. The error ΔE was calculated by using the standard combination in the quadrature method as $\Delta E = \sqrt{\Delta A^2 + \Delta B^2}$, where ΔA and ΔB are the errors in the transmission measurements for both thicknesses. Unfortunately, the transmission could not be measured for the 13^{th} harmonic, since the signal was below the detection limit.

3.2.3 Comparison with numerical models

The two numerical models under test predict very distinct behaviors of free-free absorption versus temperature. The model by C. A. Iglesias predicts no increase in absorption when heating under $T_e \simeq 2\,eV$, whereas the model by S. Vinko *et al.* shows an immediate increase in absorption after heating, with a 30% decrease in transmission by $T_e \simeq 0.1\,eV$. The warm dense absorption coefficient at $25.88\,eV$ obtained in the experiment is compared in figure 3.7 with the values predicted by both numerical models with the same sample conditions. All the values are normalized with respect to the absorption coefficient for cold aluminum at $T_e \simeq 0.025\,eV$ in order to better reflect the changes upon heating. The figure clearly shows that the model by C. A. Iglesias predicts the behavior of the absorption coefficient upon heating more accurately.

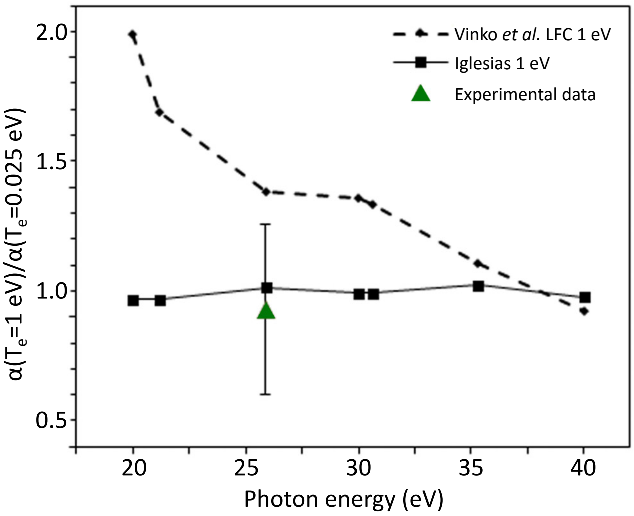

Figure 3.7: Measured warm dense absorption coefficient for the 11^{th} harmonic order with the heated aluminum sample, compared with the predictions of the two aforementioned numerical models under similar conditions of solid density and electron temperature of 1 eV.

3.3 Summary

In summary, this chapter reports an experiment based on the use of high-harmonic pulses to measure the absorption coefficient of XUV radiation in warm dense aluminum, in a tabletop setup. The samples were heated radiatively with hard X-rays to an electron temperature of $\mathrm{T_e} \simeq 1\,\mathrm{eV}$, a value for which existing numerical models predict very distinct absorption properties. Due to experimental limitations, the absorption coefficient of heated samples could only be obtained for the 11^{th} harmonic order, corresponding to a photon energy of $25.88\,\mathrm{eV}$. The results show that the value of the absorption coefficient of aluminum heated to $1\,\mathrm{eV}$ remains very similar to its value in room temperature.

The measured absorption coefficient was compared to the values calculated by two of the aforementioned numerical models for the same sample conditions. Both models predict significantly different behaviors of the warm dense aluminum in the observed temperature range, mainly due to the fact that they use different approximations. The result from this experiment is very similar to the model by C. A. Iglesias, which predicts little change in the absorption for the considered wavelength, while the S. Vinko *et al.* model predicts a 40% increase. Our result thus provides evidence in favor of the former model, in turn giving further insight about the physics of WDM.

CHAPTER 4

Temporal characterization of ultrashort XUV pulses

Contents

Since a laser pulse is an electromagnetic wave, both the amplitude and phase of its electric field must be known in order to fully characterize it in the spatial, spectral or temporal domain. Spatial characterization of XUV pulses was discussed in detail in previous chapters, specifically for the case of high harmonics. Both the intensity distribution and spatial phase, or wavefront, of an XUV pulse can be measured simultaneously with a Hartmann wavefront sensor. In the spectral domain, the spectrum of a pulse can be directly measured with spectrometers. However, these devices cannot directly measure its spectral phase, since they are based on integrating detectors. In terms of the temporal domain, direct measurements of the temporal intensity profile are impossible for pulses below a certain pulse duration.

Laser pulses of femtosecond duration are routinely used in the present day, and attosecond pulses can be generated as well. Their duration is much shorter than the response time of the fastest electronic detectors, which can only provide up to picosecond temporal resolutions [145, 146]. In order to temporally characterize ultrashort pulses, a workaround is necessary, by means of optical methods. Since the spectral and temporal domains are linked via the Fourier transform [147], different techniques can be used to measure the spectral phase of a pulse, which then can be used along with the spectrum to calculate its temporal profile and phase.

In this chapter, the problem of temporal metrology of ultrashort pulses in the XUV regime is discussed in detail, and new techniques are proposed. Section 4.1 explains the necessity of temporal characterization and the key concepts behind it. Some of the most common techniques for measurement of IR pulses are reviewed, as well as the challenges to transfer them to shorter wavelengths. The remaining sections discuss several characterization methods for different sources in the XUV domain: high harmonics in section 4.2, seeded free-electron lasers in section 4.3, and plasma-based seeded soft-X-ray lasers in section 4.4.

4.1 Theory and methods for temporal characterization of ultrashort pulses

Full temporal characterization of ultrashort XUV pulses is essential in many different applications. Additionally, experimental measurements of the pulse duration can verify the validity of numerical simulations of XUV sources, in turn leading to better understanding of the underlying physical processes.

This section presents some fundamental concepts and definitions related to the temporal properties of an ultrashort light pulse, as well several widespread methods for full characterization of ultrashort pulses in the IR domain. The possibility of transferring these methods to the XUV range is also discussed.

4.1.1 Spectral phase and temporal profile of a laser pulse

In the temporal domain, the general form of the electric field $E(t)$ of a laser pulse is $E(t) = E_0(t)e^{i(\omega_0 t - \phi(t))}$, where $E_0(t)$ is its envelope, ω_0 is its central frequency, and

$\phi(t)$ is its temporal phase. The Fourier transform of this function leads to the electric field in the spectral domain, $\tilde{E}(\omega) = \tilde{E}_0(\omega)e^{i\Phi(\omega)}$, where $\Phi(\omega)$ is its spectral phase. The temporal and spectral properties of any pulse are thus strictly related.

The minimum duration of a light pulse is inversely proportional to its spectral bandwidth. This can be seen by using the *time-bandwidth product* (TBP), a parameter derived from the properties of the Fourier transform which limits the shortest duration that a pulse can have as a function of its bandwidth. The TBP is defined as the product of the FWHM duration Δt of a given pulse and its FWHM spectral bandwidth, in terms of frequency $\Delta\nu$. The minimum possible TBP values for several pulse shapes can be seen in table 4.1.

Pulse shape	*TBP* $= \Delta t \cdot \Delta\nu$
Gaussian	0.441
Sech^2	0.315
Lorentzian	0.142

Table 4.1: Minimum values of the time-bandwidth product for different pulse shapes.

When the TBP of a pulse is minimum, it has the shortest duration allowed by its spectrum and it is said to be bandwidth-limited or, more commonly, *Fourier transform-limited*, which occurs only when its spectral phase is linear. If the spectral phase of the pulse is developed as a Taylor series around the central frequency ω_0, it can be expressed as:

$$\Phi(\omega) = \Phi_0 + \left(\frac{d\Phi}{d\omega}\right)_{\omega_0}(\omega-\omega_0) + \frac{1}{2}\left(\frac{d^2\Phi}{d\omega^2}\right)_{\omega_0}(\omega-\omega_0)^2 + \frac{1}{6}\left(\frac{d^3\Phi}{d\omega^3}\right)_{\omega_0}(\omega-\omega_0)^3 + ... \tag{4.1}$$

which allows for several parameters to be defined from each derivative: the *group delay* (GD), the *group delay dispersion* (GDD), and the *third order dispersion* (TOD). They are generally given in fs, fs^2, and fs^3, respectively. Fourth and higher orders can be defined as well, but can be neglected in most cases. GDD is also known as *chirp*, or more specifically linear frequency chirp. With these definitions, the spectral phase can be expressed as:

$$\Phi(\omega) = \Phi_0 + \mathrm{GD}(\omega-\omega_0) + \frac{\mathrm{GDD}}{2}(\omega-\omega_0)^2 + \frac{\mathrm{TOD}}{6}(\omega-\omega_0)^3 + ... \tag{4.2}$$

Figure 4.1 illustrates the effect that each component of the spectral phase has in the temporal properties of a pulse with a given spectrum. In this example, the spectrum is Gaussian and centered in $\lambda = 800\,\mathrm{nm}$, with a bandwidth corresponding to a Fourier transform-limited duration of $100\,\mathrm{fs}$ (FWHM), also included in the figure. A linear spectral phase, the GD, has no effect on the pulse duration, and is thus generally neglected.

A quadratic curvature of the spectral phase, the GDD, leads to an increase in pulse duration, without modifying its Gaussian profile or introducing any asymmetries. In this example, positive chirp was used, but negative chirp of the same magnitude has the same effect on the pulse duration. Lastly, TOD introduces asymmetry in the temporal profile. For high enough values, pre- or post-pulses may appear, depending on its sign.

Essentially, a nonlinear spectral phase means that the different spectral components of the pulse are temporally shifted with respect to one another, thus modifying its duration or temporal shape. For example, in the case of positive GDD or linear frequency chirp, lower frequencies can be found earlier within the pulse, with the higher frequencies propagating behind them. This occurs, for example, to a visible or IR laser pulse propagating through glass, due to the variation of the refraction index with wavelength.

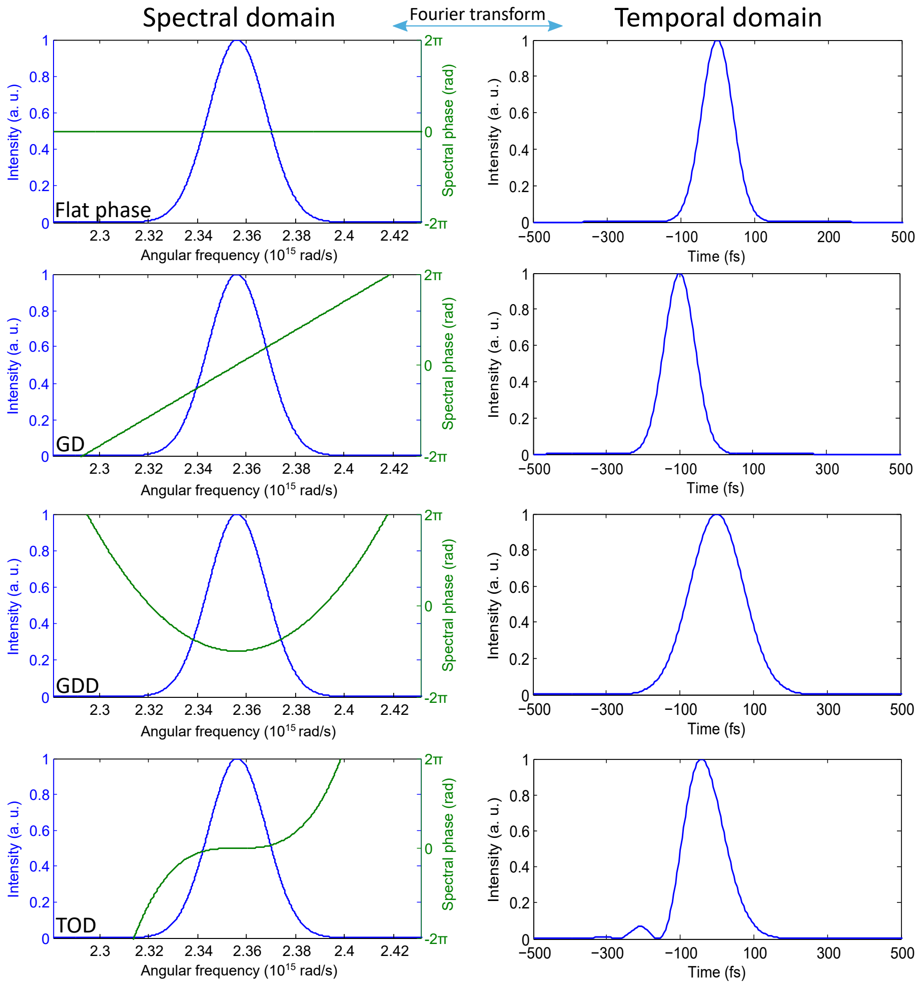

Figure 4.1: Effect of the first three components of the spectral phase on the temporal profile of a laser pulse. The following values were used for this example: GD=10^2 fs, GDD=$5{\cdot}10^3$ fs^2, and TOD=$5{\cdot}10^5$ fs^3.

In summary, this showcases how the temporal properties of a light pulse can be accessed indirectly by measuring its spectrum and spectral phase, which is the basis of some of the pulse characterization methods that are presented in the next section. Being able to measure and control the spectral phase is thus fundamental for pulse compression, pulse shaping, and ultrafast optics in general.

4.1.2 Common techniques for characterization of ultrashort infrared pulses and their transfer into the XUV range

With the advent of ultrafast optics in the last decades of the past century, significant developments in pulse metrology had to be made as well. In order to measure an event in time, a shorter event must be used. However, ultrashort laser pulses are among the fastest events in physics. The temporal resolution of devices such as ultrafast photodiodes or streak cameras is generally on the picosecond scale or, at best, of hundreds of femtoseconds [145, 146]. Streak cameras also have the drawback of being expensive and complex. Since these devices are not fast enough to measure the temporal profile of femtosecond laser pulses, optical methods became necessary instead. A plethora of techniques exist for the metrology of pulses in the IR range. When trying to characterize XUV pulses, a straightforward solution is to transfer these known techniques to the new wavelength range. This, however, is not trivial due to the vastly different sources used in each case, and the different properties of both spectral domains.

In this section, some of the most widespread methods for full temporal metrology of ultrashort pulses in the IR region are presented, as well as the challenges that arise when trying to apply them to the XUV or soft-X-ray ranges. These methods, based either on nonlinear interactions or spectral interference, can provide both electric field and phase in the temporal domain.

4.1.2.1 Autocorrelation and cross-correlation

One of the simplest techniques that can be used to obtain information about the temporal properties of an ultrashort pulse is *optical autocorrelation* [148], introduced in the 1960s [149] and still in use today. Several types of autocorrelation techniques exist, such as intensity or interferometric autocorrelation. In this thesis, only the former will be presented. These techniques, by definition, do not provide information about the temporal or spectral phase of the test pulse, but can provide an estimate for its duration, so it can be used, for example, to monitor changes between pulses, or show if a pulse is Fourier transform-limited or not, when adjusting an optical compressor.

In an autocorrelator, two replicas of the same unknown pulse are mixed in a nonlinear crystal, and the intensity of the generated radiation is measured with an integrating detector, such as a photodiode, as a function of the delay τ between the replicas. Figure 4.2 presents a schematic drawing of simple, multishot autocorrelator based on SHG. Single-shot versions also exist, lacking a delay line and using instead a Fresnel biprism to separate the pulse into two beamlets which combine on the SHG crystal and using a linear detector.

The SHG signal depends on the temporal overlap of the two pulses, and plotting the measured signal as a function of temporal delay yields the convolution curve of the unknown pulse with itself. By measuring the FWHM duration of the convolution curve, the duration of the pulse can be obtained, although this requires assuming a particular shape for its temporal profile, such as Gaussian or Lorentzian, since this information is not given by the convolution. The curve itself is always symmetric, and thus cannot differentiate pre- or post-pulses, or any complex structure within the pulse.

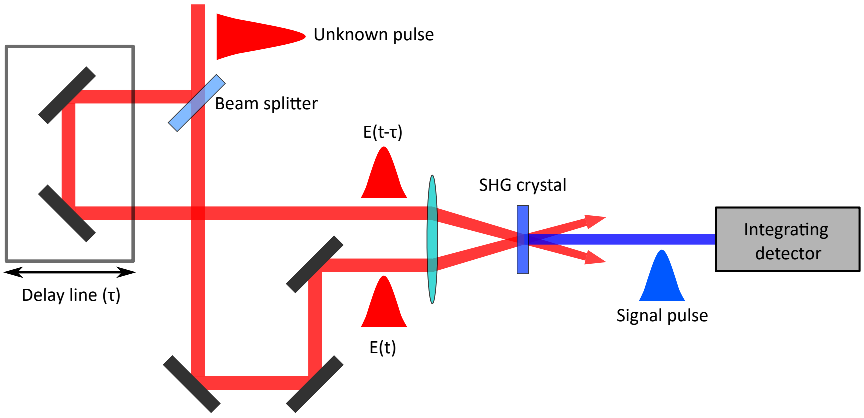

Figure 4.2: Schematic drawing of a setup for an autocorrelation based on SHG.

Cross-correlation is a similar technique, consisting on using a different pulse with known duration to gate the unknown pulse. Nevertheless, although these two techniques are experimentally simple, their limitations made it necessary to develop other methods which provide full temporal information.

4.1.2.2 FROG: Frequency-resolved optical gating

Frequency-resolved optical gating, or *FROG*, was first introduced in 1993 as an inexpensive and experimentally simple method for full temporal characterization of ultrashort laser pulses [150], in contrast to other techniques already existing at the time, such as autocorrelation, that either were too complex or did not provide phase information [151, 152, 153, 154, 155]. FROG is based on the spectrally resolved autocorrelation of laser pulses. The basic experimental setup for a FROG measurement is presented in figure 4.3. The unknown laser pulse is first divided in two with a beam splitter, creating the *probe* pulse $E(t)$ and a temporally delayed *gate* pulse $g(t-\tau) = E(t-\tau)$. Then, the gate pulse is propagated through a delay line, allowing for the control of the temporal overlap of both pulses. The pulses are then spatially overlapped with a lens on the nonlinear crystal, and the *spectrum* of the signal pulse is measured as a function of delay τ, instead of the integrated signal. In the original 1993 work, the nonlinear process of choice was self-diffraction due to electronic Kerr effect. Other effects can be used instead, as long as they provide a fast response to the variations in delay, providing different versions of the FROG setup such as the PG FROG, which uses polarization gating [156], or the SHG FROG, which uses second harmonic generation. SHG provides higher signal than other effects and is thus preferred for low-energy pulses, but it suffers from ambiguity in the direction of time [157]. Note that a version of FROG based on cross-correlation exists as well, called XFROG [158].

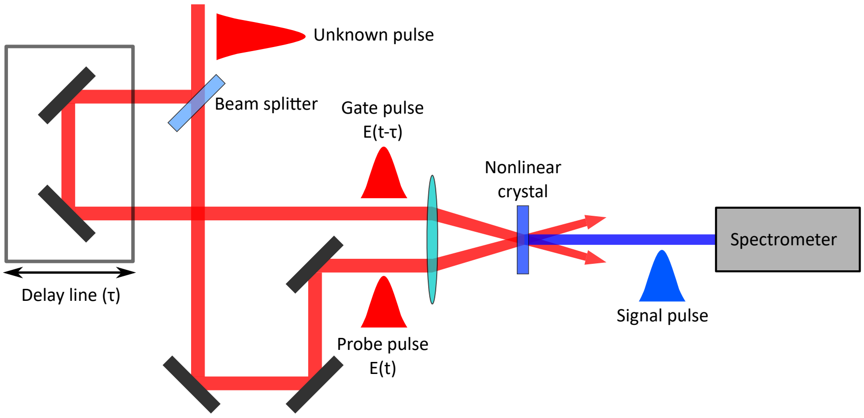

Figure 4.3: Schematic drawing of a setup for FROG measurements using SHG as the nonlinear process.

The graphical representation of the spectrum as a function of delay constitutes a 2D spectrogram [159], usually called *FROG trace*, with the general form:

$$\Sigma_E(\omega,\tau) = \left| \int_{-\infty}^{\infty} E(t) g(t-\tau) e^{-i\omega t} dt \right|^2, \tag{4.3}$$

with the gate pulse $g(t-\tau)$ being a delayed replica of the unknown pulse. The spectral phase of the pulse is encoded in the variations of the generated spectrum with the temporal overlap, and can be retrieved with an iterative and rapidly converging algorithm, and from it, the temporal intensity and phase are calculated [160]. In fact, the spectrogram itself can give information about the spectral phase of a pulse with a simple profile before a phase retrieval algorithm is applied [161]. The measured FROG trace, which uniquely determines $E(t)$ for the unknown ultrashort pulse, is given by:

$$I_{FROG}(\omega,\tau) \propto \left| \int_{-\infty}^{\infty} E_{sig}(t,\tau)^{-i\omega t} dt \right|^2, \tag{4.4}$$

where the signal pulse is given by $E_{sig}(t,\tau) \propto [E(t)]^2 E^*(t-\tau)$ when self-diffraction is used as the nonlinear effect [150], or $E_{sig}(t,\tau) \propto E(t)E(t-\tau)$ when using SHG [157]. The problem to invert the trace to find E_{sig}, and the complex $E(t)$ from it, can be considered a *2D phase retrieval problem*, which is well known in other fields as well, such as crystallography [162]. While the similar 1D phase retrieval problem has infinite solutions, two- and higher-dimensional phase retrieval leads to unique results with only trivial ambiguities such as a constant phase factor [162, 163, 164].

The FROG technique is widely used nowadays, and many different phase retrieval algorithms exist. An iterative-Fourier-transform algorithm was created in [160], and an algorithm based on the method of generalized projections was created a year after the FROG technique [165], providing much faster convergence. The signal field $E_{sig}(t,\tau)$ must follow two constraints: on one hand, the FROG trace calculated with it must match the experimentally measured trace, and on the other hand, it must be a field that can generated with a $E(t)$ as shown above. The first step for the calculation is to input a trial field $E(t)$, as hypothesis. In every iteration, $E_{sig}(t,\tau)$ is calculated, Fourier-transformed into the (ω,τ) and used to calculate its FROG trace of the trial field. Then, the measured FROG trace is used to obtain a new signal field $E'_{sig}(\omega,\tau)$, based on the first constraint. This field is inverse-Fourier-transformed back into the (t,τ) domain. Following the second constraint, a new $E(t)$ is obtained, and used as input for the next iteration, and so on. Further details can be found in [157, 165].

It must be noted that FROG is intrinsically a multishot method, given that a scan in delays must be performed. In fact, the first reported FROG measurement took 20 minutes to complete [150]. There is, however, a single-shot version of SHG FROG, in which the necessity for a delay scan is bypassed by introducing several changes to the setup that also largely simplify the system and make the alignment easier. The technique is called grating-eliminated no-nonsense observation of ultrafast incident laser light e-fields, or *GRENOUILLE* [166].

The modified setup allowing for single-shot FROG measurements is shown in figure 4.4. Instead of beam splitters, a Fresnel biprism is used to make the two beamlets, as well as making them overlap on the crystal on the horizontal direction. The temporal delay is thus mapped to horizontal position on the crystal, eliminating the need for the delay line. A cylindrical lens focuses the beamlets on the crystal along the vertical direction. The output beam has an angular dispersion of generated wavelengths, due to the variations in the phase-matching conditions along the vertical axis given by the incidence angles and the thickness of the crystal [167]. A second cylindrical lens collimates the beam, so that there is a quasi-linear relation between vertical position and wavelength, thus eliminating the need for a spectrometer as well. The system is inexpensive and compact, with the temporal ambiguities found in SHG FROG. GRENOUILLE also provides information about the spatial chirp of the pulse [168].

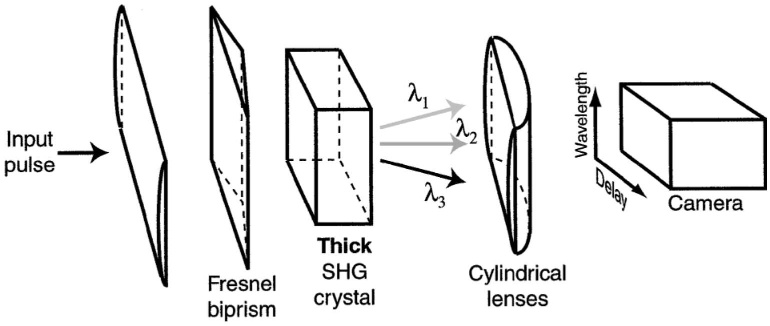

Figure 4.4: Schematic drawing of the GRENOUILLE experimental setup, in which the Fresnel biprism removes the need for a delay scan, and the thick SHG crystal replaces the spectrometer. Taken from [166].

4.1.2.3 Referenced Fourier-transform spectral interferometry

In previous chapters, it was shown that an integrating detector like a CCD camera can measure the spatial distribution of a laser pulse, but not its spatial phase or wavefront. An analogous problem is found within the spectral domain, in which spectrometers are used to measure the spectrum of a pulse, but are not sensitive to its spectral phase. Methods based on Fourier-transform spectral interferometry (FTSI) have the advantage of using direct and non-iterative algorithms to extract the spectral phase from a measured interferogram.

The spectral phase of an unknown laser pulse can be characterized with FTSI if a reference pulse is available, whose spectrum and spectral phase are known. In order to characterize the unknown pulse, the two pulses, temporally delayed with respect to each other by τ are sent to a spectrometer, and the resulting spectral interferogram is recorded. The spectrum of the reference pulse must include that of the test pulse, otherwise, the unknown spectral phase cannot be obtained for all its spectrum. The resulting interferogram $S(\omega)$ is described by $S(\omega) = |\tilde{E}(\omega) + \tilde{E}_R(\omega)e^{i\omega\tau}|^2$, which leads to:

$$S(\omega) = |\tilde{E}(\omega)|^2 + |\tilde{E}_R(\omega)|^2 + 2|\tilde{E}(\omega)\tilde{E}_R(\omega)|\cos[\Phi(\omega) - \Phi_R(\omega) + \omega\tau], \tag{4.5}$$

where $\tilde{E}_R$ and $\tilde{E}$ are the electric fields of the reference and test pulses, respectively, in the spectral domain, and Φ_R and Φ are their spectral phases. The first two terms of the sum consist on the spectra of the two pulses, and the spectral phase of the test pulse is contained in the interferometric term.

Note that the delay τ between the pulses must follow certain conditions. In short, if the delay is too low, the interfringe, which is approximately τ^{-1}, will be too wide, so not enough fringes will be measured in the interferogram. On the other hand, if it is too high, the fringes can be too narrow to be resolved by the spectrometer. Delays of several picoseconds are generally used for femtosecond-long pulses.

The phase difference is obtained via a direct three-step algorithm based on the Fourier transform [169], summarized in figure 4.5. The first step involves calculating the Fourier transform of the interferogram into the pseudo time domain t, where three peaks are found, two at $t = \pm\tau$, corresponding to the AC components, and at $t = 0$, corresponding to the DC component (see figure). The peak at $t = \tau$ is selected, generally with a Gaussian or super Gaussian function. The inverse Fourier transform has the argument $\Phi(\omega) - \Phi_R(\omega) + \omega\tau$, from which the spectral phase is obtained.

This technique has the advantage of using a direct and robust inversion algorithm, as opposed to the iterative algorithms required for FROG, and also has the potential to provide single-shot measurements if the pulses have enough energy. It requires a good spectral resolution for accurate measurement of the fringes, and, if multishot acquisitions are required, the fringes can be blurred if the laser does not have a stable carrier-envelope phase (CEP). However, the main drawback is the need for a reference pulse, which must be characterized first with other methods.

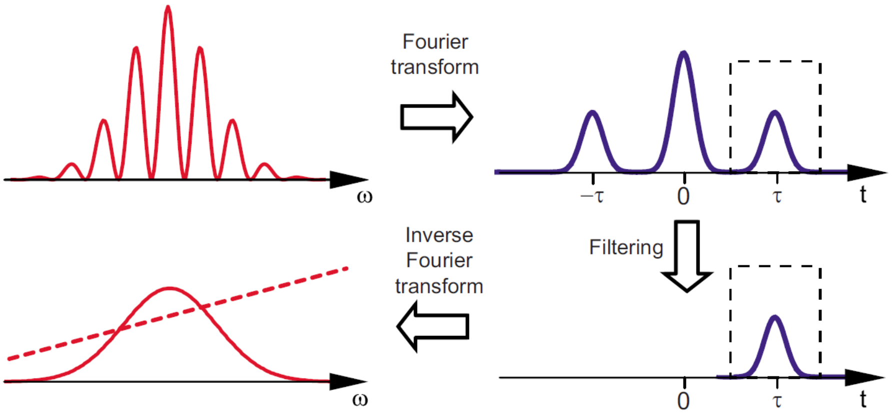

Figure 4.5: Diagram of the algorithm for phase extraction in FTSI. If the delay τ is too low, the AC component cannot be filtered. If it is too large, the peaks will be outside the t domain, whose size is determined by the spectral resolution due to the properties of the Fourier transform. Taken from [148].

4.1.2.4 SPIDER: Spectral interference for direct electric-field reconstruction

The need for a reference pulse severely limits the applicability of FTSI, hence why self-referenced techniques, which solely rely on the unknown pulse, were developed in the 1990s [170]. One of the most widespread self-reference spectral interferometry techniques is called spectral interference for direct electric-field reconstruction, or *SPIDER*, for short, introduced in 1998 [171] and based on spectral shearing interferometry. It can also perform single-shot measurements, if the signal is high enough.

In SPIDER, a spectrally sheared replica of the unknown pulse is used instead of a reference. The two pulses are identical to each other, only delayed in time and shifted in frequency. The measured interferogram has the form:

$$S(\omega) = |\tilde{E}(\omega)|^2 + |\tilde{E}(\omega+\Omega)|^2 + 2|\tilde{E}(\omega)\tilde{E}(\omega+\Omega)|\cos[\Phi(\omega+\Omega) - \Phi(\omega) + \omega\tau], \tag{4.6}$$

where Ω is the amount of spectral shear, also called spectral shift, and τ is the temporal delay. As with FTSI, the interferometric term contains the spectral phase, in the form of the phase difference between spectral components with a shift Ω.

τ and Ω cannot have arbitrary values, but must fulfill several conditions instead. The delay follows the same constraints seen above, while the spectral shear follows the Whittaker-Shannon sampling theorem [172]. It asserts that, if the pulse to be measured has nonzero energy during a time T, a spectral shear of $\Omega < 2\pi/T$, and hence a sampling of the spectrum at frequency intervals of $\Omega = 2\pi/T$, is sufficient for reconstructing amplitude and phase exactly.

Figure 4.6 shows an example of experimental setup for a SPIDER measurement. The test pulse is first separated into two by a beam splitter. One of the pulses is further divided into the two temporally delayed replicas, while the other is chirped by the use of a dispersive material or a stretcher, creating a long pulse in which each frequency propagates at a different time. Finally, the two branches recombine in the SHG crystal. The two replicas created on one branch are mixed with the chirped pulse at different times, effectively mixing with different wavelengths, and thus, producing the two temporally delayed, spectrally sheared replicas whose interference is measured with the spectrometer. The frequency of the stretched pulse must not change over the duration of one of the other pulses, which is achieved with sufficient stretching. For example, in [171], the test pulse has a duration close to $150\,\mathrm{fs}$, and the chirped pulse was stretched to a duration $T = 20\,\mathrm{ps}$. This duration is chosen as to provide the necessary value of shear between the replicas, given that it follows the expression $\Omega \simeq (\tau\Delta\omega)/T$, where $\Delta\omega$ is the bandwidth of the stretched pulse.

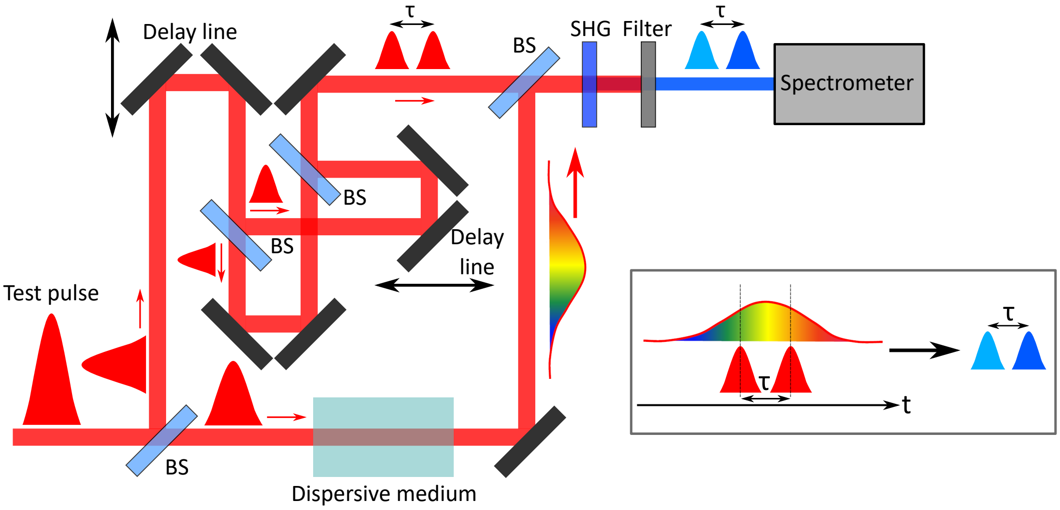

Figure 4.6: Schematic drawing of a typical setup for a SPIDER measurement. The two temporally delayed replicas combine with the stretched pulse, creating the spectrally sheared second-harmonic replicas. BS: beam splitter. The inset shows how the two replicas mix with different frequencies due to the chirp of the stretched pulse.

The procedure to extract the phase is very similar to the one described above, and is also non-iterative. First, the interferogram is Fourier transformed. The peak at $t = \tau$ is selected by filtering, and the remaining signal is inverse transformed. Its argument is extracted and the calibration term $\omega\tau$ is subtracted. What remains is the relative phase $\phi(\omega+\Omega) - \phi(\omega)$ between successive pairs of frequency components separated by Ω, which can easily be calibrated by recording the individual spectra. The spectral phase for a discrete set of frequencies separated by Ω is calculated by concatenation [173, 174]. Note that it is not necessary to directly measure the pulse spectrum, since it can also be extracted from the interferogram [175].

Several different versions of SPIDER exist as well [148], such as *SEA SPIDER* (spatially encoded arrangement for SPIDER), which is based on spectrally resolved *spatial* interference instead of spectral interference [176]. This change relaxes the spectral resolution requirements. The temporal delay τ is fixed to zero, and the interferences are caused by a spatial shift instead. The phase is calculated with a similar algorithm, which requires 2-D Fourier transforms.

4.1.2.5 Adapting these techniques to the XUV range

Several issues arise when trying to transfer these techniques to the XUV domain. Nonlinear crystals, which do not exist for short wavelengths, are necessary for autocorrelation, FROG and SPIDER measurements. Autocorrelation and cross-correlation measurements based on nonlinear phenomena can be made, but cannot fully provide the spectral phase [177, 178]. FROG measurements have been performed in the XUV range as well [179, 180], using photoelectron spectrometers. However, all these techniques rely on multishot measurements, which require good shot-to-shot stability, as well as preventing real-time pulse analysis to be performed. Additionally, their implementation is usually complex or expensive. Ideally, single-shot measurements can be performed with SPIDER-based techniques, but they require the creation of a spectrally sheared replica, which is not trivial in the XUV range.

For these reasons, no ideal technique exists for full characterization of XUV pulses from every possible source. Instead, in order to measure these pulses, one must make use of the particular properties of each source. In the following sections, some of these sources are presented, as well as some characterization methods that have been tested experimentally, or proposed theoretically.

4.2 Temporal characterization of high-harmonic pulses

High-harmonic generation is a versatile tabletop source of ultrashort pulses in the XUV and soft-X-ray domains, with applications in many different fields that would otherwise require the use of large-scale facilities such as synchrotrons or FELs (see section 1.1). Fully characterizing high-harmonic pulses is specially interesting since HHG allows for the generation of attosecond pulses, thanks to its spectral properties [17, 181]. The generation of attosecond pulses requires accurate amplitude and phase control, to ensure that all spectral components of the pulse add constructively. Spatial filtering is required as well, in order to eliminate the more divergent radiation emitted by electrons following long quantum paths [182]. Several characterization methods have been demonstrated in recent years for high-harmonic pulses.

4.2.1 Correlation and FROG-based techniques

The first estimations of high-harmonic pulse duration were based on autocorrelation measurements with fourth-order nonlinear processes [177], and in cross-correlation by means of photoionization of a gas target by the harmonic pulse in presence of the driving IR field [178]. These first measurements confirmed the shorter duration of individual harmonic orders with respect to its driving laser, around tens of femtoseconds, as well as giving limited information about the presence of chirp.

In terms of attosecond pulses generated via HHG, some of the earliest estimations were obtained by means of cross-correlation with the fundamental laser field [183, 184], since high XUV intensity is necessary to produce enough signal with nonlinear effects of high order. The first autocorrelation measurements for attosecond pulse trains were carried out some time later, with the use of a split mirror to create the two beamlets, measured by means of two-photon ionization in He. An estimated average duration of $780 \pm 80\,\mathrm{as}$ for the attosecond peaks was found [185]. However, the full spectral phase cannot be obtained with these methods. Another method called *RABITT*, or sometimes *RABBIT* (resolution of attosecond beating by interference of two-photon transitions), based on the cross-correlation of the harmonics and the driving pulse, can be used for the characterization of trains of attosecond pulses produced by HHG [22, 186, 187]. It consists on measuring the sidebands observed in the photoelectron spectrum at even integers of the driving frequency as a function of the delay between the pulses, and it provides the relative phase between harmonic orders.

Full temporal characterization of XUV pulses, including isolated attosecond pulses, can be carried out with the *FROG CRAB* technique (frequency-resolved optical gating for complete reconstruction of attosecond bursts), a version of FROG adapted for the XUV range [179, 180]. It involves the study of the photoelectron spectrum generated by two-photon ionization of a gas target as a function of delay. The shortest pulse created so far was measured with FROG CRAB, revealing a duration of $67\,\mathrm{as}$ [17].

While a single-shot version of FROG exists for IR pulses, it is based on the properties of SHG crystals and thus cannot be adapted into the XUV range, making FROG CRAB an intrinsically multishot technique.

4.2.2 SPIDER-based techniques

Characterization schemes based on the FROG principle rely on photoelectron spectroscopy, requiring complex and expensive devices such as time-of-flight magnetic bottle spectrometers. Their need for multishot acquisitions means that they provide averages, and do not account for shot-to-shot variations. In the year 2005, the first implementation of SPIDER for high-harmonic pulses was demonstrated, providing complete and single-shot characterization of a single harmonic order [188]. This scheme is called high-harmonic SPIDER, or *HHSPIDER*.

In order to carry out a SPIDER measurement, the XUV pulse must produce spectral interference with a spectrally sheared replica of itself. In HHSPIDER, a spectral shear $\delta\omega$ is introduced on the driving IR pulse, and then transferred to the harmonic pulse of order q as $\Omega = q \cdot \delta\omega$. This is experimentally simpler than other methods previously proposed for the creation of the sheared XUV replica, based on photoionization of a gas [189, 190]. The two replicas of the IR pulse, delayed by τ with respect to each other, are produced by means of an acousto-optic filter (a Dazzler [191]). They are then focused on a gas target, producing the two spectrally sheared high-harmonic replicas with the same delay τ. The resulting interferogram is recorded with an XUV spectrometer.

The IR pulses used in the experiment reported in [188] had a FWHM duration of $50\,\mathrm{fs}$ and flat spectral phase. The reconstructed temporal profile of harmonic 11, averaged over a few tens of shots, had a duration of $22\,\mathrm{fs}$ (FWHM), 1.4 times longer than its Fourier limit due to negative linear chirp. The HHSPIDER scheme can be used for single-shot, real-time pulse characterization, accounting for shot-to-shot variations and providing a useful tool for optimization. By obtaining ten successive single-shot reconstructions of the same harmonic, an average FWHM duration of $19.2 \pm 1.4\,\mathrm{fs}$ was found, showing a relatively small variation between shots for the conditions of this experiment.

A version of SEA SPIDER for high-harmonic pulses has been proposed as well, based on the same principle of manipulating the driving pulse to produce the necessary spectrally sheared high-harmonic replica pulse [192, 193], but it has not yet been experimentally implemented. However, the concept of manipulating the driving beam instead of the output can be applied to other secondary sources of ultrashort XUV pulses, as seen in the next section.

4.3 Temporal characterization of seeded free-electron lasers in the XUV domain

Invented in 1971 [194], a free-electron laser (FEL) is a type of laser in which the gain medium is a relativistic electron beam made to wiggle by a periodic magnetic field. Many such facilities exist nowadays which generate highly energetic ultrashort XUV and X-ray pulses based on the process of self-amplified spontaneous emission (SASE), such as the SACLA (SPring-8 Angstrom Compact Free Electron Laser) in Japan [195] or the LCLS (Linac Coherent Light Source) in the United States [196]. However, the limited temporal coherence provided by the SASE process led to the development of FELs where the electron beam is seeded by an external laser pulse, which leads to better coherence properties and control of the FEL pulse [197]. The FERMI facility (Free Electron laser Radiation for Multidisciplinary Investigations), in Italy, is an example of seeded FEL [197, 198]. FELs can provide XUV pulses with much higher energies than HHG, with the drawback of requiring much larger and expensive facilities, which renders them less accessible.

In this section, the basic properties of seeded FELs, in particular of the FERMI facility, are briefly presented. Then, we propose a scheme for full temporal characterization of XUV pulses from a seeded FEL based on the SPIDER technique, which takes advantage of the specific properties of these sources.

4.3.1 Theory and properties of seeded free-electron lasers

In an FEL, an electron beam is sent at relativistic speeds through a periodic and static magnetic field, provided by a device called *undulator*, which consists in a series of dipole magnets arranged periodically. In the the magnetic field, the electrons wiggle and emit bremsstrahlung, losing kinetic energy in the process. The radiation is emitted in a cone along the direction of motion of the electron beam, and its divergence is inversely proportional to the kinetic energy of the electrons [5, 199]. The wavelength of the emitted pulses depends on many parameters of the electron beam and the undulator. It is given by the so-called resonant condition and is subsequently amplified by the electrons along the undulator. When no external pulse is used to initiate the emission, the FEL is based on SASE. In this configuration, the process is initiated by the electrons emitting photons independently from each other, and thus incoherently. The energy transfer between the emitted photons and the wiggling electrons leads to *bunching* of the electrons along the undulator. In the end, the micro-bunches emit in phase, providing spatially coherent radiation [5, 199]. Figure 4.7 shows a schematic drawing of a SASE FEL.

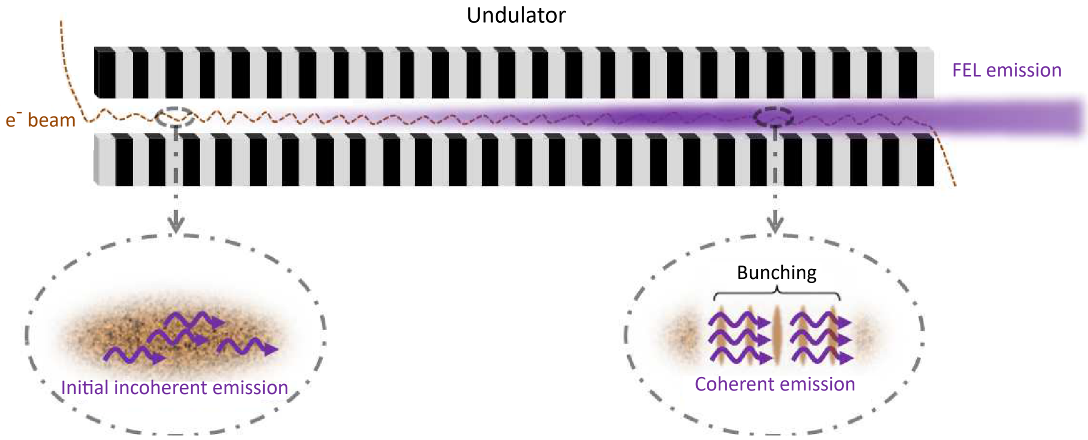

Figure 4.7: Schematic drawing of a single-pass SASE FEL. The different colors of the undulator represent different directions of the vertical magnetic field. The electrons are dumped at the end of the undulator and not reused. Taken from [200].

Due to the initial random distribution of the electrons, the first emission consists on a noisy signal, whose amplification leads to an irregular, spiky spectrum. Since the initial photons are emitted from random positions along the electron beam, the temporal profile has a similar spiky structure, with a duration similar to that of the electron beam, as well as limited temporal coherence. Additionally, the random nature of the process leads to very large shot-to-shot variations.

As a means to overcome these limitations, the use of an external coherent light field, called the *seed*, was proposed as a means to start the FEL emission rather than the amplification of random noise [201]. Seeded FELs can provide the high intensities and spatial coherence of SASE FELs, as well as high temporal coherence due to the seed preserving the longitudinal phase relation along the electron beam.

A key characteristic of seeded FELs is that the bunching of the electrons presents significant components at integer multiples of the seed's frequency. A second undulator can thus be tuned to amplify the harmonic n of the seed. This process is known as coherent harmonic generation (CHG). The typical layout of a CHG FEL can be seen in figure 4.8. In the first undulator, called the *modulator*, the seed and the electron beam overlap, and electron beam modulation is created. After the modulator, the electrons propagate through a strong magnetic chicane called the *dispersive section*, where they travel an energy-dependent path which converts the energy modulation into a tunable spatial bunching. Finally, the electrons travel through a second undulator, the *radiator*, where a harmonic of the seed is amplified. Note that the power of the seed pulse at the entrance of the system must be higher than the electron noise in order to provide efficient energy modulation. This setup offers high control of the temporal and spectral properties of the FEL pulse, which, in ideal conditions, mimic those of the seed [197]. This makes CHG FELs a very attractive source for the generation of high-power ultrashort XUV pulses.

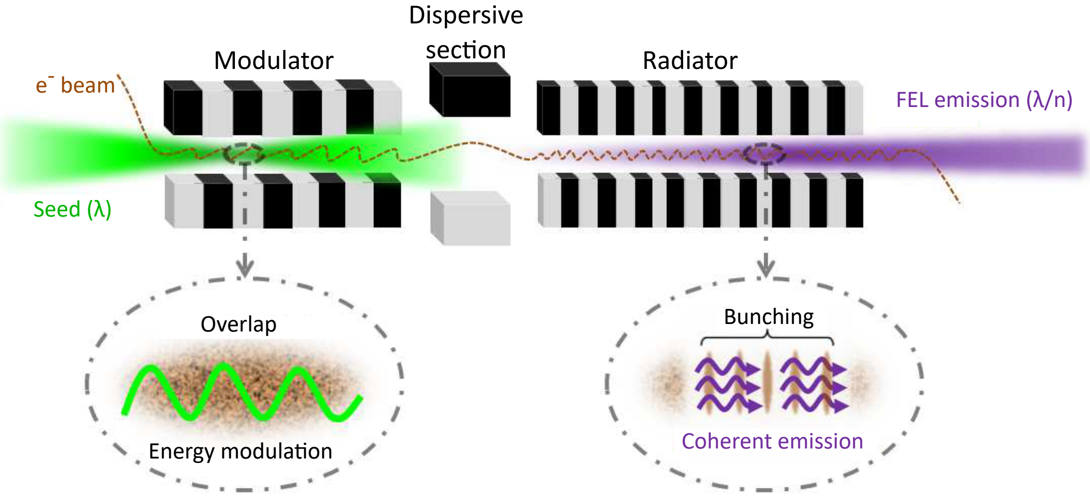

Figure 4.8: Schematic drawing of a CHG FEL, which consists in two undulators (the modulator and the radiator) separated by a magnetic chicane called the dispersive section. Taken from [200].

4.3.1.1 Electron motion within the undulator

The properties of the FEL emission are given by the motion of the electrons in the undulator. In an ideal planar undulator, and for the horizontal plane $y = 0$, the static magnetic field only has a vertical component [199] and is therefore described by $\vec{B} = -B_0 \sin(k_U z)\vec{e}_y$, where B_0 is the amplitude of the magnetic field, and $k_U = 2\pi/\lambda_U$, with λ_U being the undulator period, usually of tens of millimeters. The electrons, traveling at a relativistic speed $\vec{v}$, are subjected to a Lorentz force:

$$m\gamma \frac{d\vec{v}(t)}{dt} = -e\vec{v} \times \vec{B}, \tag{4.7}$$

where e and m are the charge and mass of the electrons, respectively, $\gamma = \frac{1}{\sqrt{1-\beta^2}}$ is the relativistic Lorentz factor, and $\beta = v/c$, being c the speed of light. The electric field emitted by the electrons has negligible effect on their motion at the beginning of the undulator. From these equations, every component of $\vec{v}(t)$ can be obtained. First, if $v_y(0) = 0$, then $v_y(t) = 0$, meaning that there is no vertical movement if the electrons were injected along the z axis. The Lorentz force for the horizontal component can be expressed as:

$$\frac{dv_x(t)}{dt} = \frac{e}{m\gamma} B_y v_z(t). \tag{4.8}$$

The longitudinal component of the electron velocity is assumed to be much larger than the transversal one, $v_x \ll v_z$, which leads to $v_z \simeq v = \beta c = \text{constant}$. By replacing z by βct in the previous equation, it can be easily integrated to yield:

$$v_x(t) = \frac{Kc}{\gamma} \cos(k_U \beta ct), \tag{4.9}$$

where $K = \frac{eB_0}{mck_u} \simeq 0.934 B_0[T] \lambda_U[cm]$ is known as the *undulator parameter*, a dimensionless quantity. Finally, in order to calculate the longitudinal component of the electron velocity, the Lorentz factor can be rewritten as $\frac{1}{\gamma^2} = 1 - \left(\frac{v}{c}\right)^2 = 1 - \frac{1}{c^2}(v_x^2 + v_z^2)$, yielding:

$$v_z(t) = \sqrt{c^2 \left(1 - \frac{1}{\gamma^2}\right) + v_x(t)^2} = c\sqrt{1 - \frac{1}{\gamma^2}\left(1 + K^2 \cos^2(k_U \beta ct)\right)} \tag{4.10}$$

In a relativistic electron beam, v_z must be close to c, so $\frac{1}{\gamma^2}(1 + K^2 \cos^2(k_U \beta ct)) \ll 1$. Equation 4.10 can be developed as a Taylor series, whose first order term is:

$$v_z(t) \simeq c \left[1 - \frac{1}{2\gamma^2}\left(1 + K^2 \cos^2(k_U \beta ct)\right)\right]. \tag{4.11}$$

Thus, the average longitudinal speed of the electrons over one undulator period is:

$$\bar{v}_z = c\left[1 - \frac{1}{2\gamma^2}\left(1 + \frac{K^2}{2}\right)\right]. \tag{4.12}$$

Having found the transversal and longitudinal components of the electron velocity, the coordinates $x(t)$ and $z(t)$ can be found by integration [199].

4.3.1.2 Energy exchange between the seed pulse and the electron beam

In a seeded FEL based on CHG, the interaction between the external electric field and the electron beam must be taken into account [202]. A horizontally polarized seed with amplitude E_0, wave number k, and frequency ω is injected into the undulator, with its envelope being $\vec{E}(z,t) = E_0 \cos(kz - \omega t)\vec{e}_x$. For simplicity, a monochromatic plane wave is assumed, copropagating with the electron beam. Its absolute phase term is not taken into account.

An electron with velocity $\vec{v}$ exchanges energy with the seed through the Coulomb force $\vec{F}$. The infinitesimal energy exchange over a time dt is thus $d(\gamma mc^2) = \vec{v} \cdot \vec{F} dt$, which demonstrates that other polarization components do not exchange any energy with the electrons. By combining this with equation 4.9, the energy exchange is expressed as the changes to the electrons kinetic energy, represented by their Lorentz factor γ, as:

$$\begin{aligned}\frac{d\gamma}{dt} &= -\frac{e}{mc^2} v_x(t)E(t) = -\frac{eK}{m\gamma c}\cos(k_U z)E_0\cos(kz - \omega t)\\ &= -\frac{eKE_0}{2m\gamma c}\left[\cos(kz + k_U z - \omega t) + \cos(kz - k_U z - \omega t)\right]\\ &= -\frac{eKE_0}{2m\gamma c}\left[\cos(\theta) + \cos(\theta - 2k_U z)\right],\end{aligned} \tag{4.13}$$

where the phase θ is defined as $\theta = (k + k_U)z - \omega t \simeq (k + k_U)\bar{v}_z t - \omega t$. Due to the conservation of energy, the light wave will be amplified when the electrons lose kinetic energy, which means $\frac{d\gamma}{dt} < 0$. Ideally, this situation should be maintained. Concerning the term $\cos(\theta)$ of the previous equation, that condition is met when:

$$\frac{d\theta}{dt} = 0 \quad \Rightarrow \quad (k + k_U)\bar{v}_z - kc = 0 \quad \Rightarrow \quad k - k_U = \frac{k_U 2\gamma^2}{1 + \frac{K^2}{2}}. \tag{4.14}$$

The undulator period is much larger than the wavelength, so $k \gg k_U$. This leads to the resonance equation for a sustained energy transfer for the amplification of light of wavelength λ in the FEL:

$$\lambda = \frac{\lambda_U}{2\gamma^2}\left(1 + \frac{K^2}{2}\right). \tag{4.15}$$

It can be shown that this wavelength corresponds to the wavelength of spontaneous emission of the electrons in the undulator along the z direction [58]. The resonance condition corresponds to a shift of λ along the z direction of the wave with respect to the electron bunch occurring after each undulator period, so that they remain in phase. This phenomenon is known as slippage, and is due to the different velocities of the wave and the electron beam. Additionally, when the resonance is maintained, the term $\cos(\theta - 2k_U z)$ from equation 4.13 does two oscillations per undulator period, so it cancels out in the energy transfer. From the resonance condition it can be seen that in order to amplify radiation in the XUV and X-ray regimes, both λ_U and K must be low, with γ being high.

Many computational codes have been developed to simulate the behavior of the electrons in the undulator and the energy exchange with the seed, such as Perseo, a one-dimensional code, [203] or GENESIS, which is three-dimensional [204]. Figure 4.9 shows the result of a Perseo simulation to illustrate the evolution of the electron-beam distribution as it travels through an undulator, showing electron bunching and saturation of the amplification. The distribution is represented in the so-called phase space, where the electrons kinetic energy is represented by their Lorentz factor γ, and the position along the bunch is represented by their phase θ. In the figure, a section of the beam of length λ is selected, equivalent to 2π in terms of phase.

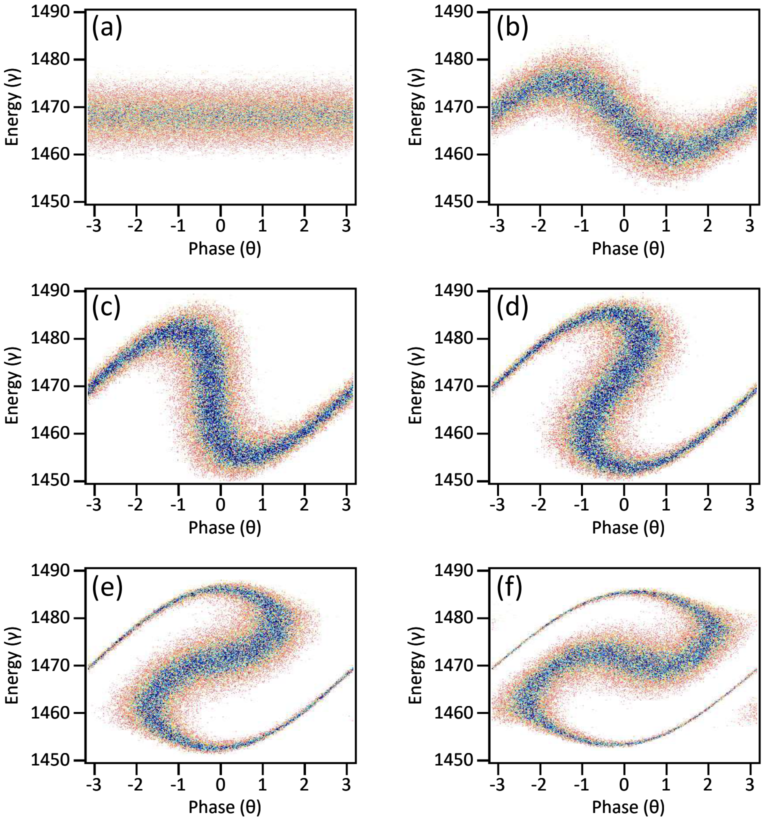

Figure 4.9: Simulated evolution of the electron-beam distribution in the phase space. (a) Initial flat distribution, (b) energy modulation, (c) bunching, (d) slight overbunching, and (e and f) overbunching. Blue colors indicate higher densities. Taken from [205].

The initial flat distribution (figure 4.9 (a)) is modulated after the beam enters the undulator (figure 4.9 (b)), as a direct effect of the energy exchange seen in equation 4.13. The distribution acquires a sinusoidal profile. Some electrons are accelerated, while others are slowed down. Their different kinetic energies lead them to new positions along the beam, effectively gathering around the center, converting the energy modulation into bunching (figure 4.9 (c)). This happens along the full beam, so many bunches separated by a distance of λ are formed, and they emit in phase at that wavelength. Along the undulator, the electrons transfer energy to the wave until they reach a point where their energy has decreased so much that the resonance condition is no longer met. Then, the wave amplification stops, reaching saturation. If the electrons continue to travel along the undulator, the direction of the energy transfer is reversed and the wave loses energy in favor of the electron beam, which starts to show overbunching (figure 4.9 (d)).

Overbunching continues to increase if the beam continues to travel along the undulator (figures 4.9 (e) and (f)). However, the energy transfer is reversed again after some time if the propagation continues. Ideally, the undulator should end when saturation is reached. A seeded FEL based on CHG has two undulators: the modulator creates the energy modulation of the electron beam, but weak bunching (figure 4.9 (b)), and then the dispersive section then enhances the transfer from energy modulation to bunching, before the electron beam is injected, with this bunched structure, into the radiator.

4.3.1.3 Bunching and harmonic generation

The bunching process occurs at a period of λ, and at its harmonics as well [206], so that slippages of a fraction of λ are also possible. This leads to the following resonance condition for harmonics of order n:

$$\lambda_n = \frac{\lambda_U}{2n\gamma^2}\left(1+\frac{K^2}{2}\right). \tag{4.16}$$

In order to understand how the harmonics are emitted, the electron motion in the CHG configuration must be studied. The modulator, with period λ_M, is resonant to the seed wavelength λ [202]. At the end of the modulator, when $z = z_M$, the phase of an electron arriving at a time t_M is given by $\theta_M = (k + k_M)z_M - \omega t_M$, with $k_M = 2\pi/\lambda_M$.

The electron is then propagated through the dispersive section, where the energy modulation $\Delta\gamma$ is transformed into temporal separation Δt:

$$\Delta t = t_R - t_M = \frac{dt}{d\gamma}\Delta\gamma, \tag{4.17}$$

where t_R is its time of arrival at the entrance of the radiator, which has a period of λ_R. At this point, the phase of the electron is given by $\theta_R = (k_n + k_R)z_R - \omega_n t_R$, where $k_R = 2\pi/\lambda_R$. By combining these relations, θ_R can be expressed as:

$$\theta_R = n\left(\theta_M + \frac{d\theta}{d\gamma}\Delta\gamma + \theta_0\right), \tag{4.18}$$

with θ_0 being an absolute phase term [202]. The term $\frac{d\theta}{d\gamma}$ represents the *strength of the dispersive section*, and it can be written as:

$$\frac{d\theta}{d\gamma} = \frac{kR_{56}}{\gamma_0}, \tag{4.19}$$

where γ_0 is the mean energy of the electron beam. The strength of the dispersive section is generally quantified by the parameter R_{56}, given in μm.

If the initial energy distribution of the electron beam is known, the phase distribution at the entrance of the radiator can be obtained. Assuming an initial Gaussian energy distribution with standard deviation σ_γ at the entrance of the modulator, Fourier analysis of the phase distribution leads to the bunching factor, or bunching function [202]:

$$b_n(\theta,\gamma,n) = \left|\left\langle e^{-in\theta}\right\rangle\right| = 2\left|J_n\left(n\Delta\gamma\frac{d\theta}{d\gamma}\right)\right| e^{-\frac{1}{2}\left(n\sigma_\gamma\frac{d\theta}{d\gamma}\right)^2}, \tag{4.20}$$

which quantifies the quality of the bunching of an electron as a function of its position along the bunch. The shape of the longitudinal profile of the FEL emission has a similar shape as this function. It must be noted, however, that this result was obtained after making several assumptions. As mentioned above, the calculation was restricted to one dimension for simplicity, not taking into account the transverse structure of the electron beam. Additionally, up to this point it was assumed that, in the modulator, energy modulation occurs without any bunching, with the latter being provided only by the dispersive section. This is not always the case, as bunching may start to happen in the modulator or may not be efficiently done at the entrance of the radiator, depending on the experimental conditions. However, this ideal result leads to two important conclusions about harmonic generation in a seeded FEL:

- From the first factor containing the J_n Bessel functions, it can be inferred that the bunching can be optimized by appropriately tuning the strength of the dispersive section R_{56}.
- The exponential dependence on n indicates that bunching quality is lower for higher-order harmonics, imposing a limit on the shortest wavelength that can be efficiently generated by CHG, in a similar way to the cutoff in HHG.

The three-dimensional dynamics of the electron beam in the undulators are described in detail in [199, 202, 207]. Taking three-dimensional effects into account, the amplification gain in the radiator is described by the factor [207]:

$$g_0 = \frac{\mu_0 e}{mc^2}\cdot\frac{I}{\sigma_x\sigma_y\sigma_z}\cdot\lambda_R^2 N_R^3\cdot\frac{K^2F_{JJ}^2}{\gamma^3}, \tag{4.21}$$

where $\mu_0 = 4\pi\cdot 10^{-7}\frac{V\cdot s}{A\cdot m}$ is the permeability of vacuum, I is the electron beam current, N_R is the number of undulator periods, and σ_x, σ_y, σ_z are the standard deviations of the electron distribution in the three axes. Lastly, for the case of a planar undulator, $F_{JJ} = J_0\left(\frac{K^2}{4+2K^2}\right) - J_1\left(\frac{K^2}{4+2K^2}\right)$.

Depending on the value of g_0, the FEL can operate in low- or high-gain regime. In low-gain regime, $g_0 < 1$, and the FEL pulse is barely amplified. High-gain regime occurs when $g_0 \gg 1$. In this regime, the amplification of the signal is exponential until it reaches saturation. In this case, CHG is referred to as high-gain harmonic generation (HGHG) [208]. In order to provide high gain for short wavelengths (see equation 4.15), long undulators, i. e. high values of N_R, must be used.

4.3.1.4 The FERMI seeded XUV free-electron laser

Section 4.3.2 presents the results of numerical FEL simulations based on the parameters of the FERMI facility [209, 210]. Additionally, an experiment conducted in the facility is reported in section 5.2. Starting operations in the year 2012, the FERMI seeded FEL can generate fully coherent and ultrashort pulses, with durations of $10-100\,\mathrm{fs}$ [198], in the XUV and soft-X-ray spectral ranges. It consists on two distinct undulator chains called FEL-1 and FEL-2. The former covers the spectral range $100-20\,\mathrm{nm}$, and the latter covers $20-4\,\mathrm{nm}$ [211], thanks to the high tunability of the harmonic generation process. A schematic drawing of the FERMI facility can be seen in figure 4.10.

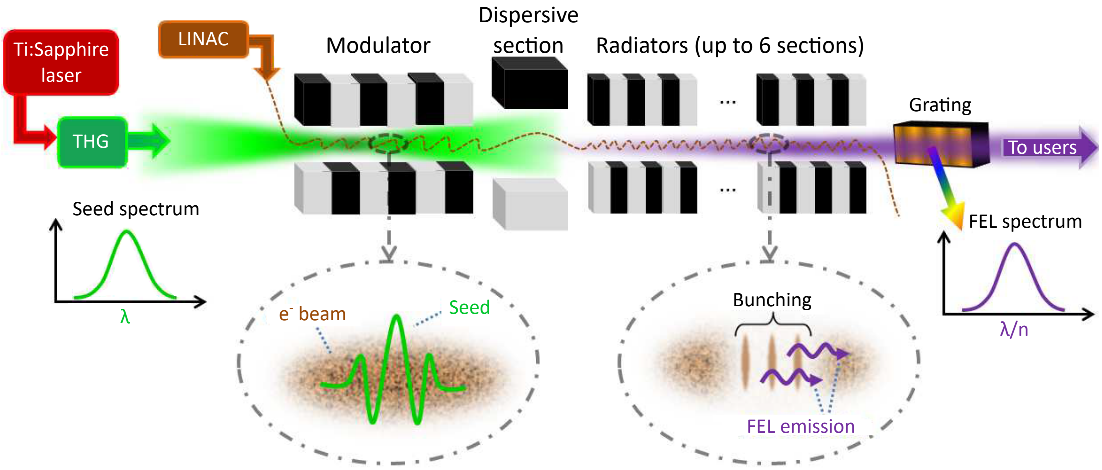

Figure 4.10: Schematic drawing of the layout of the FERMI FEL. Taken from [200].

The process starts with a linac that accelerates an electron beam to kinetic energies of $1-1.5\,\mathrm{GeV}$, which is sent through the modulator. The seed pulse is obtained by third harmonic generation (THG) of a femtosecond Ti:Sapphire IR laser, for a seed wavelength of $\lambda = 261\,\mathrm{nm}$. It has a Gaussian spectrum and a pulse energy of several tens of microjoules. The seed interacts with the electron beam in the modulator, which, in the case of FEL-1, has $\mathrm{N_M} = 32$ periods of $\lambda_\mathrm{M} = 10\,\mathrm{cm}$ and is tuned at λ. After traveling through the dispersive section, the electrons are injected into the radiator. It is divided into six successive sections, each of them consisting on $\mathrm{N_R} = 44$ periods of $\lambda_\mathrm{R} = 5.5\,\mathrm{cm}$. The transverse properties of the electron beam are adjusted between each section. The radiators are tuned at harmonic n, typically of the order of 10 or lower, thus leading to the generation of XUV wavelengths, with a repetition rate of up to $50\,\mathrm{Hz}$. The electron beam is dumped after the radiators, since FERMI is a single-pass FEL.

While in a SASE FEL the pulse duration is given by the duration of the electron bunch, in a seeded FEL it is tied to the duration of the seed. In the case of FERMI, the FWHM seed pulse duration is of the order of $200\,\mathrm{fs}$, while the duration of the electron bunch is typically $1-2\,\mathrm{ps}$, so there is a significant longitudinal portion of the bunch which does not interact with the seed. In those areas, only negligible spontaneous emission is generated, hence why the FEL pulse has femtosecond duration. The output is characterized with an on-line spectrometer based on a diffraction grating at grazing incidence. The spectrometer uses the first diffraction order, while the zeroth order, or specular reflection, is sent to the beamlines [212]. The FEL spectrum is Gaussian, with a typical bandwidth of $\Delta\lambda/\lambda \simeq 10^{-3}$. Many other diagnostics are also in place for monitoring every step of the FEL pulse generation [211]. The far-field spatial profile of the FEL beam is Gaussian, as is the seed [200]. Further details about the facility can be found in [198].

4.3.2 SPIDER for seeded XUV free-electron lasers

We propose an experimental layout for SPIDER-based full temporal characterization of a seeded XUV FEL, in which the replica pulses are generated at the seeding stage. We studied the possibility of generating suitable seed pulses for the experiment, and we obtained numerical results after FEL and SPIDER simulations. The results presented in this section have been published in [213].

4.3.2.1 Choice of characterization method

Autocorrelation [214] and cross-correlation [215] schemes, based on the photoionization of a gaseous target, have been used in the past to estimate the duration of FEL pulses. The limited information they provide can be sufficient if only an estimate of the pulse duration is wanted, since the output pulses are generally Gaussian. However, we also wish to obtain the spectral phase of the pulses to fully characterize them. Techniques like FROG CRAB, while providing full temporal characterization, require lengthy multishot measurements. A single-shot scheme is preferred.

SPIDER-based techniques have the potential of providing accurate and complete spectro-temporal information of a single pulse with a simple and robust inversion procedure. The key issue, however, is the generation of the two temporally delayed and spectrally sheared replicas of the unknown pulse. This can be done in seeded XUV FELs thanks to the properties of HGHG to generate XUV pulses which, in ideal conditions, mimic the properties of the seed pulse [216]. However, even if the phase of the seed pulse can be known, developing a method for full temporal characterization of the output XUV pulses is still necessary due to the possibility of phase distortion during the amplification process [217].

4.3.2.2 Proposed setup

As shown in section 4.1.2.4, the implementation of a classical SPIDER apparatus remains rather simple in the IR and visible domains. It has also been implemented in FELs emitting at deep-ultraviolet wavelengths [218]. However, creating a replica at shorter wavelengths requires a different arrangement, as seen with HHG sources. Following the successful pump-probe experiments on the FERMI FEL facility [219] that were based on a twin-seeding scheme, we show that the same setup is suitable for SPIDER measurements. The proposed setup, presented in figure 4.11, does not require any further implementation at the FEL output. Additionally, the interferograms are recorded with the on-line spectrometer [212], so it is non-invasive for users.

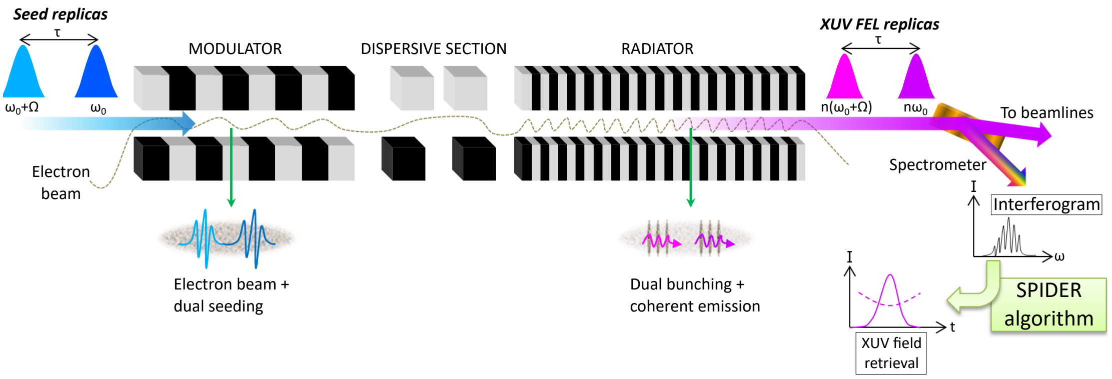

Figure 4.11: Setup for XUV SPIDER measurements on an HGHG FEL. In parallel of the measurement, the direct beam is sent to users beamlines.

Taking advantage of the HGHG configuration, the creation of the spectrally sheared and temporally delayed replica is performed with the seed pulse before harmonic frequency upconversion, and not with the FEL output. The seed is split in two replicas, with a temporal delay τ and spectral shear Ω. The successive seed pulses, with central frequencies ω and $\omega + \Omega$, then interact with a sufficiently long and uniform electron bunch, generating two spectrally sheared and temporally delayed FEL pulses. The spectral shear between them will be $n\Omega$. The two replicas of the measured pulse are thus directly produced, while in a classical SPIDER apparatus the pulse under study is indirectly characterized.

4.3.2.3 Experimental study of the seeding stage

In order to demonstrate the possibility of generating two suitable, spectrally sheared identical seed pulses that allow for SPIDER reconstruction in an FEL, we carried out a proof-of-principle experiment in the Salle Orange beamline of LOA. The experimental setup, based on a Mach-Zehnder interferometer, is presented in figure 4.12.

The fundamental IR beam is split in two paths. On each arm of the interferometer, a 200-μm-thick BBO type I crystal in the *ooe* configuration is placed to generate the second harmonic of the fundamental beam. The conversion efficiency is close to 15%. The use of this type of setup allows for independent control of the beam properties of each arm, in turn allowing for the generation of the two replicas. By slightly tilting one of the crystals, the phase-matching conditions can be changed, leading to a small and controllable spectral shift of the generated harmonic. The two beams are then recombined, with a micrometric-precision motorized stage allowing to adjust the delay between the two pulses. A bandpass filter is placed after recombination to eliminate the remaining IR energy.

After recombination, the spectra and interferogram are recorded with an Ocean Optics USB2000 commercial spectrometer. By blocking the beam in arm 1, the spectrum generated in arm 2 is measured in real time, and the BBO crystal can be tilted as much as necessary in order to obtain the desired shear Ω. The tilt was always kept smaller than 3°, providing a shear of approximately $1\,\mathrm{nm}$, following the Whittaker-Shannon sampling theorem.

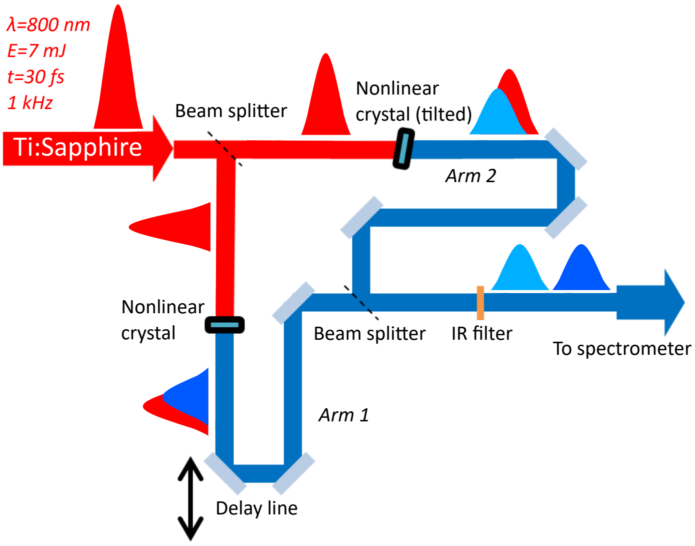

Figure 4.12: Experimental setup for the proof-of-principle SPIDER experiment carried out with SHG at the Salle Orange beamline of LOA, providing two spectrally sheared and temporally delayed replicas of the second harmonic pulse. Arm 1 refers to the arm where the delay line is located, and arm 2 refers to the arm with the tilted BBO crystal.

Figure 4.13 shows examples of measured spectra and interferograms. In figure 4.13 (a), two raw, independently measured spectra are compared. The 2ω spectrum generated in arm 1 is centered at $\lambda = 410.4\,\mathrm{nm}$. A bandwidth of $4.9\,\mathrm{nm}$ is measured after averaging ten spectrum acquisitions. The beam generated in arm 2 is slightly weaker, and spectrally shifted by $0.8\,\mathrm{nm}$. This shift can be increased by further tilting the crystal, which also reduces the conversion efficiency. By numerically shifting and normalizing the spectra, it can be seen that they are indeed nearly identical, as presented in figure 4.13 (b). Only a small discrepancy is found, for the least intense spectral components. When the delay is set to $\tau = 495\,\mathrm{fs}$, the two beams produce the interferogram shown in figure 4.13 (c), with an interfringe of $1.1\,\mathrm{nm}$. By increasing τ, the interfringe can be reduced, increasing the number of fringes in the interferogram as desired.

All data were obtained by accumulating three laser shots, since $3\,\mathrm{ms}$ was the shortest acquisition time achievable with the spectrometer used in this experiment. Since the Ti:Sapphire laser is not CEP stable, the position of the fringes can vary from shot to shot, and the fact that all acquisitions take several shots means that, for some measurements, the fringes are blurred. One such example is presented in figure 4.13 (d), measured at the exact same conditions described above. In order to test the technique, we recorded interferograms for many different values of τ, by moving the delay line in steps of $5\,\mu\mathrm{m}$, equivalent to delay steps of $6.6\,\mathrm{fs}$, from zero delay to $\tau = 1320\,\mathrm{fs}$, where the interfringe was $0.4\,\mathrm{nm}$.

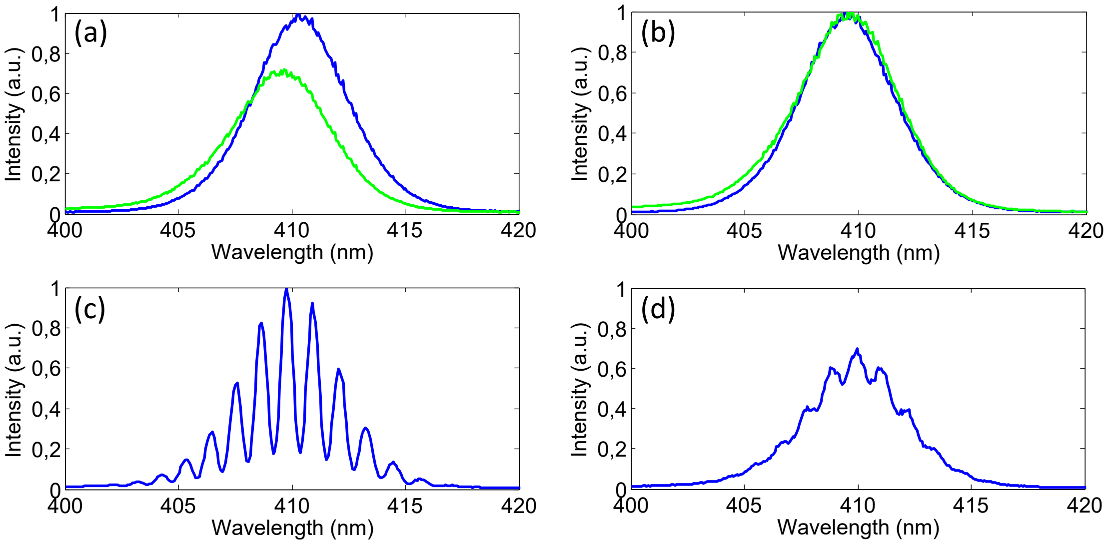

Figure 4.13: Experimental measurements in the SPIDER setup with tilted BBO crystal: (a) comparison between the spectra from arm 1 (blue line) and arm 2 (green line), (b) overlap of both spectra, showing that they are nearly identical, (c) interferogram obtained from those two pulses at delay τ=495 fs, and (d) another interferogram obtained for the same conditions, showing that the fringes can be blurred due to non-stable CEP in the driving laser.

The spectral phase of the pulses can be extracted by applying the SPIDER algorithm to the measured interferograms. The obtained phase is shown in figure 4.14 for two cases. In the first case, with no dispersive element present in the setup, a small TOD is found, most likely due to the grating-pair compressor at the end of the Ti:Sapphire laser chain. To further test the technique, a 1-cm-thick fused silica plate was placed after recombination of the two pulses to introduce a known GDD, which is correctly retrieved.

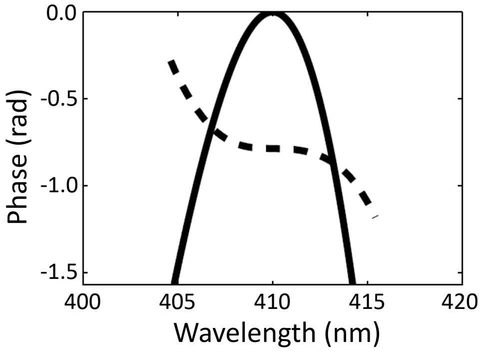

Figure 4.14: SPIDER-retrieved spectral phase as a function of wavelength, with (solid line) and without (dashed line) a 1-cm-thick fused silica plate placed after recombination of the two replicas.

Note that, in order to be consistent with previous works by other authors in the seeded XUV FEL community [220], the criterion used in this section will be that positive linear frequency chirp implies a positive quadratic curvature of the *temporal* phase, and thus negative in the spectral domain.

4.3.2.4 Simulation parameters

The FEL simulations to test this SPIDER scheme were performed with the one-dimensional Perseo code [203] and using realistic parameters for the FERMI FEL [197, 219, 221], summarized in table 4.2. The seed allows for the adoption of a twin-seeding scheme, mentioned above [219], in which two pulses are used to seed a single electron beam, producing the temporally delayed and spectrally shifted replica pulses.

Electron beam	
Mean energy	$1.2\,\mathrm{GeV}$
Energy profile	Flat
Current profile	Flat
Peak current	$500\,\mathrm{A}$
Beam duration	$1\,\mathrm{ps}$
Seed pulse	
Central wavelength	$261\,\mathrm{nm}$
Temporal and spectral profiles	Gaussian
Bandwidth	$3.8 \cdot 10^{-3}$
Pulse energy	$10 - 100\,\mu\mathrm{m}$
FEL pulse	
Harmonic order	6
Central wavelength	$43.5\,\mathrm{nm}$
Bandwidth	$\sim 2.5 \cdot 10^{-3}$
Spectrometer resolution	$4.9 \cdot 10^{-5}$

Table 4.2: Main parameters used for the simulations, based on the FERMI FEL. The bandwidths of the seed and FEL pulses, as well as the FEL spectrometer resolution are given in relative terms of their corresponding wavelengths.

For an accurate SPIDER reconstruction, the delay τ between the pulses must follow two conditions mentioned in section 4.1.2.3, depending on the spectrometer resolution $d\omega_{\mathrm{FEL}}$ and the FEL bandwidth $\Delta\omega_{\mathrm{FEL}}$ [172]. First, in order to correctly resolve the fringes in the spectrometer, the condition $\tau < \pi/d\omega_{\mathrm{FEL}} = 1.5\,\mathrm{ps}$ must be met. Additionally, in order to obtain enough fringes, the delay must follow $\tau > 4\pi/\Delta\omega_{\mathrm{FEL}} \simeq 100\,\mathrm{fs}$. A delay of $\tau = 600\,\mathrm{fs}$ is chosen for the simulations.

The spectral shear $n\Omega$ between the pulses must satisfy the Whittaker-Shannon criterion of $n\Omega < 2\pi/T$, where T is the time interval within which the FEL pulse has nonzero energy. Assuming $\mathrm{T} = 200\,\mathrm{fs}$, the maximum acceptable shear is $0.2\,\mathrm{nm}$ for the seed pulses. We chose a value of $0.1\,\mathrm{nm}$, 10% of its bandwidth, for the simulations.

In order to verify the validity of the simulations carried out with the Perseo code, three-dimensional simulations were also performed with the GENESIS code [204], which account for additional effects due to from the transverse magnetic field distribution. Given that the results of both options were very similar, the Perseo code was preferred since it is less time-consuming.

4.3.2.5 Numerical results

The output of the FEL simulation provides the temporal profile of the two FEL replica pulses. In order to consider possible uncertainties and inhomogeneities that might arise during the emission process, such as seed and electron-current shape, phase and bandwidth of the seed pulses or slice emittance, the phase and amplitude of the output have been independently multiplied by a random error, included within a range of $\pm 5\%$ of the calculated values.

The interferogram used for the SPIDER reconstruction is obtained via a Fourier transform of the temporal FEL field. Additionally, random noise was artificially added to the interferograms, to better replicate experimental conditions. Three FEL pulses generated under different conditions are simulated in order to test the robustness of the technique.

Fourier transform-limited seed

Seed pulses with a flat spectral phase are first considered. Figure 4.15 presents the output of the simulation. As expected, the FEL pulses replicate the Gaussian temporal profile of the seed, and the delay is maintained, as seen in figure 4.15 (a). The two FEL pulses have a FWHM duration of $60\,\mathrm{fs}$, and their phases present a small quadratic curvature due to the FEL dynamics [221]. Figure 4.15 (b) shows the obtained FEL interferogram, which presents about 10 fringes within a wavelength window of $0.1\,\mathrm{nm}$. Given the spectral resolution of the FERMI spectrometer at $43.5\,\mathrm{nm}$ (table 4.2), a maximum of 15 fringes can be resolved within said spectral window.

The spectrum and spectral phase retrieved by the SPIDER calculation can be seen in figure 4.16 (a). The spectral phase has a slight quadratic curvature, consistent with the FEL simulation output, thus demonstrating the accuracy of the method. The retrieved temporal intensity is shown in figure 4.16 (b) and compared with the first pulse of simulation output (the one in the left in figure 4.15 (a), corresponding to the head of the electron bunch). The agreement is quite good, and the FWHM duration of the retrieved pulse is $55\,\mathrm{fs}$, slightly shorter than the FEL simulation.

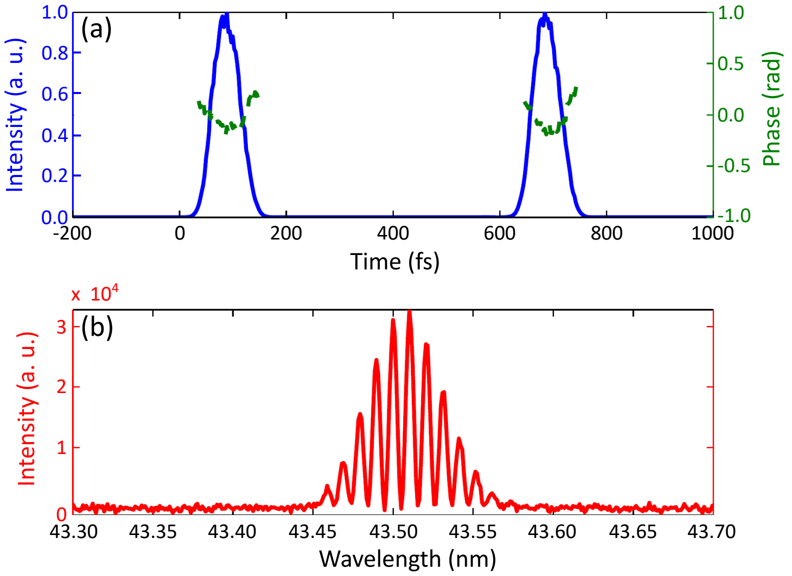

Figure 4.15: FEL simulation output with Fourier transform-limited seed pulses. (a) Temporal domain: longitudinal profile (solid line) and phase (dashed line). (b) Spectral domain: interferogram, obtained by a Fourier transform of the temporal profile.

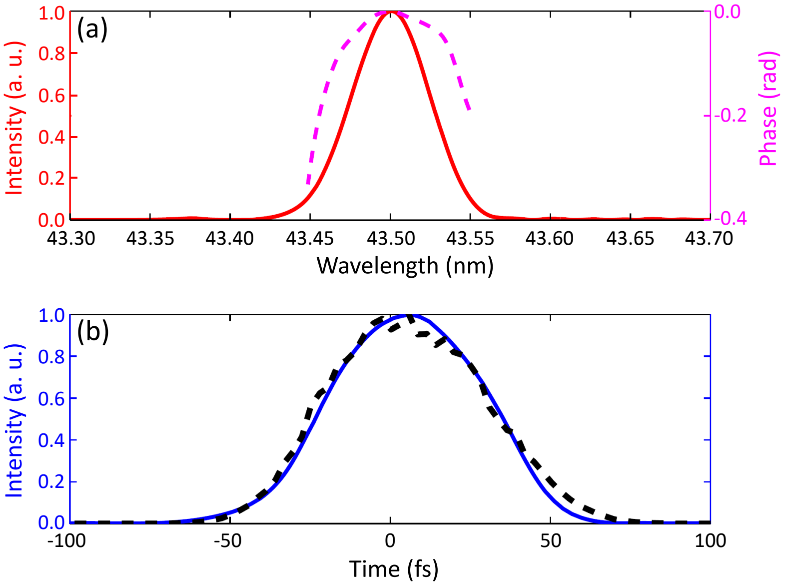

Figure 4.16: SPIDER reconstruction of the simulated FEL pulses obtained with transform-limited seeding pulses. (a) Spectrum (solid line) and spectral phase (dashed line). (b) Temporal intensity of the retrieved pulse (solid line) compared to the direct output of the FEL simulation (dashed line).

Double-peak emission

There is a particular FEL regime in which the emission originating from a single seed pulse splits temporally into two sub-pulses, each with distinct central wavelengths [221, 222]. For this regime, it is required to have a chirped seed pulse, as well as high seed intensity and/or strong dispersive section, while the rest of the simulation parameters are maintained as shown in table 4.2. The SPIDER reconstruction of the spectrum, seen in figure 4.17 (a), shows this two-color structure, as well as frequency chirp acquired from the seed. The obtained temporal profile shown in figure 4.17 (b) shows good agreement with the simulation output, as the split structure is obtained with the retrieved duration of each sub-pulse being close to the FEL simulation, as well as the duration of the overall envelope, $\simeq 300\,\mathrm{fs}$.

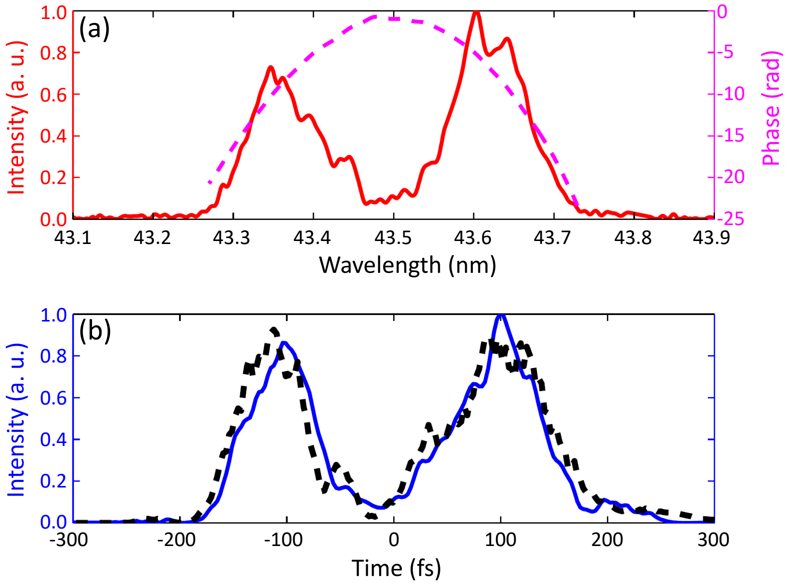

Figure 4.17: SPIDER reconstruction of the simulated FEL pulses obtained in double-peak regime. (a) Spectrum (solid line) and spectral phase (dashed line). (b) Temporal intensity of the retrieved pulse (solid line) compared to the output of the FEL simulation (dashed line).

Phase distortions

The theory of seeded FELs [223, 224] predicts that the seed phase structure is transferred to the FEL pulses. However, additional phase terms and distortion can result from the phase dynamics. This can be seen in figures 4.15 (a) and 4.16 (a) , in which two seed pulses with flat spectral phase generate FEL pulses with a small quadratic phase. This effect is more significant when the FEL amplification reaches saturation, and it stresses the need for accurate full temporal characterization of seeded FEL pulses. One example of this effect can be seen in figure 4.18, where the simulated and retrieved temporal phases are compared. The direct seed phase transfer, obtained by multiplying the seed phase by the harmonic order n, is also shown as a reference. Large deviations from this ideal parabola can be seen at the center, where the pulse is most intense, due to saturation.

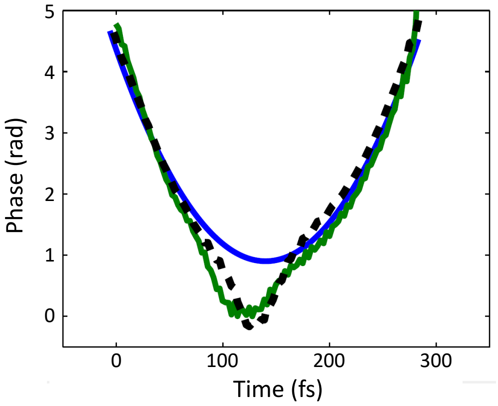

Figure 4.18: Simulated distorted FEL phase (dashed line) and its SPIDER reconstruction (green solid line). For comparison, the direct phase transfer from the seed to the FEL pulse is also shown (blue solid line).

It must also be noted that slight differences between the simulated FEL phase and the SPIDER retrieval can be seen. This is due to the dissimilarity of the two XUV replicas, which is in turn a consequence of the stochastic character of the FEL amplification process at saturation. This seems to indicate that deep saturation could be a limitation of the technique.

Nevertheless, this demonstrates the interest of FEL SPIDER measurements for studying the amplification dynamics in seeded FELs, as well as the consequences of errors or high-order terms in the seed phase and of inhomogeneities in the electron beam. This could be performed by carrying out SPIDER characterizations of both the seed pulse and the resulting FEL emission in parallel, which could allow for the use of a control loop for efficient, real-time FEL pulse shaping.

4.3.2.6 Discussion

These results demonstrate the feasibility of SPIDER measurements in seeded FELs, especially for the case of XUV pulses produced via HGHG. It can also be applied to other cases, such as direct seeding with high-order harmonics generated in gases [225], echo-enabled harmonic generation [226] or self-seeding [16, 227]. The main requirement is a sufficiently long and uniform electron bunch, which has already been experimentally achieved. This version of SPIDER is non-invasive and single-shot, and can be performed in real time alongside user experiments. Its main advantage is that all necessary handling is done within the seed stage, instead of the electron beam or the output XUV pulses. Besides, control of the FEL chirp by the seed makes feasible the generation of Fourier-limited FEL pulses that can then be measured by SPIDER.

The large scope and the robustness of this method was also demonstrated by studying a peculiar case of non-Gaussian, double-peak, emission. The characterization of the latter is specially interesting, since such emission is suitable for pump-probe experiments in the XUV region. Moreover, a single-seed SPIDER experiment in double-peak regime could be foreseen, since the split sub-pulses, originating from one seed only, are temporally delayed and spectrally sheared (see figure 4.17), and may thus be suitable replicas.

Experimental demonstration of the XUV FEL SPIDER technique would allow for the measurement of the effective transfer of the seed phase and possible phase distortions occurring through FEL amplification in different regimes. A similar SPIDER setup, based on seeding a chirped electron beam with two identical pulses, has been successfully implemented at the FERMI facility [220]. In that scheme, the spectral shear between the XUV pulses is due to the interaction of each seed with electrons with different kinetic energies. The scheme proposed in this section, however, has the advantage of not requiring any particular manipulation of the electrons. Full temporal characterization of these pulses will lead to a better understanding of FEL physics and for further developments, such as the design of chirped pulse amplification schemes [228, 229].

The idea of creating the two XUV replicas by manipulating the seed is analogous to the HHSPIDER technique used for high-harmonics [188]. However, instead of using a Dazzler, one could use a setup like the one presented in figure 4.12, using two SHG crystals, to generate the high harmonics with two temporally delayed and spectrally sheared 2ω pulses. This, in turn, will generate two spectrally sheared harmonic pulses with the same temporal delay, which can then be characterized with SPIDER measurements. Given that SHG usually has conversion efficiencies around 10%, this technique is more suitable for beamlines where high IR pulse energy is used. Another point to take into account is the blurring of the spectral fringes of multishot interferogram acquisitions if the driving laser is not CEP stable.

4.4 Temporal characterization of plasma-based seeded soft-X-ray lasers

Soft-X-ray lasers (SXRLs) based on plasmas provide a more compact and accessible alternative to FELs for the generation of high-energy pulses in the XUV and soft-X-ray domains [4]. These laser-driven plasmas can be produced in solid [230] or gaseous targets [11], where a population inversion is created for a specific electron transition. However, while these sources are able to provide very high pulse energies of the order of $10\,\mathrm{mJ}$ [231], they are based on amplified spontaneous emission (ASE) and are thus weakly coherent, generating pulses with durations of several picoseconds [232]. In order to produce shorter and coherent pulses, a laser-driven plasma can be used as an amplifier for a high-harmonic seed pulse. Plasma-based seeded SXRLs were first demonstrated in the year 1995 [233], providing weak amplification of the seed, while maintaining a significant incoherent ASE background.

Significant experimental and theoretical progress has been made in recent years towards the generation of coherent pulses with higher energies and shorter durations with these sources, such as the ones found in Colorado State University in the United States [234], LASERIX in France [235] or the Salle Jaune laboratory in LOA [11]. However, full temporal characterization of plasma-based seeded SXRL pulses has not been performed so far. Doing so could lead to better understanding of the plasma dynamics taking place in these sources, by comparing the results with the pulse profiles predicted by numerical simulations.

In this section, the basic properties of plasma-based seeded SXRLs are presented. Then, the viability of a single-shot technique allowing for full temporal characterization of seeded SXRL pulses is demonstrated. The proposed technique is based on spectrally resolved spatial interference between the seeded SXRL pulse and a previously characterized reference pulse.

4.4.1 Theory and basic properties of plasma-based seeded soft-X-ray lasers

The first seeding experiment where saturation was reached was carried out in 2004 [11]. This was achieved by focusing the high-harmonic seed pulse to high intensity on the entrance of the amplifier, vastly improving the amplification factor with respect to previous experiments. A low-density plasma, providing little refraction, was produced in a 4-mm-long Kr gas cell, pumped longitudinally by an IR laser, and the delay between plasma creation and the arrival of the seed was modified to provide maximum amplification. The population inversion was created for a transition in Kr^{8+} ions, providing high gain at $\lambda = 32.8\,\text{nm}$, which corresponds to the 25^{th} harmonic of a Ti:Sapphire laser. The linear polarization of the output pulse was observed to match that of the seed prior to amplification. This result has also been found for circularly polarized seed pulses [236].

Despite reaching saturation, a weak ASE background was still present. It was found to have much higher divergence than the amplified seed, so this incoherent radiation could be filtered with an aperture if necessary. However, ASE can be rendered much less significant by further improving the seed amplification. Additionally, the estimated Fourier transform-limited duration of the SXRL pulse obtained in this experiment was estimated to be close to $500\,\text{fs}$.

4.4.1.1 Collisionally pumped plasma amplifiers

In order to generate shorter and more energetic pulses from seeded SXRLs, the creation of suitable plasma amplifiers is required, since they determine the pulse properties. In a laser-driven plasma, the pump pulse first ionizes electrons from the target. Then, the pulse heats the plasma, transferring kinetic energy to the free electrons. Finally, these electrons collide with the ions, creating the population inversion between energy levels of their bound electrons. This process is known as *collisional pumping* [4], where two regimes can be distinguished depending on the characteristics of the pump laser [237]:

- **Quasi-steady-state** (QSS). In this regime, the plasma is pumped by a single, long laser pulse with nanosecond-scale duration. Most of the pulse energy is absorbed by ionization, plasma expansion and other phenomena. The timescales of these processes are similar to the pump pulse duration, and thus strongly compete with the collisional pumping. For this reason, high pump energies are required. Additionally, the collisions between lasing ions have a timescale lower than $10\,\mathrm{ps}$, so the ion population is never far from local thermodynamic equilibrium, thus providing low gain and requiring long plasmas of several centimeters to achieve saturation.

- **Transient collisional excitation** (TCE). In this regime, two laser pulses are used to create the plasma. The first, long pulse with moderate energy is used to ionize the plasma, creating weak population inversion. A second, ultrashort pulse then interacts with the existing plasma several nanoseconds later. Its energy is efficiently transferred to the electrons as kinetic energy, inducing very strong pumping. The plasma is far from local thermodynamic equilibrium during a few picoseconds, during which the gain is very high, thus achieving saturation faster than QSS and allowing for shorter plasmas, with lengths of some millimeters. In some setups, the first pulse is instead substituted by a sequence of two shorter pulses delayed by hundreds of picoseconds [234, 238].

4.4.1.2 Numerical simulations

It must be noted that, since seeded SXRLs are based on a specific transition of bound electrons, the gain bandwidth is several times narrower than that of the seed, thus imposing a relatively long Fourier transform-limited duration of several hundreds of femtoseconds [239]. The conditions to generate ultrashort pulses with energies of the order of millijoules can be studied by means of numerical simulations of plasma hydrodynamics, as well as the interaction of the plasma and the high-harmonic seed.

The spatiotemporal evolution of a collisionally pumped plasma can be modeled by ARWEN, a 2D hydrodynamic code with radiation transport [240], which has also been used in other fields such as inertial confinement fusion or laboratory astrophysics, and has thus been thoroughly benchmarked. The code solves equations of radiation hydrodynamics with thermal conduction in order to obtain plasma parameters such as electron density and temperature, or the ionization fraction [237]. These parameters can then be postprocessed with a three-level atomic model to obtain the gain coefficient and saturation fluence, by taking into account collisional excitation and collisional radiative de-excitation of the energy levels [241]. Based on this model, several numerical studies have been conducted to find ways to increase the gain coefficient in the TCE scheme, as well as the pumping efficiency [242], defined as the ratio between output energy and pump pulse energy. The plasma width was found to have a very significant effect on both these parameters, which can be vastly optimized by increasing the width from tens to hundreds of microns, as well as reducing the length to only a few millimeters. However, large widths of several millimeters can cause transversal lasing from the plasma, resulting in energy losses.

Hydrodynamic simulations cannot, however, provide information about the spatial and temporal profile of the seed pulse during and after amplification, or the energy it extracts from the plasma. It is thus necessary to model the amplification of the XUV pulse along the amplifier, by using the Maxwell-Bloch model [237]. A time-dependent model is necessary due to the different time scales involved in the process, tens of femtoseconds for the seed pulse duration, and several picoseconds for the plasma lifetime. The DEEPONE code is an example of a time-dependent Maxwell-Bloch code [243]. In short, this model first solves the Maxwell wave equation in a plasma using the slowly varying envelope approximation, thus obtaining the electric-field propagation through the plasma, amplification by the polarization density, and damping by the free-electron current. Finally, the standard rate equations, coupled with the electric field, are used to calculate the populations of the energy levels involved in the amplification.

Numerical studies with such computer models revealed that the temporal structure of a seeded SXRL pulse is multicomponent, and does not only consist of the amplified seed [244, 245]. The output pulse consists of ASE, the amplified seed and a wake field with a complex structure, which can last for several picoseconds due to the polarization of the plasma by the seed. Further numerical studies can lead to minimizing the wake by optimizing seed amplification, thus opening the way towards ultrashort seeded SXRLs. Figure 4.19 (a) shows the simulated temporal profile obtained with the DEEPONE code at different parts of the plasma amplifier using parameters from the experiment of Wang *et al.* [246], as calculated by Oliva *et al.* [243].

The seed, being much more intense than the ASE, immediately polarizes the plasma, which creates a wake at the beginning of the amplifier, whose duration increases until matching the time scale of the polarization. For longer distances within the plasma, amplification is saturated and the wake starts to become shorter and develop structures like Rabi oscillations [245]. The high-harmonic seed pulse, however, is only weakly amplified.

Further study of the evolution of the plasma polarization gives valuable information about the creation and amplification of the wake field [237]. Oliva *et al.* found that there is a delay between the arrival of the seed and the appearance of polarization at the beginning of the plasma, with its rising time being of tens of femtoseconds. Assuming a seed pulse of $20\,\mathrm{fs}$, the maximum polarization is found almost at the end of the seed, and thus it is weakly amplified [243]. The depolarization time is of the order of picoseconds, and is the cause of the long wake field. The latter can be reduced while amplification can be enhanced by matching the seed duration to the polarization time scale. This can be done by using a longer seed and by increasing the electron density, which increases the collisions that depolarize the medium, thus shortening the polarization decay. A simulation obtained with a longer seed of $200\,\mathrm{fs}$ and a higher density can be seen in figure 4.19 (b), where the amplified seed is much more significant than the wake field. Additionally, a wider plasma was used to increase the extracted energy, as expected from ARWEN simulations.

Seeding the amplifier at higher intensities means that the seed will saturate the plasma and thus end the population inversion, in turn preventing the appearance of ASE and the wake. They can also be inhibited by shortening the plasma, at the cost of lower amplification. As a way of implementing these two strategies without compromising the output pulse energy, the use of two amplifiers has been proposed, in which the output of the short pre-amplifier, free of ASE and wake, is used as the seed for the main one [247, 248].

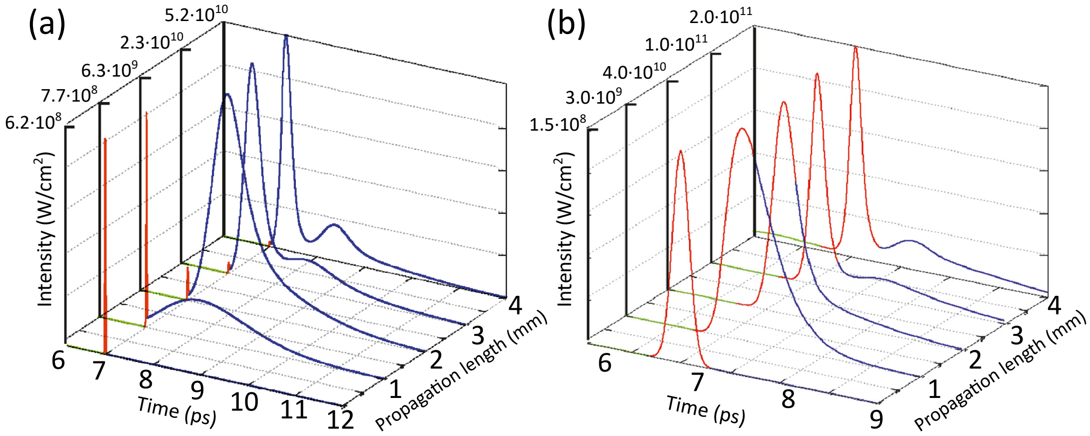

Figure 4.19: Calculated temporal intensity profile of two SXRL pulses at different parts of their respective plasma amplifiers, illustrating that seeding a wider plasma with a longer, more energetic high-harmonic pulse can lead to higher output energies and shorter durations. (a) Modeling of the Wang et al. experiment, with a 20-fs, 50-pJ seed pulse. The electron density is n_e=1.2·10^{20} cm^{-3}, and their temperature is T_e=550 eV. The plasma has a size of 4 mm x 30 μm. (b) Result of seeding a plasma of size 4 mm x 100 μm with a 200-fs, 1.5-nJ pulse, with n_e=2.2·10^{20} cm^{-3} and T_e=531 eV. The colors represent the ASE (green), amplified seed (red), and wake (blue), and the intensity is normalized for easier visualization. Taken from [237].

4.4.2 SEA TADPOLE for plasma-based seeded soft-X-ray lasers

Temporal characterization of seeded SXRL pulses is of particular interest due to the asymmetric and complex temporal structures predicted by Maxwell-Bloch simulations, as shown above. Here, we propose the transfer to the XUV and soft-X-ray spectral ranges of an existing, single-shot characterization technique based on referenced interferometry, called *SEA TADPOLE* (spatially encoded arrangement for temporal analysis by dispersing a pair of light E-fields) for the full temporal characterization of a plasma-based seeded SXRL pulse. A numerical simulation is presented as a means to showcase the phase extraction procedure.

4.4.2.1 Choice of characterization method

Numerical simulations predict pulses with complex temporal profiles due to the presence of the amplified seed, the wake radiation and the ASE. In certain cases, Rabi oscillations can be present. Since they do not provide information about the phase, autocorrelation and cross-correlation measurements are not enough to reveal such structures within the pulse. Full temporal characterization can be carried out with a FROG CRAB scheme. However, it requires the use of a magnetic bottle time-of-flight photoelectron spectrometer, a device that is expensive and complex. Additionally, this technique intrinsically requires a high number of shots for a single measurement, thus assuming shot-to-shot stability in the source. Single-shot methods are thus preferred. SPIDER-based methods have the potential to work in a single-shot regime if the test pulse provides enough signal. However, they cannot be used with seeded SXRLs due to the narrow gain bandwidth in the plasma, which prevents the creation of the spectrally sheared replica pulses. Seeding the plasma with two spectrally sheared high-harmonic pulses would thus not affect the spectral content of the amplified pulses.

Since high-harmonic pulses have already been temporally characterized with the HHSPIDER technique [188], it is theoretically possible to use referenced FTSI, using the high-harmonic seed pulse as a reference to characterize the SXRL pulse. However, given the narrow spectra typically obtained after amplification, a spectral resolution better than $\Delta\lambda/\lambda = 10^{-6}$ would be required in order to resolve the fringes. As a solution, we propose the use of a spatially encoded arrangement for referenced interferometry. By encoding the spectral phase in the spatial, rather than spectral, domain, the required spectral resolution is not as strict. A resolution allowing for a direct measurement of the SXRL spectrum, of the order of $\Delta\lambda/\lambda = 10^{-5}$, is sufficient.

4.4.2.2 Basics of the SEA TADPOLE technique

Created in the year 2006, SEA TADPOLE is an existing technique for the characterization of ultrashort IR pulses [249, 250], but has never been applied to the XUV and soft-X-ray domains. It is based on spectrally resolved spatial interference between the unknown pulse and a reference pulse, whose spectral phase is measured beforehand. In the original scheme for IR lasers, the two pulses are sent through two parallel and single-mode optical fibers. One fiber is located at a distance d above the optical axis, and the other at the same distance below it. After the fibers, a spherical lens with focal length f is used to cross the beams in the vertical plane at a small angle 2θ. The beams are then sent to a 2D spectrometer, producing a 2D interferogram with spatial and spectral information. The θ angle is defined by $\tan\theta = d/f$. Since the angle is small, by expressing it in radians, it follows that $\tan\theta = \sin\theta = \theta = d/f$.

The original setup can be seen in figure 4.20. In order for spatial interference to occur, both pulses must be temporally synchronized. Additionally, the spectrum of the reference must at least include that of the test pulse, while not necessarily having the same central wavelength.

4.4.2.3 Adaptation to plasma-based seeded soft-X-ray lasers

This technique can be used for full, single-shot temporal characterization of seeded SXRLs, by using a replica of the high-harmonic seed as a reference. As a first step, the reference should be characterized with a technique such as HHSPIDER. However, in the XUV range, optical fibers and lenses cannot be used in the same way. For this reason, the beams are simply sent to the 2D spectrometer with a small angle of 2θ along the

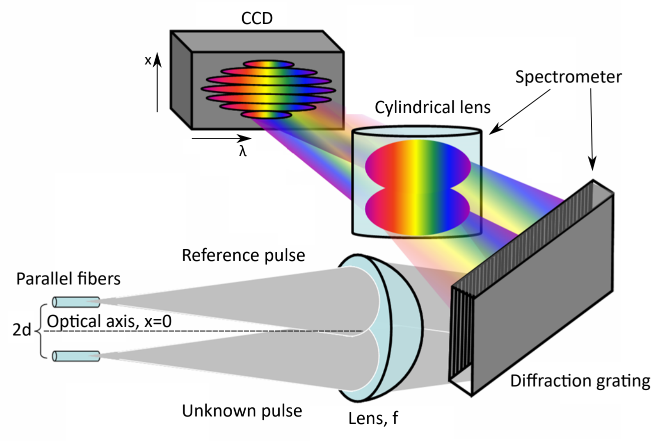

Figure 4.20: Original experimental setup for SEA TADPOLE with IR pulses. Both pulses enter the system through two parallel optical fibers. Then, a spherical lens is used to cross the beams in the vertical direction at a small angle given by its focal length f and the distance 2d between the fibers, making them overlap on the CCD. The same lens collimates the beams in the horizontal direction, before they are sent to a spectrometer based on a diffraction grating and a cylindrical lens placed afterwards. The use of a cylindrical lens ensures that the crossing angle is not affected. Taken from [249, 250].

vertical axis, with the spectral information being contained along the horizontal axis. A schematic drawing of the proposed setup is presented in figure 4.21.

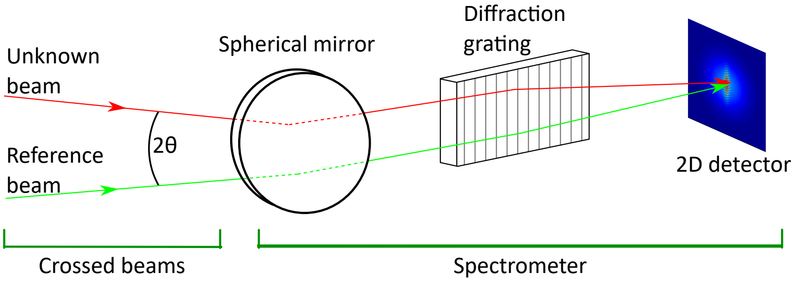

Figure 4.21: Schematic drawing of the proposed experimental setup for the use of the SEA TADPOLE technique for characterization of a seeded SXRL. A simple spectrometer is shown for the sake of visualization.

The resulting 2D interferogram, consisting on spectrally resolved spatial fringes, follows the equation:

$$S(\omega,x) = S_{unk}(\omega) + S_{ref} + 2\sqrt{S_{ref}(\omega)}\sqrt{S_{unk}(\omega)}\cos\left[2kx\sin\theta + \Phi_{unk}(\omega) - \Phi_{ref}(\omega)\right], \tag{4.22}$$

where $S_{\mathrm{unk}}(\omega)$, $S_{\mathrm{ref}}(\omega)$, $\Phi_{\mathrm{unk}}(\omega)$, and $\Phi_{\mathrm{ref}}(\omega)$ are the spectra and spectral phases of the unknown and reference pulses, respectively, and θ is the half-angle between the pulses, as seen in the figure.

Note that equation 4.22 implies that spherical wavefronts are assumed for both beams, with the same radii of curvature. Experimental measurements confirm that the wavefronts of both high-harmonic beams and seeded SXRLs are indeed spherical. In particular, experimental results presented in section 1.3.2 of this thesis show that high-harmonic beams having spherical wavefronts with RMS errors lower than $\lambda/3$ can be generated. Section 1.3.3 reports the measurement of high-harmonic wavefronts with RMS errors close to $\lambda/10$, generated by using a deformable mirror with the IR driving beam. Seeded SXRLs have been shown to have spherical wavefronts as well. In particular, seeding a plasma with a high-harmonic beam of wavefront RMS $\lambda/2$ has been observed to produce an output with an RMS of $\lambda/5$ [234]. It is thus realistic to assume spherical wavefronts for the sake of simplicity. Additionally, the equation can be modified to include different radii of curvature if necessary.

4.4.2.4 Numerical demonstration

A simulation is presented here in order to showcase the use of the technique and the phase extraction procedure. The pulse parameters are based on experimental data from the seeded SXRL located in the Salle Jaune laboratory of LOA [11]. The two pulses are assumed to have Gaussian spectra. The high-harmonic reference pulse has a FWHM bandwidth of $\Delta\omega_{\mathrm{ref}} = 1.39 \cdot 10^{14}\,\mathrm{rad/fs}$, supporting a FWHM Fourier transform-limited duration of $20\,\mathrm{fs}$, similar to the duration measured with the HHSPIDER technique [188]. The smaller bandwidth of the unknown SXRL pulse, $\Delta\omega_{\mathrm{unk}} = 1.85 \cdot 10^{13}\,\mathrm{rad/fs}$, supports a minimum FWHM duration of $150\,\mathrm{fs}$, similar to theoretical estimates [238, 247]. For simplicity, both pulses have the same central wavelength, $\lambda = 32.8\,\mathrm{nm}$, although this is not required by the method.

Seeded SXRL simulations often predict an asymmetrical temporal profile of the output pulse due to the wake emission. This could be explained by the presence of an asymmetrical spectral phase, such as TOD, or higher, odd orders of dispersion. In this case, the unknown pulse has a GDD of $10^4\,\mathrm{fs}^2$, and a TOD of $10^6\,\mathrm{fs}^3$. The reference pulse has a GDD of $-5 \cdot 10^3\,\mathrm{fs}^2$ and no TOD. The spectra and spectral phases of both pulses is shown in figure 4.22. The temporal profile of the unknown pulse is included as well.

We assume that the 2D spectrometer is based on a CCD camera consisting on $2048\mathrm{x}2048$ square pixels of side $13\,\mu\mathrm{m}$, with a spectral resolution of $\Delta\lambda/\lambda = 10^{-5}$. Since equation 4.22 assumes spherical wavefronts with the same curvature for both pulses, the source-CCD distance is assumed to be the same. Thus, the different beam sizes on the CCD are due to their different divergences. HHG usually leads to beams with divergences of the order of $1\,\mathrm{mrad}$, while SXRL has lower divergence, closer to $0.5\,\mathrm{mrad}$. Their spatial profiles are assumed to be Gaussian. The image produced by each beam on the CCD is presented in figure 4.23.

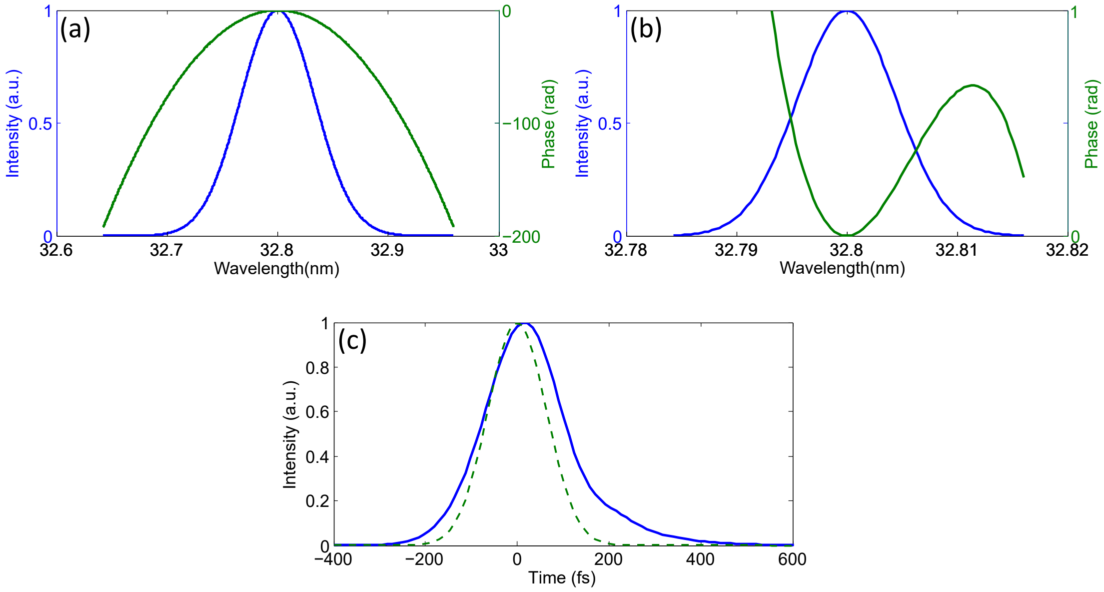

Figure 4.22: Spectrum (blue lines) and spectral phase (green lines) of the high-harmonic reference (a) and the unknown SXRL (b) pulses, and temporal profile (c) of the unknown pulse (solid line) compared to the transform-limited pulse (dashed line).

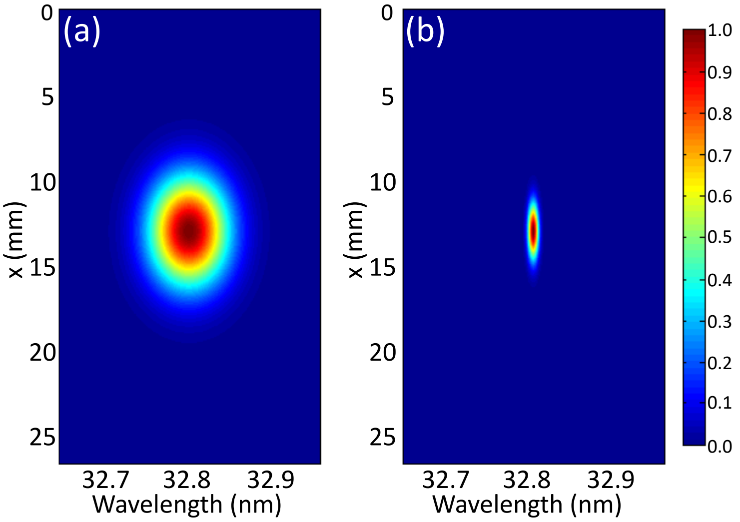

Figure 4.23: Simulated images produced by the reference (a) and unknown (b) pulses on the CCD chip. The reference is bigger due to a higher divergence and broader spectrum. Only half of the full range of the spectrometer is shown.

The beams, temporally synchronized and forming an angle of $\theta = 0.25^\circ$ along the vertical direction, produce the 2D interferogram shown in figure 4.24 (a). In order to maximize fringe visibility, the same intensity is assumed for both beams. Naturally, this would not be the case in an experimental measurement, where the higher intensity of the SXRL would reduce the contrast. Note that the fringes are *tilted* due to the variation of the interfringe with wavelength. The fringes are also *curved*, reflecting the shape of $\Phi_{\text{unk}}(\omega) - \Phi_{\text{ref}}(\omega)$. If a reference with flat phase is used, the interferogram directly replicates the shape of Φ_{unk}.

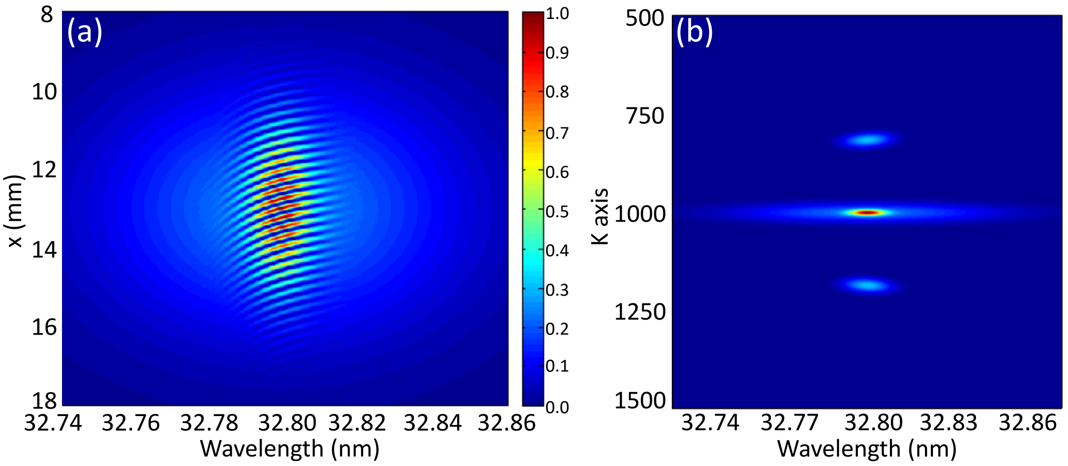

Figure 4.24: (a) Interferogram produced by the reference and unknown pulses in the 2D spectrometer (zoom) and (b) result of the 1D Fourier transform along the x axis (zoom), showing the central band and the sidebands.

Similarly to referenced FTSI, the first step to obtain the spectral phase of the SXRL pulse is to perform a 1D Fourier transform. In this case, this is done in the x direction, not in the spectral one. The resulting 2D image, presented in figure 4.24 (b), contains a central band and two sidebands at different positions of the K axis, of which one is filtered.

After filtering, an inverse Fourier transform is applied, and the phase term is extracted, obtaining $2kx\sin\theta + \Phi_{\text{unk}}(\omega) - \Phi_{\text{ref}}(\omega)$. To retrieve the phase of the unknown pulse, the phase of the reference pulse and the spatial interference term must be subtracted. The latter term depends linearly with the angular frequency, since $k = \omega/c$, so it does not change the measured temporal profile. This is analogous to the calibration term $\omega\tau$ that appears in referenced FTSI and SPIDER (see sections 4.1.2.3 and 4.1.2.4).

The spectral phase $\Phi_{\text{unk}}(\omega)$ is thus obtained from the interferogram. The spectrum of the SXRL, $S_{\text{unk}}(\omega)$, can be measured directly by simply blocking the reference beam. Alternatively, it can also be extracted from the interferogram if $S_{\text{ref}}(\omega)$ is known (see equation 4.22). A comparison between the input and calculated spectral phases can be seen in figure 4.25 (a). The same comparison is made in the temporal domain in figure 4.25 (b), demonstrating that the phase of a seeded SXRL can be accurately retrieved with this technique.

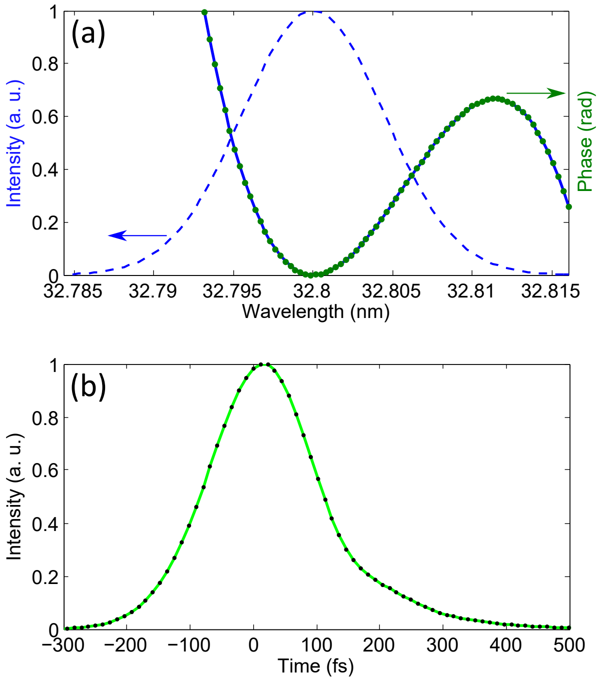

Figure 4.25: Comparison of the input and calculated SXRL pulses: (a) input (blue solid line) and calculated (green circles) spectral phases, with the pulse spectrum also included (blue dashed line), and (b) input (green solid line) and calculated (black circles) temporal profile.

4.4.2.5 Discussion

SEA TADPOLE is a technique for full temporal characterization of ultrashort light pulses, already demonstrated in the IR range but not yet transferred to the XUV and soft-X-ray ranges. It can, in principle, allow for single-shot measurements, in turn allowing for the study of the shot-to-shot stability of plasma-based seeded SXRL, by using a replica of the high-harmonic seed pulse as a reference, whose spectral phase must be obtained beforehand through other characterization techniques.

The experimental setup is simple, consisting only of a 2D spectrometer, towards which the two beams are sent at a small angle, and the spectral phase is retrieved with a fast, non-iterative calculation. The main challenges for the experimental implementation of the technique are the high spectral resolution required, of the order of $\Delta\lambda/\lambda = 10^{-5}$, due to the narrow SXRL spectrum, and the small angles between the beams that lead to broad spatial fringes, generally $2\theta < 0.5°$. Although challenging, an experimental implementation of this scheme can lead to valuable information about seeded SXRL pulses, and ultimately about the validity of numerical simulations of the laser-produced plasmas used in these sources.

4.5 Summary

Being able to measure the duration of XUV pulses is fundamental for applications involving time-resolved measurements, as well as the development of sources capable of generating shorter pulses. Additionally, experimental measurements can be compared with the results of numerical simulations, thus giving insight into the physics involved in these sources. While many techniques exist for full temporal characterization of IR laser pulses, this is still challenging in the XUV range, especially since most existing schemes for IR pulses are based on nonlinear phenomena.

XUV pulses, including those with attosecond durations, have been fully measured with the FROG CRAB technique in recent years. This technique, however, requires the acquisition of multiple shots, thus assuming source stability. This stability is not always found for the case for coherent XUV sources, which are based on nonlinear phenomena. Additionally, FROG CRAB requires the use of a magnetic bottle time-of-flight photoelectron spectrometer, an expensive and complex device. Any characterization technique aimed at providing single-shot measurements, as well as using a simple setup, must be source-specific.

A new technique based on SPIDER has been proposed in this chapter for single-shot temporal metrology in seeded XUV FELs working in the HGHG regime, and designed for the particular case of the FERMI facility. The technique is based on a twin-seeding scheme, in which two temporally delayed and spectrally sheared replica pulses seed the electron beam. The FEL thus emits two XUV pulses whose spectral shear is the original one multiplied by the harmonic order, and is thus tunable. The two XUV replicas then interfere spectrally, which is measured with an on-line spectrometer, so that it is not invasive for users. This scheme is supported by a proof-of-principle experiment carried out at LOA, and numerical FEL simulations based on the PERSEO code, and has the advantage over other schemes of not requiring any specific manipulation of the electron beam.

Temporal characterization of SXRLs seeded by high-harmonics is more complex since the narrow gain bandwidth prevents the use of the same strategy described above. In this chapter, the use of the SEA TADPOLE technique for seeded SXRLs has been proposed. This scheme requires a reference pulse, which can be found in a replica of the high-harmonic seed that must be previously characterized by a method such as HHSPIDER. The experimental setup is relatively simple and the scheme allows for single-shot measurements, in turn allowing for real-time monitoring and optimization of the source.

CHAPTER 5

Temporal compression and chirped pulse amplification of XUV pulses

---

Contents

Chirped pulse amplification (CPA) is a technique for the amplification of ultrashort laser pulses allowing for high peak powers to be achieved, first implemented in the year 1985 [21]. For example, in the case of a solid-state laser, the high peak power achieved by a pulse upon amplification can cause damage to the amplifier crystal, as well as non-linear propagation due to self-focusing. This can be prevented by temporally stretching the pulse prior to amplification by propagating it through a dispersive medium or optical system to reduce its peak power, and recompressing it afterwards back to its initial duration. This potential to generate higher peak powers makes CPA schemes very attractive for XUV sources such as seeded FELs [228] or SXRLs seeded by high harmonics [248], where implementation faces different challenges than for the visible or IR domains.

This chapter reports the first experimental implementation of the CPA technique in a seeded XUV FEL. First, section 5.1 discusses the basic characteristics of pulse compression and CPA in solid-state lasers, as well as the challenges faced when implementing it for the amplification of XUV pulses. Section 5.2 shows the details of the CPA experiment, carried out in the FERMI facility. Lastly, section 5.3 discusses the properties of optical compressors based on conical diffraction, which can provide much higher efficiencies at the cost of a more complex design.

5.1 Principles of chirped pulse amplification

The stretching and compression of the amplified pulse is done by introducing to it a known linear frequency chirp or GDD (see section 4.1.1). In order to achieve this, optical pulse *compressors* and *stretchers* based on reflective diffraction gratings are used. The spectral phase that these systems introduce to the pulse can be obtained from geometrical considerations.

In this section, the characteristics of optical compressors and CPA in solid-state lasers are presented. The motivations and challenges of transferring this technique to XUV sources are discussed as well.

5.1.1 Optical pulse compressors and stretchers

The use of a pair of diffraction gratings to create a pulse compressor was first proposed in the year 1969 [251]. In an optical grating-pair compressor, two plane gratings are placed in parallel to each other. When the pulse is propagated through the compressor, the first grating introduces angular dispersion, and the second one recollimates the beam. This introduces frequency chirp to the light pulse, since each spectral component travels a different optical path between the gratings.

The geometry of the optical compressor presented in this section is based on the *classical* or *on-plane* diffraction mount, in which the incident and diffracted beams are all contained in a plane perpendicular to the grating's grooves. Classical diffraction is described by the expression [252]:

$$\sin\alpha + \sin\beta = n\lambda\sigma, \tag{5.1}$$

where α is the angle of incidence of the beam of wavelength λ on the grating with groove density (grooves per unit length) σ, which is diffracted with an angle β dependent on the diffraction order n. Alternatively, the groove separation $d = 1/\sigma$ can be used as well. Note that negative diffraction orders may not be present for high enough values of α, since β becomes an imaginary number following equation 5.1. The angles are defined with respect to the normal to the grating surface, as illustrated in figure 5.1.

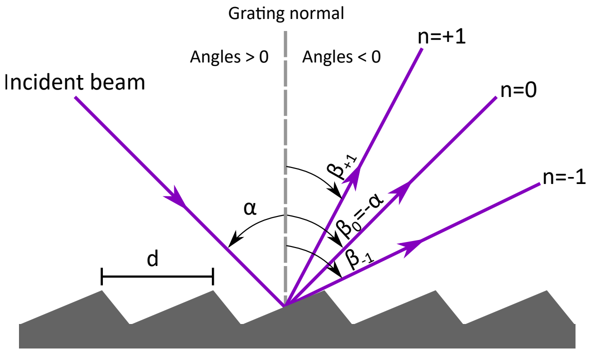

Figure 5.1: Schematic drawing showing the relevant angles and their sign convention. All angles are measured from the normal, and α is always positive. The zeroth diffraction order corresponds to specular reflection.

Figure 5.2 shows a schematic drawing of the grating-pair compressor under study, highlighting the relevant distances. P is the distance between the centers of the gratings, and D is the distance between the planes containing the grating surfaces.

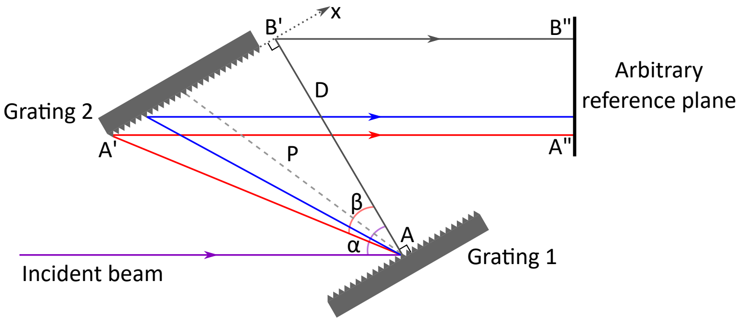

Figure 5.2: Schematic drawing of a grating-pair compressor based on classical or on-plane diffraction mount. The incident beam is diffracted at the point A and arrives at the wavelength-dependent point A' on the second grating. The direction of propagation is retrieved upon diffraction by the second grating. The red and blue colors represent different wavelengths, each traveling different paths. Based on [251, 253].

The spectral phase introduced by the gratings in the laser pulse is given by the wavelength-dependent optical path traversed by each spectral component, with the form [251, 253]:

$$\Phi(\omega) = \Phi_1(\omega) + k \cdot AA' + \Phi_2(\omega) + k \cdot A'A'', \tag{5.2}$$

where $\Phi_1(\omega)$ and $\Phi_2(\omega)$ represent the dephasing introduced by each grating, given for each one by the phase difference between the diffracted and incident beams:

$$\Phi_{1,2} = \Phi_{1,2_d} - \Phi_{1,2_i} = k_{d_x} x - k_{i_x} x, \tag{5.3}$$

where k_{i_x} and k_{d_x} are the wave vectors of the incident and diffracted beams, respectively, projected onto the x axis. Taking equation 5.1 into account, the dephasing introduced by the grating pair is:

$$\Phi_1 + \Phi_2 = 2\pi\sigma n A'B', \tag{5.4}$$

where the point B' is a projection of the point A onto the plane of the second grating. The dephasing is equivalent to a $2\pi n$ phase jump at each grating groove included between B' and A' [251].

With the diffraction equation, it can be seen that $AA' = \frac{D}{\cos\beta}$, and geometrical considerations lead to $A'A'' = B'B'' - A'B'\sin\beta - A'B'n\lambda\sigma$. The sum of these distances yields $AA' + A'A'' = B'B'' + D\cos\beta - A'B'n\lambda\sigma$. Combining this result with equations 5.2 and 5.4, and using $k = \frac{\omega}{c} = \frac{2\pi}{\lambda}$, the spectral phase introduced by the gratings in the laser pulse is found to be:

$$\Phi(\omega) = \frac{\omega}{c} B'B'' + \frac{\omega}{c} D\cos\beta. \tag{5.5}$$

With this result, analytical expressions for any order of dispersion can be found by deriving the phase with respect to the angular frequency ω. It must be noted that $B'B''$ is an arbitrary constant distance that vanishes upon second order derivation, having no effect on pulse duration. The second- and third-order derivatives yield the following expressions for the GDD and TOD [253]:

$$\mathrm{GDD} = -\frac{D\sigma^2\lambda^3 n^2}{2\pi c^2 \cos^3\beta} \tag{5.6}$$

$$\mathrm{TOD} = -\frac{3}{\omega}\mathrm{GDD}\left(1 + \frac{\sin\beta}{\omega\cos^2\beta} 2n\pi c\sigma\right). \tag{5.7}$$

Note that these equations are often shown for the particular case $n = -1$ in the literature. They show that a grating-pair compressor in classical mount always provides negative GDD. In order to stretch the pulse before amplification, positive GDD must be introduced to it. This can be done by propagating the pulse through a dispersive medium, such as a piece of glass, or with the use of a pulse stretcher, which also allows for finer control. A grating-based pulse stretcher is based on the same principles as an optical compressor. In this case, however, the gratings are set in antiparallel configuration, and a focusing system, based on lenses or mirrors, is placed between them in order to invert the sign of the GDD [254].

It must be noted that, in a single-pass setup, both compressors and stretchers introduce *spatial chirp* to the pulse. This means that there is a spatial variation of wavelength across the spatial profile (see figure 5.2). This can be avoided by placing a flat mirror at the end of the system to create a double-pass scheme, additionally doubling the compression or stretching effects.

In the example of a solid-state laser, the properties of the amplifying crystal limit the maximum peak power that can be obtained. Further amplification results in unwanted effects such as self-focusing or appearance of defects, which is avoided by stretching the initial pulse by a factor higher than 10^3 prior to amplification, thus reducing its peak power, which in turn allows for higher amplification, of a factor of 10^6 or more [255]. Then, the pulse is compressed back to its initial duration. All the IR lasers used in the experiments reported in this thesis are based on CPA.

5.1.2 Chirped pulse amplification with XUV sources

Transferring CPA to the XUV range can significantly increase the peak power obtained in existing facilities. However, the low efficiency of diffraction gratings in this spectral range, generally of a few percent even with grazing incidence, remain the main obstacle for the implementation of the technique. For this reason, single-pass stretchers and compressors might be preferred, despite the resulting spatial chirp. Moreover, a pulse stretcher requires additional focusing optics, further reducing its efficiency.

In the case of plasma-based SXRLs seeded by high-harmonics, seed pulses usually have durations of the order of $100\,\mathrm{fs}$, or lower. However, the gain lifetime in a laser-produced plasma has a much longer duration, typically of several picoseconds. As a consequence, only a small fraction of the available energy is used for amplification. The transfer of CPA to these sources has been proposed as a solution, since stretching the seed to match the gain duration vastly increases the energy output, according to hydrodynamic simulations [248].

CPA has also been proposed for seeded FELs [228, 229], and has already been experimentally implemented in spectral domains such as the deep ultraviolet [256]. Since the temporal properties of the seed pulse are transferred to the XUV output, an ultrashort FEL pulse can only be obtained if the electron beam is seeded by an ultrashort pulse. A typical seed pulse duration in the FERMI facility is of the order of $100\,\mathrm{fs}$, while the electron beam duration is closer to $1\,\mathrm{ps}$. This means that only a portion of the electrons transfer their kinetic energy to the pulse, limiting the amplification. By stretching the seed pulse to match the electron beam duration, the energy transfer can be optimized to a great extent. Additionally, the use of a stretched seed pulse increases the bandwidth of the output, so that CPA can lead to pulse shortening as well as higher pulse energies.

This is expanded upon in the following section.

The implementation of CPA in a seeded FEL requires only the addition of an XUV compressor at the output. No additional optics have to be installed to stretch the seed, since this can be done with the IR pulse compressor installed at the end of the CPA chain of the Ti:Sapphire laser which creates the seed by THG. Since it is a double-pass compressor, the seed is always free of spatial chirp. Another possibility is to propagate the seed pulse through a known dispersive material, such as a piece of glass.

5.2 Experimental implementation of chirped pulse amplification in a seeded free-electron laser

Several methods have been proposed in the past to obtain ultrashort pulses in FELs [257, 258, 259, 260, 261]. However, in these methods, the energy of the output pulse is limited by the reduced number of electrons used in the amplification process. Some theoretical schemes have also been proposed to increase the peak power of the output pulse to terawatt levels [262, 263]. Nonetheless, in all cases, the pulse shortening is limited by the FEL gain bandwidth. Additionally, none of the proposed methods allow for control of the spectro-temporal properties of the generated light, which is a key requirement for the generation of fully coherent pulses [15].

These restrictions can be overcome by applying CPA schemes to seeded FELs based on HGHG [228, 229, 256, 264]. Stretching the seed pulse allows to extract energy from the whole electron bunch, significantly increasing the FEL pulse energy at saturation. On the other hand, the bandwidth of an FEL pulse seeded by a chirped pulse increases with the harmonic order n. In doing so, the aforementioned restriction due to the low FEL gain bandwidth can be overcome, thus removing the limit on the shortest FEL pulse that can be obtained with optical compression [265, 266].

In this section, the experimental implementation of CPA in a seeded XUV FEL is reported. The experiment was carried out in the Low Density Matter beamline of the FERMI facility, introduced in section 4.3.1, as a result of a collaboration between FERMI, CNR Istituto di Fotonica e Nanotecnologie (CNR-IFN), the Max Planck Institute for the Structure and Dynamics of Matter (MPSD), IST, and LOA. The results of the experiment were published in [267].

5.2.1 Towards shorter FEL pulse duration through CPA

An FEL pulse generated by seeding the electron bunch with a Gaussian laser pulse with FWHM duration $(\Delta\mathrm{t})_{\mathrm{seed}}$ is expected to have a quasi-Gaussian pulse profile, with duration $(\Delta\mathrm{t})_{\mathrm{FEL}}$. According to the literature [268], the duration of the FEL pulse in standard working conditions (that is, without CPA) is:

$$(\Delta\mathrm{t})_{\mathrm{FEL}}^{\mathrm{no\,CPA}} \simeq \mathrm{n}^{-\alpha}(\Delta\mathrm{t})_{\mathrm{seed}}, \tag{5.8}$$

where α is a factor depending on the regime in which the FEL is operated, positive and smaller than $1/2$, and n is the harmonic order. Due to the frequency upconversion through HGHG, the temporal phase profile of the FEL pulse is n times that of the seed pulse. For this reason, if the seed carries a strong chirp, and assuming the longitudinal electron-beam energy profile to be almost flat, the FEL pulse will also carry a strong chirp. In this high-chirp regime, the GDD of the FEL pulse that must be compensated by the optical compressor is related to the GDD of the seed by the relation $\mathrm{GDD}_{\mathrm{FEL}} \simeq \mathrm{GDD}_{\mathrm{seed}}/\mathrm{n}$.

It can be demonstrated that, in the presence of a strongly chirped seed pulse, the FEL pulse bandwidth, $(\Delta\omega)_{\mathrm{FEL}}$, scales according to the relation:

$$(\Delta\omega)_{\mathrm{FEL}} = \mathrm{n}^{1-\alpha}(\Delta\omega)_{\mathrm{seed}}, \tag{5.9}$$

where $(\Delta\omega)_{\mathrm{seed}}$ is the seed pulse bandwidth. In the following, we focus on the case of an FEL in moderately saturated regime, which corresponds to $\alpha \simeq 1/3$ [268]. Equation 5.9 highlights a key difference between traditional CPA in solid-state lasers and in seeded FELs. While in a solid-state laser, the spectrum of the amplified pulse is essentially identical to that of the seed, in the case of a seeded FEL, the output bandwidth can be significantly larger than that of the seed. This is due to two competing phenomena. On one hand, the frequency upconversion process increases the FEL pulse bandwidth with respect to that of the seed by a factor n. On the other hand, this effect is partially counteracted by the dynamic reduction of the FEL pulse duration caused by the nonlinear laser-electron interaction inside the modulator, accounted for by the factor α.

From equation 5.9, the shortest FEL pulse duration that can be obtained after compression, $(\Delta\mathrm{t})_{\mathrm{FEL}}^{\mathrm{min}}$, is calculated as:

$$(\Delta\mathrm{t})_{\mathrm{FEL}}^{\mathrm{min}} = \frac{(\Delta\mathrm{t})_{\mathrm{seed}}^{\mathrm{TL}}}{\mathrm{n}^{1-\alpha}}, \tag{5.10}$$

where $(\Delta\mathrm{t})_{\mathrm{seed}}^{\mathrm{TL}}$ is the Fourier transform-limited seed pulse duration.

5.2.2 Experimental setup

A schematic drawing of the experimental setup in the FERMI facility can be seen in figure 5.3, in which a chirped seed pulse temporally overlaps the electron bunch, creating a chirped FEL pulse, which is compressed by a grating-pair optical compressor. The characteristics or the optical compressor and the relevant parameters of the experiment are presented below.

5.2.2.1 The optical compressor

The compressor used in the experiment consists on four optical elements hosted in an ultra-high vacuum chamber: two diffraction gratings (G_1 and G_2 in figure 5.3), forming a grating-pair compressor in classical geometry, and two plane mirrors (M_1 and M_2 in

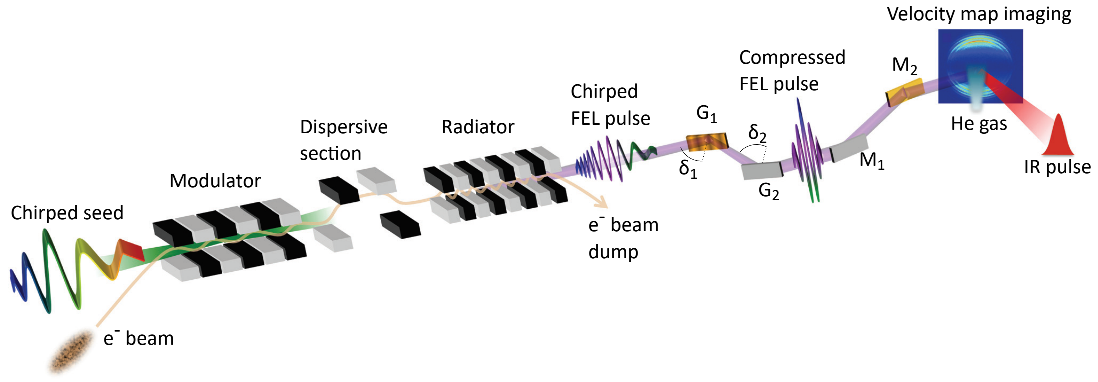

Figure 5.3: Schematic drawing of a seeded FEL in CPA mode. In this regime, the electron bunch is seeded with a Gaussian pulse carrying a linear frequency chirp. Under proper conditions, this chirp is transmitted to the FEL harmonic pulse, and can be compensated with an optical compressor installed after the radiator, consisting on two gratings and two plane mirrors. The FEL pulse duration is measured by cross-correlation with an infrared pulse.

figure 5.3), which direct the beam back to its original propagation axis. The gold-coated gratings have a uniform groove density of $\sigma = 600\,\mathrm{mm}^{-1}$, with a blaze angle [269] of 2° and a ruled area of $100\mathrm{x}25\,\mathrm{mm}^2$. The plane mirrors are also gold-coated, with a surface of $150\mathrm{x}40\,\mathrm{mm}^2$. All optics are mounted on motorized translation and rotation stages for alignment during FEL operation. G_1 and M_2 can be moved away from the optical path with the use of external translation stages, allowing the beam to bypass the compressor if necessary. Figure 5.4 shows a drawing of the top view of the compressor, including the relevant distances.

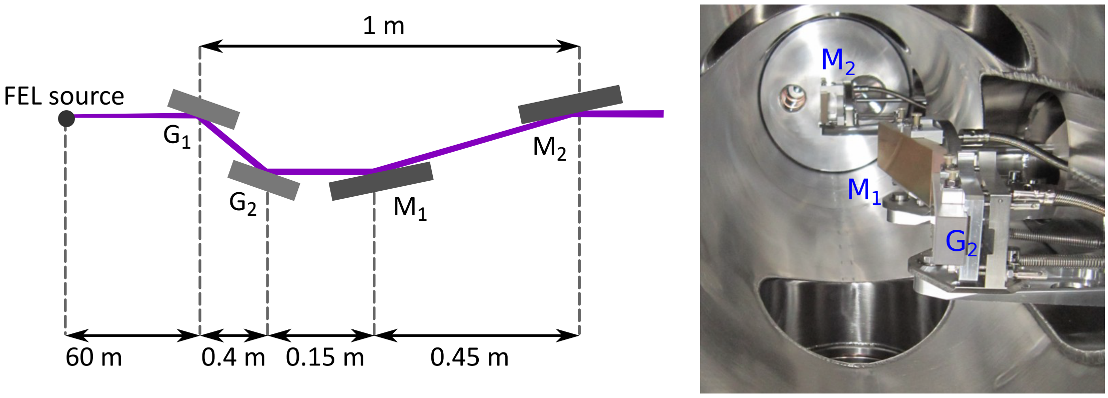

Figure 5.4: The pulse compressor used in the experiment: (left) schematic drawing including the distances between the optics and (right) photograph of the optics inside the chamber, during installation.

The GDD introduced in the FEL pulses can be varied by changing the incidence angles on the gratings, δ_1 and δ_2 (see figure 5.3). By changing these angles, the first or zeroth diffraction orders can be used, providing no compression in the latter case. Both angles can be set between -0.5° and 14.5°, with a resolution of $65.8\,\mu\mathrm{rad}$ per full step, and the controllers can provide $1/8$-step resolution. By varying δ_2 independently from δ_1, the wavefront tilt due to the divergence of the FEL beam can be compensated.

Before the experiment, the efficiency of the diffraction gratings was measured at the CNR-IFN Padova for several wavelengths and angles, using a hollow cathode lamp as a source. The efficiency of the complete compressor was found to be of a few percent in all cases, as summarized in table 5.1, where K is the subtended angle between the incident and diffracted beams. Additionally, ray-tracing simulations showed that the effect of the spatial chirp introduced on the FEL pulse is negligible.

λ (nm)	*K (°)*	*Efficiency*
25.6	158	0.040 ± 0.013
25.6	162	0.030 ± 0.009
25.6	166	0.010 ± 0.004
30.4	158	0.063 ± 0.022
30.4	162	0.036 ± 0.012
30.4	166	0.008 ± 0.002
35.3	158	0.029 ± 0.009
35.3	162	0.012 ± 0.005
35.3	166	0.002 ± 0.001

Table 5.1: Total efficiency of the compressor for different values of included angle and wavelength.

5.2.2.2 FEL parameters

The seed was provided by the third harmonic of a Ti:Sapphire laser, with a Gaussian spectral profile centered in $\lambda_{\mathrm{seed}} = 261\,\mathrm{nm}$ and a FWHM bandwidth of $\sim 0.7\,\mathrm{nm}$, for a transform-limited duration of $(\Delta t)^{\mathrm{TL}}_{\mathrm{seed}} = 145\,\mathrm{fs}$. Due to nonlinear effects during harmonic generation and transport to the undulator entrance, its FWHM duration was instead $(\Delta t)^{\mathrm{no\,CPA}}_{\mathrm{seed}} = 170\,\mathrm{fs}$ before stretching. Its power at the entrance of the modulator was approximately $\sim 250\,\mathrm{MW}$.

The FEL was tuned to generate pulses at $\lambda_{\mathrm{FEL}} = 37.3\,\mathrm{nm}$, corresponding to the harmonic order $n = 7$. The electron-beam energy was tuned to $1.2\,\mathrm{GeV}$, and the peak electron current was set to approximately $500\,\mathrm{A}$. The typical electron bunch duration was about $\sim 1.2\,\mathrm{ps}$, and the electron beam profile, shown in figure 5.5, was nearly constant in the region of interaction with the seed pulse, with a small quadratic energy curvature around $10\text{-}15\,\mathrm{MeV/ps^2}$. The strength of the dispersive section was $R_{56} \simeq 50\,\mu\mathrm{m}$.

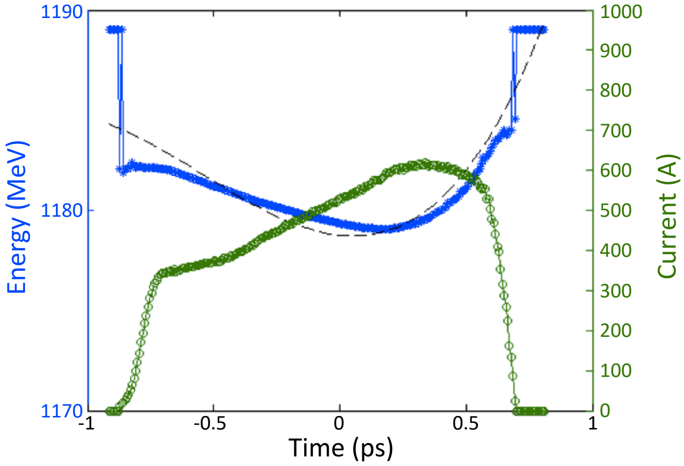

Figure 5.5: Example of electron beam profile obtained throughout the experiment. The energy profile is nearly flat for the duration of the seed pulse.

5.2.3 Results

It is important to note that the SPIDER scheme for seeded FELs presented in section 4.3.2 cannot be applied here, since the spectrally sheared pulse replicas would travel different paths in the grating compressor, therefore acquiring different phase and pointing. The FEL pulse duration was instead measured by means of cross-correlation [215] with a known infrared laser pulse with duration $90\,\mathrm{fs}$. The scheme relies on the measurement of the photoelectron distribution produced by ionization of a He gas sample as a function of the temporal overlap between the FEL and IR pulses. The delay was changed in steps of $20\,\mathrm{fs}$, with 500 shots accumulated for each step, to ensure a good signal-to-noise ratio.

Figure 5.3 includes an example of the photoelectron distribution measured with a velocity map imaging (VMI) spectrometer. It can be seen in more detail in figure 5.6 (a), with the main band highlighted. The photoelectron spectrum, as shown in figure 5.6 (b), consists of a main line, created by the direct photoionization process, and several sideband lines with lower and higher energies, which corresponding to two- and multi-photon ionization processes and whose yield depends on the FEL-IR temporal overlap. The photoelectron energy spectrum is reconstructed from the raw VMI data by using the MEVIR algorithm (maximum entropy velocity image reconstruction [270]). The spectrum is obtained for every value of the temporal delay by integrating the VMI signal over the angle of emission, leading to the results seen below in figure 5.7. Then, the cross-correlation curves are obtained for each sideband by plotting the total area under the corresponding peaks as a function of delay. The inset of the figure shows several cross-correlation curves obtained from the second sideband in standard conditions, before the seed pulse was stretched. The curves have a Gaussian profile.

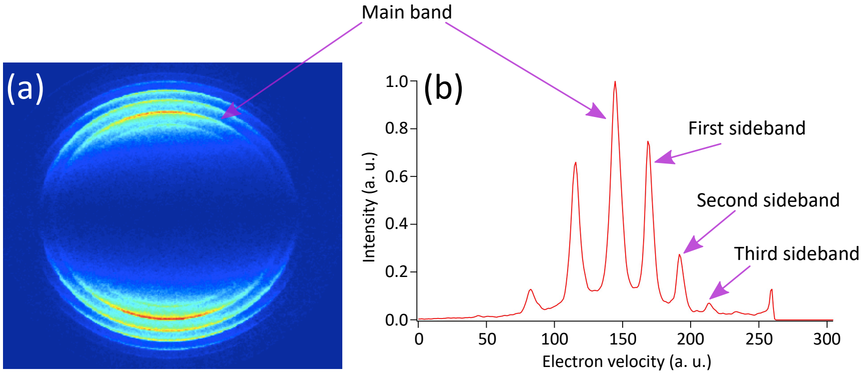

Figure 5.6: (a) Example of raw image from the VMI spectrometer, obtained by accumulating hundreds of FEL shots. One image is acquired at each FEL-IR delay in order to construct the cross-correlation curves. The distance from the center of the image represents the electron kinetic energy. (b) Example of photoelectron energy spectrum obtained from the VMI data, highlighting the sidebands that appear in the presence of the IR field. The second and third external sidebands are used to calculate the pulse duration.

The time jitter between the two pulses is neglected, and Gaussian temporal profiles are assumed. Additionally, moderate IR energies are used to avoid sideband saturation. In these conditions, the FEL pulse duration can be obtained from a curve with the following relation:

$$\Delta t_c = \sqrt{(\Delta t)^2_{FEL} + \frac{(\Delta t)^2_{IR}}{l}}, \tag{5.11}$$

where l is the sideband order, Δt_c is the FWHM of its corresponding cross-correlation curve, and $(\Delta t)_{IR} = 90\,fs$ is the known duration of the IR probe pulse. The second and third sidebands were used for the calculations, since they provided the best Gaussian fit. It will be shown below that the two sidebands produce nearly identical results. The data from higher-order sidebands do not have a good signal-to-noise ratio and are not suitable for the calculations. A deconvolved FEL pulse, measured before stretching the seed, is included in the inset of figure 5.7.

The first step of the experiment was to characterize the FEL spectrum and pulse duration in standard working conditions. The FWHM spectral width and duration were $(\Delta\lambda)_{FEL} = 3.8 \cdot 10^{-2}\,nm$ (equivalent to $(\Delta\omega)_{FEL} = 5.2 \cdot 10^{13}\,rad/s$ in the frequency domain) and $(\Delta t)^{noCPA}_{FEL} = 91\,fs$, respectively (see inset of figure 5.7), with fluctuations of a few percent between consecutive measurements. This result is in very good agreement with the theory, which predicts $89\,fs$. The time-bandwidth product of the FEL pulses is a factor of 1.7 above the Fourier-transform limit. This is due to chirp appearing on the FEL pulse [268], caused by two effects. First, the aforementioned initial chirp on the seed pulse, expected to provide the main contribution, and a residual quadratic chirp on the temporal profile of the electron-beam energy (figure 5.5).

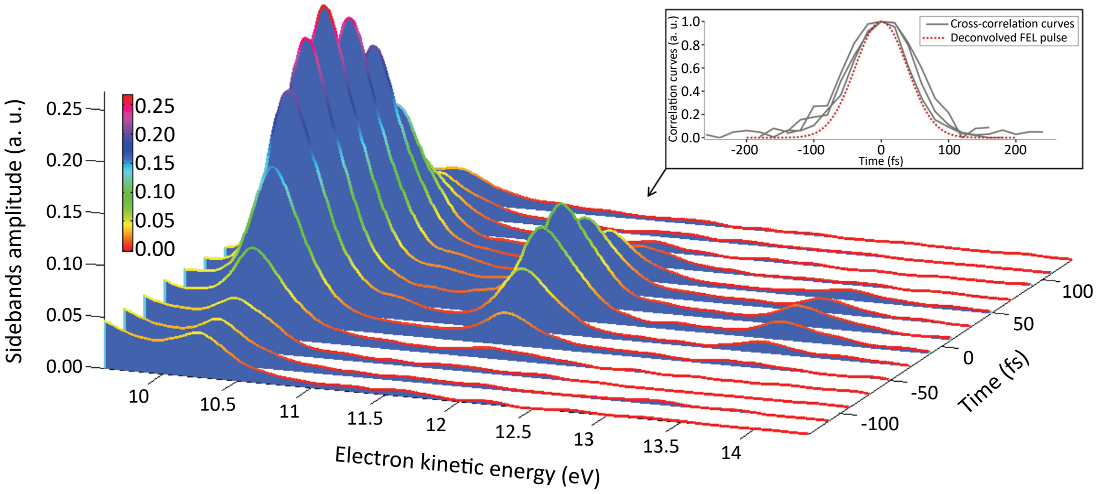

Figure 5.7: Photoelectron spectra, obtained by inverting the electron distributions measured with the VMI spectrometer, as a function of the delay between the FEL and IR pulses. This measurement was made with standard FEL working conditions, that is, with no stretching of the seed pulse and no FEL compression. Only the first, second and third sidebands are presented, normalized with the main line, not shown. The inset shows three cross-correlation curves from different VMI measurements, obtained from the second sideband. The deconvolved pulse is also shown, with an estimated duration of 91 fs.

After taking the first measurements in standard conditions, we introduced positive linear frequency chirp in the seed pulse by propagating it through a calcium fluoride plate, stretching it to $(\Delta t)_{\mathrm{seed}}^{\mathrm{CPA}} = 290\,\mathrm{fs}$, and the FEL beam was sent through the compressor by placing G_1 and M_2 in the beam path. In these conditions, the FEL pulse duration was measured before and after compression, by using the zeroth and first diffraction orders of the gratings, respectively. Figure 5.8 (a) shows five single-shot spectra of the FEL with stretched seed. The average FWHM spectral width increased to $(\Delta\lambda)_{\mathrm{FEL}} = 4.46 \cdot 10^{-2}\,\mathrm{nm}$ (that is, $(\Delta\omega)_{\mathrm{FEL}} = 6.05 \cdot 10^{13}\,\mathrm{rad/s}$), with fluctuations of a few percent between consecutive measurements. The result is close to the value predicted by equation 5.9, that is, $(\Delta\omega)_{\mathrm{FEL}}/[7^{2/3}(\Delta\omega)_{\mathrm{seed}}] \simeq 0.85$.

Three independently measured cross-correlation curves obtained from the second sideband with the stretched seed pulse are shown in figure 5.8 (b) with no FEL pulse compression (zeroth diffraction order) and in figure 5.8 (c) with maximum compression. The deconvolved FEL pulses are included as well. Without compression, the pulse had a FWHM duration of $(\Delta t)_{\mathrm{FEL}}^{\mathrm{stretched}} \simeq 143\,\mathrm{fs}$, in good agreement with the theoretical expectation of $\sim 152\,\mathrm{fs}$. The increase of the FEL pulse bandwidth obtained by stretching the seed led to a significantly shorter pulse after compression, compared to the no-CPA case measured at the beginning of the experiment. The output pulse was compressed with a GDD of approximately $-1000\,\mathrm{fs}^2$ provided by the $\mathrm{n} = -1$ diffraction order of the gratings, leading to a minimum FWHM duration of the FEL pulse of $(\Delta t)_{\mathrm{FEL}}^{\mathrm{CPA}} \simeq 50\,\mathrm{fs}$, quite

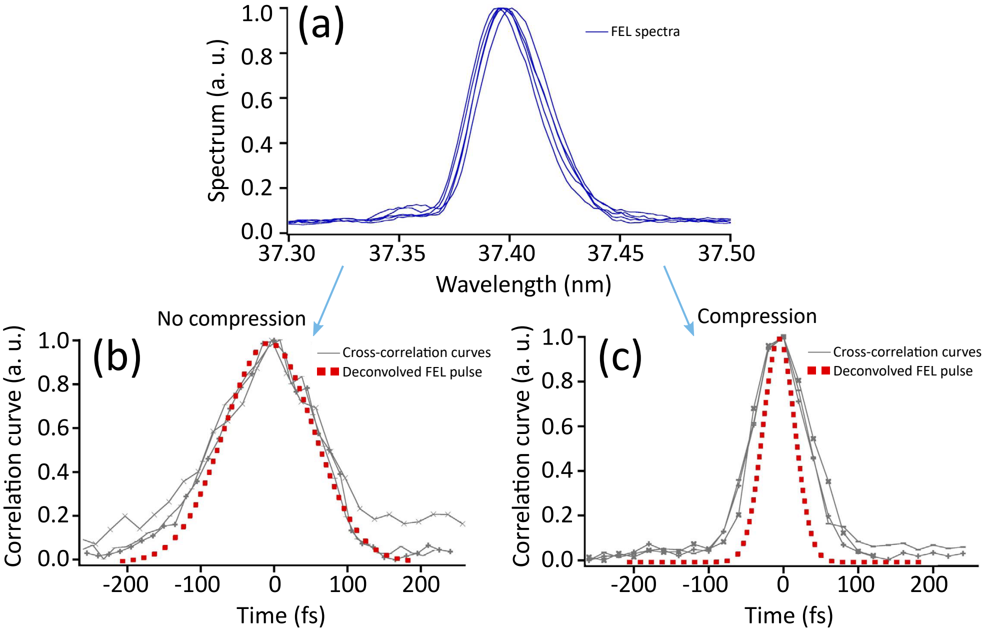

Figure 5.8: Spectro-temporal characterization of the FEL pulse, with stretched seed. (a) Normalized single-shot spectra. (b) Three independently measured cross-correlation curves obtained from the second sideband before FEL pulse compression. The dotted curve represents the deconvolved FEL pulse, assumed to be Gaussian. Calculated pulse duration is $\sim$ 143 fs. (c) Same as the latter, but with the grating angles providing maximum compression, for a pulse duration of $\sim$ 50 fs.

close to the value of $\sim 42\,\mathrm{fs}$ predicted by equation 5.10. In this case, the time-bandwidth product is above the Fourier-transform limit by a factor of only 1.1.

This result shows that the CPA technique is able to compensate not only the linear frequency chirp in the FEL pulse induced through the seed, but also the unwanted residual phase generated by other sources, such as the aforementioned seed transport and the quadratic curvature of the electron-beam energy profile (figure 5.5).

It was mentioned above that the incidence angles on the gratings (δ_1 and δ_2 in figure 5.3) could be changed independently. The effect of the compressor setting is shown in figure 5.9, in which the measured pulse duration is plotted as a function of $\delta_2 - \delta_1$. Additionally, pulse durations obtained from the second and third sidebands of the photoelectron spectra are reported in the figure, showing the good agreement between them.

5.2.4 Discussion

The results obtained in this experiment demonstrate the feasibility of CPA in a seeded XUV FEL, which can lead to a significant reduction of the FEL pulse duration with respect to that obtained in standard working conditions. In this experiment, the FEL pulse duration was shortened from $(\Delta \mathrm{t})_{\mathrm{FEL}}^{\mathrm{noCPA}} = 91\,\mathrm{fs}$ in standard operation to $(\Delta \mathrm{t})_{\mathrm{FEL}}^{\mathrm{CPA}} = 50\,\mathrm{fs}$ with CPA.

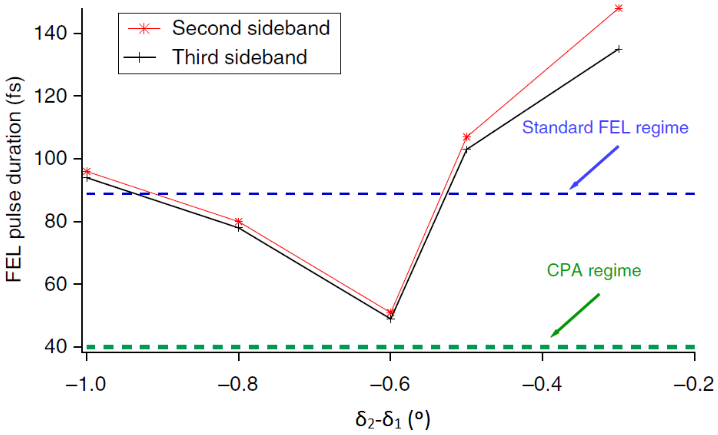

Figure 5.9: Measured FEL pulse duration as a function of the difference between the incidence angles on the gratings, calculated from the second and third sidebands of the photoelectron energy spectra. The horizontal dashed lines correspond to the pulse duration expected when the FEL is operated in standard working conditions (no seed stretching, no FEL compression) or in the CPA regime.

However, the low transmission of the compressor, close to 5%, and the low harmonic order $\mathrm{n}=7$ limited the obtained peak power to a fraction of a gigawatt. In order to increase this transmission, several authors have proposed the use the gratings in the so-called conical diffraction mount, which provides higher efficiencies [271]. Additionally, by choosing $\mathrm{n}>60$, feasible at FERMI [209], coherent, few-femtosecond gigawatt FEL pulses can potentially be generated.

5.3 Towards higher efficiencies: conical diffraction

Diffraction gratings used in the classical or on-plane mount provide poor efficiencies of a few percent for XUV radiation, even at low grazing angles, severely limiting the possibilities of the CPA technique. As a more efficient alternative, the use of optical compressors based on the *conical* or *off-plane* diffraction geometry has been proposed [272, 273, 274], since this geometry has experimentally shown efficiencies as high as 70% for wavelengths around $30\,\mathrm{nm}$ [269].

In this section, the design of grating-pair pulse compressors based on conical diffraction geometry is discussed, by analytically calculating the spectral phase they introduce in a pulse propagating through them, and deriving the resulting GDD and TOD.

5.3.1 Conical or off-plane diffraction mount

The term conical or off-plane diffraction mount refers to the case in which the incident beam is not perpendicular to the grating's grooves [275]. In this geometry, the direction of the incident beam is characterized by two angles instead of one: the altitude γ and the azimuth α. The directions of the diffracted orders are defined by the same altitude, and an output azimuth angle β. As such, the diffracted orders lie on a cone with half-angle γ, hence the name. This geometry is also referred to as off-plane mount due to the incident and diffracted beams not being contained in the plane of incidence, as is the case for the classical mount. A schematic drawing highlighting the relevant angles can be seen in figure 5.10. For a beam of wavelength λ diffracted by a grating of uniform groove density σ, the angles are related by the expression [275]:

$$\sin\gamma(\sin\alpha+\sin\beta) = n\lambda\sigma, \tag{5.12}$$

where n is the diffraction order. This equation shows that on-plane diffraction (see equation 5.1) can be seen as a particular case of the more general off-plane diffraction, when $\gamma = 90°$.

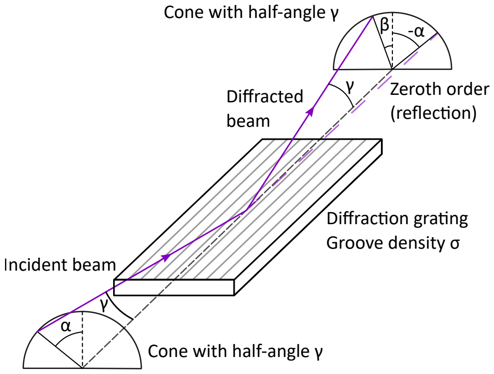

Figure 5.10: Geometry of the conical diffraction mount. As with classical diffraction, for the zeroth order, β=$-\alpha$.

A comparison of the two configurations can be found in figure 5.11, which shows two images obtained after diffracting a high-harmonic beam with the same grating in on-plane and off-plane geometries, highligthing the different distributions of the diffracted beams. We obtained both images in the Salle Orange beamline of LOA with a PI-MTE CCD camera. The harmonic beam, generated in a 15-mm-long gas cell filled with argon, was diffracted by a gold-coated reflective grating with $\sigma = 5670\,\text{mm}^{-1}$ used in grazing incidence for higher efficiency. The grating's grooves have a sinusoidal profile.

In both images, a green dashed line is used to highlight the plane and the cone containing the reflected and diffracted beams. In the classical case, the grating surface was placed vertically, and the angle of incidence was $\alpha = 62.3°$. Additionally, a spherical mirror was placed before the grating to highlight the different harmonic orders, similar to a simple spectrometer. For the conical geometry, $\gamma = 15°$ and $\alpha = 0°$ were used. It can be seen from the equation of conical diffraction that $\alpha = 0°$ causes both the positive and negative diffraction orders to be symmetric with respect to the specular reflection. Indeed, $\beta_{n=+1} = -\beta_{n=-1}$. The labeling of an order as positive or negative is thus arbitrary in this case, as included in the picture.

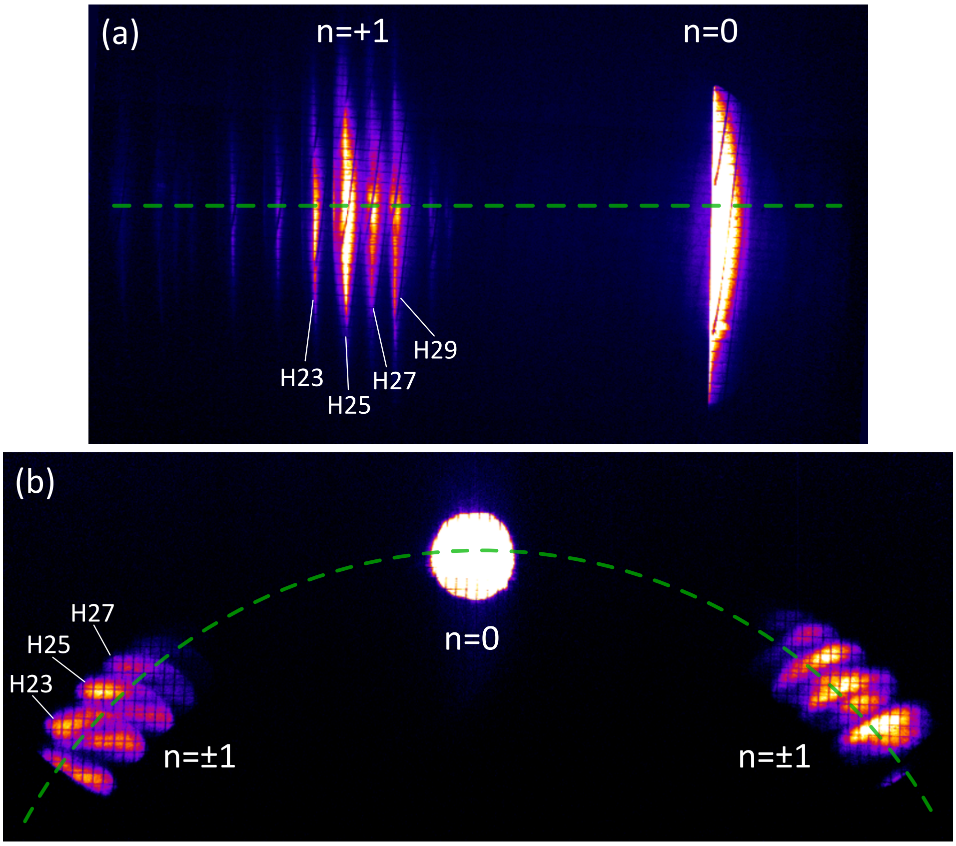

Figure 5.11: High-harmonic beam diffracted by a reflective grating in the classical (a) and conical (b) mounts. A green line is used in both cases to represent the plane and the cone which contain all diffraction orders. Several harmonic orders are labeled. The second image is a composition of two separate acquisitions obtained by moving the CCD camera. 100 pulses were accumulated in all cases. The grid-like structure observed within the illuminated areas is caused by the filters used to block the IR beam.

5.3.2 Grating-pair compressors in conical diffraction geometry

The grating-based compressor geometry under study consists on two parallel diffraction gratings used in the off-plane mount. As with a classical compressor, in order to calculate the spectral phase introduced by the system in a light pulse propagated through it, we must first obtain the wavelength-dependent optical path of a beam. We assume the pulse makes a single pass through the compressor. By analogy with classical compressors (see section 5.1), the phase follows the structure:

$$\Phi(\omega) = \Phi_1(\omega) + \frac{\omega}{c} \cdot P_1 + \Phi_2(\omega) + \frac{\omega}{c} \cdot P_2, \tag{5.13}$$

where P_1 is the distance that the beam travels after being diffracted by the first grating until reaching the second one, P_2 is the distance the beam travels after being diffracted for a second time until arriving at a reference plane. Both distances are wavelength-dependent and will be obtained by means of geometrical considerations analogous to the ones used in the classical case. The dephasing $\Phi_1(\omega) + \Phi_2(\omega)$ represents a $2\pi n$ phase change for each of the grooves included between the point where the beam reaches the first grating and the point where it reaches the second one [251] (see equation 5.4). Figure 5.12 presents a schematic drawing of the setup, including the relevant distances.

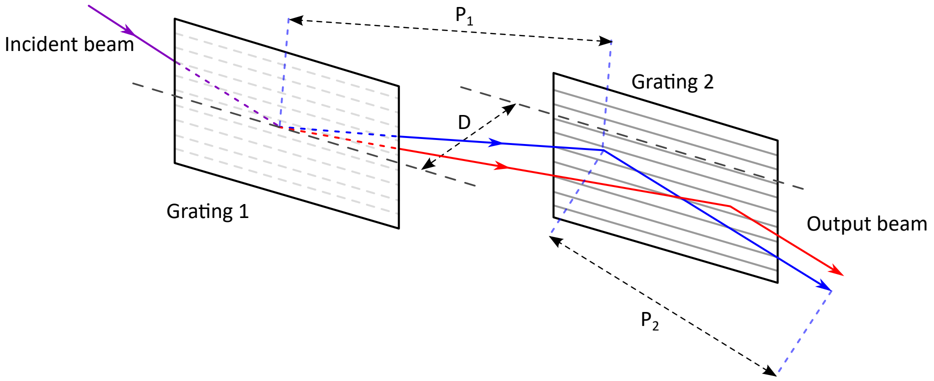

Figure 5.12: Schematic drawing of a grating-pair compressor using conical diffraction mount. The two dashed grey lines used to define the normal distance D are contained in the planes containing each grating. The red and blue colors represent different wavelengths, each traveling different paths. Note that the output beam is spatially chirped in this single-pass setup.

We define a Cartesian coordinate system in which the x axis is parallel to the grooves and y is perpendicular. We then place the origin of coordinates $(0,0,0)$ at the point where the incident beam intercepts the first grating. The diffracted beam then travels a distance of P_1 until reaching the second grating at the point (x_2, y_2, z_2), with $z_2 = D$, the normal distance between the gratings. The projection of P_1 onto the yz plane yields $P_{yz} = P_1 \sin\gamma$. By projecting this result onto the z axis, we obtain $z_2 = D = P_1 \sin\gamma \cos\beta$, thus leading to:

$$P_1 = \frac{D}{\sin\gamma\cos\beta}. \tag{5.14}$$

This, in turn, allows us to obtain the values of x_2 and y_2. Projecting P_1 onto the x axis leads to $x_2 = P_1 \cos\gamma = \frac{D}{\tan\gamma\cos\beta}$, and projecting P_{yz} onto the y axis leads to $y_2 = P_1 \sin\gamma \sin\beta = D\tan\beta$.

The next step consists on calculating the distance P_2 traversed by the ray between (x_2, y_2, z_2) and a reference plane perpendicular to the rays, placed at an arbitrary distance d. The distance from a point (X, Y, Z) to a plane $n_x x + n_y y + n_z z + d = 0$ is given by the general expression:

$$\mathrm{Dist} = \frac{|\mathrm{n_x X + n_y Y + n_z Z + d}|}{|\vec{\mathrm{n}}|}, \tag{5.15}$$

where $\vec{\mathrm{n}} = (\mathrm{n_x, n_y, n_z})$ is the normalized vector perpendicular to the plane and, by definition, also the vector defining the direction of the output rays. Since the gratings are parallel, the output azimuth angle of the second grating is α, the same as the input azimuth angle on the first one. As a consequence, a beam diffracted by the second grating has the direction:

$$\mathrm{n_x} = \cos\gamma, \qquad \mathrm{n_y} = \sin\gamma\sin\alpha, \qquad \mathrm{n_z} = -\sin\gamma\cos\alpha. \tag{5.16}$$

Following equation 5.15, $\mathrm{P_2}$ can be obtained as $\mathrm{P_2} = (\mathrm{n_x, n_y, n_z}) \cdot (\mathrm{x_2, y_2, z_2}) + \mathrm{d}$, leading to the final expression:

$$\mathrm{P_2} = \frac{\mathrm{D}\cos\gamma}{\tan\gamma\cos\beta} + \mathrm{D}\sin\gamma\sin\alpha\tan\beta - \mathrm{D}\sin\gamma\cos\alpha + \mathrm{d}. \tag{5.17}$$

The spectral phase introduced in the pulse by the compressor is thus:

$$\Phi(\omega) = \frac{\omega}{\mathrm{c}}\left(\frac{\mathrm{D}}{\sin\gamma\cos\beta} + \frac{\mathrm{D}\cos\gamma}{\tan\gamma\cos\beta} + \mathrm{D}\sin\gamma\sin\alpha\tan\beta - \mathrm{D}\sin\gamma\cos\alpha + \mathrm{d}\right) - 2\mathrm{n}\pi\sigma\mathrm{D}\tan\beta, \tag{5.18}$$

where the term $-2\mathrm{n}\pi\sigma\mathrm{D}\tan\beta$ is obtained from $\Phi_1 + \Phi_2 = -2\pi\mathrm{nN} = -2\mathrm{n}\pi\sigma\mathrm{y_2}$, with N being the number of grating grooves included between the points where the beam intercepts both gratings, analogous to the classical case [251].

Having found the analytical expression for the spectral phase, the expressions for GDD, TOD and any other dispersion order can be found by deriving it with respect to ω. While ω does not explicitly appear in the equation, it is encoded in β through equation 5.12. We thus make use of the chain rule and express the dispersion orders as a function of the derivatives of β, since $\left(\frac{d\Phi}{d\omega}\right) = \left(\frac{d\Phi}{d\beta}\right)\left(\frac{d\beta}{d\omega}\right)$.

It must be noted that the linear term $\frac{\omega}{\mathrm{c}}(-\mathrm{D}\sin\gamma\cos\alpha + \mathrm{d})$ will disappear upon second-order derivation, having no influence on the pulse duration. In fact, d is arbitrary, and a value of $\mathrm{d} = \mathrm{D}\sin\gamma\cos\alpha$ can be chosen for simplicity. The first derivative of the phase leads to the GD, which has no influence on the temporal shape of the pulse and has the form:

$$\begin{aligned}\mathrm{GD} = \left(\frac{d\Phi}{d\omega}\right) &= \frac{\mathrm{D}}{\mathrm{c}}\left(\frac{1}{\sin\gamma\cos\beta} + \frac{\cos\gamma}{\tan\gamma\cos\beta} + \sin\alpha\sin\gamma\tan\beta - \cos\alpha\sin\gamma\right) \\ &+ \frac{\omega\mathrm{D}}{\mathrm{c}}\beta'\left(\frac{\tan\beta}{\sin\gamma\cos\beta} + \frac{\sin\alpha\sin\gamma}{\cos^2\beta} + \frac{\cos\gamma\tan\beta}{\tan\gamma\cos\beta}\right) - \frac{2\mathrm{n}\pi\sigma\mathrm{D}}{\cos^2\beta}\beta',\end{aligned} \tag{5.19}$$

with:

$$\beta' = \left(\frac{d\beta}{d\omega}\right) = -\frac{A}{\omega^2\sqrt{1-(A/\omega-\sin\alpha)^2}}, \qquad \text{where} \quad A = \frac{2\pi n\sigma c}{\sin\gamma}. \tag{5.20}$$

By deriving again, the following expression for the GDD is found:

$$\begin{aligned} \mathrm{GDD} = \left(\frac{d^2\Phi}{d\omega^2}\right) &= \frac{D}{c}\left(\frac{\omega\sin\alpha\sin\gamma - 2n\pi\sigma c}{\cos^2\beta}\right)\left(2\beta'^2\tan\beta + \beta''\right) \\ &+ \frac{2D}{c}\beta'\left(\frac{\sin\beta(1+\cos^2\gamma)+\sin\alpha\sin^2\gamma}{\sin\gamma\cos^2\beta}\right) \\ &+ \frac{D\omega}{c}\left(\frac{1+\cos^2\gamma}{\sin\gamma\cos\beta}\right)\left(\frac{1+\sin^2\beta}{\cos^2\beta}\beta'^2 + \beta''\tan\beta\right), \end{aligned} \tag{5.21}$$

with:

$$\beta'' = \left(\frac{d^2\beta}{d\omega^2}\right) = \frac{A(-A^2+3A\omega\sin\alpha+2\omega^2\cos^2\alpha)}{\omega^5(1-(A/\omega-\sin\alpha)^2)^{3/2}} \tag{5.22}$$

Lastly, the third derivative of the spectral phase leads to the TOD:

$$\begin{aligned} \mathrm{TOD} = \left(\frac{d^3\Phi}{d\omega^3}\right) &= \frac{3D}{c}\frac{1+\cos^2\gamma}{\sin\gamma\cos\beta}\left(\frac{1+\sin^2\beta}{\cos^2\beta}\beta'^2 + \beta''\tan\beta\right) + \frac{3D\sin\alpha\sin\gamma}{c\cos^2\beta}\left(2\beta'^2\tan\beta + \beta''\right) \\ &+ \frac{D}{c}\left(\frac{\omega\sin\alpha\sin\gamma - 2n\pi\sigma c}{\cos^2\beta}\right)\left[\left(\frac{2}{\cos^2\beta} + 4\tan^2\beta\right)\beta'^3 + 6\beta'\beta''\tan\beta + \beta^{(3)}\right] \\ &+ \frac{D\omega}{c}\frac{1+\cos^2\gamma}{\sin\gamma\cos\beta}\left[\left(\frac{5\sin\beta+\sin^3\beta}{\cos^3\beta}\right)\beta'^3 + 3\left(\frac{1+\sin^2\beta}{\cos^2\beta}\right)\beta'\beta'' + \beta^{(3)}\tan\beta\right] \end{aligned} \tag{5.23}$$

with:

$$\begin{aligned} \beta^{(3)} &= \left(\frac{d^3\beta}{d\omega^3}\right) \\ &= \frac{A\left(4\omega^2\sin^2\alpha(3\omega^2-5A^2) + 2A\omega\sin\alpha(5A^2-9\omega^2) + 18A\omega^3\sin^3\alpha - 6\omega^4\sin^4\alpha - 2A^4 + 5A^2\omega^2 - 6\omega^4\right)}{\omega^4(-2A\omega\sin\alpha + A^2 - \omega^2\cos^2\alpha)^2\sqrt{1-\left(\frac{A-\omega\sin\alpha}{\omega}\right)^2}}. \end{aligned} \tag{5.24}$$

It was mentioned above that classical diffraction is essentially a particular case of the more general conical diffraction. As a consequence, it can be shown that choosing $\gamma = 90^\circ$ in equations 5.18, 5.21, and 5.23 leads to the corresponding expressions for the spectral phase, GDD and TOD of a classical compressor, presented in section 5.1.

The expressions for the GDD and TOD for compressors based on conical diffraction are, however, much more complex than their classical counterparts, so the influence of a given parameter is not very clear from the equations themselves. A parametric study is conducted to highlight each of them. Figure 5.13 shows the GDD and TOD introduced in a light pulse as a function of its central wavelength λ, in the XUV range. In this calculation, the other parameters are the same as those used in the CPA experiment conducted at FERMI and reported in section 5.2, i. e. groove density $\sigma = 600\,\mathrm{mm}^{-1}$ and diffraction order $n = -1$, with the centers of the gratings separated by a distance $P_1 = 0.4\,\mathrm{m}$. The main difference, however, is that the incidence is now described by two angles instead of one. Low values of γ are used, recreating the grazing incidence angles used in the experiment, close to 10°.

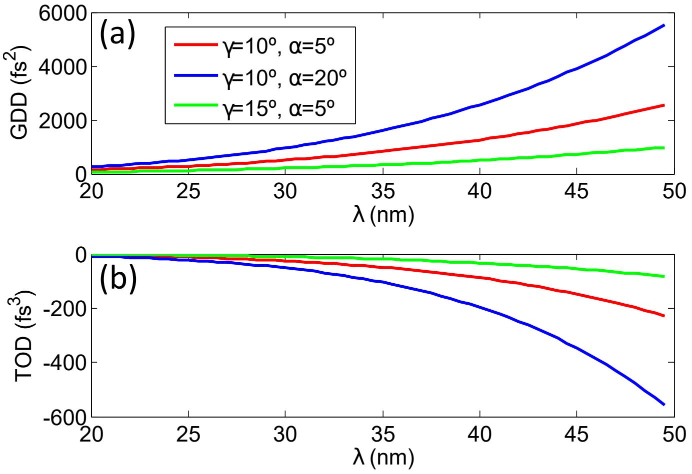

Figure 5.13: (a) GDD and (b) TOD introduced by the setup as a function of the central wavelength of the pulse for several values of altitude and azimuth. The gratings have a groove density of 600 mm^{-1} and their centers are placed at a distance of 0.4 m. The diffraction order is -1.

As with the classical case, both GDD and TOD increase nonlinearly with wavelength. However, these curves show a key difference between on-plane and off-plane compressors. As mentioned before, the GDD and TOD of a classical compressor are always negative and positive, respectively (see equations 5.7), while this can be the opposite for a conical diffraction-based compressor. The TOD is found to be negligible for these short wavelengths. The effect of groove density can be seen in figure 5.14. The central wavelength is chosen as $\lambda = 37.3\,\mathrm{nm}$, used in the experiment and generated as the 7th harmonic of the 261-nm seed pulse at FERMI.

The absolute values of both quantities are seen to increase rapidly with the density. It must be noted that gratings with several thousand mm^{-1} are commercially available, and can provide GDD of the order of $10^5\,\mathrm{fs}^2$ for XUV wavelengths in grazing incidence. In these two figures, it can be seen that the dispersion is, as expected from classical compressors, much higher when using grazing incidence angles.

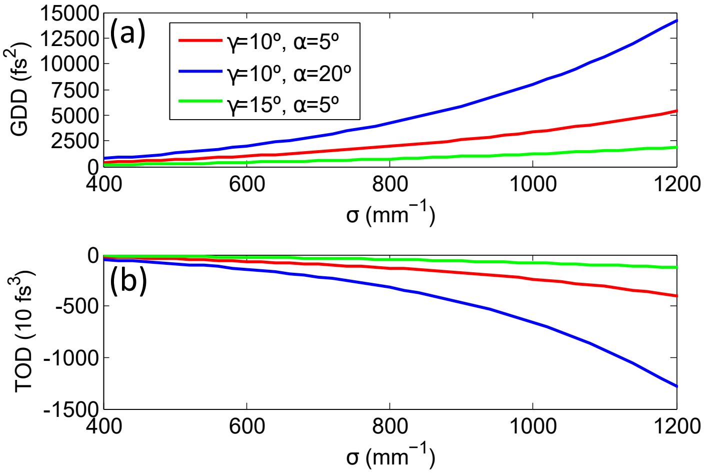

Figure 5.14: (a) GDD and (b) TOD introduced by the setup as a function of the groove density for several values of altitude and azimuth. The central wavelength is 37.3 nm, and the grating centers are placed at a distance of 0.4 m. The diffraction order is -1.

The influence of the angles α and γ can be seen in more detail in figure 5.15, for both $n = -1$ and $n = +1$. Essentially, the figure demonstrates that grazing incidence angles provide higher dispersion, with very large variations for lower values of γ and a less significant influence of α.

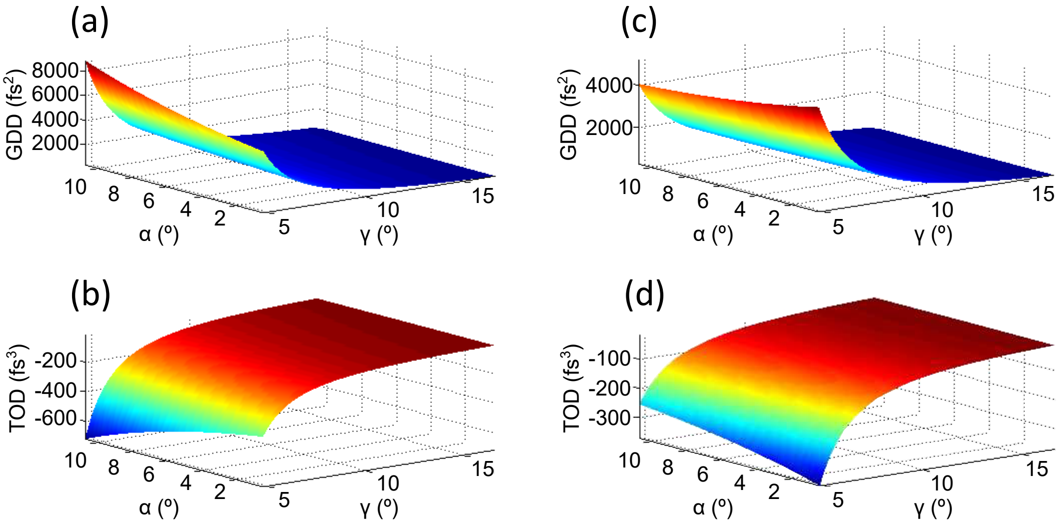

Figure 5.15: (a) GDD and (b) TOD introduced by the setup as a function of the azimuth and altitude angles for the -1 diffraction order and (c, d) for the +1 diffraction order. The central wavelength is 37.3 nm, and the gratings, with a groove density of 600 mm^{-1}, are placed at a distance of 0.4 m from each other.

For the sake of comparison, figure 5.16 shows how GDD and TOD vary with the angle of incidence α in a classical compressor, using the same values for all other parameters.

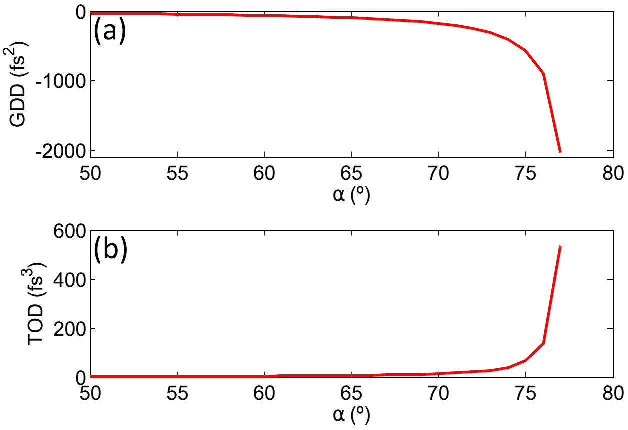

Figure 5.16: (a) GDD and (b) TOD introduced a compressor based in classical diffraction as a function of the angle of incidence for the -1 diffraction order. The central wavelength is 37.3 nm, and the gratings, with a groove density of 600 mm^{-1}, are placed at a distance of 0.4 m from each other.

5.3.3 Use with XUV sources

The fact that compressors based on conical diffraction mount can provide positive GDD, while classical compressors always provide negative values, can be useful when designing a CPA scheme.

In the case of CPA in a seeded XUV FEL, the GDD applied to the seed in order to stretch it could, in principle, have either sign, if it is provided by the compressor of the Ti:Sapphire fundamental laser. In the experiment reported in this chapter, positive GDD was applied by propagating the seed through a dispersive material, in a way that the XUV output had $\mathrm{GDD} \simeq +1000\,\mathrm{fs}^2$, then compensated with negative GDD introduced by the classical compressor. If conical diffraction is used instead, negative GDD should be applied to the seed, so no additional modification of the setup is necessary, besides the compressor itself.

For a seeded SXRL, the fact that both positive and negative chirp can be obtained by using each of the two geometries eliminates the need for a traditional pulse stretcher requiring additional optics, thus simplifying the system and increasing the overall efficiency. The high-harmonic seed pulse can be stretched with negative chirp by a classical compressor, while the output can be recompressed with a compressor in conical geometry. The lower efficiency of the classical mount would not be an issue in this case, since it is placed before amplification, while the higher efficiency of the conical mount makes it suitable for the output pulse.

5.4 Summary

The application of CPA vastly increased the pulse energy that could be obtained in optical lasers during the last decades. Transferring it to XUV sources will thus widen their range of applications. This chapter reports the first implementation of the CPA technique in a seeded XUV FEL, carried out at the FERMI facility. A stretched seed pulse can overlap with more electrons within the bunch, increasing the energy extracted from them. Additionally, it leads to an increased bandwidth of the output XUV pulse, which in turn allows for shorter pulses after compression when compared to standard operation. In this experiment, the pulse duration in standard operation, measured by cross-correlation with an IR pulse, was $91\,\mathrm{fs}$, while the use of CPA allowed for a reduced duration of $50\,\mathrm{fs}$. Further stretching the seed can lead to even shorter XUV pulse durations.

In the case of a SXRL seeded by high-harmonics, the seed has a typical duration of tens of femtoseconds, while the gain in the plasma has a lifetime of a few picoseconds up to several nanoseconds. Stretching the seed to match this duration can significantly increase the energy extracted during amplification, but this has not been experimentally implemented as of yet.

While this technique allows for enhanced amplification of the seed pulse, the output energy that can be reached is limited by the low efficiency of diffraction gratings in this spectral domain, typically of a few percent. This problem is more relevant in the case of a SXRL, since both the seed and the output are in the XUV domain, as opposed to the UV seed used in FERMI, which can be stretched more efficiently. Many authors have proposed the use of gratings in the conical or off-plane mount as a means to overcome this limitation, since efficiencies as high as 70% have been obtained with this geometry. The spectral phase introduced by a compressor based on a grating pair in conical geometry has been calculated in this chapter.

Conclusions and future developments

Ultrafast sources of XUV and soft-X-ray radiation are used today for a plethora of applications in many different fields of study. Further development of these sources in the near future will lead to better performance in their current applications, and extend their usefulness towards new ones. This development is mainly directed towards achieving higher intensities, as well as shorter pulse durations. This thesis discusses the topics of spatial and temporal metrology of ultrashort XUV pulses obtained with HHG in gases, seeded XUV FELs and plasma-based seeded SXRLs.

Increasing the intensity of ultrashort XUV pulses will allow, for instance, for better experimental accessibility to XUV nonlinear phenomena, or the realization of experiments based on XUV pump-XUV probe configurations. A straightforward solution involves increasing the pulse energies obtained in these sources. However, efficient focusing of the generated beams is also required in order to achieve high intensities. This, in turn, requires the use high-quality optics, as well as generating pulses with good wavefronts. Hartmann wavefront sensors provide a powerful tool for spatial metrology of XUV pulses, since they simultaneously provide their intensity profile and wavefront.

It is particularly interesting to improve the intensities that can be achieved with HHG sources, since this will allow for the use of tabletop setups to conduct experiments currently restricted to large-scale facilities such as FELs or synchrotrons. In this thesis, an XUV Hartmann wavefront sensor, built and calibrated at LOA, was used to study the spatial properties of single high-harmonic pulses obtained in loose focusing geometry, at LLC, as a function of the generation parameters. When averaged over five single-shot acquisitions, the measured wavefronts typically had $\mathrm{RMS} = \lambda_{\mathrm{H19}}/4$, with relative standard deviations of 15%, indicating good shot-to-shot stability. We also found that the conditions which provide the highest harmonic pulse energies were generally not the ones providing the best wavefronts, stressing the need for wavefront improvement in order to increase the intensity at focus.

All the high-harmonic wavefronts measured in the experiment were dominated by astigmatism at 0°, consistent with previous experiments performed at LOA and other laboratories, while all other aberrations remained much lower. In particular, the angle of astigmatism remained close to 10° throughout the whole experiment, but what defines this particular direction is not clear, since it is not affected by the direction of polarization of the IR driving pulses. Additionally, the IR wavefronts are free of astigmatism, showing that they are not directly transferred to the generated harmonic pulses. The two wavefronts are not unrelated, however, since we found through backpropagation that the harmonic source follows the shape and size of the IR focal spot. It seems that the basic shape of the harmonic beam is dictated by the IR focus, while the generation parameters, such as gas pressure, largely determine its wavefront. Numerical simulations of the HHG process might provide useful information on this topic in the near future.

By using three dielectric multilayer mirrors, we were also able to measure the wavefronts corresponding to single harmonic orders, revealing that lower orders are free of astigmatism and have wavefront RMS values of the order of $\lambda/10$, while the wavefronts of higher orders close to the cutoff are almost identical to that of the full beam. This result demonstrates that the wavefront in a high-harmonic beam is dominated by the higher and more aberrated orders, despite them being the least intense. This, in turn, means that the wavefronts of high-harmonic pulses can be significantly improved by filtering out the higher orders.

In order to further explore the link between IR and harmonic wavefronts, we performed a follow-up experiment, in which the HHG conditions were kept constant while the IR wavefront was changed by means of a deformable mirror. This induced significant changes in harmonic pulse energy, shape, size and wavefront throughout the experiment. In the best case, harmonic wavefronts with $\mathrm{RMS} < \lambda_{\mathrm{H19}}/11$ were obtained, significantly improving the previous measurements. This configuration was also the one providing the highest conversion efficiency. Interestingly, astigmatism at 0° still dominated the harmonic wavefronts in most cases, albeit to a lesser extent than before, even when the IR wavefront was free of astigmatism or it had angles close to 45°. Filtering out the cutoff orders when using the IR deformable mirror can potentially lead to diffraction-limited high-harmonic beams.

The astigmatism observed in the harmonic wavefronts can be corrected when focusing the beam with curved mirrors. The XUV Hartmann sensor was used in this thesis to accurately optimize the alignment of a focusing system based on two toroidal mirrors in grazing incidence, reducing the diameter of the harmonic focal spot by a factor of ~ 5 in a few minutes. The use of XUV Hartmann sensors for at-wavelength surface characterization of multilayer XUV optics with HHG was also demonstrated. These tests are generally restricted to synchrotrons, since the most common techniques, such as point diffraction interferometry, require high flux. The possibility of performing these tests in tabletop setups will be extremely useful and time-saving for manufacturers. However, currently existing XUV wavefront sensors have typical numerical apertures of the order of 0.01, which limits their range of applicability to beams with low divergence. As a solution, we recently developed an XUV wavefront sensor with $\mathrm{NA} = 0.1$, which will be used for focusing systems with short focal lengths and to study the wavefronts of divergent XUV pulses, such as those obtained via HHG in solid surfaces.

On the other hand, significant efforts are being made towards achieving shorter pulse durations with XUV sources, which will provide better temporal resolution for experiments dealing, for instance, with ultrafast dynamics of matter. In particular, sub-100-as pulses have already been obtained with HHG, in tabletop setups. Nevertheless, the possible applications of these attosecond pulses are limited by their low energies. For this reason, there is great interest in shortening the pulse durations obtained from seeded XUV FELs or seeded SXRLs, nowadays typically of the order of $100\,\mathrm{fs}$ or higher. It is important to stress, however, that the pulse durations obtained in these two sources are generally known by means of numerical simulations or incomplete measurements based on pulse correlation schemes. Furthermore, existing techniques for the full temporal characterization of XUV pulses are generally based on multishot schemes, thus requiring lengthy measurements and providing only averages. The development of accurate, reliable and single-shot methods for full temporal characterization of XUV pulses is fundamental in order to reduce pulse durations in the future. Two potentially single-shot schemes for temporal metrology in the two aforementioned sources have been proposed theoretically in this thesis. The implementation of these or similar techniques will provide accurate and real-time monitoring of the pulse duration, which will in turn allow for its direct control through the source conditions.

The use of chirped pulse amplification schemes in a seeded XUV FEL can provide both higher pulse energies and shorter durations. In the first implementation of CPA at the FERMI facility, we achieved a pulse shortening of a factor of nearly 2 with respect to standard operation, from $91\,\mathrm{fs}$ to $50\,\mathrm{fs}$, after stretching the UV seed pulse from $170\,\mathrm{fs}$ to $290\,\mathrm{fs}$. Follow-up experiments to be carried out in the near future will attempt to achieve durations close to $10\,\mathrm{fs}$ by further stretching the seed pulses.

Using longer seed pulses that match the electron beam duration, of the order of $1\,\mathrm{ps}$, will vastly increase the output pulse energy. However, this energy increase achieved with CPA is limited by the low efficiency of diffraction gratings for the XUV domain, generally of a few percent. At the cost of a more complex design, the implementation of a pulse compressor based on the conical diffraction geometry, discussed in this thesis, would provide higher efficiencies.

Appendix A

Zernike and Legendre polynomials

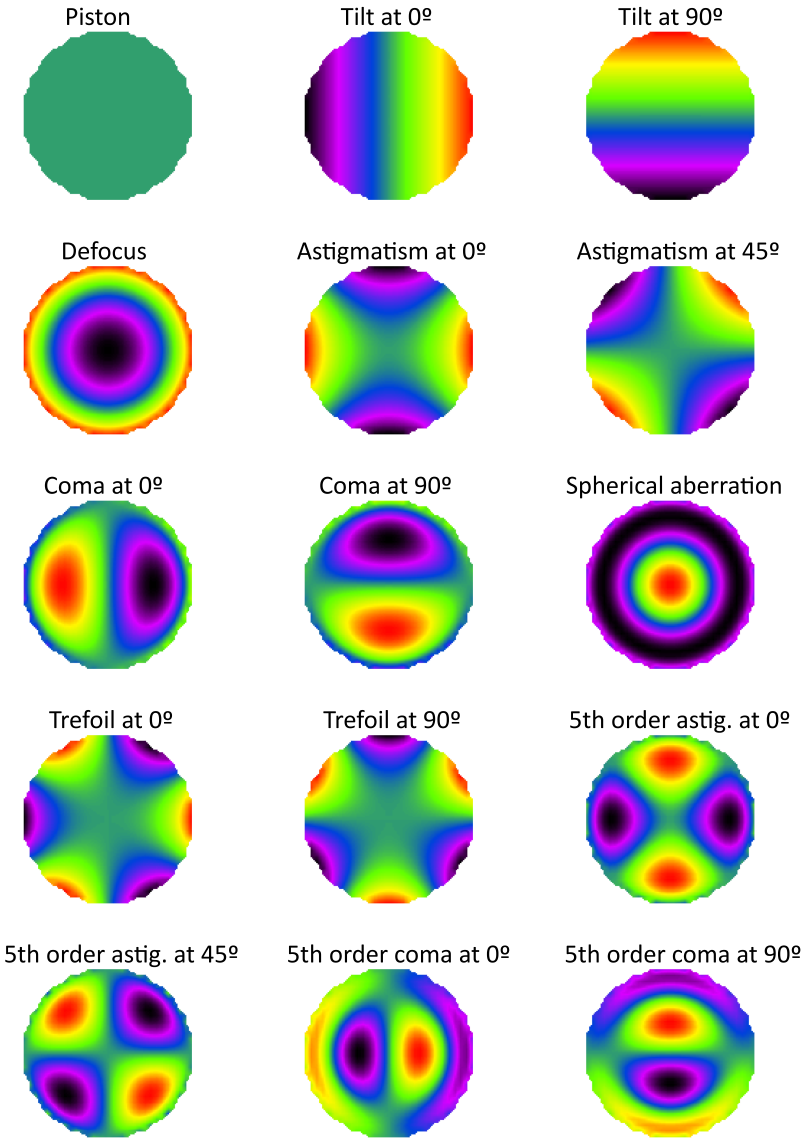

Piston

Tilt at 0º

Tilt at 90º

Defocus

Astigmatism at 0º

Astigmatism at 45º

Coma at 0º

Coma at 90º

Spherical aberration

Trefoil at 0º

Trefoil at 90º

5th order astig. at 0º

5th order astig. at 45º

5th order coma at 0º

5th order coma at 90º

Figure A.1: Graphical representation of the first 15 Zernike polynomials used by the HASO software.

N	*n*	*m*	A_n^m	*Zernike polynomial*	*Associated aberration*
0	0	0	$\sqrt{2}$	1	Piston
1	1	1	2	$\rho\cos\theta$	Tilt at 0°
2	1	-1	2	$\rho\sin\theta$	Tilt at 90°
3	2	0	$\sqrt{3}$	$(2\rho^2-1)$	Defocus
4	2	2	$\sqrt{6}$	$\rho^2\cos 2\theta$	Astigmatism at 0°
5	2	-2	$\sqrt{6}$	$\rho^2\sin 2\theta$	Astigmatism at 45°
6	3	1	$\sqrt{8}$	$(3\rho^2-2)\rho\cos\theta$	Coma at 0°
7	3	-1	$\sqrt{8}$	$(3\rho^2-2)\rho\sin\theta$	Coma at 90°
8	4	0	$\sqrt{5}$	$(6\rho^4-6\rho^2+1)$	3rd order spherical
9	3	3	$\sqrt{8}$	$\rho^3\cos 3\theta$	Trefoil at 0°
10	3	-3	$\sqrt{8}$	$\rho^3\sin 3\theta$	Trefoil at 90°
11	4	2	$\sqrt{10}$	$(4\rho^2-3)\rho^2\cos 2\theta$	5th order astig. at 0°
12	4	-2	$\sqrt{10}$	$(4\rho^2-3)\rho^2\sin 2\theta$	5th order astig. at 90°
13	5	1	$\sqrt{12}$	$(10\rho^4-12\rho^2+3)\rho\cos\theta$	5th order coma at 0°
14	5	-1	$\sqrt{12}$	$(10\rho^4-12\rho^2+3)\rho\sin\theta$	5th order coma at 90°
15	6	0	$\sqrt{7}$	$(20\rho^6-30\rho^4+12\rho^2-1)$	5th order spherical
16	4	4	$\sqrt{10}$	$\rho^4\cos 4\theta$	Tetrafoil at 0°
17	4	-4	$\sqrt{10}$	$\rho^4\sin 4\theta$	Tetrafoil at 90°
18	5	3	$\sqrt{12}$	$(5\rho^2-4)\rho^3\cos 3\theta$	7th order trefoil at 0°
19	5	-3	$\sqrt{12}$	$(5\rho^2-4)\rho^3\sin 3\theta$	7th order trefoil at 90°
20	6	2	$\sqrt{14}$	$(15\rho^4-20\rho^2+6)\rho^2\cos 2\theta$	7th order astig. at 0°
21	6	-2	$\sqrt{14}$	$(15\rho^4-20\rho^2+6)\rho^2\sin 2\theta$	7th order astig. at 45°
22	7	1	4	$(35\rho^6-60\rho^4+30\rho^2-4)\rho\cos\theta$	7th order coma at 0°
23	7	-1	4	$(35\rho^6-60\rho^4+30\rho^2-4)\rho\sin\theta$	7th order coma at 90°
24	8	0	3	$(70\rho^8-140\rho^6+90\rho^4-20\rho^2+1)$	7th order spherical
25	5	5	$\sqrt{12}$	$\rho^5\cos 5\theta$	Pentafoil at 0°
26	5	-5	$\sqrt{12}$	$\rho^5\sin 5\theta$	Pentafoil at 90°
27	6	4	$\sqrt{14}$	$(6\rho^2-5)\rho^4\cos 4\theta$	9th order tetrafoil at 0°
28	6	-4	$\sqrt{14}$	$(6\rho^2-5)\rho^4\cos 4\theta$	9th order tetrafoil at 90°
29	7	3	4	$(21\rho^4-30\rho^2+10)\rho^2\cos 3\theta$	9th order trefoil at 0°
30	7	-3	4	$(21\rho^4-30\rho^2+10)\rho^2\sin 3\theta$	9th order trefoil at 90°
31	8	2	$\sqrt{18}$	$(56\rho^6-105\rho^4+60\rho^2-10)\rho^2\cos 2\theta$	9th order astig. at 0°
32	8	-2	$\sqrt{18}$	$(56\rho^6-105\rho^4+60\rho^2-10)\rho^2\sin 2\theta$	9th order astig. at 45°

Table A.1: List of the first 32 Zernike polynomials used for modal reconstruction with circular pupils, as listed in the HASO software, and the normalization coefficients A_n^m for the case of RMS normalization. Note that $A_n^m = 1$ when using PV normalization.

N	*Polynomial*	*Associated aberration*
1	x	Tilt at 0°
2	y	Tilt at 90°
3	$\frac{1}{2}(3\mathrm{x}^2-1)$	Cylinder at 0°
4	xy	Astigmatism at 45°
5	$\frac{1}{2}(3\mathrm{y}^2-1)$	Cylinder at 90°
6	$\frac{1}{2}(5\mathrm{x}^3-3\mathrm{x})$	Linear coma at 0°
7	$\frac{1}{2}(3\mathrm{x}^2-1)\mathrm{y}$	-
8	$\frac{1}{2}(3\mathrm{y}^2-1)\mathrm{x}$	-
9	$\frac{1}{2}(5\mathrm{y}^3-3\mathrm{y})$	Linear coma at 90°
10	$\frac{1}{8}(35\mathrm{x}^4-30\mathrm{x}^2+3)$	-
11	$\frac{1}{2}(5\mathrm{x}^3-3\mathrm{x})\mathrm{y}$	-
12	$\frac{1}{4}(3\mathrm{x}^2-1)(3\mathrm{y}^2-1)$	-
13	$\frac{1}{2}(5\mathrm{y}^3-3\mathrm{y})\mathrm{x}$	-
14	$\frac{1}{8}(35\mathrm{y}^4-30\mathrm{y}^2+3)$	-
15	$\frac{1}{8}(63\mathrm{x}^5-70\mathrm{x}^3+15\mathrm{x})$	-
16	$\frac{1}{8}(35\mathrm{x}^4-30\mathrm{x}^2+3)\mathrm{y}$	-
17	$\frac{1}{4}(5\mathrm{x}^3-3\mathrm{x})(3\mathrm{y}^2-1)$	-
18	$\frac{1}{4}(3\mathrm{x}^2-1)(5\mathrm{y}^3-3\mathrm{y})$	-
19	$\frac{1}{8}(35\mathrm{y}^4-30\mathrm{y}^2+3)$	-
20	$\frac{1}{8}(63\mathrm{y}^5-70\mathrm{y}^3+15\mathrm{y})$	-
21	$\frac{1}{16}(213\mathrm{x}^6-315\mathrm{x}^4+105\mathrm{x}^2-5)$	-
22	$\frac{1}{8}(63\mathrm{x}^5-70\mathrm{x}^3+15\mathrm{x})\mathrm{y}$	-
23	$\frac{1}{16}(35\mathrm{x}^4-30\mathrm{x}^2+3)(3\mathrm{y}^2-1)$	-
24	$\frac{1}{4}(5\mathrm{x}^3-3\mathrm{x})(5\mathrm{y}^3-3\mathrm{y})$	-
25	$\frac{1}{16}(3\mathrm{x}^2-1)(35\mathrm{y}^4-30\mathrm{y}^2+3)$	-
26	$\frac{1}{8}(63\mathrm{y}^5-70\mathrm{y}^3+15\mathrm{y})\mathrm{x}$	-
27	$\frac{1}{16}(231\mathrm{y}^6-315\mathrm{y}^4+105\mathrm{y}^2-5)$	-
28	$\frac{1}{16}(429\mathrm{x}^7-693\mathrm{x}^5+315\mathrm{x}^3-35\mathrm{x})$	-
29	$\frac{1}{16}(231\mathrm{x}^6-315\mathrm{x}^4+105\mathrm{x}^2-5)\mathrm{y}$	-
30	$\frac{1}{16}(63\mathrm{x}^5-70\mathrm{x}^3+15\mathrm{x})(3\mathrm{y}^2-1)$	-
31	$\frac{1}{16}(35\mathrm{x}^4-30\mathrm{x}^2+3)(5\mathrm{y}^3-3\mathrm{y})$	-
32	$\frac{1}{16}(5\mathrm{x}^3-3\mathrm{x})(35\mathrm{y}^4-30\mathrm{y}^2+3)$	-
33	$\frac{1}{16}(3\mathrm{x}^2-1)(63\mathrm{y}^5-70\mathrm{y}^3+15\mathrm{y})$	-
34	$\frac{1}{16}(231\mathrm{y}^6-315\mathrm{y}^4+105\mathrm{y}^2-5)$	-

Table A.2: List of the first 34 Legendre polynomials used for modal reconstruction with square pupils, as listed in the HASO software.

Appendix B

Mirrors and filters in the LASC high-harmonic beamline

This appendix presents the spectral reflectivities of the silica plate and the rotating gold-coated mirror used during the single-shot high-harmonic wavefront measurements conducted in the LASC beamline and reported in section 1.3.2, as well as the transmission of the 200-nm-thick aluminum filter used to block the remaining IR energy.

For the silica plate, the grazing angle is fixed at 10° during the experiment. The grazing angle on the gold-coated mirror when using the Hartmann wavefront sensor was 15°. Their reflectivities are calculated for these angles and for s- and p-polarizations. The different reflectivities for each polarization lead to the different pulse energies measured when the IR polarization was changed during the experiment (figures 1.58 and 1.59). In the case of the filter, one oxide layer (Al_2O_3) has been taken into account in each side, both with 5-nm thickness. The results are shown in the figure below.

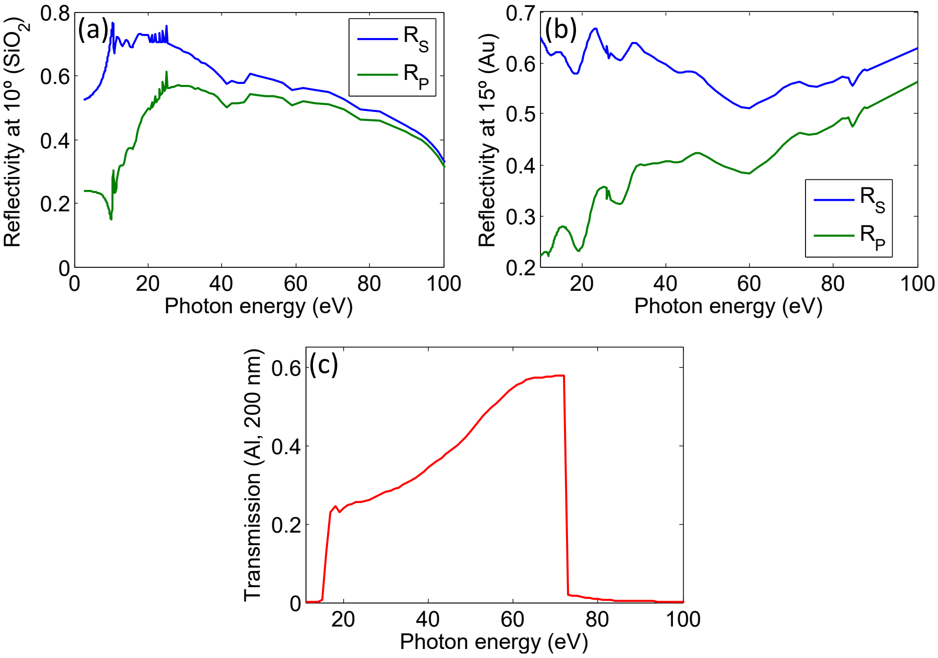

Figure B.1: Spectral reflectivity of the two flat mirrors used during the experiment: (a) SiO_2 plate at 10° and (b) gold-coated mirror at 15°, when the beam is sent to the XUV WFS; and (c) spectral transmission of the aluminum filter, with thin layers of Al_2O_3. Data for the filter taken from the CXRO X-ray database [61].

APPENDIX C

Wavefront calibration of multilayer mirrors

In section 1.3.2.4, three multilayer mirrors were used to allow for wavefront measurements of individual pulses corresponding to three different harmonic orders. After the experiment was finished, the three mirrors, mounted, were taken to LOA for at-wavelength wavefront calibration. Calibrating the mirrors allows to rule out the aberrations that they introduce in the high-harmonic beam upon reflection. This appendix presents the procedure and results of the calibration of the three mirrors, carried out in the Salle Corail beamline. The calibration is performed by generating a reference beam with a spherical wavefront, which is measured after reflection by the mirror under test. Any aberrations present in the measured beam are thus caused by the mirror.

The experimental setup used for the calibration can be seen in figure C.1. The harmonics are generated in a 20-mm gas cell filled with argon at $55\,\text{mbar}$ pressure. The driving beam was apertured down to a diameter of $9\,\text{mm}$. The test mirror is mounted on a motorized translation stage, allowing for it to be moved in and out of the beam path, and thus allowing for the use of an XUV CCD or the Hartmann XUV WFS.

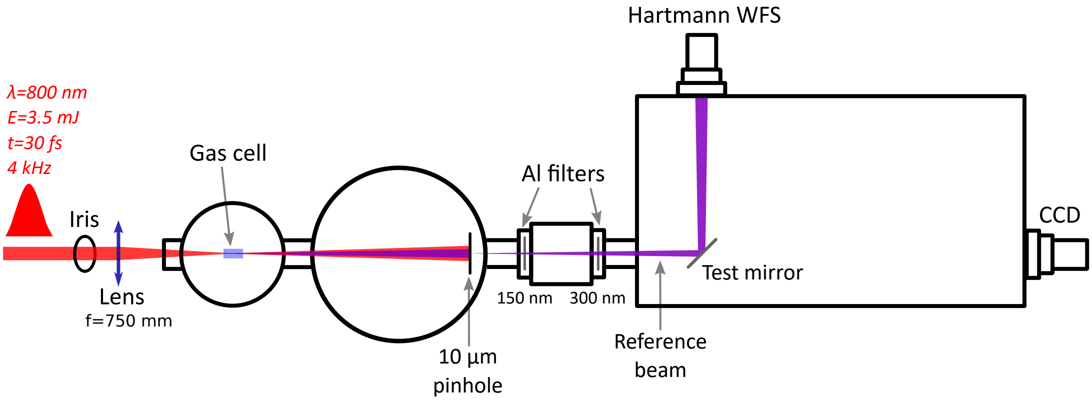

Figure C.1: Experimental setup for the wavefront calibration of the three multilayer mirrors in the Salle Corail beamline.

At the start of the experiment, the test mirror was placed out of the beam path, so that the direct beam was measured with a CCD camera in order to optimize the generation parameters. Once this was done, the reference beam was created by placing a pinhole with a diameter of $10\,\mu\text{m}$ in the beam path inside the second chamber, by means of two-dimensional motorized translation stages. The transmission through the pinhole remains low, however, since the harmonic beam has an approximate diameter of $1\,\mathrm{mm}$ and is not focused. Due to the absence of focusing optics, the alignment of the setup is very simple. Additionally, the pinhole itself, specifically manufactured for use with high-power lasers, can be used to filter out the driving IR beam without being damaged, and can thus be placed close to the cell, at approximately $80\,\mathrm{cm}$. This, in turn, means that a single 150-nm aluminum filter is sufficient to fully eliminate any remaining IR energy. Next, the test mirror was placed in the beam path, $1\,\mathrm{m}$ after the pinhole, sending the beam to the Hartmann WFS. Once the first mirror was calibrated, it was simply replaced by the next one, without any other changes to the setup. The calibration wavefronts obtained for all three mirrors can be seen in figure C.2, expressed in units of the corresponding wavelengths for each case. These wavefronts were subtracted from the wavefront measurements reported in section 1.3.2.4.

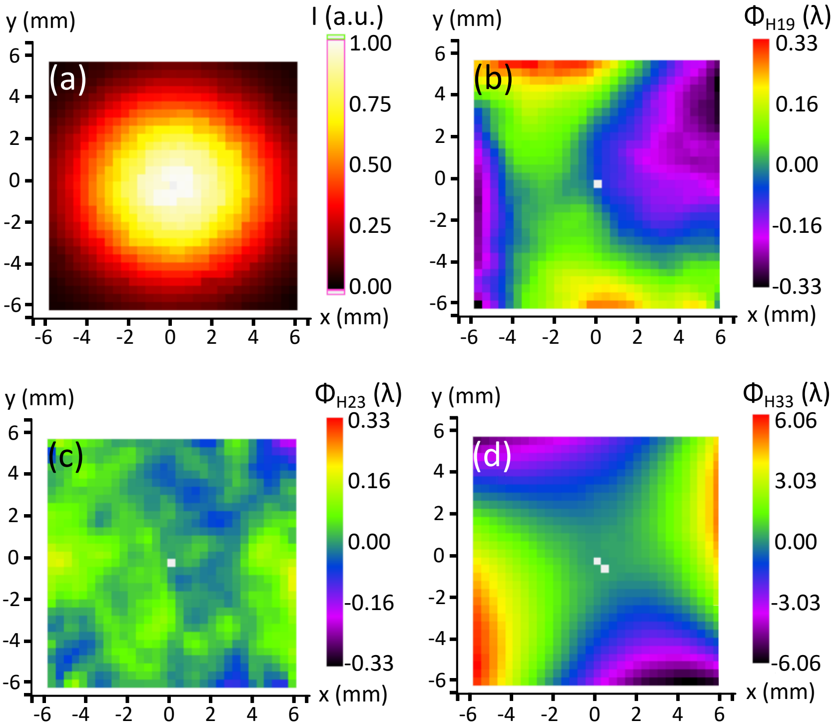

Figure C.2: Intensity distribution of the reference beam obtained with the 10-µm pinhole, as reflected by mirror 1 (a), and calibration wavefronts for mirrors 1, 2 and 3 (b, c, and d, respectively).

In the experiment carried out at LASC, an area around the central part of each mirror was used, with an approximate diameter of $1\,\mathrm{mm}$. During calibration, the reference beam covered an area with an estimated FWHM diameter of $4\,\mathrm{mm}$ around its center, ensuring that the area used in the experiment was characterized. Due to the low transmission through the pinhole, as well as the mirrors selecting a single harmonic order each, the acquisition of a calibration wavefront took several minutes for every mirror. Five measurements were made in each case to verify their repeatability.

Table C.1 shows the obtained RMS and PV values for each case, averaged over five measurements. It is important to note, however, that only a small portion of the probed surface was actually used in the experiment from section 1.3.2.4, so the aberrations introduced by the mirrors were also less significant.

Mirror	*RMS (λ)*	*PV (λ)*	*RMS (nm)*
Mirror 1 (λ_{H19}=41.4 nm)	0.144 $\pm$ 0.008	0.693 $\pm$ 0.059	5.962 $\pm$ 0.331
Mirror 2 (λ_{H23}=35.0 nm)	0.052 $\pm$ 0.004	0.385 $\pm$ 0.045	1.820 $\pm$ 0.140
Mirror 3 (λ_{H33}=23.9 nm)	2.383 $\pm$ 0.025	12.171 $\pm$ 0.250	56.954 $\pm$ 0.598

Table C.1: Results of the mirror calibration. The values and uncertainties are obtained with the average and standard deviation of five separate acquisitions. The RMS and PV are expressed in terms of the corresponding wavelength for each case.

The measured RMS of the three mirrors is approximately $\lambda_{\mathrm{H19}}/7$, $\lambda_{\mathrm{H23}}/19$, and $2.4\lambda_{\mathrm{H33}}$. The relative standard deviation for each case is 5.55%, 7.69%, and 1.05%, respectively, indicating good repeatability. It is also interesting to express the measured RMS values in terms of the wavelength of He-Ne lasers, $\lambda_{\mathrm{He-Ne}} = 633\,\mathrm{nm}$, typically used for mirror surface metrology. Doing so results in the values $\mathrm{RMS}_1 \simeq \lambda_{\mathrm{He-Ne}}/106$, $\mathrm{RMS}_2 \simeq \lambda_{\mathrm{He-Ne}}/348$, and $\mathrm{RMS}_3 \simeq \lambda_{\mathrm{He-Ne}}/11$. These results thus showcase the possibility of carrying out highly accurate and repeatable at-wavelength characterization of XUV optics in tabletop setups based on high-harmonic sources. More information about this topic can be found in sections 2.1 and 2.2.

The measurements show that mirror 1 creates some astigmatism but has an overall good flatness. Mirror 2 has a particularly high optical quality, creating negligible aberrations in a diffraction-limited beam. Mirror 3, on the other hand, creates a very significant astigmatism that could be caused, for example, by the screw holding the mirror being too tight and deforming the surface, or by fabrication defects. This last result highlights the importance of carrying out this calibration, since most of the aberrations measured in the experiment when using this mirror were caused by it, and were not part of the original beam.

References

[1] J. Bokor, P. H. Bucksbaum, and R. R. Freeman, "Generation of 35.5-nm coherent radiation," Opt. Lett. **8**(4), 217-219 (1983).

[2] A. McPherson, G. Gibson, H. Jara, U. Johann, T. S. Luk, I. A. McIntyre, K. Boyer, and C. K. Rhodes, "Studies of multiphoton production of vacuum-ultraviolet radiation in the rare gases," JOSA B **4**(4) (1987).

[3] M. Ferray, A. L'Huillier, X. F. Li, L. A. Lompré, G. Mainfrays, and C. Manus, "Multiple-harmonic conversion of 1064 nm radiation in rare gases," J. Phys. B **21**(3), L31-L35 (1988).

[4] G. J. Tallens, "The physics of soft x-ray lasers pumped by electron collisions in laser plasmas," J. Phys. D.: Appl. Phys. **36**, R259-R276 (2003).

[5] P. Schmüser, M. Dohlus, and J. Rossbach, "Ultraviolet and Soft X-Ray Free-Electron Lasers," Springer tracts in modern physics **229** (2009).

[6] W. Theobald, R. Hässner, C. Wülker, and R. Sauerbrey, "Temporally Resolved Measurement of Electron Densities $(> 10^{23}\mathrm{cm}^{-3})$ with High Harmonics," Phys. Rev. Lett. **77**(2), 298-301 (1996).

[7] L. Waldecker, T. A. Miller, M. Rudé, R. Bertoni, J. Osmond, V. Pruneri, R. E. Simpson, R. Ernstorfer, and S. Wall, "Time-domain separation of optical properties from structural transitions in resonantly bonded materials," Nat. Mater. **14**(10), 991-995 (2015).

[8] H. J. Wörner, J. B. Bertrand, D. V. Kartashov, P. B. Corkum, and D. M. Villeneuve, "Following a chemical reaction using high-harmonic interferometry," Nature **466**(7306), 604-607 (2010).

[9] R. Neutze, G. Brändén, and G. F. Schertler, "Membrane protein structural biology using X-ray free electron lasers," Curr. Opin. Struct. Biol. **33**, 115-125 (2015).

[10] G. Lambert, B. Vodungbo, J. Gautier, B. Mahieu, V. Malka, S. Sebban, P. Zeitoun, J. Luning, J. Perron, A. Andreev, S. Stremoukhov, F. Ardana-Lamas, A. Dax, C. P. Hauri, A. Sardinha, M. Fajardo, "Towards enabling femtosecond helicity-dependent spectroscopy with high-harmonic sources," Nat. Commun. **6**, 6167 (2015).

[11] Ph. Zeitoun, G. Faivre, S. Sebban, T. Mocek, A. Hallou, M. Fajardo, D. Aubert, Ph. Balcou, F. Burgy, D. Douillet, S. Kazamias, G. de Lachèze-Murel, T. Lefrou, S. le Pape, P. Mercère, H. Merdji, A. S. Morlens, J. P. Rousseau, and C. Valentin, "A high-intensity highly coherent soft X-ray femtosecond laser seeded by a high harmonic beam," Nature **431**(7007), 426-429 (2004).

[12] T. Ditmire, E. T. Gumbrell, R. A. Smith, J. W. G. Tisch, D. D. Meyerhofer, and M. H. R. Hutchinson, "Spatial coherence measurement of soft x-ray radiation produced by high order harmonic generation," Phys. Rev. Lett. **77**(23), 4756 (1996).

[13] R. A. Bartels, A. Paul, H. Green, H. C. Kapteyn, M. M. Murnane, S. Backus, I. P. Christov, Y. Liu, D. Attwood, C. Jacobsen, "Generation of spatially coherent light at extreme ultraviolet wavelengths," Science **297**(5580), 376-378 (2002).

[14] C. Lyngå, M. B. Gaarde, C. Delfin, M. Bellini, T. W. Hänsch, A. L'Huillier, and C.-G. Wahlström, "Temporal coherence of high-order harmonics," Phys. Rev. A **60**(6), 4823 (1999).

[15] D. Gauthier, P. R. Ribič, G. De Ninno, E. Allaria, P. Cinquegrana, M. B. Danailov, A. Demidovich, E. Ferrari, L. Giannessi, B. Mahieu, and G. Penco, "Spectrotemporal shaping of seeded free-electron laser pulses," Phys. Rev. Lett. **98**(11), 115 (2015).

[16] J. Amann, W. Berg, V. Blank, F.-J. Decker, Y. Ding, P. Emma, Y. Feng, J. Frisch, D. Fritz, J. Hastings, Z. Huang, J. Krzywinski, R. Lindberg, H. Loos, A. Lutman, H.-D. Nuhn, D. Ratner, J. Rzepiela, D. Shu, Yu. Shvyd'ko, S. Spampinati, S. Stoupin, S. Terentyev, E. Trakhtenberg, D. Walz, J. Welch, J. Wu, A. Zholents, and D. Zhu, "Demonstration of self-seeding in a hard-X-ray free-electron laser," Nat. Photon. **6**, 693-698 (2012).

[17] K. Zhao, Q. Zhang, M. Chini, Y. Wu, X. Wang, and Z. Chang, "Tailoring a 67 attosecond pulse through advantageous phase-mismatch," Opt. Lett. **37**(18), 3891-3893 (2012).

[18] G. Lambert, F. Tissandier, J. Gautier, C. P. Hauri, P. Zeitoun, C. Valentin, T. Marchenko, J.-P. Goddet, M. Ribière, A. Sardinha, M. Fajardo, F. Hamouda, G. Maynard, G. Rey, and S. Sebban, "Aberration-free high-harmonic source generated with a two-colour field," EPL **89**(2), 24001 (2010).

[19] J. Gautier, Ph. Zeitoun, C. Hauri, A.-S. Morlens, G. Rey, C. Valentin, E. Papalarazou, J.-P. Goddet, S. Sebban, F. Burgy, P. Mercère, M. Idir, G. Dovillaire, X. Levecq, S. Bucourt, M. Fajardo, H. Merdji, and J.-P. Caumes, "Optimization of the wave front of high order harmonics," Eur. Phys. J. D **48**(3), 459-463 (2008).

[20] C. Valentin, J. Gautier, J.-Ph. Goddet, C. Hauri, T. Marchenko, E. Papalazarou, G. Rey, S. Sebban, O. Scrick, Ph. Zeitoun, G. Dovillaire, X. Levecq, S. Bucourt, and M. Fajardo, "High-order harmonic wave fronts generated with controlled astigmatic infrared laser," JOSA B **25**(7), B161-B166 (2008).

[21] D. Strickland and G. Mourou, "Compression of amplified chirped optical pulses," Opt. Commun. **56**(3), 219-221 (1985).

[22] P. M. Paul, E. S. Toma, P. Breger, G. Mullot, F. Augé, Ph. Balcou, H. G. Muller, and P. Agostini, "Observation of a Train of Attosecond Pulses from High Harmonic Generation," Science **292**(5522), 1689-1692 (2001).

[23] Z. Chang, A. Rundquist, H. Wang, M. M. Murnane, and H. C. Kapteyn, "Generation of coherent soft X rays at 2.7 nm using high harmonics," Phys. Rev. Lett. **79**(16), 2967 (1997).

[24] M. Schnürer, Ch. Spielmann, P. Wobrauschek, C. Streli, N. H. Burnett, C. Kan, K. Ferencz, R. Koppitsch, Z. Cheng, T. Brabec, and F. Krausz, "Coherent 0.5-keV X-ray emission from helium driven by a sub-10-fs laser," Phys. Rev. Lett. **80**(15), 3236 (1998).

[25] D. Descamps, L. Roos, C. Delfin, A. L'Huillier, and C.-G. Wahlström, "Two-and three-photon ionization of rare gases using femtosecond harmonic pulses generated in a gas medium," Phys. Rev. A **64**(3), 31404 (2001).

[26] N. A. Papadogiannis, B. Witzel, C. Kalpouzos, and D. Charalambidis, "Observation of attosecond light localization in higher order harmonic generation," Phys. Rev. Lett. **83**(21), 4289 (1999).

[27] Y. Mairesse, A. de Bohan, L. J. Frasinski, H. Merdji, L. C. Dinu, P. Monchicourt, P. Breger, M. Kovačev, R. Taïeb, B. Carré, H. G. Muller, P. Agostini, P. Salières, "Attosecond synchronization of high-harmonic soft x-rays," Science **302**(5650), 1540-1543 (2003).

[28] E. Goulielmakis, M. Schultze, M. Hofstetter, V. S. Yakovlev, J. Gagnon, M. Uiberacker, A. L. Aquila, E. M. Gullikson, D. T. Attwood, R. Kienberger, F. Krausz, and U. Kleineberg, "Single-Cycle Nonlinear Optics," Science **320**(5883), 1614-1617 (2008).

[29] S. L. Sorensen, O. Björneholm, I. Hjelte, T. Kihlgren, G. Öhrwall, S. Sundin, S. Svensson, S. Buil, D. Descamps, A. L'Huillier, J. Norin, and C.-G. Wahlström, "Femtosecond pump-probe photoelectron spectroscopy of predissociative Rydberg states in acetylene," J. Chem. Phys. **112**(18), 8038-8042 (2000).

[30] P. B. Corkum, "Plasma perspective on strong field multiphoton ionization," Phys. Rev. Lett. **71**(13), 1994 (1993).

[31] M. Lewenstein, P. Balcou, M. Y. Ivanov, A. L'Huillier, and P. B. Corkum, "Theory of high-harmonic generation by low-frequency laser fields," Phys. Rev. A **49**(3), 2117 (1994).

[32] P. Salières, A. L'Huillier, and M. Lewenstein, "Coherence control of high-order harmonics," Phys. Rev. Lett. **74**(19), 3776 (1995).

[33] C.-G. Wahlström, J. Larsson, A. Persson, T. Starczewski, and S. Svanberg, "High-order harmonic generation in rare gases with an intense short-pulse laser," Phys. Rev. A **48**(6), 4709 (1993).

[34] X. F. Li, A. L'Huillier, M. Ferray, L. A. Lompré, and G. Mainfray, "Multiple-harmonic generation in rare gases at high laser intensity," Phys. Rev. A **39**(11), 5751-5761 (1989).

[35] P. Salières and M. Lewenstein, "Generation of ultrashort coherent XUV pulses by harmonic conversion of intense laser pulses in gases: towards attosecond pulses," Meas. Sci. Technol. **12**(11), 1818 (2001).

[36] J. L. Krause, K. J. Schafer, and K. C. Kulander, "High-order harmonic generation from atoms and ions in the high intensity regime," Phys. Rev. Lett. **68**(24), 3535 (1992).

[37] A. L'Huillier, M. Lewenstein, P. Salières, Ph. Balcou, M. Yu. Ivanov, J. Larsson, and C. G. Wahlström, "High-order harmonic-generation cutoff," Phys. Rev. A **48**(5), R3433 (1993).

[38] Y. Tamaki, J. Itatani, M. Obara, and K. Midorikawa, "Optimization of conversion efficiency and spatial quality of high-order harmonic generation," Phys. Rev. A **62**(6), 63802 (2000).

[39] T. Ditmire, J. K. Crane, H. Nguyen, L. B. DaSilva, and M. D. Perry, "Energy-yield and conversion-efficiency measurements of high-order harmonic radiation," Phys. Rev. A **51**(2), R902-R905 (1995).

[40] E. Takahashi, Y. Nabekawa, M. Nurhuda, and K. Midorikawa, "Generation of high-energy high-order harmonics by use of a long interaction medium," JOSA B **20**(1), 158-165 (2003).

[41] E. Constant, D. Garzella, P. Breger, E. Mével, Ch. Dorrer, C. Le Blanc, F. Salin, and P. Agostini , "Optimizing High Harmonic Generation in Absorbing Gases: Model and Experiment," Phys. Rev. Lett. **82**(8), 1668-1671 (1999).

[42] J. Rothhardt, M. Krebs, S. Hädrich, S. Demmler, J. Limpert, and A. Tünnermann, "Absorption-limited and phase-matched high harmonic generation in the tight focusing regime," New J. Phys. **16**(3), 33022 (2014).

[43] Y. Tamaki, J. Itatani, Y. Nagata, M. Obara, and K. Midorikawa, "Highly Efficient, Phase-Matched High-Harmonic Generation by a Self-Guided Laser Beam," Phys. Rev. Lett. **82**(7), 1422-1425 (1999).

[44] K. S. E. Eikema, "Nonlinear optics: Twisted high-harmonic generation," Nat. Photon. **9**, 710-712 (2015).

[45] P. Agostini, G. Barjot, J. Bonnal, G. Mainfray, C. Manus, and J. Morellec, "Multiphoton ionization of hydrogen and rare gases," IEEE J. Quant. Electron. **4**(10), 667-669 (1968).

[46] L. V. Keldysh, "Ionization in the field of a strong electromagnetic wave," Zh. Éksp. Teor. Fiz. **47**, 1945 (1964) [Sov. Phys. JETP **20**, 1307 (1965)].

[47] N. B. Delone and V. P. Krainov, "Tunneling and barrier-suppression ionization of atoms and ions in a laser radiation field," Phys. Usp. **41**(5), 469 (1998).

[48] P. Salières, T. Ditmire, K. S. Budil, M. D. Perry, and A. L'Huillier, "Spatial profiles of high-order harmonics generated by a femtosecond Cr:LiSAF laser," J. Phys. B **27**(9), L217 (1994).

[49] P. Balcou, P. Salières, A. L'Huillier, and M. Lewenstein, "Generalized phase-matching conditions for high harmonics: The role of field-gradient forces," Phys. Rev. A **55**(4), 3204 (1997).

[50] E. Constant, D. Garzella, P. Breger, E. Mével, Ch. Dorrer, C. Le Blanc, F. Salin, and P. Agostini, "Optimizing High Harmonic Generation in Absorbing Gases: Model and Experiment," Phys. Rev. Lett. **82**(8), 1668-1671 (1999).

[51] X. He, M. Miranda, J. Schwenke, O. Guilbaud, T. Ruchon, C. Heyl, E. Georgadiou, R. Rakowski, A. Persson, M. B. Gaarde, and A. L'Huillier, "Spatial and spectral properties of the high-order harmonic emission in argon for seeding applications," Phys. Rev. A **79**(6) (2009).

[52] M. Lewenstein, P. Salières, and A. L'Huillier, "Phase of the atomic polarization in high-order harmonic generation," Phys. Rev. A **52**(6), 4747 (1995).

[53] M. B. Gaarde and K. J. Schafer, "Quantum path distributions for high-order harmonics in rare gas atoms," Phys. Rev. A **65**(3) (2002).

[54] P. Balcou, A. S. Dederichs, M. B. Gaarde, and A. L'Huillier, "Quantum-path analysis and phase matching of high-order harmonic generation and high-order frequency mixing processes in strong laser fields," J. Phys. B **32**(12), 2973 (1999).

[55] K. Schiessl, K. L. Ishikawa, E. Persson, and J. Burgdörfer, "Quantum Path Interference in the Wavelength Dependence of High-Harmonic Generation," Phys. Rev. Lett. **99**(25), 253903 (2007).

[56] M. Holler, A. Zaïr, F. Schapper, T. Auguste, E. Cormier, A. Wyatt, A. Monmayrant, I. A. Walmsley, L. Gallmann, P. Salières, and U. Keller, "Ionization effects on spectral signatures of quantum-path interference in high-harmonic generation," Opt. Express **17**(7), 5716-5722 (2009).

[57] A. Zaïr, M. Holler, A. Guandalini, F. Schapper, J. Biegert, L. Gallmann, U. Keller, A. S. Wyatt, A. Monmayrant, I. A. Walmsley, E. Cormier, T. Auguste, J. P. Caumes, and P. Salières, "Quantum Path Interferences in High-Order Harmonic Generation," Phys. Rev. Lett. **100**(14), 143902 (2008).

[58] D. Attwood, "Soft X-rays and Extreme Ultraviolet Radiation" (Cambridge University Press, 1999).

[59] T. W. Barbee, S. Mrowka, and M. C. Hettrick, "Molybdenum-silicon multilayer mirrors for the extreme ultraviolet," Appl. Opt. **24**(6), 883-886 (1985).

[60] J. M. Slaughter, R. N. Watts, Charles M. Falco, C. Tarrio, Brian S. Medower, and T. B. Lucatorto, "Si/B_4C narrow-bandpass mirrors for the extreme ultraviolet," Opt. Lett. **19**, 1786-1788 (1994).

[61] Website of the Center for X-Ray Optics (CXRO): http://cxro.lbl.gov/

[62] T. Popmintchev, M-C. Chen, D. Popmintchev, P. Arpin, S. Brown, S, Ališauskas, G. Andriukaitis, T. Balčiunas, O. D. Mücke, A. Pugzlys, A. Baltuška, B. Shim, S. E. Schrauth, A. Gaeta, C. Hernández-García, L. Plaja, A. Becker, A. Jaron-Becker, M. M. Murnane, and H. C. Kapteyn„ "Bright coherent ultrahigh harmonics in the keV x-ray regime from mid-infrared femtosecond lasers," Science **336**(6086), 1287-1291 (2012).

[63] S. Kazamias, "Optimisation d'une source d'harmoniques d'ordres élevés pour l'optique non-linéaire dans l'extrême UV," PhD dissertation, École Polytechnique (2003).

[64] S. Kazamias, S. Daboussi, O. Guilbaud, K. Cassou, D. Ros, B. Cros, and G. Maynard, "Pressure-induced phase matching in high-order harmonic generation," Phys. Rev. A **83**(6), 063405 (2011).

[65] Z. L. Horváth and Z. Bor, "Focusing of truncated Gaussian beams," Opt. Commun. **222**(1-6), 51-68 (2003).

[66] S. Kazamias, F. Weihe, D. Douillet, C. Valentin, T. Planchon, S. Sebban. G. Grillon, F. Augé. D. Hulin, and Ph. Balcou, "High order harmonic generation optimization with an apertured laser beam," Eur. Phys. J. D **21**(3), 353-359 (2002).

[67] R. K. Tyson, "Principles of adaptive optics" (CRC press, 2015).

[68] A. J. Corso, S. Bonora, P. Zuppella, P. Baksh, M. Miszczak, W. Brocklesby, Z. Wang, P. Nicolosi, M. G. Pelizzo, "Developing an EUV multilayer adaptive mirror: the first results," Proc. SPIE 9963, 99630K (2016).

[69] L. Huang, J. Xue, and M. Idir, "Controlling X-ray deformable mirrors during inspection," J. Synchrotron Radiat. **23**(6), 1348-1356 (2016).

[70] P. P. Naulleau, K. A. Goldberg, S. H. Lee, C. Chang, D. Attwood, and J. Bokor, "Extreme-ultraviolet phase-shifting point-diffraction interferometer: a wave-front metrology tool with sub-angstrom reference-wave accuracy," Appl. Opt. **38**(35), 7252-7263 (1999).

[71] F. Pfeiffer, O. Bunk, C. Schulze-Briese, A. Diaz, T. Weitkamp, C. David, J. F. van der Veen, I. Vartanyants, and I. K. Robinson, "Shearing Interferometer for Quantifying the Coherence of Hard X-Ray Beams," Phys. Rev. Lett. **94**(16) 164801 (2005).

[72] J. Hartmann, "Bemerkungen uber den Bau und die Justirung von Spektrographen," Z. Instrumentenkd. **20**, 47 (1900).

[73] P. Mercère, Ph. Zeitoun, M. Idir, S. Le Pape, D. Douillet, X. Levecq, G. Dovillaire, S. Bucourt, K. A. Goldberg, P. P. Naulleau, and S. Rekawa , "Hartmann wave-front measurement at 13.4 nm with λ_{EUV}/120 accuracy," Opt. Lett. **28**(17), 1534-1536 (2003).

[74] L. Li, "Metrology of High Harmonics Seeded Soft X-ray Laser Based on Solid-Plasma Amplifier," PhD dissertation, École Polytechnique (2014).

[75] S. Le Pape, Ph. Zeitoun, M. Idir, P. Dhez, D. Ros, A. Carillon, J. J. Roca, and M. François, "Wavefront measurements in the soft X-ray range," Eur. Phys. J. Appl. Phys. **20**(3), 197-203 (2002).

[76] H. F. Talbot, "Facts relating to optical science," Philos. Mag. **IV**(9) (1836).

[77] K. A. Goldberg, "Extreme Ultraviolet Interferometry," PhD dissertation, University of California (1997).

[78] "Hartmann Wavefront Analyzer Tutorial", Spiricon, Inc. (2004).

[79] W. H. Southwell, "Wave-front estimation from wave-front slope measurements," JOSA **70**(8), 998-1006 (1980).

[80] J. Y. Wang and D. E. Silva, "Wave-front interpretation with Zernike polynomials," Appl. Opt. **19**(9), 1510-1518 (1980).

[81] L. Thibos, R. A. Applegate, J. T. Schwiegerling, and R. Webb, "Standards for reporting the optical aberrations of eyes," J. Refract. Surg. **18**(5), S652-S660 (2002).

[82] HASO software user guide, Imagine Optic (2011).

[83] A. Maréchal, "Étude des effects combinés de la diffraction et des aberrations géométriques sur l'image d'un point lumineux," Rev. Opt. **26**, 257-277 (1947).

[84] D. G. Lee, J. J. Park, J. H. Sung, and C. H. Nam, "Wave-front phase measurements of high-order harmonic beams by use of point-diffraction interferometry," Opt. Lett. **28**(6), 480-482 (2003).

[85] B. Schäfer and K. Mann, "Determination of beam parameters and coherence properties of laser radiation by use of an extended Hartmann-Shack wave-front sensor," Appl. Opt. **41**(15), 2809-2817 (2002).

[86] B. Flöter, P. Juranić, S. Kapitzki, B. Keitel, K. Mann, E. Plönjes, B. Schäer, and K. Tiedtke, "EUV Hartmann sensor for wavefront measurements at the Free-electron LASer in Hamburg," New J. Phys. **12**(8), 83015 (2010).

[87] R. L. Sandberg, A. Paul, D. A. Raymondson, S. Hädrich, D. M. Gaudiosi, J. Holtsnider, R. I. Tobey, O. Cohen, M. M. Murnane, H. C. Kapteyn, C. Song, J. Miao, Y. Liu, and F. Salmassi, "Lensless Diffractive Imaging Using Tabletop Coherent High-Harmonic Soft-X-Ray Beams," Phys. Rev. Lett. **99**(9), 098103 (2007).

[88] A.-S. Morlens, J. Gautier, G. Rey, Ph. Zeitoun, J.-P. Caumes, M. Kos-Rosset, H. Merdji, S. Kazamias, K. Cassou, and M. Fajardo, "Submicrometer digital in-line holographic microscopy at 32 nm with high-order harmonics," Opt. Lett. **31**(21), 3095-3097 (2006).

[89] H. Mashiko, A. Suda, and K. Midorikawa, "Focusing coherent soft-x-ray radiation to a micrometer spot size with an intensity of $10^{14}\mathrm{W/cm^2}$," Opt. Lett. **29**(16), 1927 (2004).

[90] T. Nakajima and L. A. A. Nikolopoulos, "Use of helium double ionization for autocorrelation of an xuv pulse," Phys. Rev. A **66**(4), 041402(R) (2002).

[91] R. V. Shack and B. C. Platt, "Production and use of a lenticular Hartmann screen," J. Opt. Soc. Am. **61**(5), 656 (1971).

[92] B. C. Platt and R. Shack, "History and Principles of Shack-Hartmann Wavefront Sensing," J. Refract. Surg. **17**(5), S573-S577 (2001).

[93] K. Strehl, "Über luftschlieren und zonenfehler," Z. f. Instrumentenkunde **22**, 213-217 (1902).

[94] H. M. Milchberg, Y.-H. Chen, Y.-H. Cheng, N. Jhajj, J. P. Palastro, E. W. Rosenthal, S. Varma, J. K. Wahlstrand, and S. Zahedpour, "The extreme nonlinear optics of gases and femtosecond optical filamentation," Phys. Plasmas **21**(10), 100901 (2014).

[95] D. Yoshitomi, J. Nees, N. Miyamoto, T. Sekikawa, T. Kanai, G. Mourou, and S. Watanabe, "Phase-matched enhancements of high-harmonic soft X-rays by adaptive wave-front control with a genetic algorithm," Appl. Phys. B **78**(3), 275-280 (2004).

[96] Lord Rayleigh F. R. S., "Investigations in optics, with special reference to the spectroscope," Philos. Mag. **8**(49), 261-274 (1879).

[97] F. Brizuela, Y. Wang, C. A. Brewer, F. Pedaci, W. Chao, E. H. Anderson, Y. Liu, K. A. Goldberg, P. Naulleau, P. Wachulak, M. C. Marconi, D. T. Attwood, J. J. Rocca, and C. S. Menoni, "Microscopy of extreme ultraviolet lithography masks with 13.2 nm tabletop laser illumination," Opt. Lett. **34**(3), 271-273 (2009).

[98] A. M. Hawryluk and N. M. Ceglio, "Wavelength considerations in soft-x-ray projection lithography," Appl. Opt. **32**(34), 7062-7067 (1993).

[99] M. Idir, K. Kaznatcheev, G. Dovillaire, J. Legrand, and R. Rungsawang, "A 2 D high accuracy slope measuring system based on a Stitching Shack Hartmann Optical Head," Opt. Express **22**(3), 2770 (2014).

[100] S. N. Qian, W. Jark, and P. Z. Takacs, "The penta-prism LTP: A long-trace-profiler with stationary optical head and moving penta prism," Rev. Sci. Instrum. **66**(3), 2562-2569 (1995).

[101] S. G. Alcock, K. J. S. Sawhney, S. Scott, U. Pedersen, R. Walton, F. Siewert, T. Zeschke, F. Senf, T. Noll, and H. Lammert, "The Diamond-NOM: A non-contact profiler capable of characterizing optical figure error with sub-nanometre repeatability," Nucl. Instr. Meth. Phys. Res. A **616**(2-3), 224-228 (2010).

[102] K. Hamamoto, Y. Tanaka,T. Yoshizumi, Y. Fukushima, H. Shiotani, N. Sakaya, M. Hosoya, T. Shoki, T. Watanabe, H. Kinoshita, "Phase defect observation using an EUV microscope," Proc. SPIE 6151, 615119 (2006).

[103] I. A. Artioukov and K. M. Krymski, "Schwarzschild objective for soft x-rays," Opt. Eng. **39**(8), 2163-2170 (2000).

[104] D. Bleiner, S. Yulin, J. Martynczuk, M. Ruiz-Lopez, Y. Arbelo, J. E. Balmer, and D. Günther, "Actinic damage of Y/Mo multilayer optics in a table-top plasma-driven x-ray laser," Appl. Opt. **53**(22), 4894 (2014).

[105] J. P. Spallas, R. E. Hostetler, G. E. Sommargren, and D. R. Kania, "Fabrication of extreme-ultraviolet point-diffraction interferometer aperture arrays," Appl. Opt. **34**(28), 6393-6398 (1995).

[106] E. Tejnil, K. A. Goldberg, and J. Bokor, "Phase effects owing to multilayer coatings in a two-mirror extreme-ultraviolet Schwarzschild objective," Appl. Opt. **37**(34), 8021-8029 (1998).

[107] R. N. Smartt and W. H. Steel, "Theory and application of point-diffraction interferometers," Jpn. J. Appl. Phys. **14**, 351-356 (1975).

[108] K. Schwarzschild, "Untersuchungen zur geometrischen Optik, I, II, III," Abh. der König. Ges. der Wiss. zu Gött, Neue Folge, Band IV, Nr 1, 2, 3 (1905).

[109] I. A. Artyukov, V. E. Asadchikov, A. V. Vinogradov, Yu. S. Kas'yanov, V. V. Kondratenko, R. V. Serov, A. I. Fedorenko, and S. A. Yulin, "Reflective soft x-ray microscope for the investigation of objects illuminated by laser-plasma radiation," Quantum Electron. **25**(9), 919-922 (1995).

[110] M. Ruiz-Lopez and D. Bleiner, "Implementing the plasma-lasing potential for tabletop nano-imaging," Appl. Phys. B **115**(3), 311-324 (2014).

[111] M. Ruiz-Lopez, "Table-top nano-imaiging using plasma-photon source," PhD dissertation, Universität Bern (2015).

[112] D. Bleiner, F. Staub, V. Guzenko, Y. Ekinci, and J. E. Balmer, "Evaluation of lab-scale EUV microscopy using a table-top laser source," Opt. Commun. **284**(19), 4577-4583 (2011).

[113] H. E. Bennett and J. O. Porteus, "Relation between surface roughness and specular reflectance at normal incidence," J. Opt. Soc. Am. **51**(2), 123-129 (1961).

[114] P. Kirkpatrick and A. V. Baez, "Formation of Optical Images by X-Rays," Jour. Optical. Soc. America. **38**(9), 766 (1948).

[115] H. Wolter, "Spiegelsysteme streifenden Einfalls als abbildende Optiken für Röntgenstrahlen," Ann. Der Physik **10**, 94-114 (1952).

[116] P. Troussel, P. Munsch, and J.-J. Ferme, "Microfocusing between 1 and 5 keV with Wolter-type optics," Proceedings of SPIE 3773 60-69 (1999).

[117] Ph. Troussel, B. Meyer, R. Reverdin, B. Angelier, G. Lidove, P. Salvatore, and A. Richard, "Wolter-like high resolution x-ray imaging microscope for Rayleigh Taylor instabilities studies," Rev. Sci. Instrum. **76**(6), 063707 (2005).

[118] S. Ichimaru, "Strongly coupled plasmas: high-density classical plasmas and degenerate electron liquids," Rev. Mod. Phys. **54**(4), 1017-1059 (1982).

[119] D. Riley, N. C. Woolsey, D. McSherry, I. Weaver, A. Djaoui, and E. Nardi, "X-Ray Diffraction from a Dense Plasma," Phys. Rev. Lett. **84**, 1704-1707 (2000).

[120] B. Kettle, T. Dzelzainis, S. White, L. Li, A. Rigby, C. Spindloe, M. Notley, R. Heathcote, C. L. S. Lewis, and D. Riley, "M-L band x-rays (3-3.5 KeV) from palladium coated targets for isochoric radiative heating of thin foil samples," J. Phys. B **48**(22), 224002 (2015).

[121] M. Koenig, E. Henry, G. Huser, A. Benuzzi-Mounaix, B. Faral, E. Martinolli, S. Lepape, T. Vinci, D. Batani, M. Tomasini, B. Telaro, P. Loubeyre, T. Hall, P. Celliers, G. Collins, L. DaSilva, R. Cauble, D. Hicks, D. Bradley, A. MacKinnon, P. Patel, J. Eggert, J. Pasley, O. Willi, D. Neely, M. Notley, C. Danson, M. Borghesi, L. Romagnani, T. Boehly, and K. Lee, "High pressures generated by laser driven shocks: applications to planetary physics," Nucl. Fusion **44**(12), S208-S214 (2004).

[122] N. Nettelmann, R. Redmer, and D. Blaschke, "Warm dense matter in giant planets and exoplanets," Phys. Part. Nucl. **39**(7), 1122-1127 (2008).

[123] R. Ernstorfer, M. Harb, C. T. Hebeisen, G. Sciaini, T. Dartigalongue, and R. J. Dwayne Miller, "The Formation of Warm Dense Matter: Experimental Evidence for Electronic Bond Hardening in Gold," Science **323**(5917), 1033-1037 (2010).

[124] S. H. Glenzer, B. J. MacGowan, P. Michel, N. B. Meezan, L. J. Suter, S. N. Dixit, J. L. Kline, G. A. Kyrala, D. K. Bradley, D. A. Callahan, E. L. Dewald, L. Divol, E. Dzenitis, M. J. Edwards, A. V. Hamza, C. A. Haynam, D. E. Hinkel, D. H. Kalantar, J. D. Kilkenny, O. L. Landen, J. D. Lindl, S. LePape, J. D. Moody, A. Nikroo, T. Parham, M. B. Schneider, R. P. J. Town, P. Wegner, K. Widmann, P. Whitman, B. K. F. Young, B. Van Wonterghem, L. J. Atherton, and E. I. Moses, "Symmetric Inertial Confinement Fusion Implosions at Ultra-High Laser Energies," Science **327**(5970), 1228-1231 (2010).

[125] B. Kettle, T. Dzelzainis, S. White, L. Li, B. Dromey, M. Zepf, C. L. S. Lewis, G. Williams, S. Künzel, M. Fajardo, H. Dacasa, Ph. Zeitoun, A. Rigby, G. Gregori, C. Spindloe, R. Heathcote, and D. Riley, "Experimental measurements of the collisional absorption of XUV radiation in warm dense aluminium," Phys. Rev. E **94**(2), 023203 (2016).

[126] B. Kettle, "XUV interaction with Warm Dense Matter," PhD dissertation, Queen’s University Belfast (2015).

[127] R. W. Lee, H. A. Baldis, R. C. Cauble, O. L. Landen, J. S. Wark, A. Ng, S. J. Rose, C. Lewis, D. Riley, J.-C. Gauthier, and P. Audbert, "Plasma-based studies with intense X-ray and particle beam sources," Laser. Part. Beams **20**, 527-536 (2002).

[128] P. Renaudin, C. Blancard, J. Clérouin, G. Faussurier, P. Noiret, and V. Recoules, "Aluminum Equation-of-State Data in the Warm Dense Matter Regime," Phys. Rev. Lett. **91**(7), 075002 (2003).

[129] X. Vaisseau, A. Debayle, J. J. Honrubia, S. Hulin, A. Morace, Ph. Nicolaï, H. Sawada, B. Vauzour, D. Batani, F. N. Beg, J. R. Davies, R. Fedosejevs, R. J. Gray, G. E. Kemp, S. Kerr, K. Li, A. Link, P. McKenna, H. S. McLean, M. Mo, P. K. Patel, J. Park, J. Peebles, Y. J. Rhee, A. Sorokovikova, V. T. Tikhonchuk, L. Volpe, M. Wei, and J. J. Santos, "Enhanced relativistic-electron beam energy loss in warm-dense aluminum," Phys. Rev. Lett. **144**, 095004 (2015).

[130] S. White, G. Nersisyan, B. Kettle, T. W. J. Dzelzainis, K. McKeever, C. L. S. Lewis, A. Otten, K. Siegenthaler, D. Kraus, M. Roth, T. White, G. Gregori, D. O. Gericke, R. Baggott, D. A. Chapman, K. Wünsch, J. Vorberger, D. Riley, "X-ray scattering from warm dense iron," High Energy Density Phys. **9**(3), 573-577 (2013).

[131] P. K. Patel, A. J. Mackinnon, M. H. Key, T. E. Cowan, M. E. Foord, M. Allen, D. F. Price, H. Ruhl, P. T. Springer, and R. Stephens, "Isochoric Heating of Solid-Density Matter with an Ultrafast Proton Beam," Phys. Rev. Lett. **91**(12), 125004 (2003).

[132] R. J. Trainor, J. W. Shaner, J. M. Auerbach, and N. C. Holmes, "Ultrahigh-Pressure Laser-Driven Shock-Wave Experiments in Aluminum," Phys. Rev. Lett. **42**(17), 1154 (1979).

[133] C. S. Yoo, N. C. Holmes, M. Ross, D. J. Webb, and C. Pike, "Shock temperatures and melting of iron at Earth core conditions," Phys. Rev. Lett. **70**(25), 3931 (1993).

[134] D. L. Matthews, E. M. Campbell, N. M. Ceglio, G. Hermes, R. Kauffman, L. Koppel, R. Lee, K. Manes, V. Rupert, V. W. Slivinsky, R. Turner, and F. Ze, "Characterization of laser-produced plasma x-ray sources for use in x-ray radiography," J. Appl. Phys. **54**(8), 4260-4268 (1983).

[135] D. W. Phillion and C. J. Hailey, "Brightness and duration of x-ray line sources irradiated with intense 0.53-μm laser light at 60 and 120 ps pulse width," Phys. Rev. A **34**(6), 4886 (1986).

[136] D. Riley, N. C. Woolsey, D. McSherry, F. Y. Khattak, and I. Weaver, "He-like x-ray line emission from laser irradiated sources," Plasma Sources Sci. Technol. **11**(4), 484 (2002).

[137] S. M. Vinko, G. Gregori, M. P. Desjarlais, B. Nagler, T. J. Whitcher, R. W. Lee, P. Audebert, and J. S. Wark, "Free-free opacity in warm dense aluminum," High Energy Density Phys **5**(3), 124-131 (2009).

[138] C. A. Iglesias, "XUV absorption by solid-density aluminum," High Energy Density Phys. **6**(3), 311-317 (2010).

[139] I. Ross, M. White, J. Boon, D. Craddock, A. Damerell, R. Day, A. Gibson, P. Gottfeldt, D. Nicholas, and C. Reason, "Vulcan - A versatile high-power glass laser for multiuser experiments," IEEE J. Quant. Electron. **17**(9), 1653-1661 (1981).

[140] T. Kita, T. Harada, N. Nakano, and H. Kuroda, "Mechanically ruled aberration-corrected concave gratings for a flat-field grazing-incidence spectrograph," Appl. Opt. **22**(4), 512-513 (1983).

[141] R. Keenan, C. L. S. Lewis, J. S. Wark and E. Wolfrum, "Measurements of the XUV transmission of aluminium with a soft x-ray laser," J. Phys. B **35**(20), L447-L451 (2002).

[142] E. M. Gullikson, P. Denham, S. Mrowka, and J. H. Underwood, "Absolute photoabsorption measurements of Mg, Al, and Si in the soft-x-ray region below the $L_{2,3}$ edges," Phys. Rev. B **49**(23), 16283 (1994).

[143] B. L. Henke, E. M. Gullikson, and J. C. Davis, "X-ray interactions: photoabsorption, scattering, transmission, and reflection at $E=50-30{,}000$ eV, $Z=1-92$," At. Data Nucl. Data Tables **54**, 181-342 (1993).

[144] J. T. Larsen and S. M. Lane, "HYADES - A plasma hydrodynamics code for dense plasma studies," J. Quant. Spectrosc. Radiat. Transfer. **51**(1-2), 179-186 (1994).

[145] H. Ito, T. Furuta, S. Kodama, and T. Ishibashi, "InP/InGaAs uni-travelling-carrier photodiode with 310 GHz bandwidth," Electron. Lett. **36**(21), 1809-1810 (2000).

[146] G. Szabó, A. Müller, and Z. Bor, "A sensitive single shot method to determine duration and chirp of ultrashort pulses with a streak camera," Opt. Commun. **82**(1-2), 56-62 (1991).

[147] A. E. Siegman, "Lasers" (University Science Books, 1986).

[148] I. A. Walmsley and C. Dorrer, "Characterization of ultrashort electromagnetic pulses," Adv. Opt. Photon. **1**, 308-437 (2009).

[149] Swamp Optics tutorials on temporal characterization of ultrashort laser pulses: http://www.swampoptics.com/tutorials.html

[150] D. J. Kane and R. Trebino, "Characterization of arbitrary femtosecond pulses using frequency-resolved optical gating," IEEE J. Quant. Electron. **29**(2), 571-579 (1993).

[151] R. L. Fork, W. J. Tomlinson, C. V. Shank, C. Hirlimann, and R. Yen, "Femtosecond white-light continuum pulses," Opt. Lett. **8**(1), 1-3 (1983).

[152] R. L. Fork, C. B. Cruz, P. C. Becker, and C. V. Shank, "Compression of optical pulses to six femtoseconds by using cubic phase compensation," Opt. Lett. **12**(7), 483-485 (1987).

[153] J. E. Rothenberg and D. Grischkowsky, "Measurement of optical phase with subpicosecond resolution by time-domain interferometry," Opt. Lett. **12**(2), 99-101 (1987).

[154] F. Reynaud, F. Salin, and A. Barthelemy,"Measurement of phase shifts introduced by nonlinear optical phenomena on subpicosecond pulses," Opt. Lett. **14**(5), 275-277 (1989).

[155] T. F. Albrecht, K. Seibert, and H. Kurz, "Chirp measurement of large-bandwidth femtosecond optical pulses using two-photon absorption," Opt. Commun. **84**(5-6), 223-227 (1991).

[156] K. W. DeLong and R. Trebino, "Improved ultrashort pulse-retrieval algorithm for frequency-resolved optical gating," JOSA A **11**(9), 2429-2437 (1994).

[157] K. W. DeLong, R. Trebino, J. Hunter, and W. E. White, "Frequency-resolved optical gating with the use of second-harmonic generation," JOSA B **11**(11), 2206-2215 (1994).

[158] S. Linden, H. Giessen, and J. Kuhl, "XFROG - A New Method for Amplitude and Phase Characterization of Weak Ultrashort Pulses," Phys. Status Solidi (b), **206**(1), 119-124 (1998).

[159] W. Koenig, H. K. Dunn, and L. Y. Lacy, "The sound spectrograph," J. Acoust. Soc. Am. **18**(1), 19-49 (1946).

[160] R. Trebino and D. J. Kane, "Using phase retrieval to measure the intensity and phase of ultrashort pulses: frequency-resolved optical gating," JOSA A **10**(5), 1101-1111 (1993).

[161] Website of the Ultrafast Optics Group at the Georgia Instite of Technology: http://frog.gatech.edu/index.html

[162] R. P. Millane, "Phase retrieval in crystallography and optics," JOSA A **7**(3), 394-411 (1990).

[163] R. Lane, W. Fright, and R. Bates, "Direct phase retrieval," IEEE Trans. Acoust. **35**(4), 520-526 (1987).

[164] R. Barakat and G. Newsam, "Necessary conditions for a unique solution to two-dimensional phase recovery," J. Math. Phys. **25**(11), 3190-3193 (1984).

[165] K. W. DeLong, B. Kohler, K. Wilson, D. N. Fittinghoff, and R. Trebino, "Pulse retrieval in frequency-resolved optical gating based on the method of generalized projections," Opt. Lett. **19**(24), 2152-2154 (1994).

[166] P. O'shea, M. Kimmel, X. Gu, and R. Trebino, "Highly simplified device for ultrashort-pulse measurement,"Opt. Lett. **26**(12), 932-934 (2001).

[167] C. Radzewicz, P. Wasylczyk, J. S. Krasinski, "A poor man's FROG", Opt. Commun. **186**(4-6), 239-333 (2000).

[168] S. Akturk, M. Kimmel, P. O'Shea, and R. Trebino, "Measuring spatial chirp in ultrashort pulses using single-shot Frequency-Resolved Optical Gating," Opt. Express **11**(1), 68-78 (2003).

[169] M. Takeda, H. Ina, and S. Kobayashi, "Fourier-transform method of fringe-pattern analysis for computer-based topography and interferometry," J. Opt. Soc. Am. **72**, 156-160 (1982).

[170] K. C. Chu, W. E. White, A. Sullivan, J. P. Heritage, R. S. Grant, K. X. Liu, and A. Dienes, "Direct measurement of the spectral phase of femtosecond pulses," Opt. Lett. **20**(8), 904-906 (1995).

[171] C. Iaconis and I. A. Walmsley, "Spectral phase interferometry for direct electric-field reconstruction of ultrashort optical pulses," Opt. Lett. **23**(10), 792-794 (1998).

[172] M. E. Anderson, L. E. E. de Araujo, E. M. Kosik, and I. A. Walmsley, "The effects of noise on ultrashort-optical-pulse measurement using SPIDER," Appl. Phys. B **70**(S1), S85-S93 (2000).

[173] A. S. Wyatt, "Spectral interferometry for the complete characterisation of near infrared femtosecond and extreme ultraviolet attosecond pulses," PhD dissertation, University of Oxford (2007).

[174] I. A. Walmsley, "Characterization of ultrashort optical pulses in the few-cycle regime using spectral phase interferometry for direct electric field reconstruction," Few-Cycle Laser Pulse Generation And Its Applications, 265-292 (Springer Berlin Heidelberg, 2004).

[175] A. Müller and M. Laubscher, "Spectral phase and amplitude interferometry for direct electric-field reconstruction," Opt. Lett. **26**(23), 1915-1917 (2001).

[176] E. M. Kosik, A. S. Radunsky, I. A. Walmsley, and C. Dorrer, "Interferometric technique for measuring broadband ultrashort pulses at the sampling limit," Opt. Lett. **30**(3), 326-328 (2005).

[177] T. Sekikawa, T. Ohno, T. Yamazaki, Y. Nabekawa, and S. Watanabe, "Pulse compression of a high-order harmonic by compensating the atomic dipole phase," Phys. Rev. Lett. **83**(13), 2564 (1999).

[178] E. S. Toma, H. G. Muller, P. M. Paul, P. Breger, M. Cheret, P. Agostini, C. Le Blanc, G. Mullot, and G. Cheriaux, "Ponderomotive streaking of the ionization potential as a method for measuring pulse durations in the XUV domain with fs resolution," Phys. Rev. A **62**(6), 61801 (2000).

[179] Y. Mairesse and F. Quéré, "Frequency-resolved optical gating for complete reconstruction of attosecond bursts," Phys. Rev. A **71**(1), 011401 (2005).

[180] G. Sansone, E. Benedetti, F. Calegari, C. Vozzi, L. Avaldi, R. Flammini, L. Poletto, P. Villoresi, C. Altucci, R. Velotta, S. Stagira, S. De Silvestri, and M. Nisoli, "Isolated Single-Cycle Attosecond Pulses," Science **34**(5798), 443-446 (2006).

[181] Gy. Farkas, Cs. Tóth, "Proposal for attosecond light pulse generation using laser induced multiple-harmonic conversion processes in rare gases," Phys. Lett. A **168**(5), 447-450 (1992).

[182] K. Varjú, P. Johnsson, R. López-Martens, T. Remetter, E. Gustafsson, J. Mauritsson, M. B. Gaarde, K. J. Schafer, Ch. Erny, I. Sola, A. Zaïr, E. Constant, E. Cormier, E. Mevel, and A. L'Huillier, "Experimental studies of attosecond pulse trains," Laser Phys. **15**(6), 888-898 (2005).

[183] M. Hentschel, R. Kienberger, Ch. Spielmann, G. A. Reider, N. Milosevic, T. Brabec, P. Corkum, U. Heinzmann, M. Drescher, and F. Krausz, "Attosecond metrology," Nature **414**(6863), 509-513 (2001).

[184] R. Kienberger, M. Hentschel, M. Uiberacker, Ch. Spielmann, M. Kitzler, A. Scrinzi, M. Wieland, Th. Westerwalbesloh, U. Kleineberg, U. Heinzmann, M. Drescher, and F. Krausz, "Steering Attosecond Electron Wave Packets with Light," Science **297**(5584), 1144-1148 (2002).

[185] P. Tzallas, D. Charalambidis, N. A. Papadogiannis, K. Witte, and G. D. Tsakiris, "Direct observation of attosecond light bunching," Nature **426**, 267 (2003).

[186] H. G. Muller, "Reconstruction of attosecond harmonic beating by interference of two-photon transitions," Appl. Phys. B **74**(S1), S17-S21 (2002).

[187] R. López-Martens, K. Varjú, P. Johnsson, J. Mauritsson, Y. Mairesse, P. Salières, M. B. Gaarde, . J. Schafer, A. Persson, S. Svanberg, C.-G. Wahlström, and A. L'Huillier, "Amplitude and Phase Control of Attosecond Light Pulses," Phys. Rev. Lett. **94**(3), 033001 (2005).

[188] Y. Mairesse, O. Gobert, P. Breger, H. Merdji, P. Meynadier, P. Monchicourt, M. Perdrix, P. Salières, and B. Carré, "High Harmonic XUV Spectral Phase Interferometry for Direct Electric-Field Reconstruction," Phys. Rev. Lett. **94**(17), 173903 (2005).

[189] F. Quéré, J. Itatani, G. L. Yudin, and P. B. Corkum, "Attosecond Spectral Shearing Interferometry," Phys. Rev. Lett. **90**(7), 073902 (2003).

[190] J. Mauritsson, R. López-Martens, A. L'Huillier, and K. J. Schafer, "Ponderomotive shearing for spectral interferometry of extreme-ultraviolet pulses," Opt. Lett. **28**(23), 2393-2395 (2003).

[191] P. Tournois, "Acousto-optic programmable dispersive filter for adaptive compensation of group delay time dispersion in laser systems," Opt. Commun. **140**(4), 245-249 (1997).

[192] E. Cormier, I. A. Walmsley, E. M. Kosik, A. S. Wyatt, L. Corner, and L. F. DiMauro, "Self-Referencing, Spectrally, or Spatially Encoded Spectral Interferometry for the Complete Characterization of Attosecond Electromagnetic Pulses," Phys. Rev. Lett. **94**(3), 033905 (2005).

[193] E. Cormier, L. Corner, E. M. Kosik, I. A. Walmsley, and A. S. Wyatt, "Spectral phase interferometry for complete reconstruction of attosecond pulses," Laser Phys. **15**(6), 909-915 (2005).

[194] J. M. J. Madey, "Stimulated Emission of Bremsstrahlung in a Periodic Magnetic Field," J. Appl. Phys. **42**(5), 1906-1913 (1971).

[195] T. Ishikawa, H. Aoyagi, T. Asaka, Y. Asano, N. Azumi, T. Bizen, H. Ego, K. Fukami, T. Fukui, Y. Furukawa, S. Goto, H. Hanaki, T. Hara, T. Hasegawa, T. Hatsui, A. Higashiya, T. Hirono, N. Hosoda, M. Ishii, T. Inagaki, Y. Inubushi, T. Itoga, Y. Joti, M. Kago, T. Kameshima, H. Kimura, Y. Kirihara, A. Kiyomichi, T. Kobayashi, C. Kondo, T. Kudo, H. Maesaka, X. M. Maréchal, T. Masuda, S. Matsubara, T. Matsumoto, T. Matsushita, S. Matsui, M. Nagasono, N. Nariyama, H. Ohashi, T. Ohata, T. Ohshima, S. Ono, Y. Otake, C. Saji, T. Sakurai, T. Sato, K. Sawada, T. Seike, K. Shirasawa, T. Sugimoto, S. Suzuki, S. Takahashi, H. Takebe, K. Takeshita, K. Tamasaku, H. Tanaka, R. Tanaka, T. Tanaka, T. Togashi, K. Togawa, A. Tokuhisa, H. Tomizawa, K. Tono, S. Wu, M. Yabashi, M. Yamaga, A. Yamashita, K. Yanagida, C. Zhang, T. Shintake, H. Kitamura, and N. Kumagai, "A compact X-ray free-electron laser emitting in the sub-ångstrom region," Nat. Photon. **6**(8), 540-544 (2012).

[196] P. Emma, R. Akre, J. Arthur, R. Bionta2, C. Bostedt, J. Bozek, A. Brachmann, P. Bucksbaum, R. Coffee, F.-J. Decker, Y. Ding, D. Dowell, S. Edstrom, A. Fisher, J. Frisch, S. Gilevich, J. Hastings, G. Hays, Ph. Hering, Z. Huang, R. Iverson, H. Loos, M. Messerschmidt, A. Miahnahri, S. Moeller, H.-D. Nuhn, G. Pile3, D. Ratner, J. Rzepiela, D. Schultz, T. Smith, P. Stefan, H. Tompkins, J. Turner, J. Welch, W. White, J. Wu, G. Yocky and J. Galayda , "First lasing and operation of an ångstrom-wavelength free-electron laser," Nat. Photon. **4**(9), 641-647 (2010).

[197] E. Allaria, R. Appio, L. Badano, W.A. Barletta, S. Bassanese, S. G. Biedron, A. Borga, E. Busetto, D. Castronovo, P. Cinquegrana, S. Cleva, D. Cocco, M. Cornacchia, P. Craievich, I. Cudin, G. D'Auria, M. Dal Forno, M. B. Danailov, R. De Monte, G. De Ninno, P. Delgiusto, A. Demidovich, S. Di Mitri, B. Diviacco, A. Fabris, R. Fabris, W. Fawley, M. Ferianis, E. Ferrari, S. Ferry, L. Froehlich, P. Furlan, G. Gaio, F. Gelmetti, L. Giannessi, M. Giannini, R. Gobessi, R. Ivanov, E. Karantzoulis, M. Lonza, A. Lutman, B. Mahieu, M. Milloch, S. V. Milton, M. Musardo, I. Nikolov, S. Noe, F. Parmigiani, G. Penco, M. Petronio, L. Pivetta, M. Predonzani, F. Rossi, L. Rumiz, A. Salom, C. Scafuri, C. Serpico, P. Sigalotti, S. Spampinati, C. Spezzani, M. Svandrlik, C. Svetina, S. Tazzari, M. Trovo, R. Umer, A.

Vascotto, M. Veronese, R. Visintini, M. Zaccaria, D. Zangrando and M. Zangrando, "Highly coherent and stable pulses from the FERMI seeded free-electron laser in the extreme ultraviolet," Nat. Photon. **6**(10), 699-704 (2012).

[198] FERMI@Elettra Conceptual Design Report.

[199] P. Schmüser, M. Dohlus, J. Rossbach, and C. Behrens, "Free-Electron Lasers in the Ultraviolet and X-Ray Regime. Physical Principles, Experimental Results, Technical Realization," Springer tracts in modern physics **258** (2014).

[200] B. Mahieu, "Cohérence, accordabilité, propriétés spectrales et spatiales de sources de lumière extrême-ultraviolette femtoseconde," PhD dissertation, Université Paris-Sud (2013).

[201] I. Boscolo, V. Stagno, "The converter and the transverse optical klystron," Nuovo Cimento B **58**(2), 267-285 (1980).

[202] L. H. Yu, "Generation of intense UV radiation by subharmonically seeded single-pass free-electron lasers," Phys. Rev. A **44**(8), 5178 (1991).

[203] L. Giannessi, "Overview of Perseo, a system for simulating FEL dynamics in Mathcad," Proc. FEL conf. 2006, 91-94 (2004).

[204] S. Reiche, "GENESIS 1.3: a fully 3D time-dependent FEL simulation code," Nucl. Instr. Meth. Phys. Res. A **429**(1-3), 243-248 (1999).

[205] F. Curbis, "Generation of VUV ultra-short coherent optical pulses using electron storage rings," PhD dissertation, Università degli studi di Trieste (2008).

[206] R. Bonifacio, L. Di Salvo Souza, P. Pierini and N. Piovella, "The superradiant regime of a FEL: analytical and numerical results," Nucl. Instr. Meth. Phys. Res. A **296**(1-3), 358-367 (1990).

[207] A. Amir and Y. Greenzweig, "Three-dimensional free electron laser gain and evolution of optical modes," Nucl. Instr. Meth. Phys. Res. A **250**(1-2), 404-412 (1986).

[208] L.-H. Yu, M. Babzien, I. Ben-Zvi, L. F. DiMauro, A. Doyuran, W. Graves, E. Johnson, S. Krinsky, R. Malone, I. Pogorelsky, J. Skaritka, G. Rakowsky, L. Solomon, X. J. Wang, M. Woodle, V. Yakimenko, S. G. Biedron, J. N. Galayda, E. Gluskin, J. Jagger, V. Sajaev, I. Vasserman, "High-Gain Harmonic-Generation Free-Electron Laser," Science **289**, 932-934 (2000).

[209] E. Allaria, D. Castronovo, P. Cinquegrana, P. Craievich, M. Dal Forno, M. B. Danailov, G. D'Auria, A. Demidovich, G. De Ninno, S. Di Mitri, B. Diviacco, W. M. Fawley, M. Ferianis, E. Ferrari, L. Froehlich, G. Gaio, D. Gauthier, L. Giannessi, R. Ivanov, B. Mahieu, N. Mahne, I. Nikolov, F. Parmigiani, G. Penco, L. Raimondi, C. Scafuri, C. Serpico, P. Sigalotti, S. Spampinati, C. Spezzani, M. Svandrlik, C. Svetina, M. Trovo, M. Veronese, D. Zangrando and M. Zangrando, "Two-stage seeded soft-X-ray free-electron laser," Nat. Photon. **7**(11), 913-918 (2013). 2013.

[210] E. Allaria, R. Appio, L. Badano, W. A. Barletta, S. Bassanese, S. G. Biedron, A. Borga, E. Busetto, D. Castronovo, P. Cinquegrana, S. Cleva, D. Cocco, M. Cornacchia, P. Craievich, I. Cudin, G. D'Auria, M. Dal Forno, M. B. Danailov, R. De Monte, G. De Ninno, P. Delgiusto, A. Demidovich, S. Di Mitri, B. Diviacco, A. Fabris, R. Fabris, W. Fawley, M. Ferianis, E. Ferrari, S. Ferry, L. Froehlich, P. Furlan, G. Gaio, F. Gelmetti, L. Giannessi, M. Giannini, R. Gobessi, R. Ivanov, E. Karantzoulis, M. Lonza, A. Lutman, B. Mahieu, M. Milloch, S. V. Milton, M. Musardo, I. Nikolov, S. Noe, F. Parmigiani, G. Penco, M. Petronio, L. Pivetta, M. Predonzani, F. Rossi, L. Rumiz, A. Salom, C. Scafuri, C. Serpico, P. Sigalotti, S. Spampinati, C. Spezzani, M. Svandrlik, C. Svetina, S. Tazzari, M. Trovò, R. Umer, A. Vascotto, M. Veronese, R. Visintini, M. Zaccaria, D. Zangrando and M. Zangrando, "Highly coherent and stable pulses from the FERMI seeded free-electron laser in the extreme ultraviolet," Nat. Photon **6**, 699-704 (2012).

[211] M. Zangrando, A. Abrami, D. Cocco, C. Fava, S. Gerusina, R. Gobessi, N. Mahne, E. Mazzucco, L. Raimondi, L. Rumiz, C. Svetina, and F. Parmigiani, "The photon beam transport and diagnostics system at FERMI@Elettra, the Italian seeded FEL source: commissioning experience and most recent results," Proc. SPIE 8504, 850404 (2012).

[212] C. Svetina, A. Abrami, I. Cudin, C. Fava, S. Gerusina, R. Gobessi, L. Rumiz, G. Sostero, M. Zangrando, and D. Cocco, "Characterization of the FERMI@Elettra's on-line photon energy spectrometer," Proc. SPIE 8139, 81390J (2011).

[213] B. Mahieu, D. Gauthier, G. De Ninno, H. Dacasa, M. Lozano, J.-Ph. Rousseau, Ph. Zeitoun, D. Garzella, and H. Merdji, "Spectral-phase interferometry for direct electric-field reconstruction applied to seeded extreme-ultraviolet free-electron lasers," Opt. Express **23**(14), 17665 (2015).

[214] R. Mitzner, A. A. Sorokin, B. Siemer, S. Roling, M. Rutkowski, H. Zacharias, M. Neeb, T. Noll, F. Siewert, W. Eberhardt, M. Richter, P. Juranic, K. Tiedtke, and J. Feldhaus, "Direct autocorrelation of soft-x-ray free-electron-laser pulses by time-resolved two-photon double ionization of He," Phys. Rev. A **80**(2), 025402 (2009).

[215] P. Radcliffe, S. Dsterer, A. Azima, H. Redlin, J. Feldhaus, J. Dardis, K. Kavanagh, H. Luna, J. Pedregosa Gutierrez, P. Yeates, E. T. Kennedy, J. T. Costello, A. Delserieys, C. L. S. Lewis, R. Taïeb, A. Maquet, D. Cubaynes, and M. Meyer, "Single-shot characterization of independent femtosecond extreme ultraviolet free electron and infrared laser pulses," App. Phys. Lett. **90**, 131108 (2007).

[216] G. De Ninno, E. Allaria, M. Coreno, F. Curbis, M. B. Danailov, E. Karantzoulis, A. Locatelli, T. O. Mentes, M. A. Nino, C. Spezzani, and M. Trovò, "Generation of Ultrashort Coherent Vacuum Ultraviolet Pulses Using Electron Storage Rings: A New Bright Light Source for Experiments," Phys. Rev. Lett. **101**(5), 053902 (2008).

[217] J. Wu, J. B. Murphy, P. J. Emma, X. Wang, T. Watanabe, and X. Zhong, "Interplay of the chirps and chirped pulse compression in a high-gain seeded free-electron laser," JOSA B **24**(3), 484-495 (2007).

[218] Z. Wu, H. Loos, Y. Shen, B. Sheehy, E. D. Johnson, S. Krinsky, J. B. Murphy, J. Rose, T. Shaftan, X.-J. Wang, and L. H. Yu, "Spectral phase modulation and chirped pulse amplification in high gain harmonic generation," Proc. FEL conf. 2004, 285-288 (2004).

[219] E. Allaria, F. Bencivenga, R. Borghes, F. Capotondi, D. Castronovo, P. Charalambous, P. Cinquegrana, M. B. Danailov, G. De Ninno, A. Demidovich, S. Di Mitri, B. Diviacco, D. Fausti, W. M. Fawley, E. Ferrari, L. Fröhlich, D. Gauthier, A. Gessini, L. Giannessi, R. Ivanov, M. Kiskinova, G. Kurdi, B. Mahieu, N. Mahne, I. Nikolov, C. Masciovecchio, E. Pedersoli, G. Penco, L. Raimondi, C. Serpico, P. Sigalotti, S. Spampinati, C. Spezzani, C. Svetina, M. Trovò, and M. Zangrando, "Two-colour pump-probe experiments with a twin-pulse-seed extreme ultraviolet free-electron laser," Nat. Comm. **4**, 2476 (2013).

[220] G. De Ninno, D. Gauthier, B. Mahieu, P. R. Ribič, E. Allaria, P. Cinquegrana, M. B. Danailov, A. Demidovich, E. Ferrari, L. Giannessi, G. Penco, P. Sigalotti, and M. Stupar, "Single-shot spectro-temporal characterization of XUV pulses from a seeded free-electron laser," Nat. Commun. **6**, 8075 (2015).

[221] B. Mahieu, E. Allaria, D. Castronovo, M. B. Danailov, A. Demidovich, G. De Ninno, S. Di Mitri, W. M. Fawley, E. Ferrari, L. Fröhlich, D. Gauthier, L. Giannessi, N. Mahne, G. Penco, L. Raimondi, S. Spampinati, C. Spezzani, C. Svetina, M. Trovò and M . Zangrando, "Two-colour generation in a chirped seeded Free-Electron Laser: a close look," Opt. Express **21**(19), 22728-22741 (2013).

[222] G. De Ninno, B. Mahieu, E. Allaria, L. Giannessi, and S. Spampinati, "Chirped seeded free-electron lasers: self standing light sources for two-color pump-probe experiments," Phys. Rev. Lett. **110**, 064801 (2013).

[223] G. Stupakov, "Effect of finite pulse length and laser frequency chirp on HGHG and EEHG seeding," SLAC Report No. SLAC-PUB-14639 (2011).

[224] D. Ratner, A. Fry, G. Stupakov and W. White, "Laser phase errors in seeded free electron lasers," Phys. Rev. ST Accel. Beams **15**, 030702 (2012).

[225] G. Lambert, T. Hara, D. Garzella, T. Tanikawa, M. Labat, B. Carré, H. Kitamura, T. Shintake, M. Bougeard, S. Inoue, Y. Tanaka, P. Salières, H. Merdji, O. Chubar, O. Gobert, K. Tahara, and M.-E. Couprie, "Injection of harmonics generated in gas in a free-electron laser providing intense and coherent extreme ultraviolet light," Nat. Phys. **4**, 296 (2008).

[226] D. Xiang, E. Colby, M. Dunning, S. Gilevich, C. Hast, K. Jobe, D. McCormick, J. Nelson, T. O. Raubenheimer, K. Soong, G. Stupakov, Z. Szalata, D. Walz, S. Weathersby, M. Woodley, and P.-L. Pernet, "Demonstration of the echo-enabled harmonic generation technique for short-wavelength seeded free-electron lasers," Phys. Rev. Lett. **105**, 114801 (2010).

[227] A.A. Lutman, F.-J Decker, J. Arthur, M. Chollet, Y. Feng, J. Hastings, Z. Huang, H. Lemke, H.-D. Nuhn, A. Marinelli, J. L. Turner, S. Wakatsuki, J. Welch, and D. Zhu, "Demonstration of single-crystal self-seeded two-color X-ray free-electron lasers," Phys. Rev. Lett. **113**, 254801 (2014).

[228] L. H. Yu, E. Johnson, D. Li, and D. Umstadter, "Femtosecond free-electron laser by chirped pulse amplification," Phys. Rev. E **49**, 4480-4486 (1994).

[229] C. Feng, L. Shen, M. Zhang, D. Wang, Z. Zhao, and D. Xiang, "Chirped pulse amplification in a seeded free-electron laser for generating high-power ultra-short radiation," Nucl. Instr. Meth. Phys. Res. A **712**, 113-119 (2013).

[230] Y. Wang, E. Granados, M. A. Larotonda, M. Berrill, B. M. Luther, D. Patel, C. S. Menoni, and J. J. Rocca, "High-Brightness Injection-Seeded Soft-X-Ray-Laser Amplifier Using a Solid Target," Phys. Rev. Lett. **97**(12), 123901 (2006).

[231] T. Mocek, B. Rus, M. Kozlová, J. Polan, P. Homer, K. Jakubczak, M. Stupka, D. Snopek, J. Nejdl, M. H. Edwards, D. S. Whittaker, G. J. Tallents, P. Mistry, G. J. Pert, N. Booth, Z. Zhai, M. Fajardo, P. Zeitoun, J. Chalupský, V. Hájková, and L. Juha, "Plasma-based X-ray laser at 21 nm for multidisciplinary applications," Eur. Phys. J. D **54**(2), 439-444 (2009).

[232] A. Klisnick, J. Kuba, D. Ros, R. Smith, G. Jamelot, C. Chenais-Popovics, R. Keenan, S. J. Topping, C. L. S. Lewis, F. Strati, G. J. Tallents, D. Neely, R. Clarke, J. Collier, A. G. MacPhee, F. Bortolotto, P. V. Nickles, and K. A. Janulewicz, "Demonstration of a 2-ps transient x-ray laser," Phys. Rev. A **65**(3), 033810 (2002).

[233] T. Ditmire, M. H. R. Hutchinson, M. H. Key, C. L. S. Lewis, A. MacPhee, I. Mercer, D. Neely, M. D. Perry, R. A. Smith, J. S. Wark, and M. Zepf, "Amplification of xuv harmonic radiation in a gallium amplifier," Phys. Rev. A **51**(6), R4337 (1995).

[234] L. Li, Y. Wang, S. Wang, E. Oliva, L. Yin, T. T. T. Le, S. Daboussi, D. Ros, G. Maynard, S. Sebban, B. Hu, J. J. Rocca, and Philippe Zeitoun, "Wavefront improvement in an injection-seeded soft x-ray laser based on a solid-target plasma amplifier," Opt. Lett. **38**(20), 4011 (2013).

[235] D. Ros, K. Cassou, B. Cros, S. Daboussi, J. Demailly, O. Guilbaud, S. Kazamias, J.-C. Lagron, G. Maynard, O. Neveu, M. Pittman, B. Zielbauer, D. Zimmer, T. Kuhl , S. Lacombe, E. Porcel, M.-A. du Penhoat, P. Zeitoun, and G. Mourou, "LASERIX: An open facility for developments of EUV and soft X-ray lasers and applications - Developments of XUV sources using high power laser facilities: ILE, ELI," Nucl. Instr. Meth. Phys. Res. A **653**(1), 76-79 (2011).

[236] A. Depresseux, E. Oliva, J. Gautier, F. Tissandier, G. Lambert, B. Vodungbo, J-P. Goddet, A. Tafzi, J. Nejdl, M. Kozlova, G. Maynard, H. T. Kim, K. Ta Phuoc, A. Rousse, P. Zeitoun, and S. Sebban, "Demonstration of a Circularly Polarized Plasma-Based Soft-X-Ray Laser," Phys. Rev. Lett. **115**(8), 083901 (2015).

[237] P. Zeitoun, E. Oliva, T. T. T. Le, S. Sebban, M. Fajardo, D. Ros, and P. Velarde, "Towards Tabletop X-Ray Lasers," Attosecond and XUV Physics, 135-176 (Eds. Wiley-VCH Verlag GmbH and Co. KGaA, 2014).

[238] A. Depresseux, E. Oliva, J. Gautier, F. Tissandier, J. Nejdl, M. Kozlova, G. Maynard, J. P. Goddet, A. Tafzi, A. Lifschitz, H. T. Kim, S. Jacquemot, V. Malka, K. Ta Phuoc, C. Thaury, P. Rousseau, G. Iaquaniello, T. Lefrou, A. Flacco, B. Vodungbo, G. Lambert, A. Rousse, P. Zeitoun, and S. Sebban, "Table-top femtosecond soft X-ray laser by collisional ionization gating," Nat. Photon. **9**(12), 817-821 (2015).

[239] Y. Wang, L. Yin, S. Wang, M. C. Marconi, J. Dunn, E. Gullikson, and J. J. Rocca, "Single-shot soft x-ray laser linewidth measurement using a grating interferometer," Opt. Lett. **38**(23), 5004-5007 (2013).

[240] F. Ogando and P. Velarde, "Development of a radiation transport fluid dynamic code under AMR scheme," J. Quant. Spectrosc. Radiat Transf. **71**, 541 (2001).

[241] E. Oliva, Ph. Zeitoun, S. Sebban, M. Fajardo, P. Velarde, K. Cassou, and D. Ros, "Optimization of soft x-ray amplifier by tailoring plasma hydrodynamics," Opt. Lett. **34**(17), 2640-2642 (2009).

[242] E. Oliva, Ph. Zeitoun, P. Velarde, M. Fajardo, K. Cassou, D. Ros, S. Sebban, D. Portillo, and S. le Pape, "Hydrodynamic study of plasma amplifiers for soft-x-ray lasers: A transition in hydrodynamic behavior for plasma columns with widths ranging from 20 μm to 2 mm," Phys. Rev. E **82**(5), 056408 (2010).

[243] E. Oliva, Ph. Zeitoun, M. Fajardo, G. Lambert, D. Ros, S. Sebban, and P. Velarde, "Comparison of natural and forced amplification regimes in plasma-based soft-x-ray lasers seeded by high-order harmonics," Phys. Rev. A **84**(1), 013811 (2011).

[244] I. R. Al'miev, O. Larroche, D. Benredjem, J. Dubau, S. Kazamias, C. Möller, and A. Klisnick, "Dynamical Description of Transient X-Ray Lasers Seeded with High-Order Harmonic Radiation through Maxwell-Bloch Numerical Simulations," Phys. Rev. Lett. **99**(12), 123902 (2007).

[245] C. M. Kim, J. Lee, and K. A. Janulewicz, "Coherent Amplification of an Ultrashort Pulse in a High- and Swept-Gain Medium with Level Degeneracy," Phys. Rev. Lett. **104**(5), 053901 (2010).

[246] Y. Wang, E. Granados, F. Pedaci, D. Alessi, B. Luther, M. Berrill, and J. J. Rocca, "Phase-coherent, injection-seeded, table-top soft-X-ray lasers at 18.9 nm and 13.9 nm," Nat. Photon. **2**(2), 94-98 (2008).

[247] E. Oliva, M. Fajardo, L. Li, S. Sebban, D. Ros, and P. Zeitoun, "Soft x-ray plasma-based seeded multistage amplification chain," Opt. Lett. **37**(20), 4341-4343 (2012).

[248] E. Oliva, M. Fajardo, L. Li, M. Pittman, T. T. T. Le, J. Gautier, G. Lambert, P. Velarde, D. Ros, S. Sebban, and Ph. Zeitoun, "A proposal for multi-tens of GW fully coherent femtosecond soft X-ray lasers," Nat. Photon. **6**, 764-767 (2012).

[249] P. Bowlan, P. Gabolde, A. Shreenath, K. McGresham, R. Trebino, and S. Akturk, "Crossed-beam spectral interferometry: a simple, high-spectral-resolution method for completely characterizing complex ultrashort pulses in real time," Opt. Express **14**(24), 11892-11900 (2006).

[250] P. Bowlan, "Measuring the spatiotemporal electric field of ultrashort pulses with high spatial and spectral resolution," PhD dissertation, Georgia Institute of Technology (2009).

[251] E. Treacy, "Optical pulse compression with diffraction gratings," IEEE J. Quant. Electron. **5**(9), 454-458 (1969).

[252] C. A. Palmer, E. G. Loewen, "Diffraction grating handbook, fifth edition" (Thermo RGL, 2002).

[253] G. Chériaux, "Influences des distorsions de phase sur le profil d'impulsions femtoseconde dans l'amplification à dérive de fréquence," PhD dissertation, Université Paris XI Orsay (1997).

[254] O. Martinez, "3000 times grating compressor with positive group velocity dispersion: Application to fiber compensation in 1.3-1.6 μm region," IEEE J. Quant. Electron. **23**(1), 59-64 (1987).

[255] S. Backus, C. G. Durfee III, M. M. Murnane, and H. C. Kapteyn, "High power ultrafast lasers," Rev. Sci. Instrum. **69**(3), 1207-1223 (1998).

[256] A. Doyuran, L. DiMauro, W. Graves, R. Heese, E. D. Johnson, S. Krinsky, H. Loos, J. B. Murphy, G. Rakowsky, J. Rose, T. Shaftan, B. Sheehy, Y. Shen, J. Skaritka, X. Wang, Z. Wu, and L. H. Yu, "Chirped pulse amplification of HGHG-FEL at DUV-FEL facility at BNL," Nucl. Instr. Meth. Phys. Res. A **528**(1-2), 467-470 (2004).

[257] P. Emma, K. Bane, M. Cornacchia, Z. Huang, H. Schlarb, G. Stupakov, and D. Walz, "Femtosecond and Subfemtosecond X-Ray Pulses from a Self-Amplified Spontaneous-Emission-Based Free-Electron Laser," Phys. Rev. Lett. **92**(7), 074801 (2004).

[258] A. A. Zholents and W. M. Fawley, "Proposal for Intense Attosecond Radiation from an X-Ray Free-Electron Laser," Phys. Rev. Lett. **92**(22), 224801 (2004).

[259] E. L. Saldin, E. A. Schneidmiller, and M. V. Yurkov, "Self-amplified spontaneous emission FEL with energy-chirped electron beam and its application for generation of attosecond x-ray pulses," Phys. Rev. ST Accel. Beams **9**(5), 050702 (2006).

[260] N. R. Thompson and B. W. J. McNeil, "Mode Locking in a Free-Electron Laser Amplifier," Phys. Rev. Lett. **100**(20), 203901 (2008).

[261] L. Giannessi, A. Bacci, M. Bellaveglia, F. Briquez, M. Castellano, E. Chiadroni, A. Cianchi, F. Ciocci, M. E. Couprie, L. Cultrera, G. Dattoli, D. Filippetto, M. Del Franco, G. Di Pirro, M. Ferrario, L. Ficcadenti, F. Frassetto, A. Gallo, G. Gatti, M. Labat, G. Marcus, M. Moreno, A. Mostacci, E. Pace, A. Petralia, V. Petrillo, L. Poletto, M. Quattromini, J. V. Rau, C. Ronsivalle, J. Rosenzweig, A. R. Rossi„ V. Rossi Albertini, E. Sabia, M. Serluca, S. Spampinati, I. Spassovsky, B. Spataro, V. Surrenti, C. Vaccarezza, and C. Vicario, "Self-Amplified Spontaneous Emission Free-Electron Laser with an Energy-Chirped Electron Beam and Undulator Tapering," Phys. Rev. Lett. **106**(14), 144801 (2011).

[262] T. Tanaka, "Proposal for a Pulse-Compression Scheme in X-Ray Free-Electron Lasers to Generate a Multiterawatt, Attosecond X-Ray Pulse," Phys. Rev. Lett. **110**(8), 084801 (2013).

[263] E. Prat and S. Reiche, "Simple Method to Generate Terawatt-Attosecond X-Ray Free-Electron-Laser Pulses," Phys. Rev. Lett. **114**(24), 203901 (2015)

[264] L. H. Yu, T. Shaftan, D. Liu, T. Tsang, J. Rose, X. J. Wang, and T. Watanabe, "Chirped pulse amplification experiment at 800 nm," Proc. FEL conf. 2006, 194-197 (2006).

[265] G. T. Moore, "Frequency chirping of the free-electron laser," Phys. Rev. Lett. **60**(18), 1825 (1988).

[266] X. Shu, T. Peng, and Y. Dou, "Chirped pulse amplification in a free-electron laser amplifier," J. Electron Spectrosc. Relat. Phenom **184**(3-6) 350-353 (2011).

[267] D. Gauthier, E. Allaria, M. Coreno, I. Cudin, H. Dacasa, M. B. Danailov, A. Demidovich, S. Di Mitri, B. Diviacco, E. Ferrari, P. Finetti, F. Frassetto, D. Garzella, S. Künzel, V. Leroux, B. Mahieu, N. Mahne, M. Meyer, T. Mazza, P. Miotti, G. Penco, L. Raimondi, P. R. Ribič, R. Richter, E. Roussel, S. Schulz, L. Sturari, C. Svetina, M. Trovò, P. A. Walker, M. Zangrando, C. Callegari, M. Fajardo, L. Poletto, Ph. Zeitoun, L. Giannessi, and G. De Ninno, "Chirped pulse amplification in an extreme-ultraviolet free-electron laser," Nat. Commun. **7**, 13688 (2016).

[268] D. Ratner, A. Fry, G. Stupakov, and W. White, "Laser phase errors in seeded free electron lasers," Phys. Rev. Accel. Beams. **15**(3), 030702 (2012).

[269] W. Werner, "X-ray efficiencies of blazed gratings in extreme off-plane mountings," Appl. Opt. **16**(8), 2078-2080 (1977).

[270] B. Dick, "Inverting ion images without Abel inversion: maximum entropy reconstruction of velocity maps," Phys. Chem. Chem. Phys. **16**(2), 570-580 (2014).

[271] M. Pascolini, S. Bonora, A. Giglia, N. Mahne, S. Nannarone, and L. Poletto, "Gratings in a conical diffraction mounting for an extreme-ultraviolet time-delay-compensated monochromator," Appl. Opt. **45**(14), 3253-3262 (2006).

[272] M. Nevière, D. Maystre, and W. R. Hunter, "On the use of classical and conical diffraction mountings for XUV gratings," J. Opt. Soc. Am. **68**(8), 1106-1113 (1978).

[273] F. Frassetto, P. Villoresi, and L. Poletto, "Optical concept of a compressor for XUV pulses in the attosecond domain," Opt. Express **16**(9), 6652-6667 (2008).

[274] H. Dacasa, B. Mahieu, M. Fajardo, T. T. T. Le, L. Li, E. Oliva, and Ph. Zeitoun, "Chirped pulse amplification in x-ray free-electron lasers," Proc. SPIE 9589, 95890G (2015).

[275] G. H. Spencer and M. V. R. K. Murty, "General Ray-Tracing Procedure," J. Opt. Soc. Am. **52**, 672-678 (1962).

List of Figures

List of Tables

Résumé détaillé en français

Les impulsions ultra-brèves de rayonnement ultraviolet extrême (UVX) ont un grand champ d'application dans des domaines tels que le diagnostic de plasmas, la biologie ou l'étude de la dynamique ultra-rapide des atomes et molécules. Aujourd'hui, il existe trois sources délivrant ce genre d'impulsions. Les harmoniques d'ordre élevé générées (*high-order harmonic generation*, HHG) dans les gaz rares peuvent fournir des impulsions attosecondes. Cependant, leur énergie, le plus souvent de l'ordre du nanojoule, limite ses applications. L'amplification des impulsions harmoniques dans les plasmas créés par laser (*soft-X-ray laser*, SXRL) a démontré pouvoir fournir des énergies de plusieurs dizaines de microjoules. Des énergies plus élevées peuvent être obtenues avec les lasers à électrons libres (LEL) UVX injectés, mais ce sont des très grandes infrastructures ayant un accès plus limité.

La HHG dans les gaz est un processus optique hautement non-linéaire par lequel une impulsion laser, polarisée linéairement, est focalisée sur un jet de gaz ou une cellule à des intensités de l'ordre de $10^{14-15}\,\mathrm{W/cm^2}$, produisant des impulsions ultra-brèves spatialement et temporellement cohérentes, dans le domaine de l'UVX ou les rayons X mous. Le spectre des impulsions harmoniques consiste à des multiples impaires de la fréquence du laser initial. Malgré avoir été démontrée dans les années 1980, son nombre d'applications, ainsi que celles des SXRLs injectés et LELs UVX, a été fortement étendu dans les 2000. Comme les lasers visibles, ces sources génèrent des faisceaux collimatés et généralement polarisés avec des bonnes propriétés de cohérence. Dans les années récentes, leur gamme spectrale $(10\,\mathrm{eV} - 1\,\mathrm{keV})$ a été prolongé vers les rayons X durs $(1 - 10\,\mathrm{keV})$, grâce au développement des LELs.

Malgré leur mise en œuvre réussie pour un large éventail d'applications, le développement ultérieur de ces sources reste limité par la difficulté d'effectuer une métrologie spatiale et temporelle complète des faisceaux qu'elles fournissent. En particulier, le développement de techniques précises pour la caractérisation temporelle complète des impulsions UVX est fondamental pour obtenir des durées plus courtes. Des progrès significatifs ont été réalisés ces dernières années sur la mesure de la durée des impulsions harmoniques, qui peuvent fournir des impulsions des durées plus courtes que $100\,\mathrm{as}$. Néanmoins, la plupart des techniques pour les impulsions harmoniques ne peuvent pas être appliquées aux SXRLs injectés en raison de leurs propriétés particulières ou aux LELs à cause de leur instabilité tir à tir intrinsèque. En effet, les LELs sont basés sur l'amplification de l'émission stochastique, sauf si une impulsion externe est injectée. Cette thèse présente l'adaptation de deux techniques, potentiellement monocoup, pour la métrologie temporelle complète des LELs UVX injectés et les SXRLs à plasmas injectés par des impulsions harmoniques.

En plus d'atteindre des durées d'impulsion plus courtes, l'un des principaux objectifs de la communauté des sources UVX et des rayons X a été d'atteindre des intensités plus élevés, ce qui nécessite une focalisation efficace. Les installations LEL sont généralement équipées d'optiques à rayons X de très haute qualité, qui assurent une focalisation précise si le faisceau entrant a un bon front d'onde et que les optiques sont correctement alignées. Ces deux problèmes nécessitent l'utilisation de senseurs de front d'onde dédiés, disponibles dans le commerce pour les domaines des UVX et rayons X.

La situation est différente pour les sources HHG. Peu d'expériences ont été réalisées jusqu'à présent sur le sujet de la métrologie spatiale de ces impulsions. En plus, elles montrent une grande disparité dans les fronts d'onde obtenus. Ces sources deviennent de plus en plus courantes grâce à leurs capacités de produire des expériences compactes dans le domaine UVX. Cependant, l'étude des phénomènes non-linéaires nécessite des intensités élevées, et donc une focalisation efficace des faisceaux harmoniques. Puisque les harmoniques élevées sont utilisées pour leur amplification dans des plasmas ou des LELs, il est essentiel d'améliorer notre compréhension de leurs propriétés spatiales et, en particulier, du lien entre le laser fondamental et les fronts d'onde des harmoniques. Ce sujet est exploré de façon expérimentale dans cette thèse. De plus, un senseur de front d'onde UVX est utilisé pour l'optimisation en temps réel de l'alignement d'un système optique de focalisation pour des harmoniques.

En plus d'une bonne focalisation, atteindre des intensités plus élevées nécessite également d'augmenter l'énergie des impulsions. Une façon d'y parvenir est la mise en œuvre de schémas d'amplification à dérive de fréquence (*chirped pulse amplification*, CPA) pour les sources UVX injectées. Ce sujet est également abordé dans cette thèse, et la première implémentation de ce schéma dans un LEL UVX injecté est présentée.

Le chapitre 1 présente la théorie et les propriétés de base de la HHG. Il présente aussi les principes de la métrologie du front d'onde avec des senseurs de front d'onde UVX de type Hartmann. Grâce à ses propriétés spectrales et temporelles, ainsi que sa cohérence, la HHG est une source utile de rayonnement de courte longueur d'onde pour un large éventail d'applications, y comprises l'optique non-linéaire dans le domaine UVX, la spectroscopie UVX ou la physique des plasmas. En termes simples, les harmoniques d'ordre élevé sont générées lorsque le laser fondamental ionise les électrons des atomes du milieu, qui sont ensuite accélérés dans son champ électrique, puis recombiné avec leur ion parent, convertissant leur énergie cinétique en photons. Ceci est connu comme le modèle en trois étapes de la HHG. Ce chapitre présente aussi la Salle Corail, une nouvelle ligne de lumière HHG au LOA, ainsi que plusieurs aspects expérimentaux de la HHG. Le chapitre décrit aussi deux expériences dans lesquelles ce senseur est utilisé pour étudier les propriétés spatiales des impulsions HHG en fonction des conditions de génération, ainsi que l'influence du front d'onde du faisceau fondamental, avec des mesures monocoup. Enfin, ce chapitre rapporte deux expériences réalisées au LLC, en Suède. Dans ces expériences, notre senseur Hartmann UVX est utilisé pour étudier en détail les propriétés spatiales des impulsions harmoniques en fonction des conditions de génération, ainsi que l'influence du laser fondamental et son front d'onde.

Le senseur Hartmann UVX s'est avéré être un outil puissant pour la métrologie spatiale des impulsions UVX. Avec cela, nous avons mesuré comment les fronts d'onde des impulsions harmoniques sont affectées par les paramètres de génération, ainsi que le front d'onde de l'impulsion infrarouge fondamentale. Dans les deux cas, l'énergie des impulsions harmoniques était suffisamment haute pour permettre des mesures monocoup de front d'onde.

Dans la première expérience, le front d'onde du faisceau infrarouge était constant, avec une erreur RMS de $\lambda_{\mathrm{IR}}/10$ ($\lambda_{\mathrm{IR}} = 800\mathrm{nm}$). Le front d'onde harmonique typique avait un RMS proche de $\lambda_{\mathrm{UVX}}/4$ ($\lambda_{\mathrm{UVX}} = 42\mathrm{nm}$), avec une bonne stabilité tir à tir, représentée par un écart-type relative généralement inférieur à 25% lorsqu'on considère cinq mesures indépendantes.

Nous avons observé que les fronts d'onde harmoniques avaient toujours un astigmatisme significatif à 0°, une aberration qui semble être absente de l'impulsion infrarouge. Ceci, avec la grande différence dans leurs RMS, indique qu'il n'y a pas de transfert direct du front d'onde d'une impulsion vers l'autre. Toutes les autres aberrations, telles que le coma ou l'aberration sphérique, sont beaucoup moins pertinentes. Ceci est particulièrement utile pour focaliser le faisceau harmonique, car l'astigmatisme peut être corrigé lors de l'utilisation d'optiques incurvées. L'utilisation de miroirs multicouches nous a permis de mesurer les fronts d'onde des harmoniques individuels, ce qui révèle que l'astigmatisme est causé par les ordres les plus hauts, étant presque entièrement absent des harmoniques du plateau. En conséquence, le front d'onde du faisceau complet pourrait également être amélioré en filtrant les harmoniques de la coupure.

Les calculs de rétropropagation suggèrent que la forme du faisceau infrarouge au foyer dicte largement la forme de la source harmonique, avec les différents paramètres de génération, tels que la pression dans la cellule de gaz, ayant une grande influence sur le RMS du front d'onde en général, et l'astigmatisme en particulier. De plus, nous avons trouvé que les paramètres de la HHG qui conduisent aux énergies d'impulsion les plus élevées ne donnent pas les meilleurs fronts d'onde. En fait, le contraire est normalement observé.

Pour la deuxième expérience, un miroir déformable a été installé dans le trajet du faisceau infrarouge afin d'obtenir plus d'informations sur la façon dont le changement de son front d'onde peut affecter la HHG. Nous avons constaté qu'il a une influence très significative sur son front d'onde, sa forme et sa taille, ainsi que l'efficacité du processus. Avec ce miroir, des fronts d'onde infrarouges avec des RMS inférieurs à $\lambda_{\mathrm{IR}}/20$ ont été obtenus, conduisant à la génération d'harmoniques avec $\mathrm{RMS} < \lambda_{\mathrm{XUV}}/11$, une amélioration significative par rapport aux résultats de l'expérience précédente. Lors de l'utilisation du miroir déformable, les impulsions harmoniques avec le meilleur front d'onde étaient aussi celles qui présentaient l'énergie d'impulsion la plus élevée, ainsi que la forme la plus circulaire.

Ces mesures soulignent l'importance d'utiliser un faisceau fondamental de bonne qualité spatiale pour obtenir des harmoniques non seulement avec de bons fronts d'onde, mais aussi des profils de faisceaux circulaires et de haute énergie. En outre, l'utilisation du miroir déformable pour le laser infrarouge permet un certain degré de contrôle sur la forme des impulsions harmoniques, principalement leur ellipticité et leur orientation.

Le chapitre 2 explore la possibilité d'utiliser des faisceaux d'harmoniques élevés pour la caractérisation d'optiques multicouches pour le domaine UVX sur table et à la longueur d'onde au moyen de la métrologie de front d'onde. Ce chapitre présente aussi l'utilisation du senseur Hartmann pour l'optimisation rapide et précise de systèmes de focalisation UVX pour des rayons harmoniques.

La résolution limitée par diffraction d'un système d'imagerie avec une ouverture numérique NA utilisé avec une source de longueur d'onde λ est donnée par le critère de Rayleigh comme $\mathrm{Res} = \frac{0.61\lambda}{\mathrm{NA}}$. En conséquence, les sources UVX et X peuvent fournir des résolutions plus fines que les sources infrarouges ou visibles. En fait, des résolutions inférieures à $50\,\mathrm{nm}$ ont été obtenues avec des microscopes réfléchissants, en utilisant un éclairage UVX.

Pour la nanoimagerie avec des sources UVX, des optiques de haute qualité sont également requises pour les meilleures résolutions. La même chose se produit pour d'autres applications telles que la lithographie EUV, où de meilleures optiques sont capables de produire des détails plus petits. Les longueurs d'onde UVX, de l'ordre de dizaines de nanomètres, sont sensibles à de plus petits défauts de surface que la lumière visible ou infrarouge. Pour cette raison, les exigences de qualité de surface pour les optiques UVX sont beaucoup plus strictes. Les sources de lumière visible, telles que les lasers de He-Ne ($\lambda = 632.8\,\mathrm{nm}$), souvent utilisées pour la métrologie optique en raison de leur simplicité, ne sont pas toujours suffisamment précises pour le cas des optiques UVX, qui pourraient bénéficier des tests à la longueur d'onde. En raison du haut flux UVX requis, ces tests prennent généralement beaucoup de temps car ils doivent être effectués dans des synchrotrons, où l'accès est limité. Être capable d'effectuer ces tests dans des configurations compactes serait extrêmement bénéfique pour le processus de fabrication de ces optiques.

Ce chapitre décrit l'utilisation de notre senseur de front d'onde Hartmann UVX avec deux systèmes optiques UVX utilisés avec des faisceaux harmoniques. En particulier, nous avons utilisé la HHG et le senseur pour la caractérisation sur table du miroir multicouche primaire d'un objective Schwarzschild UVX, ainsi que l'optimisation de son alignement dans la ligne de lumière de la Salle Orange du LOA. Ce chapitre présente également l'utilisation du capteur pour optimiser rapidement et efficacement la focalisation d'un télescope Wolter UVX pour des harmoniques, composé de deux miroirs toroïdaux.

Le développement de systèmes optiques UVX de haute qualité conduira à une meilleure résolution dans les applications d'imagerie à l'échelle nanométrique, ainsi qu'à des temps d'acquisition de données plus courts grâce à des efficacités plus élevées. Afin de fournir une bonne réflectivité, les systèmes d'imagerie et de focalisation pour l'UVX doivent utiliser des miroirs en incidence rasante, comme le télescope de type Wolter montré dans cette thèse, ou des miroirs multicouches, comme l'objective Schwarzschild, où les miroirs sont utilisés en incidence normale. La caractérisation des défauts à la longueur d'onde est importante pour les optiques UVX multicouches car elle offre plus de résolution que la caractérisation avec, par exemple, les lasers He-Ne. Les synchrotrons sont nécessaires pour effectuer de telles mesures en raison du haut flux requis pour des autres techniques utilisées normalement. Ce chapitre présente l'utilisation d'un senseur de front d'onde UVX pour mesurer la surface d'un miroir multicouches avec une source harmonique. Les résultats de ces mesures montrent un bon accord avec des simulations de tracé de rayons, confirmant ainsi la haute qualité du miroir testé.

Cependant, un système optique doit être bien aligné pour fournir ses meilleures performances d'imagerie ou de focalisation. Une mesure directe d'un point focal d'un diamètre de quelques microns ne peut généralement pas être prise en plaçant directement une caméra CCD sur le plan focal, car le foyer est typiquement plus petit que la taille de pixel, et la possibilité d'endommager le dispositif si l'intensité est trop élevée. Les mesures de points focaux UVX sont généralement effectuées en plaçant un cristal scintillateur, tel que Ce:YAG, dans le plan focal. Le cristal émet alors de la lumière visible par fluorescence, et son image est reprise au microscope afin de mesurer la taille du point. La précision de ce schéma est cependant limitée par l'apparition d'effets non-linéaires dans le cristal, ainsi que par sa saturation.

Notre senseur Hartmann UVX s'est avéré être un outil fondamental pour la mesure de faisceaux focalisés, par rétropropagation de fronts d'onde mesurés quelques dizaines de centimètres après le plan focal. Il peut ainsi être utilisé pour optimiser l'alignement des optiques de focalisation en temps réel avec d'excellents résultats. Dans ce chapitre, le senseur a été utilisé pour optimiser l'alignement d'un télescope de type Wolter UVX basé sur deux miroirs toroïdaux, réduisant le diamètre du foyer d'un facteur de plus de 5, et donc augmentant l'intensité de près de 30, dans un processus qui ne prend que quelques minutes, en fonction de l'alignement initial.

Le chapitre 3 décrit une expérience pompe-sonde réalisée au RAL, en Angleterre, dans laquelle des impulsions harmoniques ont été utilisées pour sonder les propriétés d'échantillons d'aluminium chauffé par des rayons X durs. Les résultats ont été comparés aux prédictions de deux modèles numériques existants. L'une des nombreuses applications des impulsions UVX, et en particulier des harmoniques d'ordre élevé, est le diagnostic de plasmas. De même, ils peuvent également être utilisés pour sonder des autres états de la matière, comme la *warm dense matter* (WDM). La WDM est un état transitoire entre la matière condensée et le plasma chaud, en termes de densité et de température. Les états WDM sont typiquement définis comme ceux avec une densité solide $(1-10\,\mathrm{g/cm^3})$ et une température d'électrons modérée $(10-100\,\mathrm{eV})$, donc simultanément trop froids et denses pour être décrits par la physique des plasmas, et trop chaud pour être décrits par la physique de la matière condensée. La WDM est présente dans des domaines tels que l'astrophysique, la science des matériaux ou la fusion par confinement inertiel.

Nous avons utilisé des impulsions harmoniques d'ordre élevé pour mesurer le coefficient d'absorption du rayonnement UVX dans des échantillons d'aluminium chaud. Les échantillons ont été chauffés radiativement avec des rayons X durs à une température électronique de $\mathrm{T_e} \simeq 1\,\mathrm{eV}$, une valeur pour laquelle les différents modèles numériques existants prédisent des propriétés d'absorption très différentes entre eux. En raison de limitations expérimentales, le coefficient d'absorption des échantillons chauffés n'a pu être obtenu que pour le 11^{e} ordre harmonique, correspondant à une énergie des photons de $25.88\,\mathrm{eV}$. Les résultats montrent que la valeur du coefficient d'absorption de l'aluminium chauffé à $1\,\mathrm{eV}$ reste très similaire à sa valeur à température ambiante.

Le coefficient d'absorption mesuré a été comparé aux valeurs calculées par deux des modèles numériques susmentionnés pour les mêmes conditions d'échantillon. Le résultat de cette expérience est très similaire au modèle de C. A. Iglesias, qui prédit peu de changement dans l'absorption pour la longueur d'onde considérée, tandis que le modèle de S. Vinko *et al.* prédit une augmentation de 40%. Notre résultat fournit donc des preuves en faveur du modèle précédent, donnant à son tour de nouvelles informations sur la physique de la WDM.

Le problème de la métrologie temporelle des impulsions ultra-brèves dans le domaine UVX est discuté en détail dans le chapitre 4. Comme une impulsion laser est une onde électromagnétique, il faut connaître l'amplitude et la phase de son champ électrique pour la caractériser complètement dans le domaine spatial, spectral ou temporel. La caractérisation spatiale des impulsions UVX a été discuté en profondeur dans les chapitres précédents, spéficiquement pour les harmoniques. La distribution d'intensité et la phase spatiale, ou front d'onde, d'une impulsion UVX peuvent être mesurés simultanément avec le senseur Hartmann. Dans le domaine spectral, le spectre d'une impulsion peut être mesuré directement avec des spectromètres. Cependant, ces appareils ne peuvent pas mesurer directement leur phase spectrale, puisqu'ils sont basés sur des détecteurs intégrateurs. En termes de domaine temporel, les mesures directes du profil d'intensité temporel sont impossibles pour des impulsions de durée trop courte.

Des impulsions laser femtoseconde sont couramment utilisées de nos jours, et des impulsions attosecondes peuvent également être générées. Leur durée est beaucoup plus courte que le temps de réponse des détecteurs électroniques les plus rapides, qui ne peuvent fournir que des résolutions temporelles jusqu'à la picoseconde. Afin de caractériser temporellement les impulsions ultra-brèves, des méthodes optiques sont nécessaires. Puisque les domaines spectral et temporel sont reliés par la transformée de Fourier, différentes techniques peuvent être utilisées pour mesurer la phase spectrale d'une impulsion, qui peut ensuite être utilisée avec le spectre pour calculer son profil et sa phase temporels.

La possibilité de mesurer la durée des impulsions UVX est fondamentale pour les applications impliquant des mesures résolues en temps, ainsi que le développement de sources capables de générer des impulsions plus courtes. En outre, les mesures expérimentales peuvent être comparées aux résultats de simulations numériques, donnant ainsi un aperçu de la physique impliquée dans ces sources. Bien que de nombreuses techniques existent pour la caractérisation temporelle complète des impulsions laser dans l'infrarouge, cela reste difficile dans l'UVX, d'autant plus que la plupart des schémas existants pour les impulsions infrarouges sont basés sur des phénomènes non-linéaires.

Les impulsions UVX, y comprises celles avec des durées attoseconde, ont été mesurées avec la technique FROG CRAB au cours des dernières années. Cette technique nécessite toutefois l'acquisition de plusieurs tirs, en supposant ainsi la stabilité de la source. Cette stabilité n'est pas toujours trouvée dans les cas des sources UVX cohérentes, basées sur des phénomènes non-linéaires. De plus, FROG CRAB nécessite l'utilisation d'un spectromètre d'électrons à bouteille magnétique, un dispositif coûteux et complexe. Toute technique de caractérisation visant à fournir des mesures monocoup, ainsi qu'à utiliser une configuration simple, doit être spécifique à chaque source.

Une nouvelle technique basée sur SPIDER est proposée dans ce chapitre pour la métrologie temporelle monocoup des impulsions des LELs UVX injectés, et conçue pour le cas particulier de l'installation FERMI, en Italie. La technique est basée sur un schéma de double injection, utilisant deux impulsions réplique, décalées spatialement et temporellement. Le LEL émet donc deux impulsions UVX dont le décallage spectral est l'original multiplié par l'ordre harmonique. Les deux répliques UVX interfèrent alors spectralement, ce qui est mesuré avec un spectromètre en ligne, de sorte que la technique n'est pas invasive pour les utilisateurs. Ce schéma a été testé lors d'une expérience de démonstration réalisée au LOA, et des simulations numériques LEL basées sur le code PERSEO, et présente l'avantage sur d'autres schémas de ne nécessiter aucune manipulation spécifique du faisceau d'électrons.

La caractérisation temporelle des SXRLs injectés par des harmoniques d'ordre élevé est plus complexe, car la largeur spectrale du gain est étroite et empêche l'utilisation de la même stratégie décrite ci-dessus. Dans ce chapitre, l'utilisation de la technique SEA TADPOLE pour ces sources a été proposée. Ce schéma nécessite une impulsion de référence, qui peut être trouvée dans une réplique de l'impulsion harmonique utilisée pour l'amplification, qui doit être préalablement caractérisée par une méthode telle que le HHSPIDER. La configuration expérimentale est relativement simple et le système permet des mesures monocoup, permettant à son tour d'optimiser la source en temps réel.

Le chapitre 5 présente la première implémentation de la technique CPA dans un LEL UVX injecté. La possibilité d'appliquer cette technique à des SXRLs est également discutée, ainsi que la mise en œuvre de compresseurs optiques plus efficaces grâce à l'utilisation de la diffraction conique. La CPA est une technique pour l'amplification d'impulsions laser ultra-brèves permettant d'obtenir de puissances de crête élevées, mise en œuvre pour la première fois en 1985. Par exemple, dans le cas d'un laser à état solide, la forte puissance d'une impulsion lors de l'amplification peut causer des dommages au milieu amplificateur, ainsi que des effets de propagation non-linéaire. Ceci peut être évité en étirant temporellement l'impulsion avant l'amplification en la propageant à travers un milieu ou un système optique dispersif, pour réduire la puissance de crête, et en la recomprimant ensuite à sa durée initiale. Ce potentiel de génération de hautes puissances rend les systèmes CPA très attractifs pour les sources UVX, où la mise en œuvre est confrontée à des défis différents que pour les lasers de lumière visible et infrarouge.

L'expérience CPA a été réalisée avec le LEL UVX FERMI. Une impulsion étirée injectée dans le LEL peut interagir avec plus d'électrons dans le paquet, augmentant l'énergie extraite de ceux-ci. De plus, cela conduit à une augmentation de la largeur spectrale UVX de sortie, qui à son tour permet d'obtenir des impulsions plus courtes après la compression par rapport à l'opération standard. Dans cette expérience, la durée des impulsions LEL en conditions standard, mesurée par corrélation croisée avec une impulsion infrarouge, était $91\,\mathrm{fs}$, tandis que l'utilisation de la CPA a permis de réduire la durée à $50\,\mathrm{fs}$. Des durées plus courtes peuvent être obtenues en étirant l'impulsion initiale plus fortement.

Dans le cas d'un SXRL injecté par des harmoniques, l'impulsion à amplifier a une durée typique de dizaines de femtosecondes, alors que le gain dans le plasma a une vie de quelques picosecondes ou nanosecondes. L'étirement de l'impulsion harmonique pour correspondre à cette durée peut augmenter considérablement l'énergie extraite pendant l'amplification, mais cela n'a pas encore été expérimentalement mis en œuvre.

Bien que cette technique permette une amplification améliorée de l'impulsion initiale, l'énergie de sortie qui peut être atteinte est limitée par la faible efficacité des réseaux de diffraction dans ce domaine spectral. Ce problème est plus pertinent dans le cas d'un SXRL, puisque l'impulsion initiale et celle de sortie sont dans le domaine UVX, par opposition à l'impulsion initiale de FERMI, dans le domaine UV, qui peut être étirée plus efficacement. De nombreux auteurs ont proposé l'utilisation de réseaux dans la géométrie conique comme moyen de surmonter cette limitation, étant donné que des efficacités atteignant 70% ont été obtenues avec cette géométrie. Dans ce chapitre, la phase spectrale introduite par un compresseur basé sur une paire de réseaux en géométrie conique est calculée.

En résumé, les sources d'impulsions ultra-brèves dans les domaines UVX et X mous sont utilisées aujourd'hui pour une multitude d'applications dans de nombreux domaines d'étude différents. La poursuite du développement de ces sources dans un proche avenir conduira à de meilleures performances dans leurs applications actuelles et étendra leur utilité à de nouvelles applications. Ce développement vise principalement à atteindre des intensités plus élevées, ainsi que des durées d'impulsion plus courtes. Cette thèse traite des sujets de la métrologie spatiale et temporelle des impulsions ultra-brèves UVX obtenues avec HHG dans les gaz, les LEL UVX injectés et les SXRLs injectés par des harmoniques.

L'augmentation de l'intensité des impulsions UVX ultra-brèves permettra, par exemple, une meilleure accessibilité expérimentale aux phénomènes non-linéaires UVX, ou la réalisation d'expériences basées sur des configurations de pompe-sonde UVX. Une solution directe consiste à augmenter lénergie des impulsions obtenues dans ces sources. Cependant, une focalisation efficace des faisceaux générés est également nécessaire pour atteindre des intensités élevées. Ceci, à son tour, nécessite l'utilisation d'optiques de haute qualité, ainsi que la génération d'impulsions avec de bons fronts d'onde. Notre senseur Hartmann est un outil puissant pour la métrologie spatiale des impulsions UVX, car il peut fournir simultanément leur profil d'intensité et leur front d'onde.

En particulier, il est intéressant d'améliorer les intensités qui peuvent être obtenues avec les sources HHG, car cela permettra d'utiliser des configurations compactes pour réaliser des expériences actuellement limitées à des installations de grande envergure telles que les LELS ou les synchrotrons. Dans cette thèse, un senseur de front d'onde Hartmann, construit et calibré au LOA, a été utilisé pour étudier les propriétés spatiales d'impulsions harmoniques en fonction des paramètres de génération et du front d'onde infrarouge, avec des mesures monocoup. Nous avons également observé les fronts d'onde de trois ordres harmoniques individuels en utilisant trois miroirs multicouches.

L'astigmatisme observé dans les fronts d'onde harmoniques peut être corrigé lors de la focalisation du faisceau avec des miroirs incurvés. Le senseur Hartmann UVX a été utilisé dans cette thèse pour optimiser précisément l'alignement d'un système de focalisation basé sur deux miroirs toroïdaux en incidence rasante, réduisant le diamètre du foyer harmonique d'un facteur de ~ 5 en quelques minutes. Ce senseur a été utilisé aussi pour la caractérisation de surfaces de miroirs multicouches UVX avec un faisceau harmonique. Ces tests sont généralement limités aux synchrotrons, car les techniques les plus courantes nécessitent un flux élevé. La possibilité d'effectuer ces tests dans des configurations compactes sera extrêmement utile pour les fabricants. Cependant, les senseurs de front d'onde existants pour l'UVX ont des ouvertures numériques typiques de l'ordre de 0.01, ce qui limite leur plage d'applicabilité aux faisceaux à faible divergence. Comme solution, nous avons récemment développé un senseur UVX avec une $\mathrm{NA} = 0.1$, qui sera utilisé pour des systèmes de focalisation avec des courtes distances focales et pour étudier les fronts d'onde des impulsions UVX divergentes, telles que celles obtenues par HHG avec des cibles solides.

D'autre part, des efforts significatifs sont faits pour obtenir des durées d'impulsion plus courtes avec des sources UVX, ce qui fournira une meilleure résolution temporelle pour des expériences traitant, par exemple, de la dynamique ultra-rapide de la matière. En particulier, des impulsions sub-100-as ont déjà été obtenues avec des configurations compactes basés sur la HHG. Néanmoins, les applications possibles de ces impulsions attosecondes sont limités par leurs faibles énergies. Pour cette raison, il y a un grand intérêt à raccourcir les durées d'impulsions obtenues avec des LELs UVX injectés ou les SXRLs injectés, aujourd'hui typiquement de l'ordre de $100\,\mathrm{fs}$, ou plus. Il est important de souligner, cependant, que les durées d'impulsion obtenues dans ces deux sources sont généralement connues au moyen de simulations numériques ou de mesures incomplètes basées sur des schémas de corrélation d'impulsions. De plus, les techniques existantes pour la caractérisation temporelle complète des impulsions UVX sont généralement basées sur des schémas multicoup, ce qui nécessite de longes mesures et ne fournit que des moyennes. Le développement de méthodes précises, fiables et monocoup pour la caractérisation temporelle des impulsions UVX est fondamental afin de réduire les durées d'impulsion dans le futur. Deux schémas potentiellement monocoup pour la métrologie temporelle des deux sources susmentionnées ont été proposés théoriquement dans cette thèse. La mise en œuvre de ces techniques ou de techniques similaires fournira un contrôle précis et en temps réel des durées d'impulsion.

L'utilisation de schémas CPA dans un LEL UVX injecté peut fournir à la fois des énergies d'impulsion plus élevées et des durées plus courtes. Lors de la première implémentation du schéma à FERMI, nous avons obtenu un raccourcissement des impulsions UVX d'un facteur de près de 2 par rapport aux conditions standard, de $91\,\mathrm{fs}$ à $50\,\mathrm{fs}$, après avoir étiré l'impulsion UV initiale de $170\,\mathrm{fs}$ à $290\,\mathrm{fs}$. Des expériences de suivi qui seront effectuées dans un proche avenir tenteront d'atteindre des durées proches de $10\,\mathrm{fs}$ en étirant davantage l'impulsion initiale. L'utilisation d'impulsions initiales plus longues qui correspondent à la durée du faisceau d'électrons, de l'ordre de $1\,\mathrm{ps}$, augmentera considérablement l'énergie de l'impulsion LEL. Cependant, cette augmentation d'énergie obtenue avec la CPA est limitée par la faible efficacité des réseaux de diffraction du compresseur pour le domaine UVX. Au prix d'une conception plus complexe, la mise en œuvre d'un compresseur basé sur la diffraction conique, discutée dans cette thèse, fournirait des efficacités plus élevées.

ÉCOLE DOCTORALE
Ondes et Matière
(EDOM)

Titre : Métrologie spatiale et temporelle des impulsions cohérentes et ultra-brèves dans le domaine ultraviolet extrême

Mots clefs : Harmonique d'ordre élevé, Laser à électrons libres, Front d'onde, Laser X, Métrologie temporelle, Amplification à dérive de fréquence

Résumé : Aujourd'hui, il existe trois sources principales délivrant des impulsions ultra-brèves de rayonnement ultraviolet extrême (UVX). Les harmoniques d'ordre élevé (HHG, en anglais) générés dans les gaz rares peuvent fournir des impulsions attosecondes. Cependant, leur énergie, le plus souvent de l'ordre du nanojoule, limite les applications. L'amplification des impulsions harmoniques dans les plasmas créés par laser (SXRL, en anglais) peut fournir des énergies de plusieurs dizaines de microjoules. Des énergies plus élevées peuvent être obtenues avec les lasers à électrons libres (LEL) UVX injectés, mais ce sont des très grandes infrastructures ayant un accès plus limité.

Ces dernières années, des progrès significatifs ont été réalisés avec chacune des ces sources, avec pour objectif la génération d'impulsions plus brèves. Il est devenu nécessaire de développer des nouvelles techniques de métrologie temporelle des impulsions XUV ultra-brèves. De plus, beaucoup d'expériences, comme celles impliquant des phénomènes non-linéaires, nécessitent de hautes intensités UVX. La focalisation efficace des impulsions de faibles énergies peut significativement augmenter le domaine d'application. De bons fronts d'onde sont nécessaires pour focaliser les impulsions UVX à haute intensité, et les optiques doivent aussi être de bonne qualité et alignées avec précision.

Dans cette thèse, les propriétés spatiales des harmoniques d'ordre élevé ont été étudiées en profondeur grâce à un senseur de front d'onde UVX. Cet appareil, couplé à une source HHG a démontré être utile pour la caractérisation de table et à la longueur d'onde ainsi que pour l'optimisation de systèmes optiques UVX. Le problème de la mise en place de la caractérisation temporelle d'impulsions UVX est aussi discuté en détail, et deux nouveaux schémas pour la complète reconstruction d'impulsions de LEL injectés et de lasers X à plasma sont présentés. Finalement, la première implantation d'un système d'amplification à dérive de fréquence (CPA, en anglais) sur un LEL UVX est présentée et son implantation pour les lasers X à plasmas est aussi discutée.

Title : Spatial and temporal metrology of coherent ultrashort pulses in the extreme-ultraviolet domain

Keywords : High-harmonic generation, Free-electron laser, Wavefront, X-ray laser, Temporal metrology, Chirped pulse amplification

Abstract : Nowadays, there are three main of ultrashort pulses in the extreme-ultraviolet (XUV) spectral domain. High-order harmonic generation (HHG) in rare gases is able to provide attosecond pulses. However, their energy, often of the order of nanojoules, limits their number of applications. Amplification of such pulses in laser-driven plasmas can provide energies of tens of microjoules. Higher pulse energies can be obtained from seeded XUV free-electron lasers (FELs), large-scale facilities with more limited accessibility.

In recent years, significant progress has been made with each of these sources towards the generation of shorter pulses. It is thus necessary to develop new techniques for full temporal metrology of ultrashort XUV pulses. Additionally, many experiments, such as those involving nonlinear phenomena, require high XUV intensities. Efficient focusing of low-energy pulses can significantly increase their range of application. Good wavefronts are required in order to focus light pulses to high intensities, and the optics must be of high quality and precisely aligned.

In this thesis, the spatial properties of high-harmonic pulses are extensively explored thanks to the use of an XUV Hartmann wavefront sensor. This device is also proven here to be useful for tabletop, at-wavelength characterization and optimization of XUV optical systems with HHG sources. The problem of performing full temporal characterization of XUV pulses is also discussed in detail, and two new schemes for complete pulse reconstruction for seeded XUV FELs and seeded SXRLs are presented. Finally, the first implementation of chirped pulse amplification (CPA) in a seeded XUV FEL is reported, and its implementation in seeded SXRLs is discussed as well.

Université Paris-Saclay
Espace Technologique / Immeuble Discovery
Route de l'Orme aux Merisiers RD 128 / 91190 Saint-Aubin, France